In-depth Understanding of the Stability Response of a Novel 3D Fiber-Metal
Laminate under Axial Impact Loading

by

Davide De Cicco

Submitted in partial fulfilment of the requirements

for the degree of Doctor of Philosophy

at

Dalhousie University

Halifax, Nova Scotia

August 2019

To my Mother,

Who has always done her best to support me.

Table of Contents

List of Tables

List of Figures

Abstract

Environmental concerns have developed significant challenges for various industries, including the automotive industry. In fact, the industry has been challenged to halve vehicles' fuel consumption by 2025. Considering the fact that engine efficiency has been approaching a plateau, the other effective means for reaching the set target is believed to be achieved by reducing the weight of various components of vehicles. It should be noted that, unfortunately, vehicles collisions occur frequently; consequently, vehicles must be designed in such a way to assure the maximum safety of the occupants, thereby generating an additional constraint to the weight-reduction approach.

To address the latter design constraint, the automotive industry has been conducting an extensive series of research over the recent decades to explore the utilization of different light-weight metallic alloys and fiber-reinforced plastic composites (FRPs). However, relatively recently, it was proved that one could achieve optimal results by taking advantage of the marriage of the positive attributes of two distinctly different classes of materials (i.e., metallic alloys (preferably, the light-weight alloys), and FRPs). The aforementioned material combination is referred to as a fiber-metal laminate (FML) and was first used in aviation field (e.g., Airbus A380). The resulting hybrid combination enables one to take advantage of the unique properties of each constituent. Following this path, our research group recently developed a new class of three-dimensional FML that offers exemplary specific strength and stiffness, superior energy absorption capacity, and excellent damping properties compared to the traditional materials used throughout the industry, in a cost-effective manner. It takes advantage of a recently marketed 3D-knitted fiberglass fabric, infilled with a resilient foam, and sandwiched between thin sheets of light-weight magnesium alloy.

The primary application target of this 3D fiber-metal laminate (3D-FML) has been transport vehicles' body components, which are subjected to various loadings, including impacts. The superior energy absorption capacity of this new FML under a lateral impact, in comparison to traditional fiber-reinforced composite materials, has already been demonstrated by our research group. However, the targeted components may also

encounter in-plane compressive loading applied at various loading rates, which could lead to the instability of the structural system.

The overall aim of this work is to provide a deeper insight into the response of slender structural components made with the 3D-FML, when subjected to in-plane compressive load applied at various strain rates (particularly, to low-velocity impact loading). The task will be done by conducting a series of systematic and comprehensive experimental and numerical investigations. The finite element method is utilized to carry out the parametric studies, identifying and ranking the material properties that would most affect the response of the system. In addition, the interface bond strength (which will be shown to be the Achilles' heel of the introduced hybrid system), is optimized, thereby improving the overall fabrication process of the FML in an efficient and cost-effective manner. In addition, the feasibility of graphene nanoparticles (GNPs) as a means of enhancing the interface bond strength of the system was explored. The results revealed that the lack of chemical bond between the GNP-reinforced resin and the magnesium skins of the hybrid material system significantly limited the potential influence of the GNPs.

It is also well-known that composites' performance is strongly affected by the existence of delamination(s) within them. Therefore, the effect of initial delamination on the performance of the material system is also systematically investigated.

Finally, a set of simple semi-empirical equations is developed by which practicing engineers could quickly evaluate the buckling and maximum load bearing capacities of the 3D-FML subjected to in-plane static and low-velocity impact loading states.

List of Abbreviations and Symbols Used

3D-FGF	Three-dimensional fiberglass fabric
3D-FML	Three-dimensional fiber-metal laminate
Al	Aluminum
BC	Boundary conditions
CCE	Cold-cured epoxy
Cf	Carbon fiber
CFRP	Carbon fiber-reinforced plastic
CNT	Carbon nanotubes
CPU	Central processing unit
CZM	Cohesive zone model(ling)
DCB	Double-cantilever beam
DLVDT	Dynamic linear variable displacement transducer
EA	Epoxy adhesive
ERR	Energy release rate
FD	Finite difference
FE	Finite element
FEA	Finite element analysis
FEM	Finite element method
Fg	Fiberglass
Fix	Fixed boundary condition
FML	Fiber-metal laminate
Fo	Foam
Fs	Foam with higher density

Fw	Foam with lower density
FRP	Fiber-reinforced plastic composite
HCE	Hot-cured epoxy
HSS	High-strength steel
GLARE	Glass laminate aluminum reinforced epoxy
GNP	Graphene nano-platelets
LN_2	Liquid nitrogen
MA	Methyl-methacrylate adhesive
ME	MasterEmaco adhesive
Mg, MG	Magnesium
N	Neat specimen
ND	No initial delamination
NSERC	Natural sciences and engineering council Canada
Pin	Pinned boundary condition
PL	Plexus adhesive
OPI	Out-of-plane impact
QB	QuakeBond adhesive
RMS	Root mean square
RT	Room temperature
SB	Sandblasting method
SBC	Sandblasting with resin coating method
SHELL	Thin shell model
SI	Stability index
SOLID	Solid model
sr	Strain rate

ST	Steel
TSHELL	Thick shell model
V	Fiberglass veil
VCCT	Virtual crack closure technique
UV	Ultra-violet
WS	West System
wt%	Weight percentage
xFEM	Extended finite element method

Note: "s" following above acronyms makes them plural.

A	Cross-sectional area – imperfection amplitude
$\underline{A}, \underline{B}$	Matrix
$A_n, D_n,$	Fourier series coefficients
A_c, A_{MG}, A_{ST}	Cross-sectional area of the sandwich core, magnesium- and steel-based sandwich skins
$\mathcal{A}$	Area under the normalized traction-separation curve
b	Specimen's width
c	Dimensionless parameter – speed of sound
$\underline{C}$	Damping matrix
$\underline{\underline{C}}$	Fourth-order constitutive tensor
D_{11}	Flexural rigidity in the longitudinal direction
G	Shear modulus
G_c	Shear modulus of the sandwich core
G_{IC}, G_{IIC}	Mode I and II fracture toughness
E	Modulus of elasticity – energy

E_c, E_s	Modulus of elasticity of the sandwich core and skin
E_{MG}, E_{ST}	Equivalent modulus of elasticity of the magnesium- and steel- based skins
E_p	Energy to peak
E_{tot}	Total energy
f	General function - frequency
$\underline{f_s}$	Surface forces vector
$\underline{f_v}$	Volume forces vector
h	Finite difference step – specimen height
H	Heaviside function
i	Integer constant
$\underline{\underline{K_T}}$	Tangent matrix
$\underline{\underline{K_{Tot}}}$	Nonlinear rigidity matrix
I	Moment of inertia
k	Linear spring
L	Length
L_{max}	Maximum length
L_{tot}	Total length
M	Bending moment
$\underline{\underline{M}}$	Mass matrix
n	Mode number – Integer constant
$\underline{n}$	Vector normal to a surface
N_i, N_i^*, N_i^{**}	Shape functions
P	Point load

p	Dimensionless parameter – magnitude of lateral imperfection
P_{cr}	Critical buckling capacity
Q	Shear
$q, \underline{q}$	Distributed load (scalar, vector)
r	Dimensionless parameter
$\underline{R}^i$	Internal forces vector
$\underline{R}^e$	External forces vector
S	Shear stiffness
SI	Stability index
t_c	Thickness of the sandwich core
t_f	Thickness of the sandwich faces
T	Transpose operator
$\underline{u}$	Displacement vector
$\underline{u}_0$	Initial position vector
U	Potential energy
$\underline{v}$	Eigenvector
W	Weight
$\underline{x}$	Position vector
$\hat{\underline{x}}$	Position of the closest projected point
X_c, X_T	Longitudinal strength in compression and tension
$y, \underline{y}$	Deflection (scalar, vector)
$\tilde{y}, \underline{\tilde{y}}$	Deflection of the initial imperfection (scalar, vector)
y_b, y_s	Deflections due to bending and shear
Y_c, Y_T	Transverse strength in compression and tension

β	Effective length parameter
$\delta_N, \delta_N^{fail}$	Normal separation displacement and separation displacement at failure
$\delta_T, \delta_T^{fail}$	Tangential separation displacement and separation displacement at failure
Δt	Time step
Δt	Critical time step
ε_{max}	Maximum strain
$\underline{\underline{\varepsilon}}$	Strain matrix
η	Wave number
λ	Eigenvalue – scalar parameter
$\lambda_1, \lambda_2, \lambda_{fail}$	Cohesive material model's non-dimensional parameters
ν	Poisson's ration
ξ	Damping coefficient
ρ	Material density
σ	Standard deviation – stress
σ_y	Yield stress
$\underline{\underline{\sigma}}$	Stress matrix
σ_{cr}	Critical wrinkling stress
$\sigma_c, \sigma_{MG}, \sigma_{ST}$	Stress in the sandwich core, the magnesium- and steel-based sandwich skins
$\sigma_{MG}^{cr}\ \sigma_{ST}^{cr}$	Critical stress in magnesium and steel skins
σ_{max}	Maximum tensile and shear stress
σ_N, σ_T	Normal and tangent surface traction
τ	Normalized pulse duration
φ	Potential function

ω	Angular frequency
φ	Potential function
Ω	Domain
$\partial\Omega$	Surface of a domain

Acknowledgements

First, I wish to express my sincere gratitude to my research supervisor, Dr. Farid Taheri, without whom this Ph.D. adventure would not have happened. I am grateful for all his help, support, guidance, patience, and invaluable advice.

Second, I would like to acknowledge the help of the Mechanical and Civil Engineering technicians, especially Mark MacDonald, Albert Murphy, Brian Kennedy, and Jesse Keane during the experimental part of my work. I would also like to extend my gratitude to Dr. Andrew Corkum and Dr. Stephen Corbin for providing some very useful pieces of equipment for the research.

I would like to extend my gratitude to my Guiding Committee members Dr. Darrel Doman, Dr. Dmitry Garagash, and the external examiner, Dr. Mehdi Hojjati for their review of this research work, their comments and suggestions, as well as their technical feedback.

Last, but not least, I wish to thank all my colleagues and office friends, in particular, Dr. Zohreh Asaee and Mehdi Ghasemi. Without their support and collaboration, these years of difficult work would have been far less enjoyable.

Chapter 1: Introduction

1.1. Context of the Present Research

Environmental concerns have created significant challenges for various sectors. The North American auto industry has been challenged to halve vehicles' fuel consumption by 2025. In addition, many countries have already established fuel consumption regulations that are extremely difficult to meet. Therefore, the market competition towards the production of low-energy consumption and low emission vehicles has never been so fierce. Engine efficiency has received significant attention during the past few decades; however, it has matured, and its future advancements appears to be approaching a plateau. Therefore, the next logical avenue that would facilitate reaching the said goal has been deemed to be reducing the weight of various components of vehicles while maintaining or even improving occupant safety standards. Indeed, the safety of drivers and passengers has presented a significant issue as a primordial design constraint. According to the 2017 Canadian Motor Vehicle Traffic Collision Statistics, there have been 1,841 fatalities and 9,960 serious injuries as a result of a total of 114,158 collisions in a country with a comparatively low population. Although these numbers are the lowest on record, it can be seen that vehicle collision is, unfortunately, still very frequent; therefore, vehicles must be designed to provide the maximum safety to the occupants.

To address these two demanding design challenges, the automotive industry has conducted an extensive research over several decades in search of the optimal metallic alloys and lightweight and non-corrosive fiber-reinforced polymer composites (FRPs). However, the cost of FRPs has impeded their widespread use and has limited their utilization to a few luxury vehicles. Therefore, it was envisaged that the best results could be achieved by taking advantage of the positive attribute of two materials used in the industry (i.e., metals and composites), as was done a few decades ago by the aviation industry. The outcome of such a combination is referred to as fiber-metal laminate (FML); it consists in an association of FRP layers interleaved with thin metallic sheets. By taking advantage of the unique properties of each constituent, FMLs offer more superior attributes

in terms of specific stiffness and strength, durability and resistance against impact, all with a significantly reduced weight compared to bulk metals or FRP counterparts.

Following this path, our research group recently developed a new class of FML to meet the design criteria and aforementioned challenges. The resulting FML, shown in Figure 1-1, provides the required attributes (i.e. impressive specific stiffness, strength and energy absorption capacity, as well as superior fatigue and damping characteristics), in a cost-effective fashion. It takes advantage of a recently marketed 3D-knitted E-type fiberglass fabric (3D-FGF) filled with a resilient foam, sandwiched in between thin sheets of magnesium, an alloy 75% lighter than steel and 35% lighter than aluminum. The outcome is a very resilient and strong light-weight material, with a significantly lower cost than conventional FRPs. Note that to generate thicker panels, either a taller 3D-FGF fabric could be used, or the aforementioned configuration could be repeated to achieve the desired thickness. Another positive attribute of this 3D-FML, especially for the transport vehicle sector, is its excellent vibration damping properties, as demonstrated by the author (De Cicco & Taheri, 2018c).

(a)   (b)
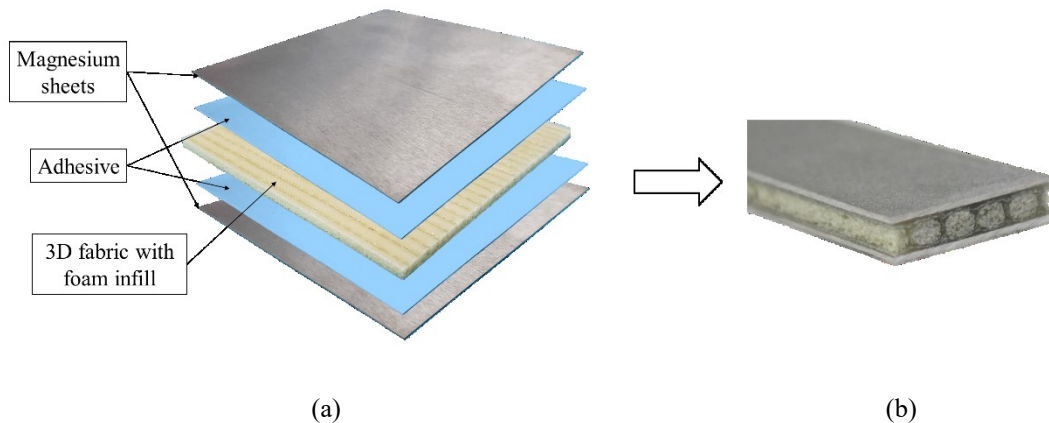
Figure 1-1. A rendition of the 3D-FML hybrid composite: (a) exploded view, showing the various components, and (b) the final product.

The initial target application of this 3D-FML has been to fabricate transport vehicle body components (e.g., doors, and fenders) and enclosures (e.g., trucks, buses and trains) all of which could be subjected to various loadings, including impacts. Its superior energy absorption capacity in case of a lateral impact compared to traditional FRP has already been demonstrated by our research group (Asaee et al., 2017; Asaee et al., 2015; Asaee &

Taheri, 2016, 2017). However, many structural components also become subject to in-plane loading. Therefore, buckling, which occurs as a result of the loss of stability of the structure in most cases due to an in-plane compressive loading, would have to also be considered when designing slender structural components, especially if the component would be subjected to a high rate of loading. The effect of such a phenomenon can be clearly seen in Figure 1-2, which exhibits the response of a vehicle's door, which is made of thin sheets of steel, in a collision event.

Figure 1-2. Small overlap frontal crash test of a 2012 Volkswagen CC[1]. Buckling of the front door is highlighted.

Depending on the loading intensity and speed, buckling may induce large deformations that need to be characterized and quantified to guarantee a minimum survivable space to the vehicle's passengers in case of a collision. Therefore, the impact response and energy absorption capacity of any FML candidate for such applications should be comprehensively investigated and understood. Furthermore, it is well-known that the Achilles' heel of all laminated composites is their relatively weaker interlaminar strength compared to their bending and axial strengths, and the 3D-FML is no exception. The likelihood of initiation of a delamination within such materials becomes even greater when they become subjected to a suddenly applied axial compressive loading, as will be discussed throughout this work.

The effective assessment of performances of today's lightweight hybrid materials and complex structural components made by such materials requires cost-effective

---
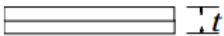
[1] The Insurance Institute for Highway Safety report, 2013 (https://www.iihs.org/).

methodologies and approaches. Therefore, numerical simulation has become an indispensable and effective tool used in characterizing new materials and products, for their parametric studies, and even for obtaining certification of certain classes of structures. One of the main challenges when conducting numerical analysis is the balance between the accuracy of the results, effort put into modelling, and computational cost. In particular, despite the remarkable advancements that have been made in computational mechanics in the past few decades, the reliable simulation and prediction of fracture and failure of bulk materials and bonded interfaces are still challenging. The latter issue will also be discussed in the present work.

1.2. Introduction to Sandwich structures

In their most basic form, sandwich structures consist of a pair of stiff external thin plates, often called skins, and a lightweight internal core, mated together with an adhesive. The lightweight core distances the skins, thus increasing the bending rigidity of the component, with a marginal increase in total weight. Table 1-1 shows an estimation of the relative properties of two sandwich plates, having different core thicknesses, compared to a monolithic plate. The advantage of such a structure is clearly visible: a 37-fold higher stiffness can be obtained with just 1.06 times increase in weight compared to the monolithic counterpart. However, the downside of such structures is their increased thickness (four times for the reported example) which must be accounted for in applications where the components thickness must be below a certain thickness.

Table 1-1. Example of structural efficiency of sandwich panels as a function of weight (Petras, 1999).

	t	$2t$	$4t$
Relative bending stiffness	1	7.0	37
Relative bending strength	1	3.5	9.2
Relative weight	1	1.03	1.06

Virtually any material available as a thin sheet can be used as the skins; however, their desired properties usually are: high stiffness and strength; good resistance to abrasion, impact and chemicals; wear resistance; and, for some specific applications, resistance to UV rays and radiation. Therefore, metals, such as steel and aluminum, or FRPs are the most commonly used materials for the skins. Regarding the core, lightweight and relatively high shear stiffness are the two main sought properties, but thermal or acoustical insulation properties could also be critical. Therefore, common core materials are balsa wood, thermoplastics, thermosets and metallic foams, and honeycomb core-structures.

Because of their complex structure and depending on the loading type and geometry, sandwich panels may experience multiple modes of failure. These are briefly presented in Figure 1-3 from a qualitative point of view. In mode (a) the structure is subjected to pure bending and the failure is caused by fracture or yielding of the skins. The skin in tension is more prone to fracture, while the one in compression is more prone to yielding. In case (b), the shear load is applied to the plate; therefore, the core is the component most likely to fail, and the failure takes the characteristic diagonal shape. For cases (c) and (d), the plate is under bending and/or axial compression, which leads to a localized indent of the core or delamination-buckling of the skin. The geometry of the plate, initial imperfections, interfacial bond strength (between the skins and core), as well as the tensile and compressive and shear strengths of the skins and core are all parameters influencing the resulting damage mode. In case (e), further discussed in the next section, the plate is under axial compression and when it becomes too slender, it may experience global buckling. It should be noted that the material in the buckled structure might still be in the elastic range, thus not damaged; however, since many buckling modes are unstable, it is recommended to avoid such a situation. An axial load is also applied for damage case (f), which is in the form of a shear crimping failure. The excessive shear stress generated by the axial compression, associated with the presence of eccentricity of the load, leads to the yielding of the skins and a shear fracture of the core. The failure mode (g) is referred to as face wrinkling, which is highly influenced by the core compressive strength and face sheets properties. This failure is often seen under impact buckling load and will be further discussed in the oncoming sections. Last, failure can be caused by a static or dynamic load applied transversely to the sandwich faces, as shown for the case (h). Depending on the

load intensity and speed, as well as skin and core thicknesses, the damage can be limited to the faces on which the load is applied or can reach the other side of the plate. The reader should refer to Zenkert (1997) for additional information, including the practical design equations.
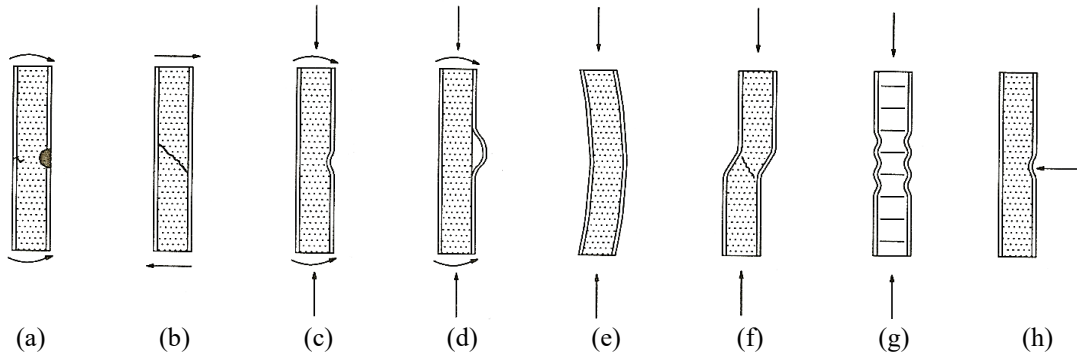
Figure 1-3. Different failure modes in sandwich structures (Zenkert, 1997).

1.3. Buckling

1.3.1. Introduction

As briefly mentioned earlier, buckling can be defined as the sudden advent of a large deformation resulting from an equilibrium instability. It occurs in slender structures when the compressive stress state exceeds a threshold and deforms the structure suddenly and excessively. Mathematically, it is a bifurcation in the equations of static or dynamic equilibrium.

The stress state determines if the buckling is elastic, i.e., the structure is able to recover its original shape once the load is removed, or plastic. For each of these types, the loading rate determines if the buckling is static or dynamic. Buckling is considered quasi-static if the strain rate is lower than 10^{-1} s^{-1} and medium rate if the rate is in the range of 10^{-1} to 10^2 s^{-1}. Generally, the inertia effects can be neglected for these ranges. Higher ranges define dynamic buckling. In static buckling analysis, the focus is on the displacement response, the stress state, and the load amplitude. In dynamic buckling, both the load amplitude and load duration affect the overall response. Also, the inertia effects, unless demonstrated differently, must be accounted for. Dynamic buckling generated by a transient load

6

consisting of a single pulse characterized by its amplitude, shape, and duration leads to what is referred to as pulse buckling. The structure deforms to an unacceptably large amplitude as the result of the transient response to the applied load. If the load is oscillatory, it is referred to as vibration buckling. In vibration buckling, the amplitudes of vibration caused by an oscillating load become unacceptably large at the specific critical combinations of load amplitude, load frequency, and structure damping properties.

A further distinction between load types in a dynamic analysis is done by distinguishing a high intensity load applied for short or even very short ($\sim 10^{-6}/10^{-8}$ s) period of time versus a relatively low loads applied for a longer time. The critical buckling state is generally identified when a large change in the structural response occurs in response to a small increase in the applied load (Ari-Gur & Elishakoff, 1997). However, the limiting criteria are still open to interpretation and are highly dependent on the application and design constraints. In fact, a structure can survive a large axial load before reaching the limit condition if the load duration is less than a certain limit. Furthermore, under a short duration intense loading, a structure's preferred buckling mode would be at a much higher order than the one taking place under a static buckling event. An illustration of this phenomenon is provided in Figure 1-4. It can be seen that for the static case, buckling occurs in the middle of the cylindrical shell, while in the dynamic case, the buckling occurs at the bottom-end of the shell. Also, note the drastic reduction of the buckled wavelength in the dynamic case.

(a)   (b)

Figure 1-4. Comparison between (a) static and (b) dynamic buckling patterns for a thin cylindrical shell (Lindberg & Florence, 1987).

1.3.2. Buckling of Beams

1.3.2.1. Equation of Motion

The work presented in this thesis relates to the buckling behaviour of composites panels. Since beam-like specimens are investigated experimentally in this work, therefore, the theoretical basis of buckling of beams is briefly presented.

Consider the free-body diagram of an infinitesimal portion of a beam shown in Figure 1-5. The beam is subjected to an axial load, P, a distributed lateral load, $q(x,t)$, and rests on an elastic foundation having linear stiffness k. Furthermore, the beam has an initial imperfection defined by the function $\tilde{y}(x)$. Writing the equilibrium of forces, we obtain:

$$\rho A \frac{\partial^2 y}{\partial t^2} + ky - q = \frac{\partial Q}{\partial x} \tag{1-1}$$

where $y(x,t)$ is the deflection of the beam, ρ is the material density, and A is the cross-sectional area. Additionally, the equilibrium of the bending moments gives:

$$Q = \frac{\partial M}{\partial x} - P\frac{\partial}{\partial x}(y + \tilde{y}) \tag{1-2}$$

Considering the Euler-Bernoulli beam theory, we know that:

$$M = -EI\frac{\partial^2 y}{\partial x^2} \tag{1-3}$$

where E and I are the beam's modulus of elasticity and the second moment of area (or moment of inertia). Therefore, combining equations (1-1) to (1-3), the following general form of the equation of motion is obtained:

$$EI\frac{\partial^4 y}{\partial x^4}(x,t) + P\frac{\partial^2 y}{\partial x^2}(x,t) + \rho A \frac{\partial^2 y}{\partial t^2}(x,t) + ky(x,t) = -P\frac{\partial^2 \tilde{y}}{\partial x^2}(x) + q(x,t) \tag{1-4}$$

In addition to the loads, geometry and material properties of the beam, this equation accounts for the inertia effects, thus allowing for the modelling of impact buckling as well as static buckling.
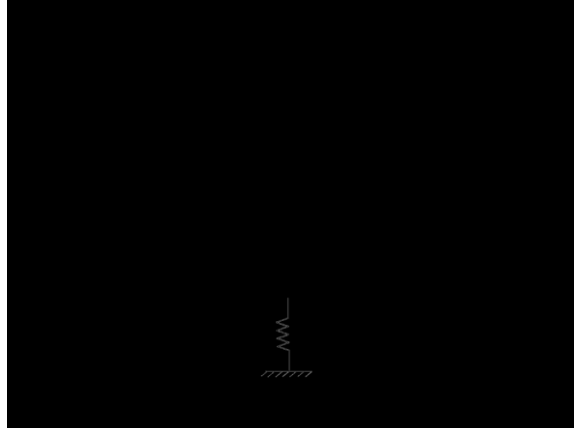
Figure 1-5. Free-body diagram of an infinitesimal portion of a beam under axial compression, resting on an elastic foundation and subjected to a distributed lateral load.

1.3.2.2. Static Elastic Buckling

The most fundamental and common buckling case is the case of a perfectly straight beam under axial compressive static load, with no lateral support or distributed load. For such a case, equation (1-4) simplifies to:

$$EI \frac{\mathrm{d}^4 y}{\mathrm{d}x^4}(x) + P \frac{\mathrm{d}^2 y}{\mathrm{d}x^2}(x) = 0 \qquad (1\text{-}5)$$

Note that the partial derivative is replaced by a total derivative since there is no dependence on time. The solution of this equation is in the following form:

$$y(x) = A \sin \sqrt{\frac{P}{EI}} x + B \cos \sqrt{\frac{P}{EI}} x + Cx + D \qquad (1\text{-}6)$$

The constants A, B, C and D are found using the boundary conditions. Note that an analytical solution exists only for some boundary conditions. In other cases, approximated values would have to be obtained numerically.

The solution of equation (1-6) leads to the well-known Euler's buckling formula, which predicts the buckling load for a beam:

$$P_{cr} = \frac{\pi^2 EI}{(\beta L)^2}$$

(1-7)

where the parameter β is used to define the effective length of the beam. Its value depends on the boundary condition and its values are shown in Figure 1-6.

$\beta=2$ $\qquad$ $\beta=1$ $\qquad$ $\beta=0.5$ $\qquad$ $\beta\approx0.7$
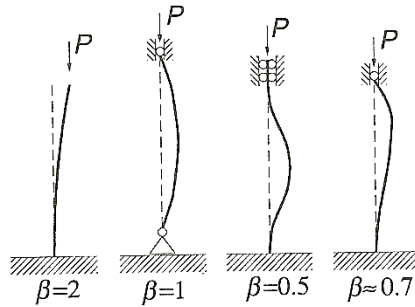
Figure 1-6. Effective length coefficients for the Euler buckling load (Zenkert, 1997).

1.3.2.3. Initial Imperfections

The initial imperfection of a beam can be measured or expressed via a mathematical function. An effective and convenient way to model it is by using the Fourier series, i.e.:

$$\tilde{y}(x) = \sum_{n=1}^{\infty} A_n \sin(\eta x)$$

(1-8)

where A_n is the amplitude of the perturbation and $\eta = \frac{n\pi}{L}$ is the wave number. The practicality of representing the perturbation in such a mathematical form is that it allows to easily express random imperfections in the beam. Specifically, this is done by defining the values of the coefficients A_n using a Gaussian distribution of mean zero and standard deviation $\sigma(\eta)$. If σ is independent from of the wave number, then this random perturbation is called white noise. The random imperfections can be used for analytical calculation as well as numerical simulations. In fact, random initial imperfections can be generated and implemented in finite element models.

1.3.2.4. A General Numerical Solution

The analytical buckling solutions for more complex scenarios than the one presented in section 1.3.2.2. are available in the literature (Davalos & Qiao, 1997; Sotiropoulou & Panayotounakos, 2004; Wang & Wang, 2004). However, analytical solutions are not always convenient to use or obtain. A more practical method for obtaining the buckling load of beams is the use of the finite difference method (FDM). An example is presented here, for the case of a beam having fixed-fixed boundary condition, resting on elastic support, subjected to both an in-plane compressive load and out-of-plane distributed load, hosting an initial imperfection (cf. Figure 1-7(a)).
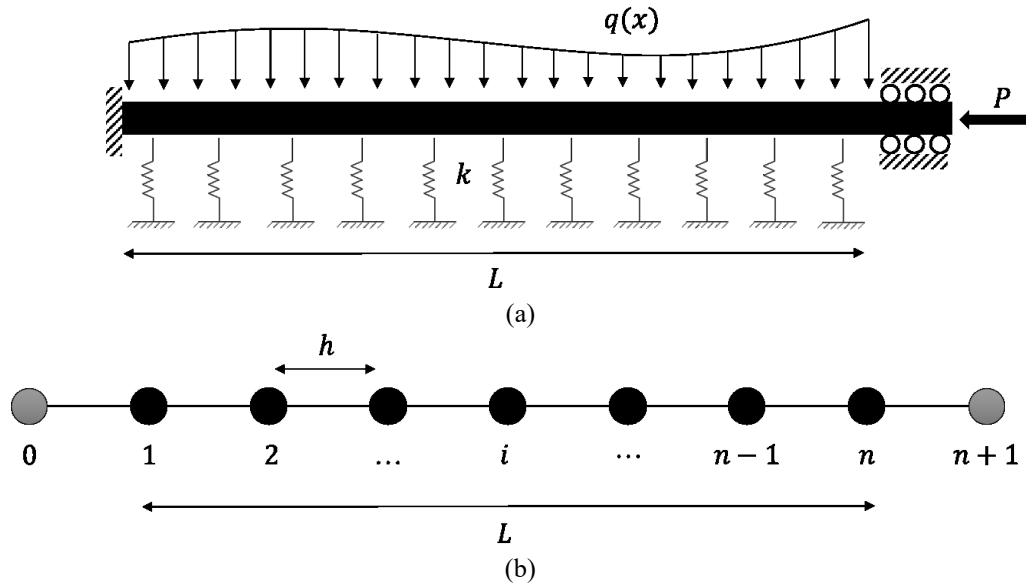
Figure 1-7. (a) Schematics of a beam having fixed-fixed boundary condition, resting on elastic support, subjected to both an in-plane compressive load and out-of-plane distributed load, (b) its finite difference discretization.

The equation representing the behaviour of the beam is as follows:

$$EI\frac{d^4y}{dx^4}(x) + P\frac{d^2y}{dx^2}(x) + ky(x) = -P\frac{d^2\tilde{y}}{dx^2}(x) + q(x) \tag{1-9}$$

The beam is discretized using n nodes spaced at a constant interval h (see Figure 1-7(b)). Choosing a central finite difference scheme in $O(h^2)$, equation (1-9) can be written in a discretized fashion, for any node i:

$$\frac{EI}{h^4}(y_{i-2} - 4y_{i-1} + 6y_i - 4y_{i+1} + y_{i+2}) - \frac{P}{h^2}(y_{i-1} - 2y_i + y_{i+1}) + ky_i$$

$$= -\frac{P}{h^2}(\tilde{y}_{i-1} - 2\tilde{y}_i + \tilde{y}_{i+1}) + q_i \tag{1-10}$$

Note that nodes 0 and $n+1$ are fictitious but are required for the central difference scheme. We are looking for the solution at nodes 2 to $n-1$. Therefore, we need to write an equation for each of these nodes:

$$\frac{EI}{h^4}(y_0 - 4y_1 + 6y_2 - 4y_3 + y_4) - \frac{P}{h^2}(y_1 - 2y_2 + y_3) + ky_2$$

$$= -\frac{P}{h^2}(\tilde{y}_1 - 2\tilde{y}_2 + \tilde{y}_3) + q_2$$

$$\frac{EI}{h^4}(y_1 - 4y_2 + 6y_3 - 4y_4 + y_5) - \frac{P}{h^2}(y_2 - 2y_3 + y_4) + ky_3$$

$$= -\frac{P}{h^2}(\tilde{y}_2 - 2\tilde{y}_3 + \tilde{y}_4) + q_3$$

$$\dots$$

$$\frac{EI}{h^4}(y_{i-2} - 4y_{i-1} + 6y_i - 4y_{i\mp1} + y_{i+2}) - \frac{P}{h^2}(y_{i-1} - 2y_i + y_{i+1}) + ky_i$$

$$= -\frac{P}{h^2}(\tilde{y}_{i-1} - 2\tilde{y}_i + \tilde{y}_{i+1}) + q_i \tag{1-11}$$

$$\dots$$

$$\frac{EI}{h^4}(y_{n-4} - 4y_{n-3} + 6y_{n-2} - 4y_{n-1} + y_n) - \frac{P}{h^2}(y_{n-3} - 2y_{n-2} + y_{n-1}) + ky_{n-2}$$

$$= -\frac{P}{h^2}(\tilde{y}_{n-3} - 2\tilde{y}_{n-2} + \tilde{y}_{n-1}) + q_{n-3}$$

$$\frac{EI}{h^4}(y_{n-3} - 4y_{n-2} + 6y_{n-1} - 4y_n + y_{n+1}) - \frac{P}{h^2}(y_{n-2} - 2y_{n-1} + y_n) + ky_{n-1}$$

$$= -\frac{P}{h^2}(\tilde{y}_{n-2} - 2\tilde{y}_{n-1} + \tilde{y}_n) + q_{n-2}$$

There is an excess of unknowns due to the use of the two extra points. We can use the boundary conditions to eliminate these unknowns:

At $x = 0$:
$$y(0) = 0 \qquad \rightarrow y_1 = 0$$

$$\frac{dy}{dx}(0) = 0 \qquad \rightarrow \frac{1}{2h}(y_2 - y_1) = 0 \qquad \rightarrow y_2 = y_0$$

$$(1\text{-}12)$$

At $x = L$:
$$y(L) = 0 \qquad \rightarrow y_n = 0$$

$$\frac{dy}{dx}(L) = 0 \qquad \rightarrow \frac{1}{2h}(y_{n+1} - y_{n-1}) = 0 \qquad \rightarrow y_{n+1} = y_{n-1}$$

Applying these boundary conditions to the set of equations (1-11), we obtain a linear system of the form:

$$\frac{EI}{h^4}\underline{\underline{A}}\,\underline{y} - \frac{P}{h^2}\underline{\underline{B}}\,\underline{y} + k\,\underline{y} = -\frac{P}{h^2}\underline{\underline{B}}\,\underline{\tilde{y}} + \underline{q} \qquad (1\text{-}13)$$

where the matrices $\underline{\underline{A}}$ and $\underline{\underline{B}}$ have a size $n - 2 \times n - 2$, and are defined as follows:

$$\underline{\underline{A}} = \begin{pmatrix} 7 & -4 & 1 & & & & & \\ -4 & 6 & -4 & 1 & & & & \\ 1 & -4 & 6 & -4 & \ddots & & & \\ & \ddots & \ddots & \ddots & \ddots & \ddots & & \\ & & \ddots & \ddots & 6 & -4 & 1 \\ & & & \ddots & -4 & 6 & -4 \\ & & & & 1 & -4 & 7 \end{pmatrix}$$

$$(1\text{-}14)$$

$$\underline{\underline{B}} = \begin{pmatrix} -2 & 1 & & & & & \\ 1 & -2 & 1 & & & & \\ & 1 & -2 & 1 & & & \\ & & \ddots & \ddots & \ddots & & \\ & & & \ddots & -2 & 1 & \\ & & & & 1 & -2 & 1 \\ & & & & & 1 & -2 \end{pmatrix}$$

while the vectors $\underline{y}$, $\underline{\tilde{y}}$, and $\underline{q}$ have a size $n - 2$ and are defined as follows:

$$\underline{y} = \begin{pmatrix} y_2 \\ y_3 \\ \vdots \\ y_{n-1} \end{pmatrix}; \qquad \underline{\tilde{y}} = \begin{pmatrix} \tilde{y}_2 \\ \tilde{y}_3 \\ \vdots \\ \tilde{y}_{n-1} \end{pmatrix}; \qquad \underline{q} = \begin{pmatrix} q_2 \\ q_3 \\ \vdots \\ q_{n-1} \end{pmatrix} \qquad (1\text{-}15)$$

13

The differential equation (1-9) was turned into a linear system of equations that can be solved using any numerical software, such as MATLAB or Python. The right-hand term is known a priory or measurable experimentally; thus, the load-deflection curve can be obtained by iteratively solving (1-13) for various values of the loads P and q. For the particular case where the beam does not rest on elastic support and no lateral load is applied to it, equation (1-13) becomes an eigenvalue problem. The critical buckling load P_{cr} is, then, directly obtained by calculating the lowest eigenvalue. Furthermore, this method allows to easily account for any initial imperfection, including white noise (cf. equation (1-8)) and imperfections measured experimentally, by simply providing the vector $\tilde{\underline{y}}$.

Note that, although this method allows for an efficient way of solving buckling problems for beams with various load types and boundary conditions, for more complex geometries, loadings, or when nonlinear material models need to be considered, then the finite element method is preferred.

1.3.2.5. Dynamic Elastic Buckling

In static buckling, the load is applied slowly, and the inertia effects can be neglected. In the case of dynamic pulse buckling, the load is applied for a short period of time and then removed. The magnitude of loading amplitude usually exceeds the static Euler buckling load but does not necessarily generate large deformations. Instead, higher buckling modes are generated compared to the static buckling (i.e., the wavelength of the deformation is shorter). Also, the load can exceed the elastic limit without causing plastic deformation as long as the load is applied for a relatively short period of time. In contrast to static buckling in which the magnitude of the largest load supported by the structure is sought, in pulse buckling studies, the load intensity is fixed, and the response of the structure is obtained. Therefore, since the response is dependent on the time period during which the load could be maintained without causing a failure, it is possible to determine the safe duration of an applied load.

The equation of motion of a beam with initial imperfection, subjected to an axial compressive load can be written by using Eq (1-4) by using the following parameters: $p^2 = \frac{P}{EI}, r^2 = \frac{E}{A}$, and $c^2 = \frac{E}{\rho}$, as follows (Lindberg & Florence, 1987):

$$\frac{\partial^4 y}{\partial x^4} + p^2 \frac{\partial^2 y}{\partial x^2} + \frac{1}{r^2 c^2} \frac{\partial^2 y}{\partial t^2} = -p^2 \frac{\partial^2 \tilde{y}}{\partial x^2} \tag{1-16}$$

Similar to the static case, the solution of (1-16) and the initial imperfections can be expressed by the following Fourier series:

$$y(x, t) = \sum_{n=1}^{\infty} D_n(t) \sin \frac{n\pi x}{L}$$

$$\tag{1-17}$$

$$\tilde{y}(x) = \sum_{n=1}^{\infty} A_n \sin \frac{n\pi x}{L}$$

Substituting equations (1-17) into (1-16) gives the following relationship between the Fourier coefficients D_n, A_n and the buckling mode n:

$$\ddot{D}_n + \left(\frac{rcn\pi}{L}\right)^2 \left[\left(\frac{n\pi}{L}\right)^2 - p^2\right] D_n = (rpc)^2 \left(\frac{n\pi}{L}\right)^2 A_n \tag{1-18}$$

where " ¨ " denotes the second derivative with respect to time. The solution of equation (1-18) depends on the sign of the quantity $\left[\left(\frac{n\pi}{L}\right)^2 - p^2\right]$. If $p > \frac{n\pi}{L}$ the solution would be hyperbolic, and the imperfections will be exponentially amplified. If $p < \frac{n\pi}{L}$, the solution would be trigonometric, and the amplifications are bounded. Therefore, the mode n has to be approaching a certain threshold in order for the beam to have a bounded buckling deformation.

Note that the limit $n = \frac{pL}{\pi}$, which switches the trigonometric and hyperbolic solutions, provides the wavelength of the static buckling capacity of a simply supported beam under a given load. The buckling capacity of beams with other boundary conditions can be obtained by using the coefficient β from Figure 1-6.

The condition $\left(\frac{n\pi}{L}\right)^2 - p^2 < 0$ would indicate that a load greater than $P = \frac{\pi^2 EI}{L^2}$ would cause an unstable response. In such a case, p^2 would be positive, resulting in an undesirable response for $n = 1$. In other words, when $n = 1$, it would result in $\left(\frac{n\pi}{L}\right)^2 - p^2 < 0$ for all values of $P > \frac{\pi^2 EI}{L^2}$. Thus, the solution of the equation of motion would become hyperbolic, leading to an unstable response.

The condition of $P > \frac{\pi^2 EI}{L^2}$ commonly occurs in pulse buckling loading situations. In such cases, the unstable modes would be associated to high order functions. Moreover, the buckling would take place before the axial compressive wave reaching the non-impacted end of the beam. Therefore, the length of the beam has no influence on the buckling behaviour.

When considering beams with initial imperfections, a function, referred to as amplification function, is often used; given a normalized pulse duration τ, this function essentially indicates how a given wave number is amplified. An example is illustrated in Figure 1-8(a). As time progresses, the band of harmonics that are amplified would become smaller, but the amplitude would become drastically larger. Interestingly, it is also visible from the curves that some wavelengths would not be affected by the buckling phenomenon.

(a) (b)
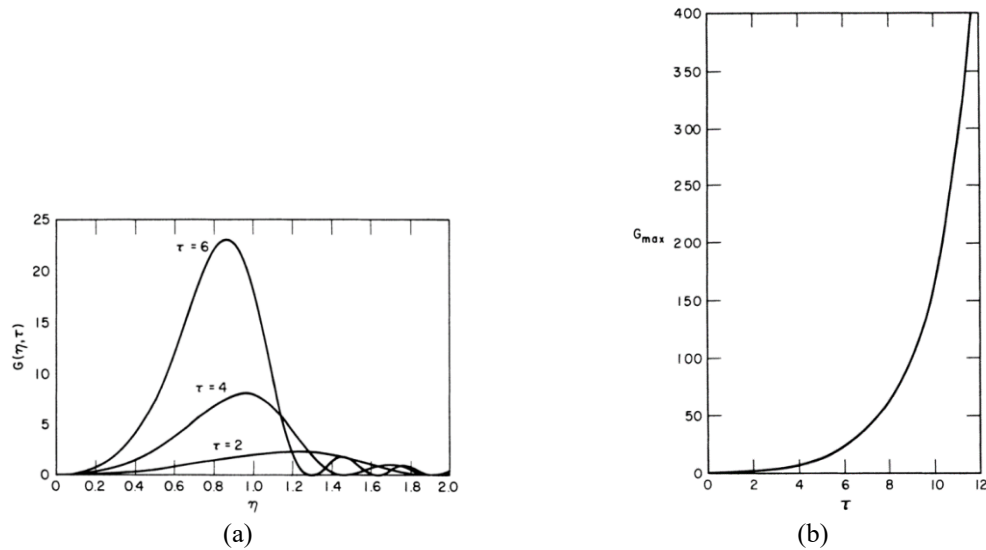
Figure 1-8. (a) Amplification function vs. wave number and (b) influence of the pulse duration on the maximum value of the amplification function (Lindberg & Florence, 1987).

16

Furthermore, as mentioned earlier, the pulse duration greatly affects the behaviour of the beams. An example is given by the graph of the maximum amplification function vs. pulse duration shown in Figure 1-8(b). As can be seen, the maximum buckling amplitude grows exponentially as a function of the applied loading time period (pulse duration).

1.3.3. Buckling of Sandwich Structures

1.3.3.1. Global Buckling of Sandwich Beams

In this section, the static buckling of sandwich beams is briefly covered. The procedure is similar to that described for evaluating the static Euler load, with the difference that, in this case, the influence of shear would be accounted for. Therefore, the total beam's deflection is represented by:

$$y = y_b + y_s \tag{1-19}$$

where y_b and y_s are the beam's deflections due to bending and shear loads, respectively. The governing buckling equation for slender sandwich beams having clamped-clamped boundary conditions is the following (Zenkert, 1997):

$$\frac{\partial^2 y}{\partial x^2} + a^2 y = \frac{a^2}{P}\left(-Tx + \frac{TL}{2} - M\right) \tag{1-20}$$

where $a^2 = \frac{PS}{bD_{11}(bS-P)}$, S is the shear stiffness, b is the beam width, and D_{11} is the beam flexural rigidity in the longitudinal direction. From these equations, considering a beam with an infinitely large bending stiffness, it can be shown that the shear buckling load P_s would be independent of the boundary conditions. This leads to the following formula, which is the extension of the Euler's buckling formula applied to sandwich beams:

$$\frac{1}{P_r} = \frac{1}{P_b} + \frac{1}{bS} \qquad \text{with} \qquad P_b = \frac{\pi^2 bD_{11}}{(\beta L)^2} \tag{1-21}$$

The coefficient β, as introduced earlier, accounts for different boundary conditions, as illustrated in Figure 1-6.

1.3.3.2. Local Buckling or Wrinkling

Apart from few exceptional cases, the deformability of the core of sandwich beams has limited influence on the global buckling behaviour of beams. However, it has a contribution in a particular type of local buckling called "face wrinkling". The phenomenon occurs due to loss of stability of the sandwich's skins, which buckle in a wave-like fashion, while the beam remains globally stable. Figure 1-9(a) shows the two cases of instability that might occur depending on the core thickness (i.e., anti-symmetrical or symmetrical wrinkling with respect to the middle plane). For a sufficiently thin core, the displacement generated by the wrinkled skin (cf. Figure 1-9(b)) will be transmitted to the other skin, while this would not occur if the core is sufficiently thick. Usually, the wrinkle's wavelength is short and depends on the structure of the core and the mechanical properties of the skins. For instance, for non-continuous cores such as honeycombs, the minimum wavelength is directly proportional to the size of the cells.
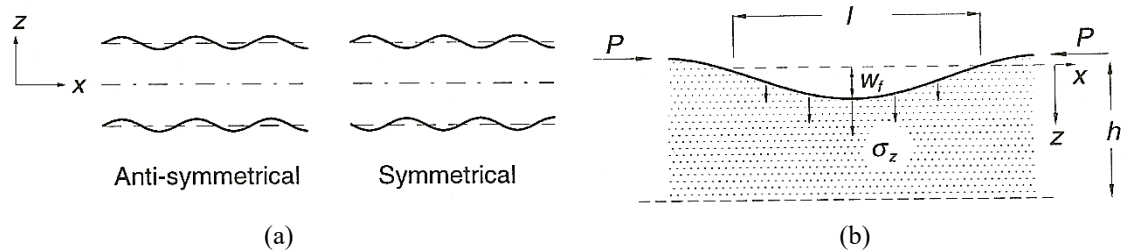
Figure 1-9. (a) Schematic representation of the wrinkling instabilities and (b) a close-up view of the indent generated by the wrinkles (Zenkert, 1997).

To predict the onset of buckling and to define the design criteria, two different methods are presented by Zenkert (1997): (i) the energy method, and (ii) the differential equation method. The energy method involves minimization of the total energy of the system, defined as the sum of the potential energy of the deformed skin and core, minus the work done by the applied axial load. In the differential equation method, each skin is modelled as a beam resting on an elastic foundation (accounting for the support provided by the core) and subjected to an axial compressive load. Subsequently, the differential equilibrium equations of the system are constructed and solved. Note that in both approaches, the displacement of the skins is assumed to follow a sinusoidal form (cf. Figure 1-9(b)).

For the sake of consistency, the equations are omitted in this manuscript and the reader is referred to Zenkert (1997) for further details. Nevertheless, a summary of the behaviour is shown in Figure 1-10, which illustrates the dependency of the critical wrinkling stress of the skin, σ_{cr}, with respect to the specimen slenderness ratio, t_c/t_f, between the thickness of the core and of the skin, for both symmetrical and anti-symmetrical cases. Anti-symmetrical buckling is more likely to occur when $t_c/t_f < r$, while if $t_c/t_f > r$, buckling would be in a symmetrical mode, where r is the intersection of the two curves, as seen in the figure. Also, note that, for the symmetrical case only, the critical stress reaches a plateau, while in the asymmetric case, it increases linearly. It should be noted that the approach used for defining the behaviour of sandwich beams can be extended to sandwich plates.
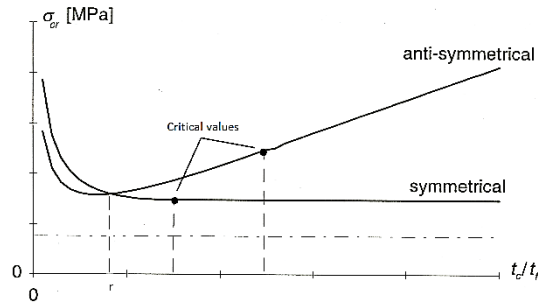
Figure 1-10. Variation of the critical wrinkling stress as a function of the ratio of skin to core thicknesses (Zenkert, 1997).

Lastly, to summarize the approaches introduced in this section, a general comparison of the various load estimation methods is shown in Figure 1-11. As can be seen, skin wrinkling is the only phenomenon that is independent of the beam's length. For beams having a weak core, the resistance to buckling decreases drastically as the length is increased. It is worth noting that all the noted approaches are more conservative than the simpler and widely used Euler approach. This is an important observation when one want to design and spec sandwich structures.

19
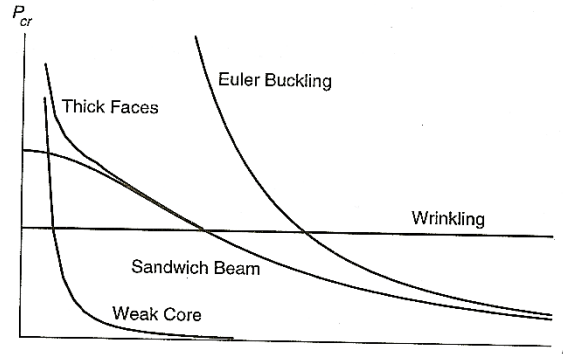
Figure 1-11. Variation of the critical buckling load of a sandwich beam as a function of beam's length predicted by the various approaches (Zenkert, 1997).

1.3.4. Numerical Analysis of Pulse Buckling

In general, there are three classes of mechanical nonlinearities: (i) geometric, (ii) material, and (iii) contact. Geometric nonlinearities occur in structures or systems when they undergo large displacements, but small deformations (which is often the case experienced by slender structures). The material nonlinearity occurs when the material is pushed beyond its elastic limit, categorized as plastic deformation, damage or fracture and it is accounted for by an appreciate constitutive law. In such cases, the stress-strain relationship would be nonlinear. Lastly, the contact nonlinearity originates from, as the name suggests, contacts between two or more parts. Based on a given situation, the parts may come into contact with one-another (i.e., press against or slide atop one-another and separate). Buckling phenomenon mainly involves the first category, because it involves instability, thus, large displacements. However, material nonlinearities are often introduced to study the post-buckling behaviour.

In this section, the fundamentals of numerical analysis of buckling and nonlinear phenomena are presented, with focus on their application to the finite element method (FEM). Also, the basis of dynamic simulation is discussed.

1.3.4.1. Numerical Analysis of Buckling

Stability analysis of structures can be divided into three phases: (i) analysis of the pre-buckling status (i.e., computation of the stress and strain fields before the onset of

20

instability; usually handled by a linear analysis), (ii) determination of the stability limit (i.e., the establishment of the bifurcation point(s), which is usually done by calculating the eigenvalues of the system); (iii) tracing of the post-buckling path, by incorporating iterative methods.

The potential energy of the system is used to establish the equilibrium limit and stability. For any structural system, the potential energy is expressed as:

$$U = \frac{1}{2} \int_V \underline{\varepsilon}^T \underline{\sigma} dV - \left(\int_V \underline{u}^T \underline{f_v} dV + \int_{\partial V} \underline{u}^T \underline{f_s} dS \right) \tag{1-22}$$

where $\underline{\varepsilon}$ and $\underline{\sigma}$ are the strain and stress tensors; $\underline{u}$ is the displacement vector; $\underline{f_v}$ and $\underline{f_s}$ are the volume and surface forces vectors, and the superscript T indicates the transpose.

The equilibrium of the system is established by evaluating a local extremum (maximum or minimum) of the potential energy, which translates to $\delta U = 0$, where:

$$\delta U = \int_V \underline{\delta \varepsilon}^T \underline{\sigma} dV - \left(\int_V \underline{\delta u}^T \underline{f_v} dV + \int_{\partial V} \underline{\delta u}^T \underline{f_s} dS \right) \tag{1-23}$$

In terms of finite element notation, (1-23) becomes:

$$\delta U = \underline{\delta u}^T \left[\int_V \underline{B}^* \underline{\sigma} dV - \left(\int_V \underline{f_v} dV + \int_{\partial V} \underline{f_s} dS \right) \right] \tag{1-24}$$

with $\underline{B}^* = \underline{B_0} + \underline{B_L}$, such that $\underline{\varepsilon} = \underline{B}^* \underline{u}$, where $\underline{B_0}$ is the matrix of the linear infinitesimal strains and $\underline{B_L}$ is the matrix containing the nonlinear components of strain.

An equilibrium would be unstable if it assumes the maximum value of the potential energy, while it would remain stable if it is a minimum. The stability condition is, therefore, given by the second variation of the potential energy, $\delta^2 U$, defined as:

$$\delta^2 U = \underline{\delta u}^T \left[\int_V \underline{\delta B}^* \underline{\sigma} dV + \int_V \underline{B}^{*T} \underline{C} \underline{B}^* \underline{\delta u}^T dV \right] \tag{1-25}$$

with $\underline{\underline{C}}$ being the fourth-order constitutive tensor.

Thus, we obtain the following scenarios:

- $\delta^2 U > 0$: stable equilibrium;
- $\delta^2 U < 0$: unstable equilibrium;
- $\delta^2 U = 0$: undetermined equilibrium, almost impossible from a mechanical point of view.

In finite element, this quantity is calculated as follows:

$$\delta^2 U = \underline{\delta u}^T \, \underline{\underline{K_{Tot}}} \, \underline{\delta u} \qquad\qquad (1\text{-}26)$$

where $\underline{\underline{K_{Tot}}}$ is the nonlinear rigidity matrix of the system; thus, it contains both the linear and nonlinear stiffness information. It can be shown that solving the equilibrium problem (i.e., obtaining the equilibrium and stability information), is equivalent to solving the following eigenvalue problem (Han, 2006):

$$\underline{\underline{K_{Tot}}} \, \underline{v_i} = \lambda_i \, \underline{v_i} \qquad\qquad (1\text{-}27)$$

where λ_i and $\underline{v_i}$ are, respectively, the i-th eigenvalue and the corresponding eigenvector.

Therefore, the first step of the analysis involves the computation of the equilibrium configuration under a given load P, which is done via iterative methods (see section 1.3.4.2. The second step involves the computation of the eigenvalues of the tangent matrix $\underline{\underline{K_T}}$. If the lowest eigenvalue is positive, then the equilibrium is stable, otherwise, the equilibrium is unstable.

The first analysis provides information regarding the buckling load and mode. However, structures are often able to carry load beyond the buckling limit. This is particularly the case for laminate composites, especially if they do not have a symmetrical layup. A post-buckling analysis is, therefore, necessary to trace and understand the behaviour beyond the bifurcation stage. This is done by constructing the load-deformation

curve through an iterative process involving computation of the structure's equilibrium under several load increments. During such incremental analysis, the stability at each increment can be verified using the eigenvalues of the tangent matrix. Note that, so long as the equilibrium is stable, the structure would be able to sustain the applied load at that increment.

1.3.4.2. Search for the Equilibrium

It should be noted that seldom an analytical solution exists by which one could assess the performance of slender systems undergoing compressive loading in real-life situations. Therefore, numerical methods are often utilized to approximate the solution, which as stated, involves assessment of the eigenvalues and establishment of the equilibrium when the system undergoes nonlinearity.

A large number of numerical methods is available for solving eigenvalue problems. The two particularly effective methods used for assessing the eigenvalues of very large systems are the Lanczos and subspace methods. A comparison of these methods, as well as an improvement to the subspace iteration method, is presented by Bathe (2013).

As for the solution method of nonlinear equations, the two most widely used methods are the Newton-Raphson and the arc-length methods. Given an equation of the form $f(x_1, x_2, \dots) = \lambda$, the Newton-Raphson method aims to establish the intersection of the function with the specific value λ by using the tangent of the function. As illustrated in Figure 1-12, the first tangent is computed at a prescribed starting point. The intersection between the tangent and λ established the point for constructing the second tangent, and so on. The algorithm stops when the difference between two successive approximation points is less than a threshold value, defined by the user. This method has a fast convergence rate (second-order); however, the computation of the tangent can be numerically costly, and the method tends to diverge in case of where large nonlinearities, spring-back, and bifurcation are encountered.

To overcome the aforementioned issues, variations of the Newton-Raphson method have been developed. For instance, to reduce the computation cost of obtaining the tangent

for every step, the tangent can be computed only once every n steps. For addressing the convergence issues, the method was expanded and is referred to as the arc-length method. This method uses a different approach to overcome the issues that demise the Newton-Raphson method and can cross over singular points in a given path. The length of the incremental displacement depends on the length of the previous incremental displacements, which allows for more control over each iteration. Furthermore, the load level λ is treated as a variable instead of a constant, resulting in the algorithm effectively solving $f(x_1, x_2, .. s..) = a\lambda$, where $0 < a \leq 1$. A detailed explanation of the algorithm can be found in the work of Han (2006).

Figure 1-12. Schematics of the Newton-Raphson method.

1.3.4.3. Temporal Discretization of Dynamic Problems

To account for dynamic effects in numerical analysis, in particular in an FE analysis, the equation of motion must be re-written from its continuous form into a discretized form. Therefore, the equation of motion of a structural system, at any given time n, is represented as follows:

$$\underline{\underline{M}}\,\underline{\ddot{u}}_n + \underline{\underline{C}}\,\underline{\dot{u}}_n + \underline{R}^i_{\ n} = \underline{R}^e_{\ n} \tag{1-28}$$

with $\underline{\underline{M}}$ being the mass matrix, $\underline{\underline{C}}$ is the damping matrix, $\underline{R}^i$ the internal forces vector, and $\underline{R}^e$ the external forces vector, applied to the structure. Furthermore, the time derivatives

24

are discretized using the finite difference (FD) method. The choice of the FD functions defines two schemes: explicit and implicit. In the explicit scheme, the discretized quantity at the current step n is defined only by values known at the previous times steps $n - 1, n - 2, ...$ For our purpose, therefore, the displacement can be expressed as follows:

$$\underline{u}_{n+1} = f\left(\underline{\dot{u}}_{n+1}, \underline{\ddot{u}}_{n+1}, \underline{u}_n ...\right) \tag{1-29}$$

In the implicit scheme, the discretized quantity at the current step n is defined by both previous time steps and the current step itself. Because of this, the problem cannot be written as a linear system of equations, thus must be solved using iterative methods such as the ones presented in the previous section.

In addition to the explicit/implicit classification, another sub-classification can be made. If the quantity at step $n + 1$ depends only on the value at step n, it is referred to as single-step method; when it depends on the value at steps further back in time, it is referred to as multi-step method. The implementation of the boundary conditions is simplified when using the single-step method and has less impact on the accuracy of the results. However, special initialization procedures, often counter-intuitive, are required.

In the work presented in this thesis, the finite element simulations were conducted using an explicit, single step time discretization. Therefore, this method is briefly presented here. The reader is referred to the work of Kharab & Guenther (2012) for more information regarding the implicit method.

Using the central difference with an error margin of $O(h^2)$ and a constant time step Δt, the expressions for the derivatives in equation (1-28) are as follows:

$$\underline{\dot{u}}_n = \frac{1}{2\Delta t}\left[\underline{u}_{n+1} - \underline{u}_{n-1}\right] \tag{1-30}$$

$$\underline{\ddot{u}}_n = \frac{1}{\Delta t^2}\left[\underline{u}_{n-1} - 2\underline{u}_n + \underline{u}_{n+1}\right] \tag{1-31}$$

Substituting equations (1-30) and (1-31) into the equation of motion (1-28), the displacement at any given time can be obtained knowing the value of displacements at the previous time step by the following equation:

$$\underline{u}_{n+1} = \left[\frac{\underline{\underline{M}}}{\Delta t^2} + \frac{\underline{\underline{C}}}{2\Delta t}\right]^{-1} \left[\underline{R}^e_n - \underline{R}^i_n + \frac{\underline{\underline{M}}}{\Delta t^2}\left(2\underline{u}_n - \underline{u}_{n-1}\right) + \frac{1}{2\Delta t}\underline{\underline{C}}\,\underline{u}_{n-1}\right] \qquad (1\text{-}32)$$

However, to be able to compute the displacement at the initial time-step $n = 0$, equations (1-30) and (1-31) must be re-written to obtain the expression of $\underline{u}_{-1}$:

$$\underline{u}_{-1} = \underline{u}_0 - \Delta t\, \underline{\dot{u}}_0 + \frac{\Delta t^2}{2}\underline{\ddot{u}}_0 \qquad (1\text{-}33)$$

where $\underline{u}_0$ and $\underline{\dot{u}}_0$, are the known initial position and velocity, and the initial acceleration $\underline{\ddot{u}}_0$ can be calculated by:

$$\underline{\ddot{u}}_0 = \underline{\underline{M}}^{-1}\left\{-\underline{\underline{C}}\,\underline{u}_0 + \underline{R}^e_n - \underline{R}^i_n\right\} \qquad (1\text{-}34)$$

It is possible to show that the described explicit FD method is stable as long as the following criterion hold, respectively (Han, 2006):

$$\Delta t \leq \frac{2}{\omega_{max}} \qquad \text{for systems without damping} \qquad (1\text{-}35)$$

$$\Delta t \leq \frac{2}{\omega_{max}\left[\sqrt{1 + \xi^2_{max}}\right]} \qquad \text{for systems with damping} \qquad (1\text{-}36)$$

with $\omega_{max} = 2\pi f_{max}$, with f_{max} being the highest natural frequency of the system and ξ_{max} being the corresponding damping coefficient. In the finite element method, this stability condition is obtained from the frequency of the smallest element of the mesh. Therefore, the critical time-step, at each computation time-step, can be approximated by the Courant criterion:

$$\Delta t_{crit} = \min_e\left\{\frac{L^e_{max}}{c^e}\right\} \qquad (1\text{-}37)$$

where e refers to any element of the model, L^e_{max} is the characteristic dimension of the smallest element of the mesh and c^e the speed of sound in the material.

From a computational point of view, if both $\underline{\underline{M}}$ and $\underline{\underline{C}}$ are diagonal, then the equations are uncoupled and $\underline{u}_{n+1}$ is obtained without the need for solving a linear system of equations, thereby reducing the computation time significantly. Moreover, if both $\underline{\underline{M}}$ and $\underline{\underline{C}}$ are diagonal, then the explicit method is competitive compared to the implicit method. In fact, implicit schemes are stable for larger time-steps, therefore requiring fewer steps to be computed. However, the computational cost per step is greater than that in the explicit schemes. Note that LS-DYNA software offers automatic switching between explicit and implicit schemes to optimize the computation time.

1.4. Thesis Objectives and Layout

The aims of the research presented in this thesis are as follows: (i) to provide a deep insight into the characterization of the delamination-buckling behaviour of the complex 3D-FML composite material under in-plane loadings with various strain rates (particularly, under low-velocity impact); (ii) to enhance the load-carrying capacity, stability and delamination propagation resistance of the 3D-FML under impact loading; and (iii) to prepare practical design guidelines to facilitate the widespread use of this hybrid composite material system in various applications. The goals are met by performing a systematic series of experimental investigations, coupled and stream-lined by a series of computational simulations, using the finite element method (FEM).

A general introduction of the various topics mentioned in this thesis has been provided in this introductory chapter. In the subsequent chapter, a literature review of the research related to the specific subject of the thesis is presented. The review covers the works conducted on: experimental and numerical impact buckling and delamination-buckling of composites, bonding enhancement between hybrid composite constituents, and numerical analysis of impact and buckling/post-buckling.

As stated, chapters 1 and 2 present the introductory sections of the chapters that form the main body of the thesis. It should be noted, however, that this thesis follows the "collection of published papers" format option sanctioned by the Faculty of Graduate Studies of Dalhousie University. Therefore, while each paper (published, in-press or submitted) has its own literature review section, to reduce redundancy, those sections are truncated for the purpose of inclusion in this thesis. In another word, the sustained literature reviews of the manuscript presented in chapters 3 to 10 are limited to stating the novelty of the work disclosed in the respected manuscripts. Moreover, the reference section of all papers has been consolidated into one reference section.

Chapter 3 covers the study of the behaviour of short specimens subjected to compressive loadings at various strain rates. In Chapter 4, a simplified numerical analysis is developed for conducting a parametric study to establish the buckling response of slender 3D-FML beams subjected to static buckling in an accurate and efficient manner. Chapter 5 is dedicated to the FE modelling of the behaviour of the slender beams under low-velocity impact using the commercial FE software LS-DYNA. For this, various modelling approaches, using different element formulations, are considered in order to establish the most cost-effective and accurate modelling technique when considering the impact response of such complex hybrid material systems.

In Chapter 6 the research highlights the critical dependency of the performance of 3D-FML on the magnesium/core interface bond strength. A simple, but effective new surface preparation procedure is proposed, by which the issue is alleviated significantly, thereby enhancing the performances of the 3D-FML under both in-plane and out of plane impact. Chapter 7 discloses the details of the additional remedy sought to improve the interface bonding issue. The procedure involves incorporation of graphene nanoplatelets (GNPs) in the resin forming the interface bond. The effect of the nanoparticles on the interface bond strength is also characterized at both room and sub-freezing temperatures.

In Chapter 8, the performance of 3D-FML with steel skin is investigated. Once again, the performances are characterized under in-plane static and impact loadings, as well as out-of-plane loading. The viability of coupling LS-DYNA's xFEM and cohesive elements

to model the delamination propagation in 3D-FMLs is considered and discussed in Chapter 9. The study also highlights the inherent behaviour of the crack that is developed within the resin layer and subsequently diverted towards the magnesium skin. Chapter 10 is dedicated to some guidelines and semi-empirical equations useful for conveniently establishing a preliminary design of panels made of the 3D-FML composite. The thesis is concluded with a summary and conclusion section and future recommendations (Chapter 11).

Chapter 2: Literature Review

This literature review is intended to be a summary of the work closely related to the buckling and delamination-buckling of 3D fiber-metal laminates subjected to in-plane low-velocity impact. It covers buckling of composites and fiber-metal laminates (FMLs), the impact response of structures, bonding, as well as numerical modelling techniques. The literature concerning these topics is relatively vast and only some selected papers are presented in this manuscript. However, to the best of author's knowledge, other than a preliminary study conducted by a former PhD student of our research group (Asaee et al., 2017), no other public domain literature could be found regarding the specific subjects presented in this thesis.

2.1. General Background

As mentioned in Chapter 1, the term fiber-metal laminate (FML) is used to refer to any combination of fiber-reinforced plastics (FRPs) and metal. The first FML was developed in the late 1970s and entailed staking of thin glass reinforced FRP plies interleaved with thin sheets of aluminum. As also briefly stated earlier, FMLs present many advantages compared to their bulk constituents. They offer high specific strength and stiffness, have, in most part, better damage tolerance, superior energy absorption capacities, greater resistance to fatigue and impressive damping characteristics. This is because they take advantage of the properties of each constituent. The metals used in FMLs have an elasto-plastic behaviour, which in general enhances the impact absorption capacities of the FRP constituent. In addition, the metallic constituent is in general stiffer than the FRP constituent, thus increasing the overall rigidity of the FML. The FRP plies incorporated in most FMLs generally exhibit brittle elastic characteristics. With majority of FRP used in FMLs are made of glass and thermoset resins, FMLs are also made with thermoplastic resins and other reinforcing fibers (carbon, aramid…), each determining a different type of response in terms of the transmitted load, deflection, and damage, thus allowing for a tailored design (Sinmazçelik et al., 2011; Vlot et al., 1999). Comparatively, however, FMLs are often a more expensive solution. This is due to various factors, such as the costs associated with the materials, layup and curing and surface treatment. FMLs

also require more attention in their inspection and joining of the different constituents and parts present additional challenges, requiring dedicated tooling.

A brief summary of the various FML combinations is given in Figure 2-1. Historically, aluminum, due to its excellent specific mechanical properties (Asundi & Choi, 1997), was the first alloy used as the metallic constituent of FMLs; however, other metals have also been used. For instance, a magnesium-based version of FML has also been considered by researchers with the aim of further reducing the overall weight of the produced components. In fact, as previously mentioned, magnesium's density is approximately 35% and 75% lower than that of aluminum and steel, respectively. Cortes and Cantwell (2005) conducted low-velocity impact tests on magnesium/polypropylene-based FML. The FML showed higher specific energy absorption capacities than a similar aluminum-based one, and outperformed fiberglass-epoxy/aluminum FMLs. However, the improved results could not be consistently corroborated by other researchers. For instance, Sadeghi et al. (2012) and Pärnänen et al. (2012) compared the performances of GLARE and magnesium/fiberglass-epoxy laminated plates subjected to a lateral impact. They showed that magnesium-based FMLs could not achieve the performances of GLARE. However, the comparatively lower cost of magnesium was not accounted for in the normalization of their results.
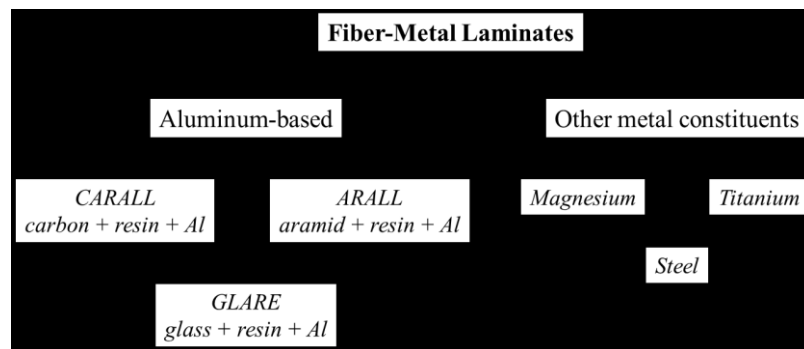
Figure 2-1. Summary of various FML types.

Another effective approach to reach further weight-savings, which has been in use for several decades, is achieved using sandwich materials (i.e., using relatively thick and very lightweight core materials and sandwiching them in between thin strong and stiff metallic or FRP skins). An application of such a hybrid system, proposed for the automobile

industry, can be seen in the works of Palkowski and Lange (2008) and Sokolova et al. (2012). These researchers investigated the mechanical performance and formability of steel-polymer-steel sandwiches. The sandwich materials demonstrated to possess excellent specific stiffness; however, the authors also showed such sandwich composites present a significant challenge when relatively thicker cores were used. They also showed that the sandwich configuration provided advantageous damping characteristics, which would lead to the reduction of vibration in automobile components.

A combination of these two approaches has led to the development of a new 3D class of FML by our research group. The new class of FML is formed by using a 3D E-glass fabric and a magnesium alloy (Mg). Because of its potential application in transport vehicles' body and shell components, an extensive effort was expended to characterize the static and out-of-plane (or lateral) impact response of the FML (Asaee et al., 2015; Asaee & Taheri, 2016, 2017). Failure modes, type and extent of damage, as well as quantification of the energy absorption capacity, maximum displacement, and permanent displacement were all considered in the studies. Moreover, an analysis of the performance of the FML based on the variation of the stacking configuration showed that when two layers of FGF were sandwiched between two magnesium sheets, the combination resulted in the highest performances compared to several other configurations that were examined when the performances were normalized with respect to weight and cost.

In general, when panels made of monolithic and sandwich composites and FMLs are used as exposed shells, they become prone to impacts of various intensities, such as an impact caused by a falling tool or a blast impact. Therefore, their behaviour under such loading conditions has been studied extensively, as evident by the relevant literature. For instance, the behaviour of balanced angle-ply epoxy/fiberglass laminates under out-of-plane weight-drop impact was examined by Lifshitz (1976), who showed that the tensile strength under impact was higher than that exhibited under an equivalent static loading. Zhu and Chai (2012) conducted drop-weight impact tests on aluminum/fiberglass/epoxy FMLs. The FML with unidirectional plies was shown to be more efficient in absorbing impact energy compared to that with cross-ply FRP, and that the response under quasi-

static and low-velocity impact was similar when the impactor's mass was much greater than the specimen's mass.

The influence of impactor shape and size on the behaviour of FRPs and FMLs was also taken into consideration by, for instance, Liu and Liaw (GLARE), Mitrevski et al. (woven carbon/epoxy), and Siow and Shin (woven carbon/epoxy) (Liu & Liaw, 2004; Mitrevski et al., 2005; Siow & Shim, 1998). Sharp-edged impactors were found to generate predominantly localized damage, consisting mainly of fiber breakage and, in the case of FMLs, permanent indentation on the impacted face, while hemispherical impactors generated larger permanent displacement and a larger delaminated area. A reduction of the mechanical properties after impact was also reported. Similar conclusions were drawn by De Cicco et al. (2016) who investigated the low-velocity impact response of magnesium/fiberglass-epoxy FMLs with two and three magnesium layer configurations. The hemispherical impactors led to higher delamination and permanent deformation, while more localized damage and fiber failure was reported for the sharp impactor. It was also observed that the three-layer configuration could absorb more energy than the two-layer one.

Thermoset polymers are the most widely used type of resin in the formation of laminate composites used in load-bearing applications. However, the superior toughness of thermoplastics has attracted researchers' attention for use in the formation of composite structures subjected to impact. Compston et al. (2001) conducted impact perforation tests on aluminum/fiberglass-polypropylene FMLs by propelling hemispherical and flat-ended impactors using a gas gun, and compared their performance with that of bulk aluminum plates. Plastic deformation and back-plate cracking were the main types of failure modes observed for the hemispherical impactor, while the flat-end impactor caused predominantly shear failure. The superior performances of the FML compared to bulk aluminum were attributed to the high fracture energy endurance of the glass fibers and the energy absorbed by the delamination buckling of the aluminum sheets. Abdullah and Cantwell (2006) worked on the high-velocity impact of aluminum/fiber-reinforced polypropylene plates using two types of aluminum alloys (2024-O and 2024-T3), in both two and three metal layer configurations. For an equal thickness, the stronger 2024-T3 alloy showed a better

impact resistance, and the three-layer component performed better than the two-layer one. Moreover, the highest specific perforation energy was obtained with a thick composite core and thin outer aluminum plates. Many failure mechanisms were reported by the authors, such as ductile tearing, delamination, fiber failure, permanent displacement and metal cracking, all contributing to energy absorption.

2.2. Delamination-Buckling and Pulse-Buckling

As mentioned previously, the term buckling is associated to a sudden change in the stability of a structure - potentially leading to a complete loss of load-bearing capacity- primarily caused by a compressive state of stress. The critical buckling load, buckling modes and post-buckling behaviour depend on the geometry of the structure, the aspect ratio of cross-sectional dimensions, the laminate configuration, as well as the type of loading. Moreover, initial flaws (delamination being a type of such flaws) are often found in laminated composite components, mainly due to unintentional anomalies occurring during their fabrication or by accidental tool drop. It is, therefore, necessary to understand the behaviour of such structures hosting an initial imperfection.

Gong et al. (2016) compared the buckling behaviour and delamination growth in carbon fiber-reinforced plastics (CFRPs) subject to a four-point bending test, with artificial and impact-induced initial delamination. The artificial delamination was created by inserting a thin sheet of Teflon between the outer lamina and the immediate sub-surface lamina, while a low energy impactor was used in the other case. Results showed that an appropriately chosen artificial initial delamination could replace an impact induced one, leading to very similar buckling behaviours. Hwang and Liu (2002) conducted experimental studies on both buckling and post-buckling response of laminated composites hosting multiple delaminations. They highlighted the different buckling modes with respect of delamination position in the stacking sequence. They also showed that the specimens could carry load after reaching their buckling stage. Esfahani et al. (2010) analyzed the critical delamination-buckling load and buckling modes for different laminated composite beams (carbon fibers, glass fibers or hybrid) by varying the position of a single initial delamination through the thickness. A lower buckling load was reported

for delaminations closer to the surface. Also, hybrid composite beams exhibited higher buckling resistance compared to non-hybrid ones. Gu and Chattopadhyay (1999) analyzed the buckling and post-buckling mechanism of graphite/epoxy composite flat plates with built-in delamination of different sizes and positioned at various locations, introduced by inserting two very thin Teflon sheets between the plies. It was demonstrated that the studied structures could carry load beyond the buckling limit. In the case of the slender specimens, the buckling load was found to be up to three times lower than the ultimate load of the material. Moreover, the buckling modes were dependent on the delamination length and location, with a delamination closer to the surface leading to a lower buckling load. Kollár (2003) developed a series of simple analytical equations for predicting the buckling of thin-walled FRP beams of various cross-sections. The validity of their analytical results was corroborated with finite element simulations. Kim and Hong (1997) used numerical simulation to analyze the buckling and post-buckling behaviour of composite laminates with embedded initial delamination. They identified three possible modes of instability, depending on the delamination size and types of boundary conditions. The influence of these parameters over the buckling load and post-buckling behaviour was also shown. The numerical model permitted to conclude that: under a certain delamination size, the buckling load and post-buckling behaviour were not affected, and that the buckling mode depended on the delamination size and the boundary conditions and affected the buckling load and post-buckling behaviour.

From an analytical point of view, Wang et al. (2015) improved an analytical theory concerning the buckling driven delamination in bi-layered composite beams. The modification of the expression of the total energy release rate (ERR) consisted in adding an axial strain energy contribution and developing a more accurate expression for the post-buckling mode shape. The study also focused on finding the critical buckling strain and describing the post-buckling behaviour, quantify the influence of fracture modes I and II in governing the propagation of the delamination, and, therefore, predicting the propagation. The authors showed that an accurate calculation of the total ERR is required in order to obtain reliable and accurate results. The comparison between the three beam theories, namely the Euler, Timoshenko and 2D elasticity, on predicting the delamination propagation behaviour was also presented. The best results (i.e. the closest to the

experimental measurements), were obtained with the Euler beam partition theory. Finally, the authors concluded that buckling-driven delamination was a major failure in composite materials. A new definition of upper and lower bound solutions for composite columns buckling was proposed by Yap et al. (2015). They also compared the effectiveness of three analytical methods for calculating the effective flexural stiffness, for both the case of a perfectly bonded and single-delaminated composite beam, and could validate all three methods. The study of the influence of ply orientation, stacking sequence, delamination length and boundary conditions were also carried out by mean of FE analysis and the results were compared to the experimental and analytical solutions. The consistency of the data proved the validity of FE analysis as a predictive tool. More related to the delamination-buckling, Taheri and Moradi (2000) worked on the use of the differential quadrature method to analyze the behaviour of laminated composites as an efficient method for the analysis of the behaviour of laminated composites hosting a delamination. Accurate prediction of the buckling load, buckling mode and post-buckling behaviour were obtained.
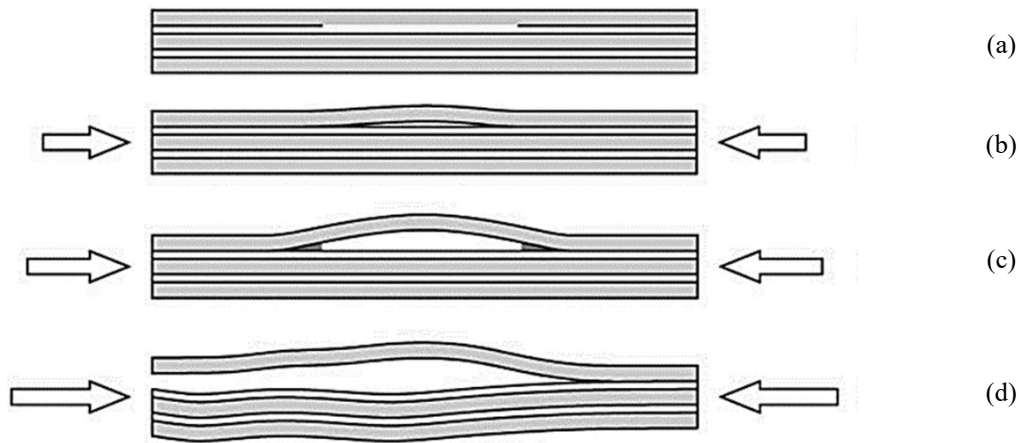
Figure 2-2. Schematic representation of the delamination buckling failure mechanism: (a) unloaded specimen hosting an initial delamination; (b) local buckling; (c) delamination growth; (d) failure (Remmers & de Borst, 2001).

The literature related to the buckling and delamination-buckling response of FRP is relatively extensive. However, fewer studies have focused on sandwich and FML composites. Some of the few notable works are briefly discussed here. Remmers and de Borst (2001) worked on the delamination-buckling of GLARE beams under static loading. The authors demonstrated that, first, the non-bonded part of the metal layer started to buckle, inducing localized stress at the extremities of the delamination; then, as the load

was increased, the delamination grew, until complete failure of the assembly occurred. This behaviour is reported in Figure 2-2. Frostig (1998) developed a higher-order theory to predict the buckling behaviour of sandwich panels having a flexible core. The analytical predictions were validated with numerical results. Gdutos et al. (2003) studied the face wrinkling failure of aluminum-honeycomb sandwich columns under various loading conditions. They concluded that wrinkling of the faces was more likely to occur in specimens with long spans. They also observed that delamination of the faces was another phenomenon that could likely occur. Similarly, Vonach and Rammerstorfer (2000) examined the wrinkling of thick orthotropic plates subjected to general loading conditions, both analytically and numerically. The numerical results were in accordance with the analytical ones.

2.3. Bonding

The relatively lower through-thickness properties of composite materials compared to their in-plane properties makes them prone to delamination (Kim & Mai, 1998). In particular, delamination of the metal sheets is a typical failure for both axial and transversal loadings in FMLs. Therefore, a strong bond between the two components is a critical constraint to obtain an FML with good performances. As a first step, adequate preparation of the surfaces to mate is necessary (Baldan, 2004; Sinmazçelik et al., 2011), which can be done using various methods.

Several methods and techniques have been developed for enhancing the bond strength of joints consisting of metallic substrates. Some of these methods are at research/trial stages, and some are practiced industrially. The simplest and most commonly used technique involves abrading the bonding surfaces by an appropriate grade sandpaper or grit blasting (Baldan, 2004; Harris & Beevers, 1999; Shahid & Hashim, 2002). The procedure creates micro-irregularities on the bond surface of a substrate to which the adhesive could grip mechanically, more effectively. For instance, Harris and Beevers (1999) discussed the effects of this technique on steel and aluminum plates, showing that a higher bonding strength was obtained by abrading the surfaces compared to the "as-rolled" surfaces. The authors also investigated the effect of the grit size and showed that a finer grit would leave

more residues on the treated surface. In addition, abrasion removes the oxide layer formed on metallic substrates. However, to prevent recurrence of this oxide layer, the substrate must be bonded immediately after its treatment. This widely used simple method, however, does not work for all metallic materials, as the degree of oxidation varies from one metal to another. Other, more advanced methods to generate such irregularities also exist, such as the soft lithography technique (Soltannia & Sameoto, 2014).

Appropriate chemicals (referred to as chemical etching) can also be used to alter the chemical structure of bond surfaces, thereby promoting enhanced substrate/adhesive bond strength (Lefebvre et al., 2002; Livadifiis, 1986; Prolongo & Ureña, 2009; Sang Park et al., 2010). With this process, a very thin layer of material is removed from the bonding surface in order to obtain a non-contaminated surface. This method involves bathing the substrates in a series of appropriate chemicals. The chemicals can be tailored such that, after the treatment, the surface remains covered in molecules that are able to create strong bonds with both the adhesive and the metallic substrate (Khorshidi et al., 2017), thereby enhancing the bonding strength of metals to adhesives.

Alternatively, the bond surfaces can also be effectively and non-intrusively treated by plasma activation method (Collaud et al., 1994; Difelice et al., 2005; Gonzalez et al., 2010; Kim et al., 2003; Williams et al., 2013; Zaldivar et al., 2009). In this method, a jet of plasma removes surface impurities and, at the same time, alters the chemical structure of the treated surface leading to a stronger chemical bond with the adhesive. An advantage of this technique is its effectiveness on both metallic and polymeric substrates. For instance, Noeske et al. (2004) studied the effect of plasma activation treatment on five polymers and showed that an increase in the lap-shear strength was obtained for all specimens, leading to an outstanding gain of 1750% in the lap shear-strength of their polypropylene substrates. However, because the procedure requires expensive equipment, it has not been widely used. Therefore, when bonding metallic substrates (including aluminum and magnesium alloys), the common practice has been the use of combined abrasive and chemical surface preparation procedures (Taheri, 1997; The Adhesives Design Toolkit, n.d.), which are very elaborate and time-consuming tasks.

Another innovative method for enhancing the strength of a bond consists in adding nanoparticles to the adhesive, so that both the strength of the adhesive and its adhesion properties are improved (Soltannia & Taheri, 2015; Soltannia & Taheri, 2013). Kubit et al. (2016) and Zielecki et al. (2017) performed peel tests using aluminum and steel adherends, respectively, bonded with multi-walled carbon nanotubes enhanced epoxy, and reported an increase in fatigue life compared to bond with the neat epoxy. The addition of nanoparticles showed another advantage, which is the possibility of monitoring the damage of the bond directly from the change of conductivity in the bond, as demonstrated by Mactabi et al. (2013).

An additional surface preparation procedure that has been found to improve the bonding strength and used in a variety of sectors involves applying a coating to protect the substrate from damage by external agents (Grujicic et al., 2008; Monticelli et al., 2008; Zhao et al., 2003). This procedure improves the interfacial strength between the adherend and the adhesive, particularly when the bonded components have very dissimilar compositions (Ishida, 1984). For instance, Shah (2005) carried out a comprehensive study on the use of a primer for bonding metal and thermoplastic components in injection molding parts, describing in detail how the primers enhanced the bond strength. Wang et al. (2017) developed an efficient coating technique to improve the interfacial strength between the substrate and the adhesive. The authors diluted resin (without hardener) in acetone, then applied a thin layer of the mix onto steel coupons that were previously grit blasted. The acetone improved the wettability of the substrate, therefore, guarantying a more efficient penetration of the resin in the surface micro-irregularities. This resin layer subsequently cures through diffusion when the adhesive (containing hardener) is applied onto the surface, therefore, mechanically interlocking the surface asperities. The aforementioned procedure resulted in 25% improvement in the lap-shear strength of their bonded joints. The authors further evolved the technique by adding aramid fibers (2016), and nanoparticles (2018) to the interface resin layer. Other, more elaborate procedures involve the use of plasma jet for coating. For instance, Fernandes et al. (2002) successfully used plasma treatment to clean, etch, and deposit hexamethyldisiloxane monomer onto an aluminum alloy, all in one operation, therefore, removing the need for multiple steps in the

surface preparation. Similarly, Ko et al. (2013) coated magnesium substrates with a polymeric film, using low-temperature low-frequency discharge plasma.

2.4. Numerical Simulations

Simulations of diverse classes of composite materials are widely available in the literature (Han & Taheri, 2006; Menna et al., 2011; Montemurro et al., 2012; Schweizerhof et al., 1998; Song et al., 2010; Xiao et al., 2009; Yen, 2002). To cite a few of the notable buckling research works, especially those related to FMLs, one can, for instance, mention the study conducted by Remmers and de Borst (2001), who simulated the delamination buckling of GLARE FML under quasi-static compressive force, with emphasis on the influence of the presence of an initial delamination. Solid-like shell elements were used to represent each different layer of the FML, with one layer of element modelling each constituent in the thickness direction. The failure phenomenon was described as a combination of structural instability (buckling) and interlaminar bond failure (delamination). In fact, the non-bonded part of the metal layer was observed to buckle first, inducing localized stress at the extremities of the free part. Subsequently, as the load was increased, the delamination started propagating until complete failure was reached. Solid-like shell elements were chosen to model the composite and metallic layers in their numerical study and interface elements were used to model plies interface regions in order to model the delamination.

Esfahani et al. (2010) also performed a numerical analysis of the influence of the through-thickness initial delamination in composite beams using ANSYS. They obtained good agreement between their numerically and experimentally obtained buckling loads. They concluded that a delamination located closer to the surface reduced the most the buckling capacity of their specimens. They also showed that hybrid composite beams (a combination of carbon- and glass-fiber reinforced plastics) provided a higher buckling capacity than the non-hybrid counterpart. Kim and Hong (1997) numerically simulated the different modes of instability in composite laminates caused by various sizes of a delamination located at various through-thickness positions. They also examined the influence of boundary conditions, focusing mainly on the post-buckling behaviour of their

40

laminates. They demonstrated the existence of a threshold for a given initial delamination size, below which the buckling load would not be affected; however, the buckling mode and post-buckling behaviour were affected.

Other works pertinent to our interest, that is, works considering impact simulations (though not specifically on in-plane axial impact), are also available in the literature. Abedrabbo et al. (2009) simulated the crushing behaviour of steel tubes of different cross-sectional geometries after hydroforming, obtaining good agreement with experimental data. Mamalis et al. (2003) performed a numerical simulation of the crushing behaviour of square sandwich composite beams for use in vehicles using a commercial FE software (LS-DYNA). The composite plies were modelled using shell elements, while solid elements were used to model the foam core. Furthermore, their approach for modelling the contact and the choice of material models were explained in detail by the authors. The numerical results were validated via both qualitative and quantitative comparison with experimental data (i.e., impact-induced deformation and load-history curves, respectively), demonstrating the reliability of their modelling approach. Kenny et al. (2002a, 2002b) used both the finite difference and finite element methods to analyze the elastic and plastic impulse buckling behaviour of slender metallic beams. The authors highlighted the importance of accounting for the beam's random initial imperfections in order to fully capture their behaviour. The authors also introduced a practical criterion for defining a threshold between elastic and plastic buckling. Zhang & Taheri (2002, 2004) also used the finite difference and finite element methods to simulate the pulse buckling response of E-glass/epoxy and carbon-epoxy beams with the objective of studying the effect of various parameters, such as initial imperfection and slenderness ratio. The higher-order shear deformation theory along with the von-Karman strain–displacement nonlinear relationship were incorporated to model the deformation of the beam, while the Hashin's failure criterion was used to predict the damage of beams. The presence of an initial imperfection proved to have more influence on the pulse buckling behaviour than the slenderness ratio. The results also revealed that the beam's momentum had the potential of being used as a parameter for predicting the pulse buckling response. The FE method was also chosen by Han et al. (2011, 2007) to model the behaviour of glass-fiber pultruded tubes overwrapped with glass- and carbon-fiber ±45° braided FRPs. The tubes were subjected to axial impact

and compared in terms of energy absorption capacity. The accordion crushing pattern obtained with the hybrid pipes was deemed more performant compared to the glass-based pipes, which failed in an asymmetric pattern and report a longitudinal split. Gao and Hoo Fatt (2012) used ABAQUS/Explicit FE software to perform a numerical simulation of the buckling response of cylindrical shells under radial compressive blast. In the study, the authors examined the influence on the buckling response of different parameters, such as shell thickness, load duration, element aspect ratio, composite layup and fiber-orientation angle.

Specific to the 3D-FML composite, Asaee et al. (2015; 2016) conducted numerical simulations of various configurations of 3D-FML panels subjected to the out-of-plane low-velocity impact, using ABAQUS/Explicit. After validation of their models by comparison of their results with experimental data, the authors used the FE approach to reduce the number of experimental tests necessary for the optimization of the stacking sequence of the different configurations of their 3D-FMLs. The authors also studied the potential of further strengthening the panels by insertion of glass and carbon fabrics adjacent to the 3D fiberglass fabric of their 3D-FMLs. In another study, Asaee et al. (2017) also modelled the delamination-buckling behaviour of short 3D-FML beams, whose metal/FRP interface was reinforced with graphene nanoplatelets, subjected to in-plane quasi-static loading.

Furthermore, as was previously underlined, a critical aspect involved in the analysis of 3D-FMLs, or FMLs in general is the delamination phenomenon that may occur within the interfaces of various constituents forming such hybrid systems. In FE modelling, the main techniques used to simulate fracture initiation and propagation are the (i) element erosion approach, (ii) cohesive zone modelling (CZM), and (iii) extended finite element method (xFEM). It should be noted that other techniques, like the Virtual Crack Closure Technique (VCCT) may also be coupled with other algorithms to simulate crack propagation in a body; however, only the techniques that could individually simulate crack propagation are briefly discussed in here.

The element erosion approach entails deleting elements based on an appropriate stress or strain criterion, therefore, leading to the formation of a crack path. It is the simplest of

the mentioned methods but is significantly mesh-dependent, thus, often lacking an acceptable accuracy (Tsuda et al., 2015).

CZM is a relatively easy method to implement (Barenblatt, 1962); however, it requires a priori knowledge of the crack path, unless coupled with an advanced re-meshing technique (Wang & Waisman, 2016; Xu & Needleman, 1994). The technique has been used in a variety of applications (Alfano et al., 2004; Kim et al., 2011; Ranatunga, 2011; Yelve & Khan, 2013), because it is especially suitable for modelling interfaces in hybrid material systems; it also works well under large deformation conditions. Moreover, CZM can also be used to account for thermal effects (Sapora & Paggi, 2014), moisture (Sugiman et al., 2013), and fatigue (Giuliese et al., 2014; Johar et al., 2014). For instance, Marzi et al. (2008) used CZM to model the low-velocity impact of a vehicle's sub-structure consisting of various bonded components. Accurate results were obtained when the mesh used to discretize the cohesive zone was significantly fine. Moreover, the suitability of the method for large-scale simulations was also demonstrated. Lemmen et al. (1999) showed another application of CZM, when it was used to assess the performance of bonded joints mating composite components in a ship, obtaining a close agreement between the numerical results and experimental data. Dogan et al. (2012) used cohesive elements and tiebreak contact in LS-DYNA to simulate delamination between plies of fiber-reinforced polymers (note that tiebreak contact is also based on a cohesive zone algorithm). They obtained excellent results compared to their experimental results. In that study, each composite ply was modelled separately with either thin or thick shell elements, and the elements were then mated using cohesive elements or tiebreak contact.

The xFEM approach involves "enriching" the finite element formulation to account for the presence of a discontinuity, without the need for creating an actual discontinuity between the elements, thus removing the need for remeshing. Therefore, xFEM can simulate the onset of a crack and its propagation in multiple directions (Belytschko & Black, 1999; Goyal et al., 2004; Krueger, 2004; Moës et al., 1999). A detailed explanation of the method's implementation in LS-DYNA can be found in (Pascoe et al., 2013). The use of xFEM would be most effective when the crack path is unknown, or in cases where a crack is suspected to kink or bifurcate. This method has been recently utilized by several

researchers to simulate crack initiation and propagation in various media. For instance, Serna Moreno et al. (2014) analyzed the failure of a biaxially loaded cruciform specimen made of quasi-isotropic chopped strand mat-reinforced composite using xFEM and showed that no prior knowledge of the onset location of the crack was necessary to obtain an accurate prediction of crack initiation and propagation. This is a significant advantage of xFEM compared to CZM. Wang and Waisman (2015) used xFEM to model delamination in composites and showed that the interfacial failure of the plies and cracking of the laminate could be simulated with virtually no-mesh dependency. Mollenhauer et al. (2016) demonstrated the capability of the tiebreak contact and xFEM for modelling crack propagation in a precracked thick beam, under mode I loading. They showed the deviation of the crack that originally started in 0°/90° ply-interface, propagating into the adjacent 90°/0° interface. Motamedi and Mohammadi (2012) used the xFEM approach by further enriching the element formulation to obtain a more accurate crack propagation in an orthotropic media. Bhattacharya et al. (2013) also incorporated xFEM to simulate the fatigue crack growth at the interface of aluminum-ceramic bi-layered material, subjected to thermo-mechanical load. Accurate values of crack tip stress intensity factors were evaluated by extending the domain-based interaction integral approach. They also successfully simulated the fatigue response of the bi-material system under various fracture modes.

Although xFEM is a promising technique, it should be noted that in general, however, the accuracy of the results is highly dependent on the xFEM formulation, which is considerably more complex than the conventional finite element formulations (Wang et al., 2017; Wang & Waisman, 2017). As a result, xFEM is not readily available in all commercial finite element software, and if it is, the formulation is usually limited to very few element types.

Moreover, it is worth mentioning that there are a few studies that have compared the integrity of the three approaches when used in simulating crack propagation. For instance, Tsuda et al. (2015) used the erosion and xFEM elements of LS-DYNA for simulating the crack propagation resulting from the impact of a rectangular cast iron specimen in three-point bending configuration. The xFEM results were found to be in excellent agreement

with the experimental results, while the erosion elements could not accurately simulate the experimentally observed response. Curiel Sosa and Karapurath (2012) compared capabilities of the xFEM element against both cohesive and erosion elements for simulating the response of a standard double cantilever beam modelled using 3D elements in ABAQUS. They found their xFEM results to be more consistent and closer to the experiment results, and not too sensitive to mesh density. However, they observed xFEM's tendency to underestimate the fracture energy, while CZM overestimated it.

Chapter 3: Delamination Buckling Response of 3D Fiber-Metal Laminates Subjected to Different Loading Rates

Davide De Cicco and Farid Taheri

3.1. Abstract

In this paper, the buckling response of magnesium-based 3D fiber metal laminated composites (3D-FML) subject to four different strain-rates (static, 0.01, 0.1 and 1 s^{-1}) is experimentally investigated. The effect of varying initial delamination lengths on the response is also investigated. The buckling capacity, maximum load-carrying capacity and damage mechanisms are presented, and the overall response is discussed for all the cases. As expected, specimens without initial delamination carried a higher load under all the strain-rate values. Moreover, the length of the initial delamination had a negligible effect on the maximum load-carrying capacity. The recorded images of the specimens during tests show that the buckling of the first skin always occurs prior to failure of the core, while for the second skin, buckling occurs almost simultaneously along with the onset of core's failure.

3.2. Introduction

[…]

It should be noted that to the best of authors' knowledge, no studies have considered the response of such 3D-FMLs subject to various in-plane loading rates; even those few somewhat related and available to date are limited to examination of the response of conventional 2D-FMLs.

The aim of the present investigation is to gain a thorough understanding of the behaviour of the aforementioned new 3D-FML composite under axial impact loading.

Therefore, first the response of the FML subject to various strain-rates is investigated. A systematic characterization of the in-plane behaviour of 3D-FMLs under different strain-rates (i.e., quasi-static, 0.01, 0.1 and 1 s^{-1}), is carried out. For reasons mentioned in the preceding paragraphs, the influence of initial delamination is taken into account as well. For that, 3D-FML specimens hosting a delaminations in the order of 30%, 50% and 70% of the initial gage length are considered. The buckling capacity, post buckling behaviour and the maximum load-carrying capacities are reported, with the intent to provide better understanding of the failure mechanisms of the composite.

3.3. Experimental Procedure

3.3.1. Materials

AZ31B-H24 magnesium alloy plates (0.5 mm thick) were provided by MetalMart International (Commerce, CA, USA) and the 3D fiber-glass fabric was supplied by China Beihai Fiberglass Co. (Jiujiang City, Jiangxi, China). A two-part epoxy resin was used, composed of bisphenol-A-based Araldite LY 1564 resin and Aradur 2954 (cycloaliphatic polyamine) hardener, both supplied by Huntsman Co. (West Point, GA, USA). Finally, a two-part, 8-lb density urethane foam was obtained from US Composites (West Palm Beach, FL 3340, USA).

3.3.2. Specimen Preparation

The 3D-FML specimens consisted of a 4 mm thick 3D fiber-glass fabric-reinforced epoxy, filled with high density urethane foam, sandwiched between two Mg alloy plates. Mg plates' bonding surfaces were sand-blasted to ensure a better mechanical bonding between the metal and 3D composite element. The two-part epoxy resin was mixed with a mixer at 100 rpm, then degassed for 30 min in a vacuum chamber. The resin was then applied onto the 3D fabric with a brush. The composite was cured at 60°C for 2 h, then at 120°C for 8 h. Subsequently, the foam was injected into the 3D fabric's hollow cores, let to cure, and the excess was removed by sanding. Finally, the core and the magnesium plates were assembled using the same epoxy resin as previously mentioned. The assembly was

47

vacuum-bagged to achieve an optimal adhesion between all components. For specimens with initial delamination, two very thin sheets of Teflon were added at mid-span of the panels, between the core and the magnesium plates interface, on one side of the specimens only. Finally, appropriate size specimens were extracted from the panels, and their extremities were sanded using a circular sanding machine, in order to obtain flat, parallel and smooth surfaces.

3.3.3. Test Procedure

Specimens with dimensions of 90 mm x 21 mm x 6 mm, with 50 mm gage length, were used for evaluating the buckling response of the 3D-FML. It should be noted that no standard is available for evaluating the buckling response of such sandwich components under uniaxial compressive load. Therefore, the dimensions were established based on ASTM C364 standard, suggested for evaluating the edgewise compression strength of sandwich composites (ASTM Standard, 2010). Specimens were subjected to different strain-rates; that is: quasi-static, low rate (0.01 and 0.1 s^{-1}) and medium rate (1 s^{-1}), corresponding to 0.5 mm/min, 30 mm/min, 300 mm/min and 3000 mm/min, respectively. Note that higher velocities could not be achieved by the available testing machine. Four initial delamination lengths were also used, distinguished based on the percent gage length (i.e., 0% (virgin or intact specimens), 30%, 50% and 70%). A minimum of three specimens per group was tested, or 48 specimens in total. Those specimens that became inadvertently subjected to any degree of bending during the compressive testing were discarded from the test matrix.

The experimental set up is illustrated in Figure 3-1. The static, low, and medium strain-rate tests were performed using an MTS servo-hydraulic universal test machine, equipped with a 250 kN load cell (specifications provided in Appendix A). Load, displacement, and time data were directly obtained through the MTS793 software that was used to control the testing machine. A Dino-Lite digital microscope was used to record the response of specimens subjected to the static and low strain-rate tests, at a rate of one frame per second, while a Canon Rebel T2i was used for recording the response of specimens tested at the higher strain-rate, at a frame rate of 60 fps. Specimens were clamped in a specially

designed fixture allowing the load to be applied axially to the tips of the specimens and impeding the rotation of the section. Also, aluminum tabs with edge chamfer of 45° were used to minimize the stress concentration at both ends of the specimens.

Figure 3-1. Experimental set up: MTS testing machine with a specimen in test-fixture and the camera used for recording the response.

3.4. Results and Discussion

3.4.1. Description of the Behaviour of the Specimens

A general description of the delamination buckling behaviour, as well as failure mechanisms, are presented herein. Two typical load-displacement graphs for an intact (virgin) specimen, and a specimen with 50% initial delamination length, loaded at static loading rate, are illustrated in Figure 3-2. The actual time-lapsed response of these two specimens under static and 0.01 s^{-1} loading rates are illustrated in Figure 3-3 to Figure 3-6.

Five pictures are used per case, to represent the response of specimens from the beginning of loading to the complete failure of specimens. For the sack of clarity, references to both load-displacement curves and test pictures will be done in parallel. In addition, response of the virgin specimen tested under static loading rate will be described thoroughly. For the other cases, only the differences with respect to the reference test article will be mentioned.

As seen, the specimens behave linearly (path 1, Figure 3-2(a) and (b)) for the first part of the loading regime, up to the onset of the first instability, which is accompanied by a

49

sudden appearance of a delamination. This delamination abruptly extends, leading to the buckling of one of the skins, as seen in Figure 3-2(b). This corresponds to the sudden decrease in the load, shown by the second path in Figure 3-2(a) and (b). The unbuckled portion of the specimen remains relatively and seemingly straight and takes a further load (path 3 in the figure), until the second skin delaminates and buckles (path 4). In the specimens hosting a delamination, as anticipated, the buckling is initiated first on the delaminated zone (region 2 in Figure 3-2(b)). The specimen takes a further load (path 3 in Figure 3-2(b)), and then, the other skin suddenly delaminates, which is accompanied by an abrupt drop in load (path 4). During this stage, the core also begins to shear (hence the discontinuity along path 4). At higher loading strain, this core shearing would create a detrimental effect on the skin, in that it actually indents the skin, promoting its instability (see Figure 3-5(d)). These sequences of instabilities are clearly seen in Figure 3-3 to 6).

The tests were stopped when a displacement of 2.2 mm was reached, corresponding to the stage well passed the second skin stability loss, and for which a constant residual stress is reached.
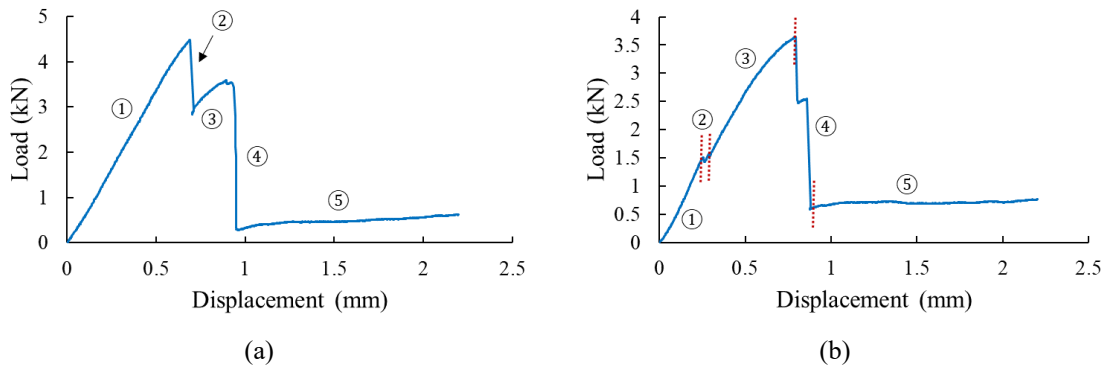
Figure 3-2. Representative graphs of specimens' behaviour under static axial loading: (a) virgin specimen, (b) specimen with 50% initial delamination.

50

(a) (b) (c) (d) (e)
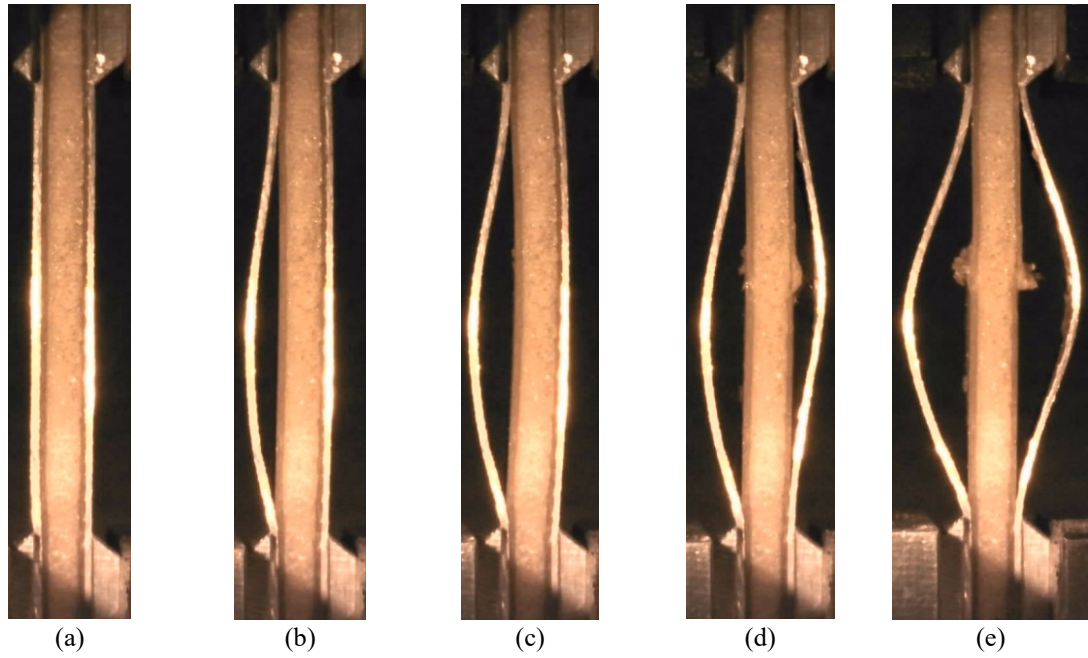
Figure 3-3. Illustration of the behaviour of the virgin 3D-FML sandwich under static compressive loading.

(a) (b) (c) (d) (e)
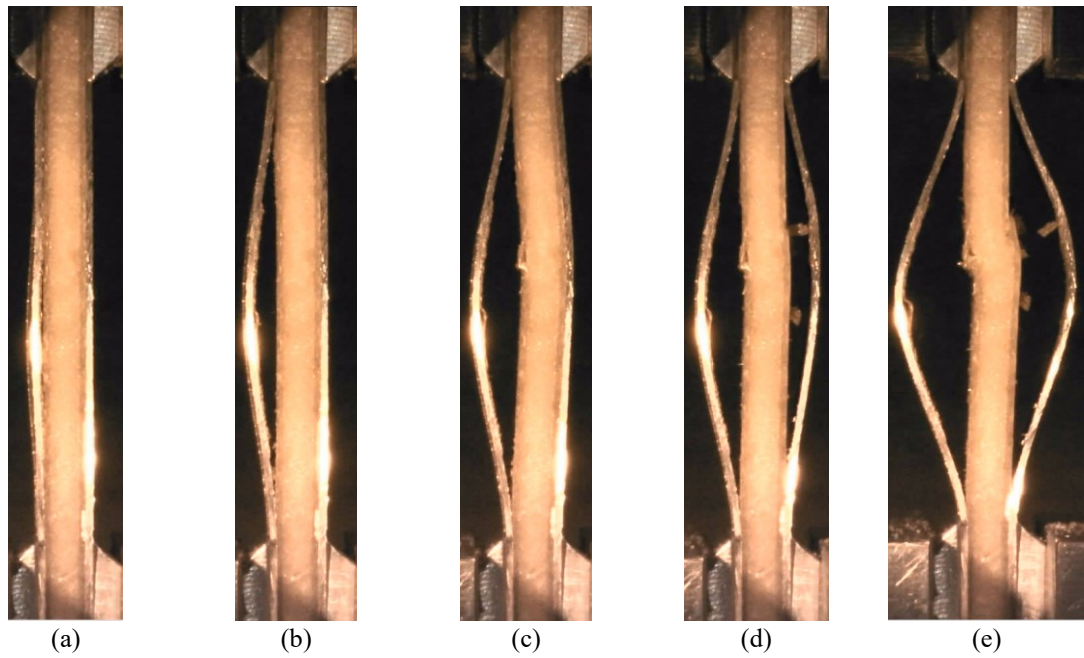
Figure 3-4. Illustration of the behaviour of the 3D-FML sandwich under static compressive loading, with 50% initial delamination.
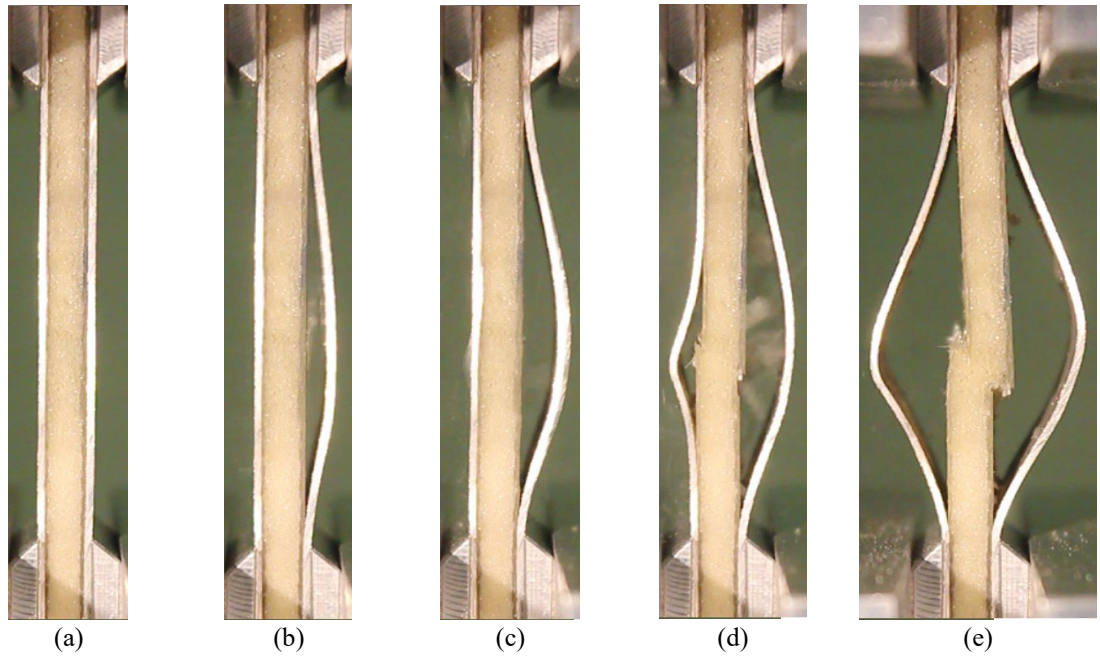
Figure 3-5. Illustration of the behaviour of the virgin 3D-FML sandwich under 0.1 s^{-1} compressive loading.
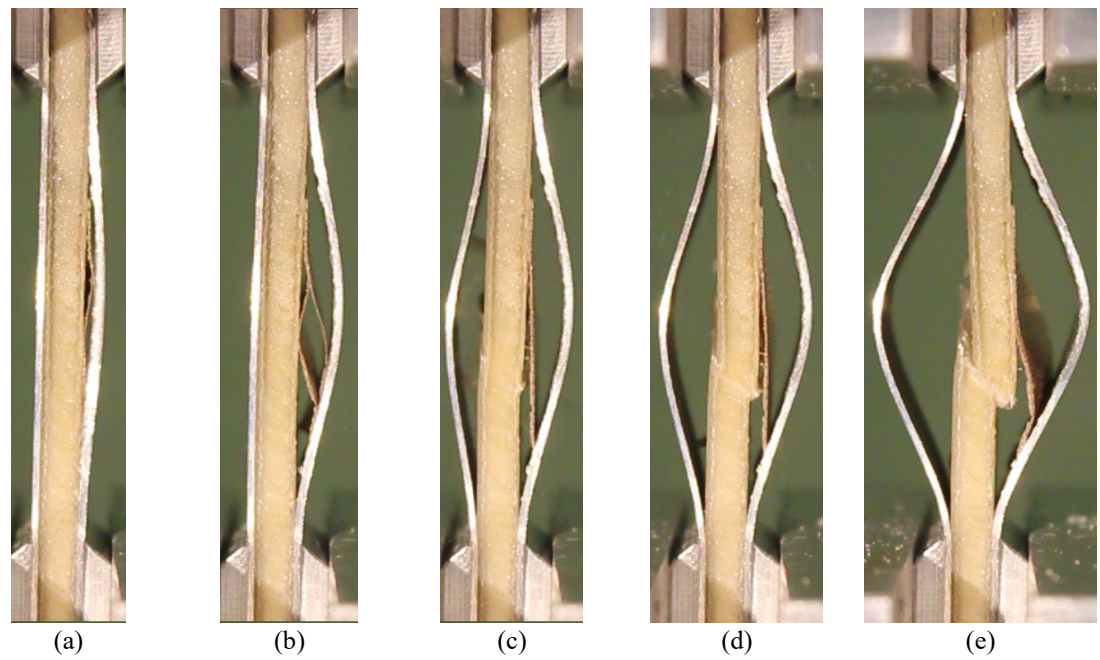
Figure 3-6. Illustration of the behaviour of the 3D-FML sandwich under 0.1 s^{-1} compressive loading, with 50% initial delamination.

3.4.2. Buckling and Loss of Stability

The values of load corresponding to the first loss of stability (i.e. delamination buckling of the first skin), are reported in Figure 3-7(a), for all delamination lengths and strain-rates. Two patterns of behaviour are observable: (i) the load decreases with the increase in delamination length; (ii) the load decreases with the increase of strain-rate as well. The exceptions would be the specimens with 30% delamination, tested at strain rate of 0.01 s^{-1} and those with 70% delamination, tested at 1 s^{-1} strain rate. In the first case, the value is slightly lower than expected, while it is higher in the second case. It should be noted that the data scatter is due to the inevitable anomalies resulting from the multi-stage fabrication process of the specimens; nonetheless, overall, the captured responses are fairly consistent. Focusing on the values, there is a decrease of approximately 50% in the capacity of the specimen hosting 30% delamination, compared to the virgin specimens' capacity. This highlights the significant influence of initial delamination on the stability of the first skin and, consequently, on the load-carrying capacity of the FML.

The load corresponding to the second stage of instability is reported in Figure 3-7 (b); the values correspond to the maximum load supported by the specimens passed the first stage of instability. The overall average capacity (see dashed line in Figure 3-7(b)) is approximately 3.573 kN. The capacity seems to be more or less independent of the initial delamination length and tested strain-rates. The maximum values are close, because, once the first skin has lost its stability, all specimens end up having the same configuration, that is, having one completely delaminated skin, but with the core well bonded to the other metallic skin, subjected to a slight bending. Therefore, one would expect that they would have a similar response. The discrepancies in the results are believed to be due to the inevitable anomalies occurring during specimen fabrication and testing. Moreover, one could attribute the relatively lower capacities corresponding to the specimens having delamination length of 30% and 50% to the fact that when the delamination of the first skin occurs in those specimens, the resulting release of energy affects the overall stability of the FML. In comparison, lesser energy is released in specimens with greater delamination length.

(a)   (b)
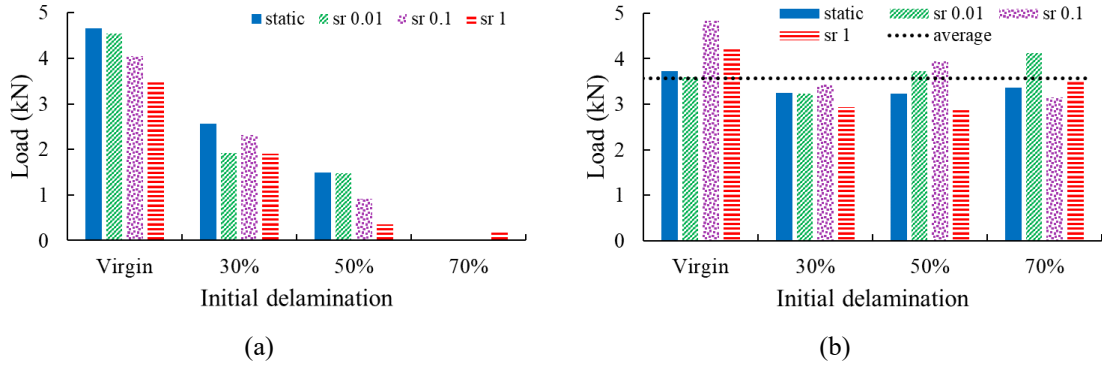
Figure 3-7. Load corresponding to: (a) first loss of stability, (b) second loss of stability, for different initial delamination lengths and strain-rates (NOTE: "sr" refers to strain rate, and "xx %" refers to the initial delamination length).
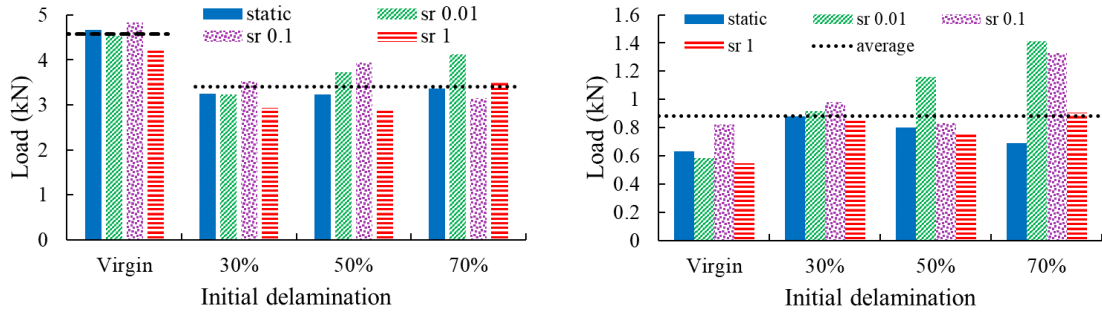
Figure 3-8. Maximum load with respect to initial length of delamination, for different strain rates.
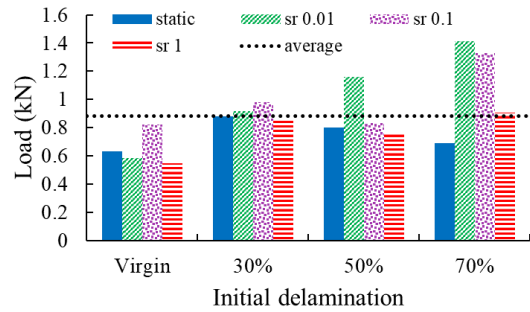
Figure 3-9. Residual load with respect to initial length of delamination, for different strain rates.

3.4.3. Maximum Load Capacity and Residual Load

The values of maximum load capacity of the specimens are shown in Figure 3-8, for all specimen categories and strain-rates. There does not appear to be any relationship between the maximum load capacity and initial delamination length, or with loading rate. However, as expected, an average increase of 50% in load capacity is demonstrated by the virgin specimens. Again, there does not appear to be any dependency between the maximum load capacity and strain-rate. It should be noted that the maximum load capacity of the virgin specimens reflects the load corresponding to the second stage of instability. The scatter in the results is attributed to the reasons mentioned earlier.

The residual load is defined here as the mean value of the load that a specimen can carry well passed the second loss of stability stage; it is calculated over the displacement range of 1.8 to 2.2 mm. Results for all specimen categories tested under different strain-rates are reported in Figure 3-9.

As can be seen, all specimens could carry a minimum of 0.5 kN after the second-stage instability. This value corresponds to 12% and 18% of the maximum load capacity for the virgin specimens and those with initial delamination, respectively. However, in average, the specimens are able to carry 0.882 kN (see dashed line in Figure 3-9). This value corresponds to approximately 30% of the maximum load carried by the virgin specimens, and 40% of the maximum load carried by specimens hosting an initial delamination.

The scatter of the results is attributed to varying lengthwise position of the crack that occurred along the core in each specimen, and the subsequent relative position of the failed core region (see Figure 3-3 and Figure 3-6). The analysis of the record images indicates that the created inclined cracks and bending of the core could lead to higher load values.

3.4.4. Stability Index

Here we introduce the concept of stability index (SI), which is a modified version of the ductility index introduced by Beaumont et al. (1975). This parameter is used to quantify the ratio of energy that corresponds to the onset of the first and second stage instabilities to the total energy, respectively, which can be represented mathematically as:

$$SI = \frac{E_p^i}{E_{tot}} \qquad (3\text{-}1)$$

In the above equation, E_{tot} is the total energy, corresponding to the area under the load displacement curve, up to a displacement of 2.2 mm, and E_p^i corresponds to the area up to the peak value of load corresponding to the i-th stage instability.

The SI values corresponding to the first (SI-1) and second stage instabilities (SI-2), are illustrated in Figure 3-10. The SI-1 values vary from 0.4 in the virgin specimens tested under static and quasi-static (0.01 s^{-1}) loading rates, to 0 for specimens with 70% initial

delamination length, regardless of the loading rate. The influence of strain rate is clearly visible in the virgin specimens. The SI-1 parameter corresponding to the faster loading rates (i.e., 0.1 and 1 s^{-1}) is approximately 40% lower than the ones corresponding to the static and quasi-static cases. Since the first loss of stability is exclusively due to the delamination buckling of one of the metallic skins, we could postulate that the strain-rate has a significant influence on delamination growth. This is also visible in specimens hosting 30% and 50% initial delaminations (note that the SI-1 is essentially zero for the specimens hosting 70% delamination length).

The values of the second stability loss show that virgin specimens could withstand higher energies. Indeed, the average value for the virgin specimens is 0.731, corresponding to a 63% increase with respect to the initially delaminated specimens, whose value is 0.449. In other words, the energy necessary to grow the delamination is much less than the energy required to initiate delamination. Moreover, no buckling is registered without a delamination, which results in even higher energy levels to be consumed by the elastic deformation of the skins. Similar to the results presented in the previous sections, the observed scatter, here, is mainly attributed to the fact that the second stability loss can be originated by both a core failure and delamination buckling of the second skin, along with the ensuing buckling. Hence, the shapes of the load-displacement curves present dissimilarities, which in turn affect the total energy.
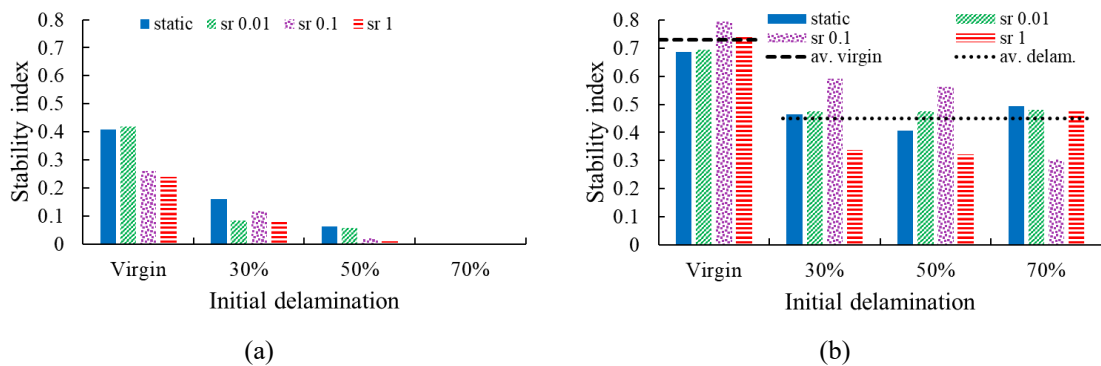
Figure 3-10. Stability index for: (a) first stability loss, (b) second stability loss, both with respect to initial delamination, for different strain-rates.

3.5. Conclusion

In this paper, the response of magnesium-based 3D fiber-metal laminates subject to in-plane compressive load applied at different strain-rates were presented. Two types of specimens where used, those hosting an initial delamination of varying lengths, and those intact or virgin. The values of loads corresponding to the onset of initial and secondary instability of the specimens were presented, as well as the maximum load-carrying capacities. A stability index, based on the ratio of energy necessary to cause instability, over the maximum energy, was introduced. The parameter was used to effectively compare the energy absorption capacities of the FML specimens. A general description of the buckling, post-buckling and failure behaviours of the composite was also presented.

It was demonstrated that the extent of initial delamination had a significant influence on the load corresponding to the first-stage instability, resulting into delamination buckling of one of the metallic skins. It, however, had a much lower impact on the ignition of the second-stage instability, which was caused by delamination buckling of the second skin and concurrent failure of the 3D glass-epoxy core. It was also observed that the strain-rate had minimal influence on the maximum load-carrying capacity of the FML specimens. Another interesting observation was the fact that the presence of an initial delamination reduced the load-carrying capacity of the specimens, as expected; however, the delamination length did not influence the capacity.

A similar trend was observed when comparing the stability indexes. The energy required to delaminate the first skin in virgin specimens was much higher than the energy required to propagate the initial delamination. This revealed relatively similar energy absorption capacity values for specimens that had an initial delamination. However, the virgin specimens exhibited 50% greater energy absorption capacity regardless of the loading rate. Therefore, one can conclude that stronger bonds between skins and core would lead to improved performances.

The recorded images of the specimens during the tests enabled us to gain a better understanding of the associated buckling and failure mechanisms. It was observed that the first loss of stability was due to the delamination buckling of one of the skins, while the

second instability stage was initiated essentially concurrent to failure of the core and delamination buckling of the second skin. It is postulated that a change in thickness of the core would lead to different mechanism after the first stage of instability.

Chapter 4: Understanding the Parameters that Influence Buckling of 3D Fiber-Metal Laminates

Davide De Cicco and Farid Taheri

4.1. Abstract

In this paper, a simple numerical model was developed using LS-DYNA, a commercially available finite element software. The model was used to conduct a parametric study with the aim of investigating the performance of the 3D fiber-metal laminate (3D-FML) developed by our research group, under axial loading. The study evaluated effects of the initial perturbation, material properties, specimen's thickness, boundary conditions and gage length on the buckling response. The results produced by the study were validated by experimental results. The buckling capacity of the 3D-FML was also compared with respect to that of specimens made of aluminum and fiber-reinforced plastics, having equivalent bending stiffness. The intricacy in properly modelling the boundary conditions, and the sensitivity of buckling response to the way the actual boundary conditions are modelled numerically are also discussed.

4.2. Introduction

[…]

To the best of authors' knowledge, works specifically exploring buckling of 3D-fiber metal laminates are limited to (Asaee et al., 2017; Asaee et al., 2015; Asaee & Taheri, 2016; De Cicco & Taheri, 2016), in which it has been demonstrated that several factors affect the response. Therefore, understanding the influence of various parameters that govern the stability of this 3D-FML under in-plane loading is of paramount importance, enabling one to optimize the performance of the material when used in vehicles. It should be noted that experimental examination of the parameters that influence the stability

response of such composites would not be a feasible approach. Therefore, the objective of this research is to conduct a numerical investigation with the aim of better understanding the influence of some of the parameters that significantly affect the stability of the 3D-FML. Finite element analysis (FEA) is considered to be one of the most effective and efficient means to conduct parametric studies (Fu et al., 2007; Fuoss et al., 1998; Stickler & Ramulu, 2002). In our preliminary investigation, we consider a relatively simple, yet relatively accurate and efficient numerical model, developed in LS-DYNA environment FEA software. MATLAB was used to facilitate the process of permutations of the considered parameters. Experimental results were used to validate the numerical predictions, rendering the simplified approach to be adequately effective and accurate. More experimental investigations will be carried out in the next phase of the study to further validate some of the FEA results.
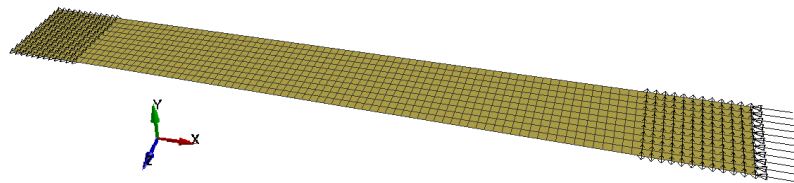
Figure 4-1. The FE mesh, boundary conditions and applied load.

4.3. Numerical Procedure

4.3.1. Modelling Approach

Numerical simulations of the buckling response of the 3D-FML under static axial compressive load were performed using LS-DYNA, a commercial finite element (FE) software. An experimental investigation was also conducted to validate the numerical results. A simplified approach was used to model the entire 3D-FML (i.e., all its constituents) using a single layer of shell elements (cf. Figure 4-1). The model, however, accounted for each of the constituents (i.e., the magnesium alloy skin, fiberglass plies and the combined glass pillars/foam core region), using their respective material properties and thickness, inputted via the keyword *PART_COMPOSITE. In this way, a separate integration point is attributed to each material constituent. Note that all layers are assumed

to be tied together, thus inhibiting modelling of any potential delamination. Table 4-1 presents a summary of the FE model.

The magnesium alloy skins were modelled using the plasticity model *MAT_PIECEWISE_LINEAR_PLASTICITY, and the fiberglass plies were modelled using *MAT_ENHANCED_COMPOSITE_DAMAGE, which is an orthotropic material model, with Chang-Chang damage criterion, recommended for modelling fiber-reinforced composites. Response of the combined glass pillars/foam of the core was modelled using the plasticity model *MAT_LAYERED_LINEAR_PLASTICITY. A better choice for modelling would be the use of crushable foam model; however, this model cannot be used in conjunction with the shell element in LS-DYNA. Therefore, the actual stress-strain curve of the foam was inputted in the model. Also, the implicit solver, with the arc-length method enabled, was used to obtain the post buckling behaviour.

Furthermore, Kenny (2001) demonstrated the need for modelling the actual restraining test fixture for obtaining accurate buckling behaviour. In our analyses, however, the fixtures themselves were not modelled, but their effect on the end portions (22 mm at each end) of the specimens was taken into account by applying the appropriate boundary conditions over the segments that were actually restrained (gripped) by the test fixture.

Table 4-1. Specifics of the FE model.

Constituent	No. of integration points	Thickness (mm)	Material model
Top skin	1	0.5	*MAT_024
Top ply	1	0.45	*MAT_054
Core	2	3.4 (1.7 at each point)	*MAT_114
Bottom ply	1	0.45	*MAT_054
Bottom skin	1	0.5	*MAT_024

The use of a perturbation (or incorporation of small imperfection) in the mesh, is a common procedure in order to initiate the buckling process. Here, the specimen imperfection was modelled by perturbing the mesh in the lateral direction by:

$$p(x) = A \sin \frac{\pi x}{L_{tot}} \qquad (4\text{-}1)$$

where $p(x)$ is magnitude of the lateral imperfection, A is the amplitude of the maximum imperfection, and L_{tot} is the total length of the specimen (including the parts held in the fixture). This imperfection was selected based on the actual imperfections extracted from the images recorded during the experimental tests; this also conforms to the natural curvature seen in most auto body components.

The material properties were obtained from in-situ tests. The modulus of elasticity and tensile strength of the 3D fiberglass fabric resulted to be substantially lower than its equivalent unidirectional counterparts, mainly due to the knitting process and the actual high resin content pockets. Note that, as seen in Figure 4-1, the in-plane axial load was applied at one of the extremities of the specimen.

(a)

(b)
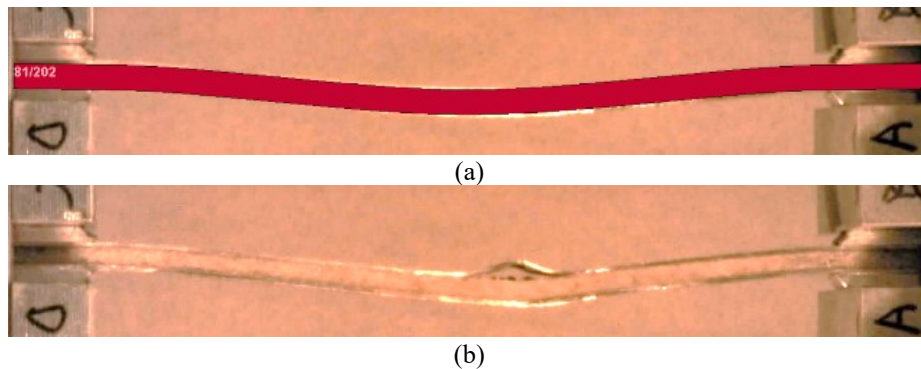
Figure 4-2. Comparison of the experimental and numerical deformed shapes; (a) FE model superimposed in red on an actual deformed specimen, (b) Actual mode of failure due to delamination of the skin.

Figure 4-2 illustrates the deformed shape obtained numerically, superimposed on the actual deformed shape of a typical specimen, at a load prior to onset of local delamination-buckling of the skin. As can be seen, the two shapes match precisely. However, the agreement holds up to the load prior to the load at which delamination buckling occurs in the specimens. As clearly visible from the load-axial shortening curve in Figure 4-3, the specimen buckles and the load capacity drops drastically once an axial shortening of around 1.5 mm is attained. The failure mechanism involves delamination of the magnesium skin from the fiberglass ply, on the surface that undergoes compression (cf. Figure 4-2(b)). As

mentioned previously, since the numerical model cannot simulate any delamination, the numerical results cannot be compared against experimental results after the onset of delamination. Moreover, the good agreement between the numerical and experimental results seen in Figure 4-3 attests to the adequacy of this relatively simple model in capturing the instability response of this complex system in a fairly accurate manner, thus rendering the model adequate for the subsequent parametric studies. In fact, the difference in the predicted buckling load capacity, which is the most commonly used design criterion, is less than 4%.

This model is, therefore, used to investigate the influence of various parameters on the stability response of the FML, and it is made available to the reader in Appendix B. The parameters that would be considered are the imperfection amplitude, component's thicknesses, material properties, as well as various boundary conditions and gage lengths. A MATLAB code was developed by which the necessary variation in the parameters used in LS-DYNA's input file could be generated and run automatically in the runs that did not require construction of a new FE mesh, thus increasing the efficacy of the numerical analyses.
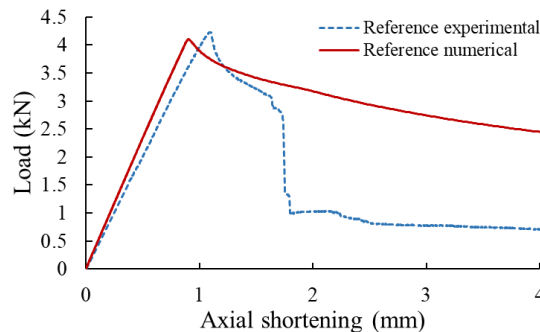
Figure 4-3. Comparison of experimental and numerical results for the reference specimen.

To facilitate readers' understanding of the parametric study, a summary of the parameters that were used in the study is provided in Table 4-2. The following abbreviations are used in this study; Mg: magnesium; Al: aluminum; Fg: fiberglass; Cf: carbon-fiber; Fo: the foam used in construction of actual specimens; Fw and Fs refer to the foams with a lower and higher density than that used in actual specimens, respectively, and Fix and Pin refer to fixed and pinned boundary conditions, respectively.

Table 4-2. Summary of the parameters used in the numerical studies.

Parameter whose effect is considered	Perturb. Amplitude (mm)	Thickness			Material type			Length		B.C.
		Skin thickness (mm)	Ply thickness (mm)	Core thickness (mm)	Skin	Ply	Core	Gage length (mm)	Length of restrained portion (mm)	
Imperfection	0, 0.05, 0.1, 0.2, 0.5, 1, 1.5, 2, 5	0.5	0.45	3.4	Mg	Fg	Fo	150	22	Fix-Fix
Thickness	1	0.5, 0.8, 1	0.45, 0.6, 1	1.4, 3.4	Mg	Fg	Fo	"	"	"
Properties	"	0.5	0.45	3.4	Mg, Al	Fg, Cf	Fo, Fw, Fs	"	"	"
B.C.	0.05	"	"	"	Mg	Fg	Fo	150	22 or none	Fix-Fix, Fix-Pin, Pin-Pin, Fix-Free
Length	"	"	"	"	"	"	"	150, 175, 200, 225, 250, 300	22	Fix-Fix
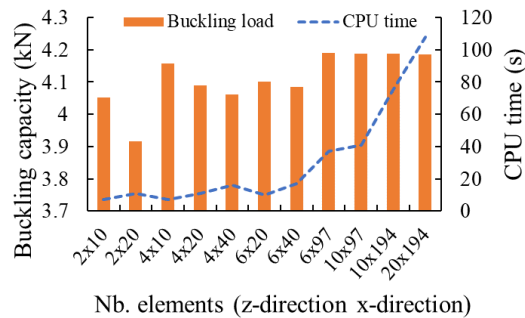
Figure 4-4. Results of the mesh convergence study.

4.3.2. Effect of Mesh Density

A mesh convergence study was carried out to establish the most appropriate mesh density by which consistent and fairly accurate results could be obtained, with minimal CPU consumption. For consistency, all models were run on a single core. Figure 4-4 shows that convergent results are achieved with a mesh of 6 x 97 elements. It can be noted that increasing the number of elements in the width direction from six to ten did not improve the computed results, but it did not increase the CPU time, either. Therefore, the chosen

mesh density for all simulations presented in this paper has been taken as 10 x 97. It should be noted the same mesh density was scaled and used in modelling longer specimens.

In addition to the mesh convergence study, the effect of the number of integration points for modelling the foam, whose thickness is relatively much greater than the thickness of the other constituents, was also investigated. Two simulations, one with two integration points, and another one with 20, were considered. No significant difference in the results was noted; therefore, the subsequent analyses were carried out with two integration points for the foam.

4.4. Results and Analysis

4.4.1. Effect of Imperfection Amplitude

As described by equation (1), the imperfection was assumed to be in a half-sine wave shape with an initial amplitude of 1 mm; however, amplitudes ranging from 0 to 5 mm were tested and their effect on the behaviour is reported in Figure 4-5 and Figure 4-6. As can be seen, the specimen with 5 mm amplitude exhibited a response that could not be considered as a buckling response; therefore, it was not be taken into account, thus not reported in Figure 4-6.
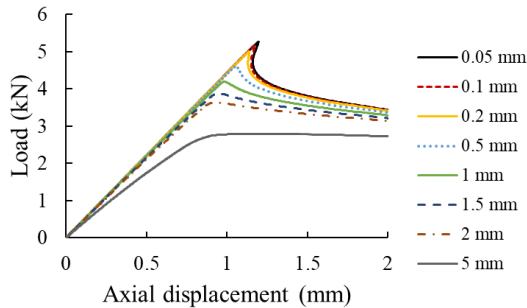
Figure 4-5. Load-axial shortening curves of models having different imperfection amplitudes.
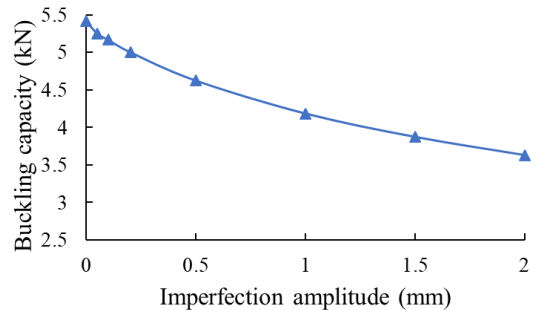
Figure 4-6. Variation of the buckling capacity as a function of imperfection amplitudes.

From Figure 4-5, it is clear that the imperfection has negligible influence on the stable or pre-buckle response of the specimen, while it clearly influences the buckling load and post buckling response of the specimens. For the lower imperfection values, the "snap-

bulking" phenomenon is noticeable. The significant decrease in the buckling capacity becomes more evidence for specimen with 0.05 mm and greater imperfections. The specimen with 1 mm imperfection exhibits 20% loss in buckling capacity compared to the one with the lowest imperfection. Also, it worth noting that buckling is observed in the specimen with no initial imperfection. The numerical uncertainties appear to be triggering the instability.

4.4.2. Effect of Constituents' Thickness

In this section the effect of constituents' thickness on buckling response is investigated. The variations in the thicknesses, as reported in Table 4-2, was selected based on the actual commercially available dimensions. The first aspect of the change in behaviour is observable in Figure 4-7, where the thickness of the core seems to greatly influence the pre-buckling or stable response of the specimens. In fact, in the case of 3.4 mm thick core, the response is linear, while it becomes nonlinear when thinner cores are considered. Also, the axial shortening at which the buckling occurs is relatively lower when a thinner core is used. On the contrary, the post-buckling behaviour seems to be influenced by the FRP plies' thickness; in fact, after the onset of buckling, the specimens with thicker FRP plies tend to carry more load than those with relatively thinner plies. Finally, as expected, the metallic skin thickness seems to have comparatively the greatest impact on the buckling capacity than the other constituents. This is because the skins, which are the outer parts of the system, encounter the greatest stress; therefore, since they are the stiffest constituent, they influence the buckling capacity significantly.
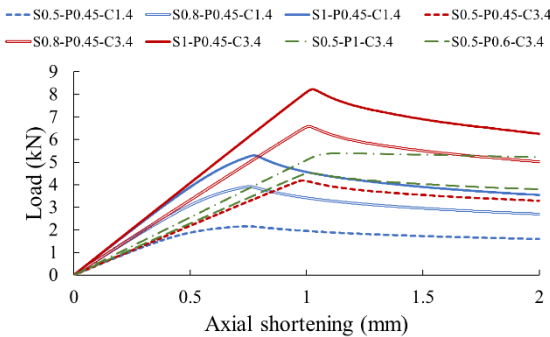
Figure 4-7. Load-axial shortening curves for different component thicknesses.
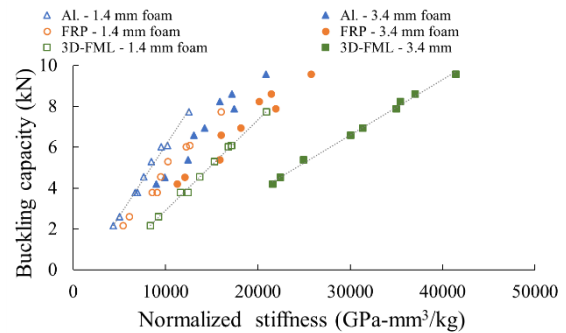
Figure 4-8. Buckling capacity versus normalized bending stiffness.

The other interesting behaviour can be seen from the results illustrated in Figure 4-8, which presents the buckling capacity as a function of the normalized flexural stiffness. The results are normalized in three different ways. First, the results are normalized with respect to the weight of the 3D-FML with x.x foam thickness (referred to as 3D-FML – x.x mm foam). The second set of results are normalized with respect to the weight of an aluminum specimen having equivalent bending stiffness as that of the 3D-FML with x.x thickness (i.e., Al.– x.x mm foam). Finally, the third set is normalized with respect to the weight of a fiber-glass/epoxy specimen, having the same bending stiffness as 3D-FML specimens with x.x foam thickness (i.e., FRP – x.x mm foam). The equivalent aluminum and FRP specimens have the same width and length as the 3D-FML. In addition, the stacking sequence of the FRP specimens were limited to biaxial fiber-orientations, with a symmetric configuration. The following configurations were considered: $[(0/90)_n/\overline{0}]_s$, $[(0/90)_n/\overline{0}]_s$, $[(0/90)_n/0/\overline{90}]_s$, and $[(0/90)_n]_s$. The normalization is done based on the following equation:

$$Normalization = \frac{D_{11}^i}{W_i} \qquad\qquad (4\text{-}2)$$

where D_{11} is the axial bending stiffness, W is the weight of 3D-FML specimen or the specimen with equivalent stiffness, and i is the specimen configuration identifier.

The normalized results illustrated in Figure 4-8 highlight the superior buckling capacity offered by the 3D-FML from the perspective of weight. One can see that the 3D-FML is clearly the most efficient configuration, followed, in order of performances, by the FRP and aluminum. A distinction between the cases, whose results were normalized with respect to the overall thicknesses, is also discernable. The buckling capacity suffers as the thickness becomes smaller, regardless of the material and configuration.

It is necessary to mention that in real applications, the above-mentioned superior buckling capacity of the 3D-FML might become affected by the onset of skin/FRP-ply interface delamination. In fact, as highlighted in previous works (Asaee et al., 2017; De Cicco & Taheri, 2016), delamination-buckling of one of the skins could occur at a load lower than the theoretically-established buckling capacity. As stated previously, the relatively simple model used here does not account for such a delamination mechanism.

However, one can confidently conclude that an improvement in the interface bond strength should enable the specimens to attain their theoretical buckling capacity.

4.4.3. Material Properties

Another focus of the study was to investigate the influence of material properties on the buckling response. For that, a different material was considered to form the skin. Aluminum 2024-T3 was selected in this part of the investigation due to its light-weight, and extensive use in various applications, especially its usage in the aerospace sector. The properties of this aluminum was extracted from (Varmint's Al, n.d.), and were considered adequate for the purpose of this preliminary work. Another permutation was achieved by replacing the 3D fiberglass fabric with an equivalent carbon-fiber fabric, whose properties were obtained through our previous mechanical tests conducted on a unidirectional carbon fabric. Finally, the stress-strain curve of the foams having lower and higher density than the one used in the actual specimens were estimated based on the supplier's information and the actual properties of the reference foam, obtained experimentally. Therefore, the lower density foam's stress-strain curve was established by degrading (scaling down) the reference foam's stress-strain curve by 33%, while the higher-density foam's stress-strain curve was scaled up by 2.5 times.

The resulting buckling capacities are summarized in Figure 4-9, and are reported with respect to the normalized stiffness, according to the same normalization procedure explained in the previous section. As seen, a similar pattern in behaviour is observed, with the best performance exhibited by the 3D-FML, followed by FRP and aluminum, respectively. Moreover, results illustrated in Figure 4-9 and Figure 4-10 reveal that a gain of 50% in the buckling capacity can be attained by replacing the magnesium skins with aluminum. This is combined with a 24% decrease in the axial shortening prior to buckling. Note that the results corresponding to the foam properties are not reported, because they did not have a significant influence on buckling response of the 3D-FML within the considered range.

The effect of carbon fabric is reported in Figure 4-9 as well. The same pattern as observed for the case of glass fabric is visible. In addition, interestingly, an overall increase of 0.8 kN in the buckling capacity is observed for all skin-foam configurations (e.g., increase from 4.2 kN to 5 kN and increase from 6 kN to 6.8 kN, as seen in Figure 4-9), which represents a 22% increase in the case where magnesium skins are used. Furthermore, the load-axial shortening curves of the four materials combinations are illustrated in Figure 4-10. The results indicate that properties of the skins have the most influence on the buckling response, while the maximum buckling capacity is both affected by properties of the skins and FRP plies.
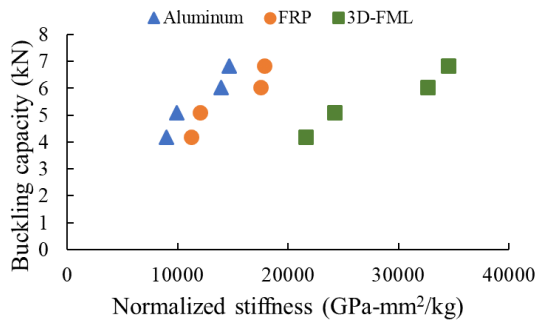
Figure 4-9. Buckling capacity versus normalized bending stiffness, for different material properties.
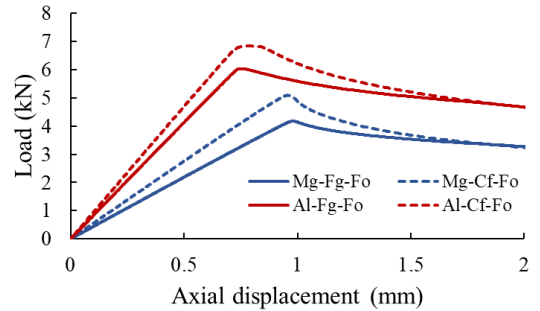
Figure 4-10. Influence of the material properties on buckling response.

4.4.4. Influence of Boundary Conditions

It is well known that boundary conditions (BCs) have a significant influence on the buckling capacity of axially loaded members. For this reason, the four most commonly used BCs, namely fixed-fixed, fixed-pinned, pinned-pinned and fixed-free, are simulated and the resulting buckling capacities are compared. The comparison is made purely from a numerical point of view; the comparison with experimental results will be the focus of our future works. For all the tests, the gage length is kept constant at 150 mm and the amplitude of the imperfection is reduced to 0.05 mm to promote a distinct buckling behaviour under all conditions.

The results are presented in Figure 4-11. As expected, the fixed-fixed setup offers the highest buckling resistance capacity, follow by the fixed-pinned specimen with 27% reduction, pinned-pinned with 62% and fixed-free, with 91% reduction in buckling

capacity. Furthermore, the critical buckling load of a composite column can be estimated with the Euler buckling equation, and the use of an appropriate factor provided to account for the boundary conditions, as follows:

$$P_{cr} = \frac{\pi^2 b D_{11}}{(\beta L)^2} \qquad \text{with:} \qquad \begin{aligned} &\beta = 0.5 \text{ for fixed-fixed} \\ &\beta \approx 0.7 \text{ for fixed-pinned} \\ &\beta = 1 \text{ for pinned-pinned} \\ &\beta = 2 \text{ for fixed-free} \end{aligned} \qquad (4\text{-}3)$$

In above equation, P_{cr} is the buckling capacity, L and b are the gage length and width of the specimen. Equation (4-3) predicts a quadratic variation of the critical buckling load with respect to the BCs. However, the result obtained from the simulations, as illustrated in Figure 4-11, reveal a linear variation.

In order to establish whether the cause of observed disagreement could be due to an incorrect modelling approach, the buckling response of the same specimen (i.e., the same FE model), but this time made of single isotropic material (i.e., the magnesium alloy) was considered. The results, also reported in Figure 4-11, show the same linear pattern as observed for the 3D-FML case. This would indicate that the way the boundary conditions have been modelled is a potential cause of the discrepancy. In fact, the conventional way of applying fixed-fixed boundary conditions is to restrain the rotation and/or the translation of the nodes of the model located immediately at the boundaries of the actual fixture. However, such a modelling practice will indeed change the effective length of the specimen held by the grips, thereby affecting the overall response. Furthermore, this phenomenon may be amplified by the complex behaviour of the 3D-FML, which has not been fully understood at this stage of the research. Although the effects of the fixture grips were taken into account, a more appropriate modelling of the BCs would necessitate the use of a 3D FE model. This approach would allow one to restrain only the nodes in contact with the fixture (in this case, the external magnesium skins).
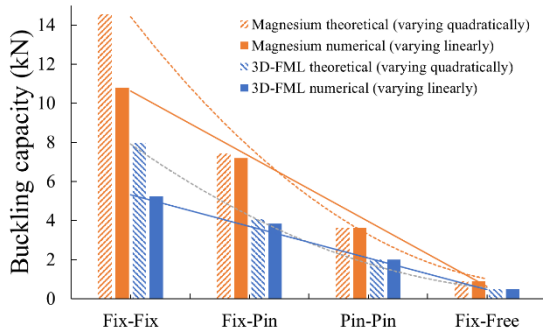
Figure 4-11. Buckling load for different boundary conditions.
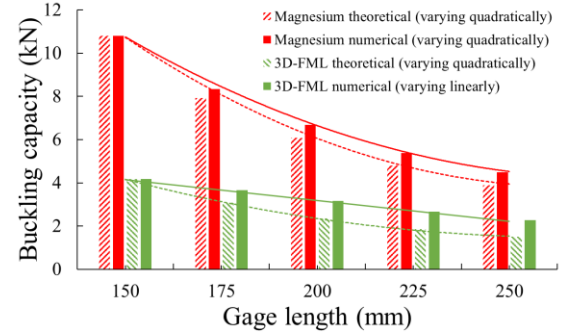
Figure 4-12. Buckling load for various gage lengths.

4.4.5. Influence of the Gage Length

The last influencing aspect investigated in this work is the effect of gage length on the buckling load capacity of the 3D-FML. Fixed-fixed boundary conditions were used and the imperfection amplitude was varied in such a way that the same curvature could be obtained for all selected lengths. In fact, as mentioned in (Zhang & Taheri, 2002), keeping the same perturbation amplitude for all specimen lengths led to more consistent results.

The results of the analyses are reported in Figure 4-12. As expected, the buckling load decreases when the gage length increases. However, equation (4-3) indicates that the variation should follow a quadratic trend, while the numerical results show a linear trend. Once again, isotropic simulation was used to pinpoint the source of the discrepancy. The obtained results, also reported in Figure 4-12, show that, in the case of isotropic material, the variation follows the expected quadratic trend. This would suggest that in the case of 3D-FMLs, additional coupling effects exist that would need to be taken into consideration. Perhaps resolution of this parameter would also resolve the trend discrepancy observed and discussed in last section.

4.5. Conclusion

A numerical model of the newly developed 3D-FML was constructed using the finite element software LS-DYNA. Parametric studies were carried out to investigate the influence of various parameters on the buckling response of the FML, highlighting the most

71

influencing factors. The influence of imperfection amplitude, constituents' thickness and properties, boundary conditions, and gage length were considered.

The results of the investigation can be summarized as follows:

- The initial perturbation or imperfection influences the buckling capacity and post-buckling behaviour of the 3D-FMLs, but its effect on the pre-buckled regime is insignificant.

- The core (or foam) thickness is the parameter that most influences the buckling capacity. This is also the parameter that enables the 3D-FML to outperform the stability response of specimens made of either aluminum or FRP possessing the same stiffness.

- The skins properties have important influence on the buckling capacity. For the majority of practical core thicknesses, the stiffer the skins, the more linear would be the pre-buckling behaviour.

- The boundary conditions and the way they are conventionally modelled numerically affect the predicted results significantly. The numerical results did not follow the trend predicted by the Euler equation, when either an isotropic or an orthotropic material was considered. This highlights the fact that when modelling thick and relatively short geometries, the use of conventionally applied FE boundary conditions would not produce accurate results, and that the actual restraining mechanism must be carefully and meticulously modelled.

- Similar to the effect of BCs, it was demonstrated that the variation of buckling load with respect to the gage length did not follow the Euler prediction in the case of the 3D-FML, while it did follow the Euler prediction when the material was isotropic. This nonconformity could be the outcome of inadequate modelling of BCs associated with the use of 2D FE modelling approach. The perturbation mode could also influence the effect of this parameter.

In closing, it is necessary to mention that the incapability of the rather simple modelling approach used in this study, in detecting delamination, limits the use of the model. This incapability results in gross over-prediction of the post-buckling load-carrying

capacity. Our experimental investigation also demonstrated that, in shorter specimens that would not buckle, the failure mode is associated with total debonding of the skin from FRP. This mechanism could not be detected by the simplified modelling approach either. However, the simplified modelling approach could be effectively used to investigate the influence of various parameters that could affect the buckling response of the 3D-FMLs. Moreover, the model clearly shows that improved buckling and post-buckling performances could be obtained by improving the bond strength of skin/FRP interface. In all, the very efficient computation CPU-time associated with the use of this simplified modelling approach warrants its use for preliminary parametric investigations.

Chapter 5: Robust Numerical Approaches for Simulating the Buckling Response of 3D Fiber-Metal Laminates under Axial Impact - Validation with Experimental Results

Davide De Cicco and Farid Taheri

5.1. Abstract

The reliability and efficiency of three different numerical modelling approaches for simulating the response of a newly developed 3D fiber-metal laminate (3D-FML), subject to axial impact loading, are considered in this paper. The main objective of the study is to establish the most robust numerical framework for analyzing the performance of such complexly configured hybrid materials subject to axial impact loading in a fairly accurate, yet efficient manner. LS-DYNA finite element software is used for the purpose. The models include: (i) a full 3D solid model, where all 3D-FML constituents are modelled with 3D elements; (ii) a model with intermediate complexity, in which two different element types are used to model the metallic skins and 3D-fiberglass/foam core, respectively; and (iii) a simplified scheme, consisting of a single layer of thin-shell elements, representing all constituents of the FML. An experimental investigation is also conducted in parallel to verify the accuracy of the modelling schemes. Force and axial-shortening histories, energy absorption capacity and overall qualitative behaviour obtained numerically are compared to experimental results. Both accuracy and computation cost are considered as the performance criteria, all with the aim of providing the reader with some perspective for robust modelling of such geometrically sophisticated composites, subject to a complex loading mechanism.

5.2. Introduction

[…]

To the best of authors' knowledge, however, there exists no information in the literature in regard to the behaviour of this newly developed 3D-FML under axial impact loading, which is an important design concern when considering the application of this FML in structural body components forming vehicles. Also, to the best of authors' knowledge, there exist no study comparing the accuracy and efficiency of the various modelling techniques that could be used to simulate the response of components made of such complexly configured materials. Furthermore, although there are a few studies reporting computational modelling of 3D braided composites (Gu & Xu, 2004; Guo-Dong et al., 2009; Miravete et al., 2006; Sun & Sun, 2004; Zeng et al., 2005; C. Zhang et al., 2017a, 2017b), numerical simulation works on 3D hollow core sandwich structures are very scarce (Hosseini et al., 2015). Therefore, computational models with various complexities are developed in order to establish an optimal modelling technique, as well to examine the influence of various parameters that govern the buckling response of this 3D-FML. The developed models included use of the conventional thin-shell, thick-shell and 3D isoparametric elements. The results from these simulations are compared with the data obtained through our experimental investigation. Moreover, as seen through the cited literature, in general, presence of a delamination adversely influences the response of laminated composites, and FMLs are no exception. Hence, the influence of an initial delamination on the response of the 3D-FML is also considered in this study. Results obtained from the analyses are compared with our experimental results. The paper, therefore, aims to provide the reader with suggestions in choosing the most computationally efficient and reliable modelling approaches, as well as providing a better insight into numerical modelling of such complex hybrid composite materials.

5.3. Materials and Experimental Procedure

5.3.1. Materials

The 3D fiberglass fabric was supplied by China Beihai Fiberglass Co. (Jiujiang City, Jiangxi, China), while the AZ31B-H24 magnesium alloy sheets, with thickness 0.5 mm, were provided by MetalMart International (Commerce, CA, USA). The epoxy resin, composed of two parts (i.e. bisphenol-A-based Araldite LY 1564 resin and Aradur 2954 (cycloaliphatic polyamine) hardener), was obtained from Huntsman Co. (West Point, GA, USA). Finally, a two-part, 8-lb density urethane foam was supplied by US Composites (West Palm Beach, FL 3340, USA).

5.3.2. Specimen Manufacturing

In brief, the 3D-FML specimens consisted of a 4-mm thick 3D fiberglass fabric (3D-FGF), impregnated in epoxy resin, cured, and subsequently filled with urethane foam, and then sandwiched between two thin sheets of magnesium alloy. The 3D-FGF consists of two layers of bidirectional fabrics, separated by approximately 4 mm long glass fiber pillars, thus leaving cavities that could be filled with a foam so to further enhance the overall performance of the fabric.

The first step of the manufacturing process entailed the impregnation of the fiberglass fabric with epoxy resin. For that, the two-part resin was mixed at 100 rpm for 10 min using a mixer and degassed for a minimum of 30 min in a vacuum chamber. The resin was then applied to the fabric using a brush. The application of resin to fabric essentially awakens the glass pillars, separating the two layers of bidirectional fabrics, leaving cavities in between. The impregnated fabric was cured for 2 h at 60°C, and then for 8 h at 120°C, according to the manufacturer recommendation. Porous peel-ply layers were placed on both 3D-FGF surfaces to guarantee homogeneous and consistent resin content on both surfaces of the fabric, and to generate surface morphologies that would facilitate improved adhesion to the magnesium sheets.

The second step involved filling in the hollow cavities of the 3D-FGF with the foam (see Figure 5-1(a)). In contrast to the procedure used in our previous works, the foaming process was switched from injection to aspiration. This procedure led to a more homogeneous dispersion of the foam within the cavities, also resulting in a significant reduction of fabrication time. It also eliminated the need for sanding the specimens to remove the excess of foam. Finally, the magnesium skins were sand-blasted with coarse 20-30 grit crushed glass to generate better mechanical bonding surface. A layer of resin was applied to one of the surfaces of the skins, and to the upper and lower surfaces of the 3D-FGF. The fabric was then sandwiched between the skins, and vacuum bagged. For the specimens with a pre-determined delamination, two very thin sheets of Teflon, of length equal to 50% of the gage length and of the same width as of the specimens, were placed at the mid-span between one of the magnesium skins and the 3D-FGF to prevent adhesion, as shown in Figure 5-2. Another curing cycle (as described above) was needed to facilitate the cure of the interface resin. Figure 5-1(a) illustrates the constituents at various stages of the manufacturing process.

(a)   (b)
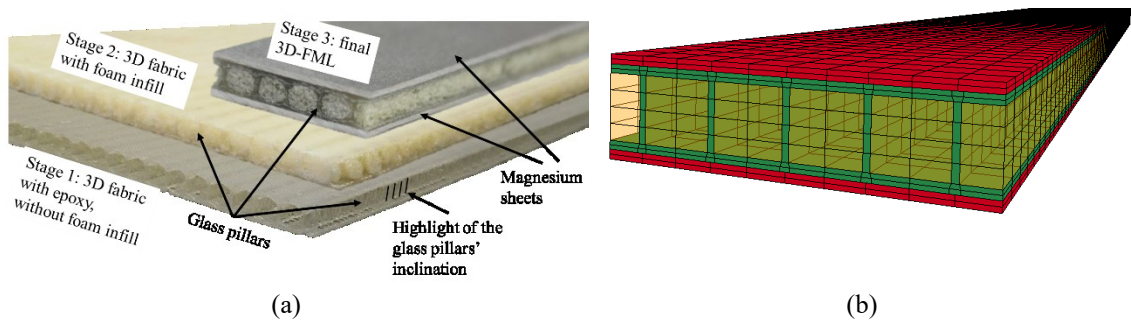
Figure 5-1. (a) 3D-FML's constituents at various stages of the manufacturing process, (b) the corresponding FE mesh using solid elements.
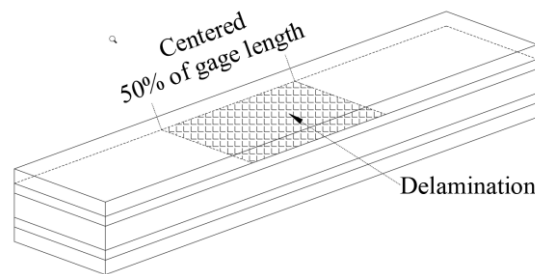
Figure 5-2. Illustration of the position of the initial delamination in the 3D-FML specimen.

5.3.3. Testing Procedure

Specimens with dimensions 190 mm x 20 mm x 5.3 mm, with 150 mm gage length, were impacted using a modified Charpy impacting machine, consisting of a pendulum, an impactor and a fixture to hold the specimens in place, as shown in Figure 5-3(a). A close view of the fixture is reported in Figure 5-3(b); it was designed to allow for the displacement of the end portion of the specimen in the longitudinal direction (on the impacted side), while preventing displacement in the other directions, as well as restraining the rotation of the ends. For this purpose, 20 mm of the specimen's ends was clamped with aluminum tabs (see Figure 5-3(b)).

Four different impact energies (i.e., 1.5 J, 3 J, 4.5 J and 7 J), were considered in this study. The initial height of the pendulum was set to have the impactor imparting the correct energy to the specimens. The choice of the impact energies was based on the damage thresholds targeted for the specimens. In other words, under the lowest energy, the behaviour was purely elastic, and the specimens recovered their initial shape after buckling. The 3 J energy caused the development of a permanent deformation after prompting the onset of buckling. The 4.5 J was the threshold energy, which caused the development of a partial delamination of one of the skins. Finally, the 7 J was selected to cause complete failure of the specimens. A minimum of three specimens was impacted to obtain consistent results. For each specimen within a given category, the root mean square (RMS) of the collected signals were evaluated and plotted. These so-called "refined" curves better illustrate the response of the material, because they do not include the inevitable and unwanted signal noise recorded by the sensors. As a typical example, Figure 5-4 illustrates the "as collected" and "refined" data for the case of baseline specimens that were subjected to the most critical impact energy (i.e., 7 J). The peak load and immediate post buckling response were the criteria for the selection of the specific curve against which the numerical results were compared. As can be seen, there are discrepancies in the beginning portion of the curves. The discrepancies are attributed to the initial settlement of each specimen within the holding jig/fixture at the onset of impact. That is why the specimens impacted at lower energies exhibited lower discrepancies with the initial portion of their response.

A Photron Fastcam PCI high speed camera was used to record the impact events at a rate of 2000 fps. The recorded images were used to verify the buckling behaviour obtained from FE simulations. In addition, impact load and axial-shortening history data was collected by means of a dynamic load cell and a dynamic linear variable displacement transducer (DLVDT), both at a sampling rate of 50 kHz.

(a)   (b)
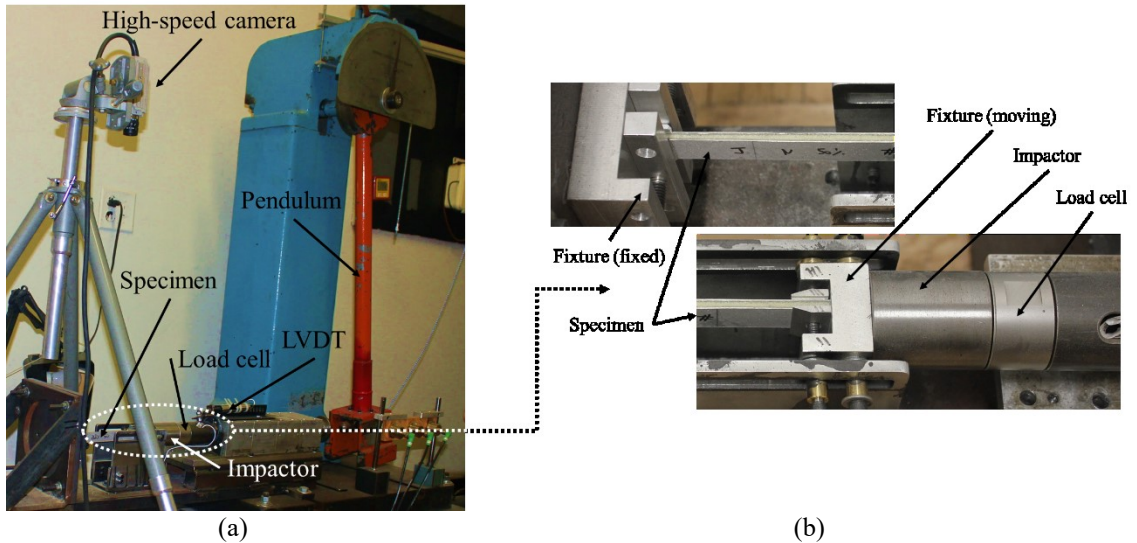
Figure 5-3. (a) overall experimental set up and (b) close-up view of the specimen in its fixture, and impactor.

(a)   (b)
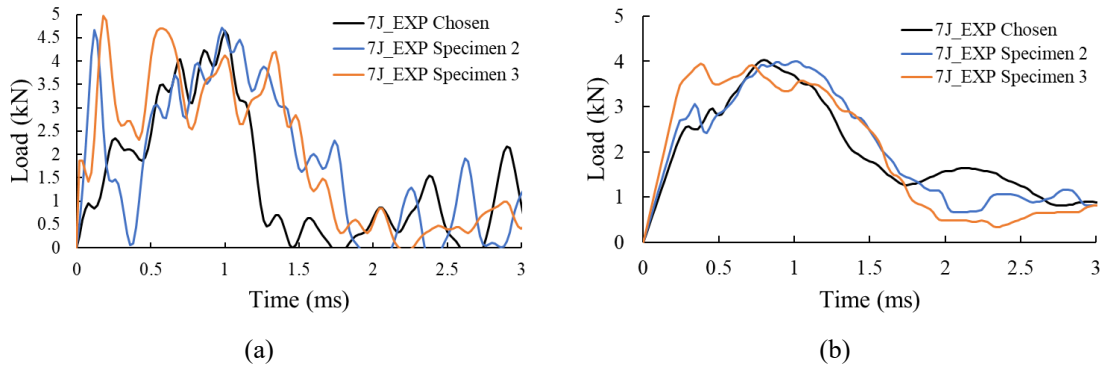
Figure 5-4. Experimental load-shortening curves for the baseline specimen under impact energy of 7 J: (a) actual signals and (b) root mean square of the signals.

Table 5-1. Summary of the FE approach, with corresponding LS-DYNA keywords

Constituent	Material model	Phenomenon	Modelling approach
Top and bottom skins	Piecewise linear plasticity *MAT_024	Junction pillars-fabric (SOLID)	Common nodes are shared
Top and bottom plies	Composite damage with Chang-Chang failure model *MAT_054	Junction core-fabric (SOLID)	Common nodes are shared
Pillars	Composite damage with Chang-Chang failure model *MAT_054	Bonding skin-plies (SOLID and TSHELL)	*AUTOMATIC_SURFACE_TO_SURFACE_TIEBREAK
Foam core	Elastic with erosion criterion *MAT_001 with *MAT_ADD_EROSION	Delamination (SOLID and TSHELL)	*AUTOMATIC_SURFACE_TO_SURFACE
		Damping	*DAMPING_FREQUENCY_RANGE_DEFORM

5.4. Numerical Simulations

The commercially available finite element software LS-DYNA was used for the simulations of the in-plane (axial) impact tests, which were conducted at different impact energies, using the three modelling schemes briefly described earlier. The intact specimens and those including an initial delamination were modelled. As stated earlier, the 3D-FML has three main components: (i) the magnesium skins, (ii) the fiberglass fabric and its pillars, and (iii) the foam core, each of which was represented in the models described in this paper (see the reduced input files provided in Appendix B). The models were run on a workstation equipped with two 2.26 GHz, 4-core/8 logical processors E5520 Intel Xeon processors. For consistency of comparing the computation CPU times, each computation was run independently on eight of the 16 available processors, with no other operations executed in parallel. The different material models (LS-DYNA R9.0, 2016b), elements formulations (LS-DYNA R9.0, 2016a), contact types (LS-DYNA R9.0, 2016a), and modelling approaches used in the analyses are reported in the following sections. For the sake of clarity, a summary of the modelling approaches is provided in Table 5-1. Note that a convergence analysis was performed for all the models discussed in this paper to establish an adequately fine mesh, so that the response of the system could be simulated with an acceptable accuracy, yet maintaining an optimal solution (CPU) time. The resulting mesh

for the model using solid elements is illustrated in Figure 5-5(a). As done in one of our previous studies (De Cicco & Taheri, 2017), the peak load was selected as the primary criterion for establishing the converted mesh, while the computation time was taken as the secondary criterion. Moreover, to prevent initiation of the undesirable hourglass mode, two layers of elements were used to model each skin thickness in the model constructed by the solid elements.

15 520 elements

Skins and core: 10x97 elements

6x97 elements

Specimen dimensions: 190 mm (L) x 20 mm (w) x 5.3 mm (t)
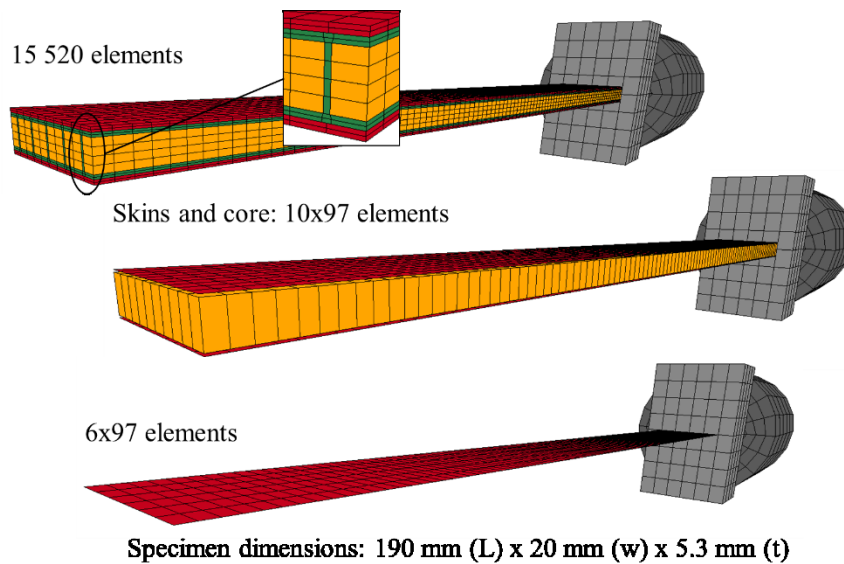
Figure 5-5. Finite element models. (a) SOLID, (b) TSHELL and (c) SHELL, with fixture (partially modelled) and impactor.

5.4.1. Models Using the 3D Isoparametric Element

As a start, a full 3D solid model was constructed, with the aim of obtaining the maximum accuracy of the results. This model would serve as a baseline to establish the degree of accuracy of the simpler modelling schemes, and the subsequent optimization work. Within this approach, every component of the 3D-FML (i.e. the magnesium skins, the 3D-FGF, and the foam), was modelled independently using 3D-solid elements. This model will be referred to as "SOLID", hereafter.

It should be noted that the pillars of the 3D-FGF were actually modelled in this approach. A more detailed comparison between the actual specimen and its FE model can

be seen in Figure 5-1. As visible from Figure 5-1(a), the actual glass fiber pillars are inclined with respect to the longitudinal direction. This inclination was accounted for by modifying the fiber-orientation of the material within the elements used to discretize the pillars. Since no separation between the fiberglass fabrics and pillars was observed during the experimental investigation, therefore, the elements representing the fabrics and pillars shared a common node in the model.

Two other variants of the SOLID model were also constructed. In one of the revised models, referred to as SOLID_NP, the pillars were not specifically modelled, but their contribution was accounted for in a smeared manner, by modifying the flexural stiffness of the bidirectional fiberglass fabrics, accordingly. This was done by increasing the longitudinal and transverse Young's modulus of the fiberglass plies slightly, in such a way so that the two fabrics would possess the same flexural stiffness as that of the actual 3D fabric, thus compensating for the stiffness that the pillars provide to the top and bottom bidirectional fabrics. In the second variant, referred to as SOLID_NF, the modelling of the boundary conditions was modified in order to study the effect of modelling of restraints on the global response of the specimens. As it will be shown, the conventional approach of restraining the translational and/or rotational degrees of freedom of the nodes located at the end boundaries of the model, as done in conventional FE simulations, would result is significant errors when simulating the impact response of axially loaded slender members. The rest of the model, for both variants, remained the same as that of the SOLID model. Full contact was assumed to hold among all the constituents.

As demonstrated in (De Cicco & Taheri, 2017), in order to obtain reliable results during the post-buckling phase of the response, the potential delamination occurring in the skin/FRP interface has to be accounted for. Therefore, the automatic surface-to-surface-tiebreak algorithm of the code was used to model the magnesium/FRP interface. This option allows for a potential delamination to initiate and propagate. It should be noted that the interface strength parameters used in the contact algorithms, as reported in Table 5-2, could be calibrated through numerical simulations only, because the interface strength was too low to be evaluated experimentally. Therefore, the case of impact at 7 J was selected as the reference for the calibration. Accordingly, the normal failure stress (NFLS) and

shearing failure stress (SFLS) were established by iterating the simulation parameters until reasonable agreements with the experimental findings were obtained in both qualitative sense (comparison with the recorded impact event) and quantitative sense (load- and axial-shortening-history data). In the models that included the initial delamination and for the portion of the interface corresponding to the location of delamination (which was on one side of the specimens), the tiebreak contact algorithm was replaced by the automatic surface-to-surface algorithm of the code to model the response of the delaminated portion of the specimen. This way, the separation of the skin from the FRP core could be accommodated, while their inter-penetration would be prevented.

Table 5-2. Material properties and tiebreak contact parameters used for the simulation.

Magnesium	E (GPa)	ν	ρ kg/m^3	σ_y (GPa)		
	36	0.35	1740	0.231		
FRP plies	E$_{11}$ (GPa)	E$_{22}$ (GPa)	ν_{21}	G$_{12}$ (GPa)	G$_{13}$ (GPa)	G$_{13}$ (GPa)
	9	9	0.05	1	1	1
	X$_C$ (GPa)	X$_T$ (GPa)	Y$_C$ (GPa)	Y$_T$ (GPa)	S$_C$ (GPa)	ρ kg/m^3
	0.173	0.173	0.173	0.173	0.03	1750
Pillars	E$_{11}$ (GPa)	E$_{22}$ (GPa)	ν_{21}	G$_{12}$ (GPa)	G$_{13}$ (GPa)	G$_{13}$ (GPa)
	3	1	0.05	1	1	1
	X$_C$ (GPa)	X$_T$ (GPa)	Y$_C$ (GPa)	Y$_T$ (GPa)	S$_C$ (GPa)	ρ kg/m^3
	0.08	0.08	0.08	0.08	0.03	1750
Foam	E (GPa)	ν	ρ kg/m^3	ε_{max}		
	0.05	0	128	0.15		
Tiebreak contact	NFLS (GPa)	SFLS (GPa)	OPTION			
	0.003	0.02	2			
Damping	CDAMP	FLOW (Hz)	FHIGH (Hz)			
	0.07	9000	11000			

5.4.2. Thick Shell Model

A second modelling approach with reduced complexity and computationally less expensive was also developed. This model consisted in modelling the 3D-FML with only two distinct components: the magnesium skins and FRP core, the latter including both the

3D-FGF and the foam. In this approach, the skins were modelled using thin shell elements, while solid-like thick shell elements were used for modelling the FRP core. Therefore, this model will be referred to as "TSHELL" hereafter. For the definition of the core materials, the *PART_COMPOSITE_TSHELL option allowed for the definition of material properties of the two fiberglass plies and the foam as distinct constituents. Indeed, as mentioned in (De Cicco & Taheri, 2017), the option allows the definition of each material's properties and its thickness at each integration point within the shell thickness. Similar to the approach used in preparing the SOLID_NP model, the properties of the fiberglass plies were also modified in this model to account for the pillars in an implicit manner. Finally, as done in the SOLID model, the interface between the magnesium and the core was modelled using the previously mentioned contact algorithm. The mesh of this model is illustrated in Figure 5-5(b).

5.4.3. Shell Model

Last, the accuracy and limitations of a relatively simple model (see Figure 5-5(c)), used by the authors in their previous work (De Cicco & Taheri, 2017), consisting of a single layer of shell elements to account for all three constituents of the 3D-FML, is investigated. Similar to the TSHELL model, the distinction between the different components was implemented using the keyword *PART_COMPOSITE, which mimics the same behaviour as the *PART_COMPOSITE_TSELL option presented previously, but it is applicable to shell elements, resulting in the implementation of five distinct material layers. These layers accounted for the two skins, the two bidirectional fabrics and the pillars/foam core section. Note that the pre-existing delamination and the potential ones that could emanate during a loading event cannot be simulated with this modelling approach, since all the constituents are contained within a single layer of element. As done for the other two cases, the properties of the bidirectional fiberglass plies were modified in order for the 3D-FGF to have the same overall bending stiffness as the actual 3D-FGF-epoxy composite. For the sake of clarity, this model will be referred to as "SHELL".

5.4.4. Modelling of Fixtures and Boundary Conditions

A component's buckling and, especially, impact-buckling responses are strongly affected by the way it is restrained, and also its initial geometric imperfection. When simulating the responses numerically, special attention should be given to the modelling of the restraints. In other words, the restraints (in our case, imposed by the fixtures) would have to be explicitly modelled as close as possible to the actual restraining mechanism. This would mean that the conventional method of applying restraints to FE models (i.e., in the case of our specimens, merely restraining the degrees of freedom of the nodes falling at the ends of the FE mesh) would not be sufficient for producing accurate results. To circumvent the issue; therefore, the clamping restraints produced by the fixtures to the end portions of the specimen were modelled in a way to generate restraints as close as possible to the actual fixtures, yet maintain the modelling efficiency. That is, the clamping portion at the non-impacted end was simulated by restraining the appropriate degrees of freedom of the nodes falling within the 20 mm clamped portions of the specimen. Moreover, the end nodes were restrained from moving in the longitudinal direction. On the impacted end of the specimen, in all three modelling approaches, the steel impactor and aluminum fixture were actually modelled with solid elements, with the appropriate elastic and geometric properties (see Figure 5-5). Note that the fixture and impactor were not in contact with the specimen in the beginning of the loading event. Moreover, the nodes falling on the surfaces within the 20-mm clamped portion were restrained from moving in the lateral directions.

The loading was simulated by applying initial velocities to the impactor, resulting in impact energies equivalent to 1.5 J, 3 J, 4.5 J and 7 J. The automatic surface-to-surface contact algorithm was used for simulating the interaction between the two parts, allowing the impactor to bounce back from the fixture if necessary. In the SHELL and TSHELL models, the link between the specimen and fixture was modelled using the tied-nodes-to-surface contact algorithm of the code (i.e., the nodes were on the specimen side, and the surface was of the fixture side). However, in the SOLID model, the tied-surface-to-surface contact algorithm was used. For the non-impacted side, the axial displacement in the longitudinal direction was simply inhibited.

5.4.5. Material Models and Element Formulations

To ensure consistent comparison of the computation CPU time and results, the same material model was used in all modelling approaches. Note that further reduction in computation times could have been achieved by establishing the most efficient constitutive model (especially for the case where thick shell elements are used); however, this was not a focus of the present study. The material properties used in the simulations are reported in Table 5-2, where E refers to the Young's modulus, ν is the Poisson's ratio, and G is the shear modulus. Moreover, X, Y, S are the longitudinal, transverse and shear strengths under compression (subscript C) and tension (subscript T), σ_y is the yield stress and ε_{max} is the maximum strain; lastly, ρ is the density of the material.

The piecewise linear plasticity material model was used for modelling the magnesium skins. The strain-rate effect is accounted for in this model, but it does not account for thermal effects or cracking. More sophisticated models, such as the Johnson-Cook model, which are available in LS-DYNA, could not be considered as a reasonable choice, because they are computationally expensive, and neither the thermal effects nor cracking was involved in the materials forming the specimens. It should, however, be noted that the interface cracking is accounted for by the appropriate contact algorithm used in our modelling approaches. Also, since no cyclic loading was involved in the experiments, the default isotropic hardening was used in the model. Moreover, in addition to the material properties reported in Table 5-2, the strain-rate effect was taken into account by providing data describing the effective stress versus plastic strain curves of the material evaluated experimentally at different strain rates by (Asaee & Taheri, 2017). LS-DYNA uses linear interpolation to extract the necessary data from the given curves during each simulation.

The bidirectional FRP and the pillars were modelled using one of the widely used composite damage models of LS-DYNA, that is: *MAT_ENHANCED_COMPOSITE_ DAMAGE. The damage mechanism in this material model is based on the Chang-Chang failure criterion, accounting for both compressive and tensile failure of the bi-directional plies and pillars, as well as inter-ply delamination. Different values were used to define and distinguish the FRP and pillars' materials.

86

From experimental observations, it was concluded that the foam behaviour could simply be modelled as a linear elastic material. The *MAT_ADD_EROSION option of the code was used in models using the solid elements to account for the failure of the foam when subjected to excessive strains. Once an element experiences strain with a value higher than the prescribed threshold strain, ε_{max}, it would be deleted. Note that this option does not work in conjunction with the *PART_COMPOSITE option used in the SHELL and TSHELL models. It should also be noted that due to the localized nature of the failure, the use of more complex and computationally demanding models, such as the crushable foam model, would not be necessary, since such models would not improve the prediction of the local failure of foam observed during the experiments with an appreciable accuracy. Finally, the materials representing the fixture and impactor were simply modelled as an elastic material, using the elastic properties of the aluminum and steel, respectively.

Concerning the elements' formulations, the thin shell element formulation used for all the modelling approaches was the Belytschko-Tsay formulation. This shell formulation is very efficient computationally, and provides results with adequate accuracy for the case being investigated. In fact, the limitations of this formulation arise in case when warping and large shear deformation mechanisms are involved, neither of which are significant in our simulation. The solid element was the conventional 8-node hexahedron formulation, with reduced integration. The hourglass option was used to overcome potential hourglass mode issues that could result by the reduced integration scheme. This formulation was also chosen for its computational efficiency.

As for the thick shell formulation, out of the four available formulations in LS-DYNA, only two are compatible with the composite material model used in this study; they are the thick shell element types 3 and 5. Both element types are layered 8-node shell/solid elements with 3D stress state and three degrees of freedom per node. The only difference is that type 5 has an enhanced strain formulation, which is an extremely efficient formulation, in part, due to the reduced integration scheme used in the formulation. As a result, the use of type 5 is recommended over type 3 shell element in problems involving bending. In our study, since bending would occur as a consequence of buckling, and establishment of a computationally efficient model is of interest, the type 5 element was

originally selected as the natural choice for the simulation. However, when the results obtained with this formulation were compared to the experimental data, large discrepancies were observed; as a result, type 3 formulation was used instead. It should be noted that comparatively, this formulation consumes 6.5-time more CPU time for our impact simulation; nevertheless, its use was deemed necessary for reaching an acceptable accuracy.

Finally, the effect of material damping on the response of the specimens subjected to axial impact has been taken into account by applying a quasi-frequency-independent damping coefficient to element deformation, in a certain range of frequencies. In this case the damping and frequency range parameter reported in Table 5-2 were calibrated by comparing the results of the numerical model SOLID and the experimental data (based on the 7 J case), which happened to be the most critical case in terms of vibration response.

5.5. Results and Discussion

5.5.1. Effect of Boundary Restraint Modelling Strategy

The effect of partially modelling the aluminum fixture restraining the specimens on the impacted side is investigated here with the SOLID model. As noted earlier, the case in which the restraint posed by the fixture was modelled with the conventional method of fixing the degrees of freedom of the end nodes instead of modelling the actual fixture is referred to as SOLID_NF (acronym for no-fixture). As can be seen from the results illustrated in Figure 5-6, both models with and without full-fixture modelling gave similar results for both the load and axial-shortening curves. The predicted buckling load, average exhibited stiffness, and decrease in load-bearing capacity after the onset of buckling are all consistent with the experimental results. However, the oscillations observed in the actual load-time curves are more accurately simulated by the model in which the fixture is modelled explicitly. In fact, it can be seen that the number of oscillations in the experimental data measured before the onset of the buckling matches that simulated by the SOLID model. Contrary to the load-time curve, the axial-shortening-time response is more accurately represented by the SOLID_NF model. However, because of the targeted

application of the 3D-FML (i.e., auto body applications), the load-history curve is deemed to be a more critical design constraint. This is because the load level is the criterion that is more commonly used for assessing both the integrity of such structural components and the effect it would have on vehicles' occupants. In addition, the buckling phenomenon can be better detected on the load history curve, as opposed using the axial-shortening history curve. Consequently, modelling of the fixture is considered essential in this case, thus the modelling scheme has been included in all the models considered in this study.
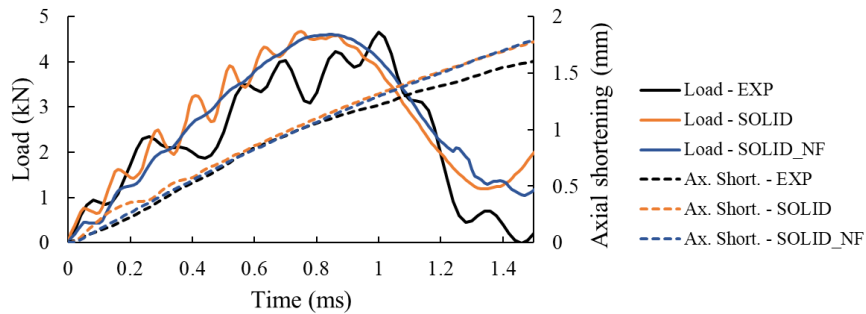
Figure 5-6. Comparison of the load and axial-shortening curves obtained through SOLID and SOLID_NF models with experimental data.

5.5.2. Effect of the Scheme Used in Modelling of 3D-FGF Pillars

Similar to the study described in the previous section, the effect of the modelling approach used to represent the response of 3D-FGF's pillars was also carried out with the SOLID model (i.e., with fixture included). As can be seen from the results shown in Figure 5-7, both the load-time and the axial-shortening-time curves produced by the full SOLID model are more consistent with the experimental results than those obtained from the model in which the effect of pillars was accounted in a smeared fashion (i.e., SOLID_NP model). Both models exhibit essentially very similar response through the first portion of the curves, up to the onset of buckling. However, SOLID_NP model predicts a lower buckling capacity, thus underestimating the specimen's capacity. On the contrary, the SOLID model's results match very closely to the experimental ones. In addition, the visual comparison of the deformation during impact between the numerical simulations and the high-speed camera's recording (not reported here) showed that a more realistic behaviour could be obtained when the pillars were explicitly modelled. Therefore, for the remainder

89

of our investigation, only the model which includes the pillars explicitly (i.e., SOLID model), will be considered.
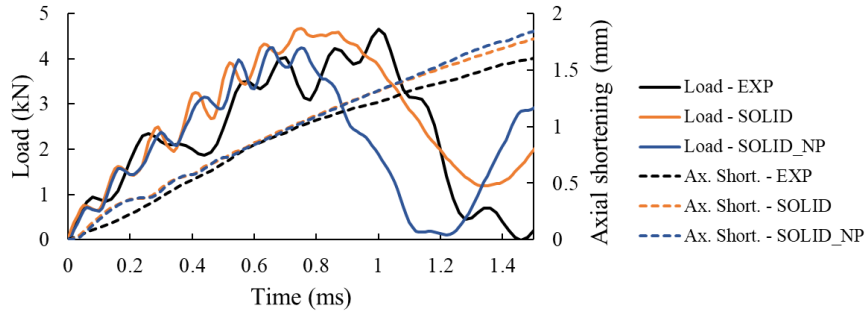
Figure 5-7. Comparison of the load and axial-shortening curves obtained through SOLID and SOLID_NP models with experimental data.

5.5.3. Impact Response Simulation – Baseline Specimens

The simulation results for all impact energy levels considered for the baseline specimens (i.e., the intact specimens with no initial delamination) are reported in Figure 5-8 (load-time curves), Figure 5-9 (axial-shortening vs. time curves), and Figure 5-10 (axial load vs. axial-shortening curves), and compared to the average values of the experimental results. Note that while an impact event of 6 ms duration was simulated, only the portions that include the onset of actual buckling is presented in the figures (in other words, the subsequent vibration response is not included). As a result, a longer portion of the load-time curve is observed in the specimens that underwent low impact energies.

Furthermore, an energy analysis was carried out to provide a better insight into the performance of the different models. The results of this analysis are reported in Figure 5-11. The reported energy corresponds to the energy absorbed by the specimen, E_{abs}. For the baseline specimens, the values are calculated by considering the area under the load-displacement curve, up to the onset of buckling. For the specimens hosting an initial delamination, the energy was calculated based on the data associated to the first 1.5 ms of the event, since no clear buckling initiation point could be discerned from the experimental curves. The following equations were used for calculating the energy values (Abrate, 2011):

90

$$E_{abs} = E_\tau \left[1 - \frac{E_\tau}{4E_0} \right] \qquad \text{with} \qquad E_\tau = \int_0^\tau p\,\mathrm{d}t \qquad (5\text{-}1)$$

where E_0 is the initial impact energy, P is the load and τ is the time period of interest for the energy estimation.
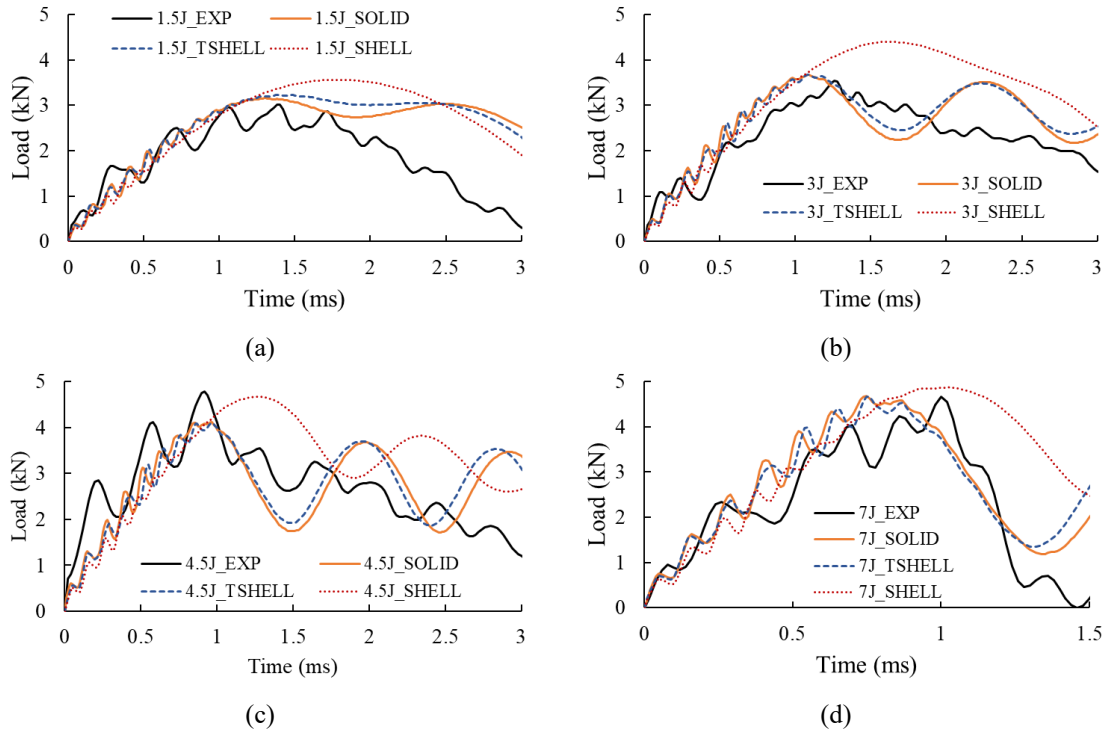
Figure 5-8. Load history graphs of the baseline specimens, produced by the models, under impact energies of: (a) 1.5 J, (b) 3 J, (c) 4.5 J and (d) 7 J.

As can be seen from Figure 5-8, for all cases, there is a good agreement between the experimental data and the numerical results up to the onset of buckling (please also note the change in the range of the abscissa of this figure). Moreover, the elastic stiffness response of each specimen is also accurately predicted. The accuracy of predicted results is improved in specimens undergoing the higher impact energy values. This is postulated to have been caused by voids and micro-damage that could have been potentially present in the specimens, which could not be accounted for by the developed FE models. The effect of such factors, however, is reduced at higher energies, primarily because other more energy-consuming damage mechanisms (e.g., skin/FRP interface delamination) are involved. Visible also from all graphs shown in Figure 5-8 is that, as anticipated, the

SHELL model produced the greatest discrepancies. For the two lower impact energy cases, the buckling capacity is, however, over-estimated. Nevertheless, this model is capable of reproducing the pre-buckling behaviour with an accuracy close to that produced by the other two more complex modelling schemes (i.e., the TSHELL and SOLID models). From the observation, one may conclude that the most efficient model (i.e., the SHELL) could be deemed as appropriate for modelling events that involve low impact energies, so long as the user is confident that no major damage or buckling would occur. This relatively very simple modelling approach would be a very efficient approach for use in linear or nonlinear static response analyses, as demonstrated in (De Cicco & Taheri, 2017).
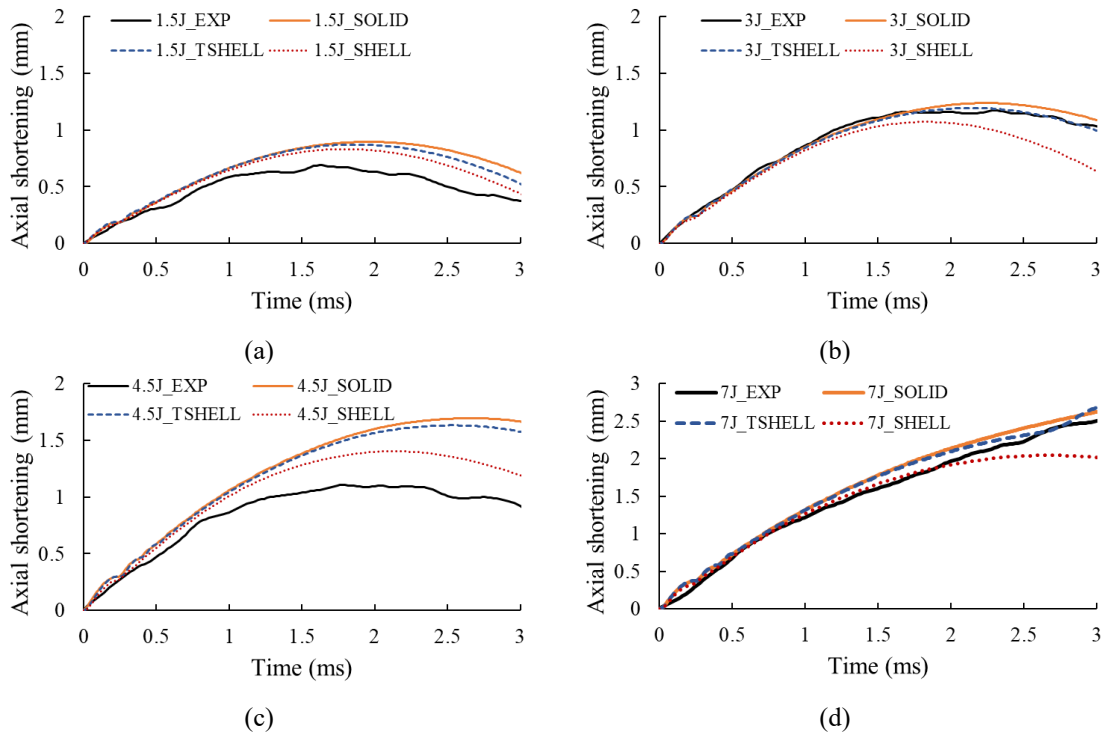
(a)   (b)

(c)   (d)

Figure 5-9. Axial-shortening history graphs of the baseline specimens, produced by the models, under impact energies of: (a) 1.5 J, (b) 3 J, (c) 4.5 J and (d) 7 J.
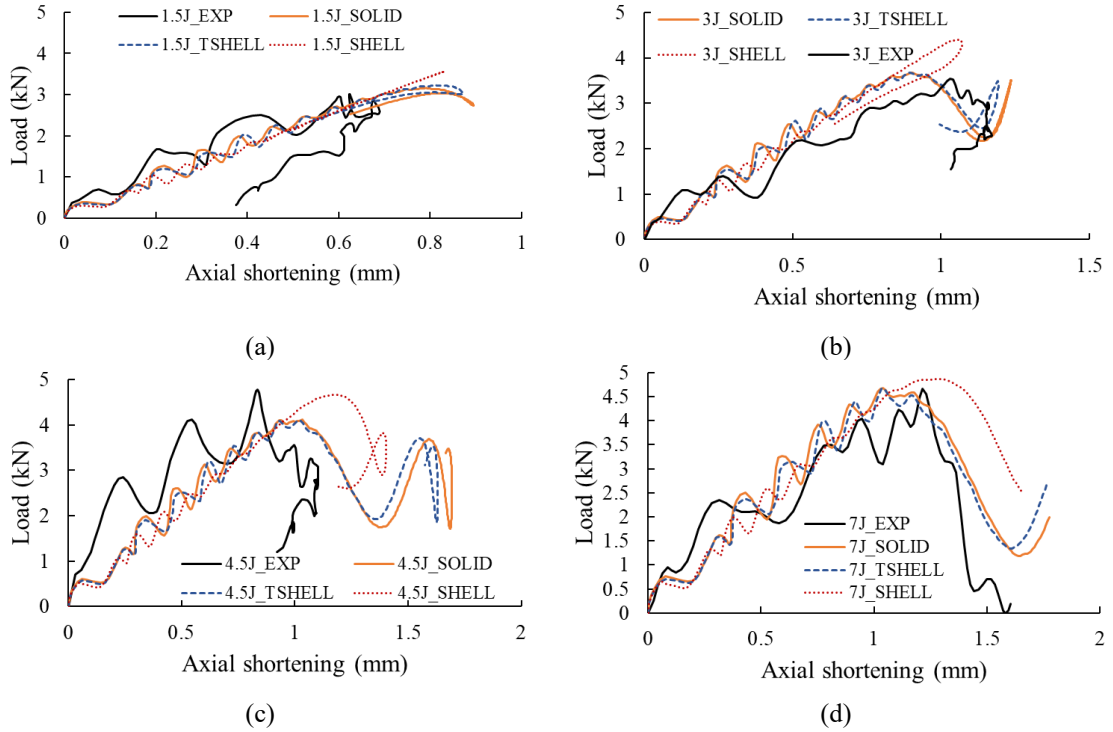
Figure 5-10. Comparison of experimental and numerical load-shortening curves of the baseline specimens under impact energies of: (a) 1.5 J, (b) 3 J, (c) 4.5 J and (d) 7 J.
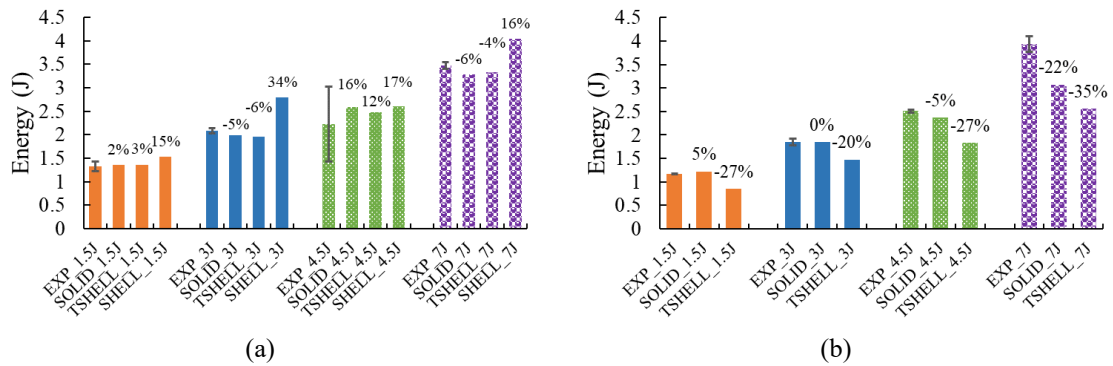
Figure 5-11. Comparison of the energy absorption capacity values predicted by the FE models and experimental results: (a) baseline specimens, (b) specimens with 50% initial delamination.

The other two models (i.e., TSHELL and SOLID) behaved very similarly in all the studied cases; they could predict the pre-buckling behaviour reliably and could estimate the buckling load corresponding to all impact energies with good accuracy. The post buckling response predicted by these models, however, could be deemed reliable only for

the highest impact energy case. As for the SHELL model, the best match with the experimental results could be obtained for only the highest impact energy.

Concerning the results depicting the axial-shortening behaviour, as illustrated in Figure 5-9, all models could produce results with good accuracy, except for the results obtained at 4.5 J impact case. The inconsistency observed in this latter case is attributed to the fact that the onset of delamination of one of the magnesium skins was experimentally observed to occur under this level of impact. Moreover, it can be noted that the numerical results are somewhat less stiff than the actual experimental results (i.e., the computed axial-shortening values are greater than those measured experimentally). Interestingly, in terms of axial-shortening history response, as illustrated in Figure 5-9, it is evident that the SHELL model could produce results with better accuracy in comparison to those produced by TSHELL and SOLID models. Another interesting observation discerned from the axial-shortening-time graphs is the appearance of a threshold in the results corresponding to the specimens undergoing 4.5 J and 7 J impact energies. In the latter case, the impactor did not bounce back during the experiment; this phenomenon can also be observed from the result depicted in Figure 5-9(c). As seen, the slope of the curves increases initially, but then the slope either flattens or decreases. In contrast, results shown in Figure 5-9(d) reveal that the slope increases monotonically, except in the case of the results produced by the SHELL model, where a decrease in slope is visible (please also note the change in the load-range in (d)). This is due to the fact that the delamination of the magnesium skins cannot be captured by a simple shell-type model, thus leading to an overestimation of the stiffness of the specimen. Such a threshold-included response was also observed in the experimental data.

The appearance of this threshold is also visible in the load-axial-shortening curves reported in Figure 5-10. The curves shown in the figure indicate that (neglecting the fluctuations) in all cases, but the 7 J case, the axial shortening increases gradually, and then decreases at a certain load value. In contrast, in the 7 J case, an increase in the load is accompanied by an increase in the axial-shortening value. From these graphs, one can also notice the accuracy of the numerical predictions for the 3 J and 7 J impact cases, while

more discrepancies are visible for the 1.5 J and 4.5 J cases. All in all, the most accurate prediction is obtained for the 7 J case, which is the most critical in real-life design cases.

In addition, the energy absorption capacity of the specimens is shown Figure 5-11. The inevitable fluctuations in the load-history curves make it difficult to quantitatively compare the results produced by the different modelling approaches. Therefore, the energy absorption capacity, a global quantity that can be obtained for all test cases, is used for comparing the results. Indeed, this is the quantity that would be most representative of the performances of a system subjected to impact. It can be seen that the values obtained from the SOLID and TSHELL numerical experiments are very close to the experimental values, in all cases but the 4.5 J one (see the reported percent-deviations illustrated in Figure 5-11(a)). The SHELL model clearly over-estimates the energy capacity of the 3D-FMLs. However, the SOLID and TSHELL models' predictions produced maximum discrepancies of only 6% compared to the experimental results, when results corresponding to the 4.5 J case are excluded.

Finally, a qualitative comparison of the experimental and numerical deformed shapes was also performed. The results for the 4.5 J case are reported in Figure 5-12. The images are taken at 1 ms, 1.5 ms and 2 ms during the events (i.e., right after the onset of buckling and afterward during the remaining portion of the events). It is clearly visible that there is a good agreement between the FE simulated and actual experimental deformed shapes; in fact, the superimposed deformed shapes predicted by the SOLID and TSHELL models match precisely at 1 ms and 1.5 ms, while that predicted by the SHELL model appears to match at 1 ms and be slightly stiffer at 1.5 ms. Conversely, at 2 ms into the impact event, the SHELL model provides a more accurate prediction of the deformed shape compared to the experimental one, while SOLID and TSHELL models' predictions exhibit more deformations than that observed experimentally. It should be noted that the reason for selecting the results related to specimens tested at 4.5 J is that the incorporated high-speed camera could only capture one image every 0.5 ms. This speed was not adequate to capture the fracture failure of the specimens tested at the higher energy.
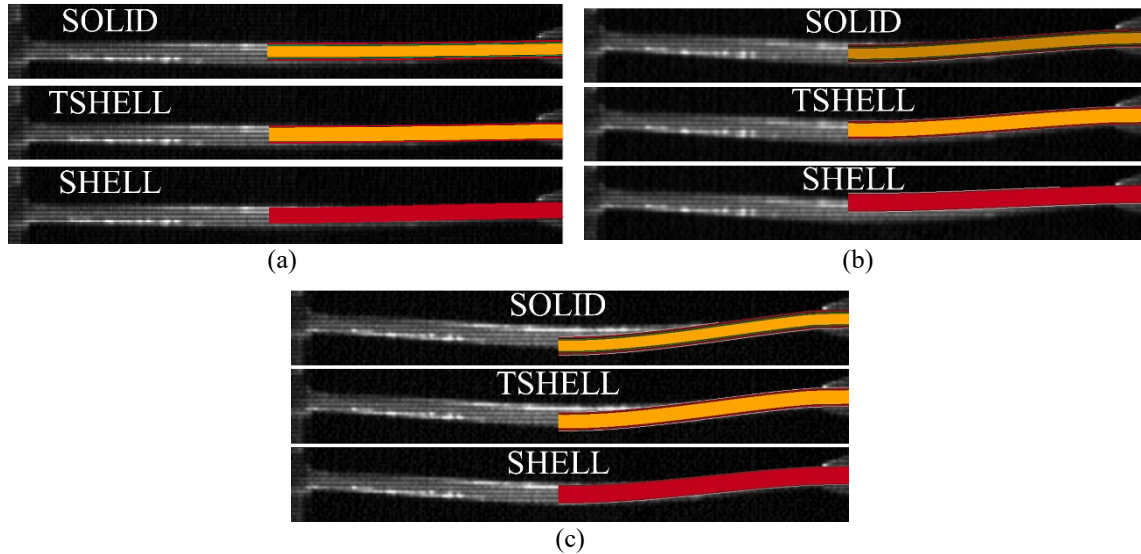
Figure 5-12. Qualitative comparison of the deformations of the baseline specimens predicted by the FE models and experiments (a) at 1 ms, (b) at 1.5 ms, and (c) at 2 ms instances during the events.

5.5.4. Impact Response of Delaminated Specimens

Impact tests were carried out on specimens hosting a delamination with its length equal to 50% of the gage length. The response of these specimens was also numerically simulated. The predicted load vs. time response, as well as axial load vs. axial-shortening results are reported in Figure 5-13-15, respectively. Obviously, the SHELL model was not considered in this part of the study, since it cannot accommodate modelling of delaminations. Contrary to what was observed when examining the baseline specimens, the predictive capabilities of the TSHELL and SOLID models became reversed in the case of delaminated specimens. In this case, the SOLID model predicted higher load values than the TSHELL model. When comparing the results of the two models with the experimental data, it is not clear which of the two models performs better in terms of load prediction due to a large discrepancy of the results. Overall, the SOLID model's predictions are on the non-conservative side. In fact, apart from the case of 1.5 J impact, where the SOLID model seems to perform better than the TSHELL model, none of the models could produce results with acceptable agreement to the experimental results. However, there is a good agreement between the experimental and numerical results when considering the axial-shortening-time curves, shown in Figure 5-14. As can be seen, apart from the results associated to the 3 J case, the experimental and numerical curves agree very closely. These observations are

96

confirmed by the load vs. axial-shortening curves reported in Figure 5-15. It is evident that at higher energies, the discrepancies are such that no objective conclusion could be made on the accuracy of the modelling approach. It is postulated that some damage (most probably at the micro-scale level), which would be difficult to account for in the numerical models, is responsible for the lager discrepancies observed between the numerical and experimental results for the 3 J case. In addition, the graphs highlight the fact that the presence of initial delamination greatly affects the overall response of the 3D hybrid composite when impacted axially; even at the lowest applied energy, the extent of damage is considerably significant.
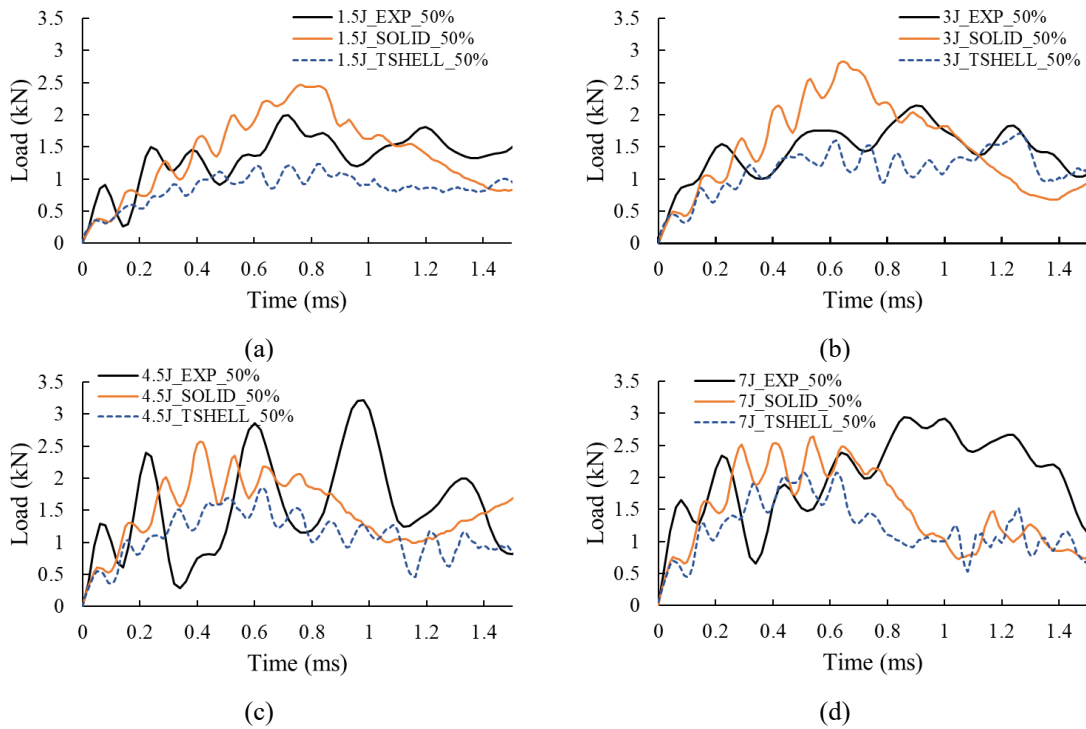
Figure 5-13. Load-history graphs of the specimens with 50% initial delamination, produced by the models, under impact energies of: (a) 1.5 J, (b) 3 J, (c) 4.5 J and (d) 7 J.
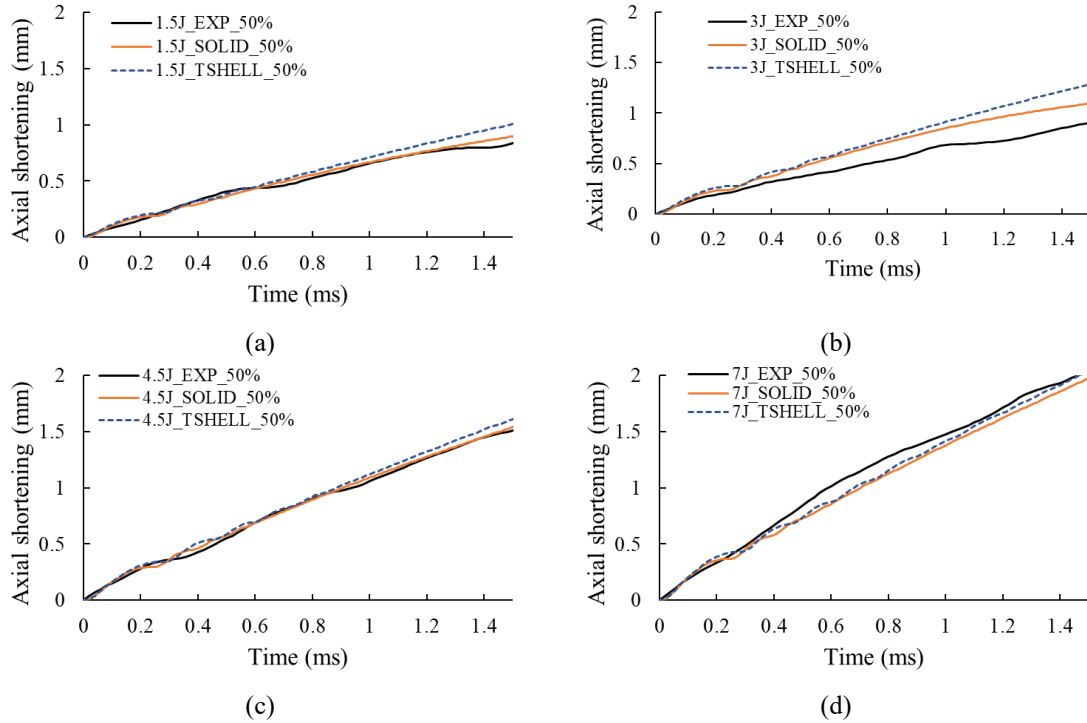
Figure 5-14. Axial-shortening-history graphs of the specimens with 50% initial delamination, produced by the models, under impact energies of: (a) 1.5 J, (b) 3 J, (c) 4.5 J and (d) 7 J.

An experimental study conducted earlier (De Cicco & Taheri, 2016) revealed the weakest link of the system to be the metallic/FRP interface bond. The brittle nature of the epoxy used in forming the interface causes a delamination to propagate under very low stresses. Therefore, cohesive material properties for use in the tiebreak contact algorithm, could not be estimated with good accuracy using the available testing equipment. It is believed that a more precise calibration of the parameters would probably lead to more consistent results. An alternative for improving the calibration of the parameters would be to use a camera with greater recording speed than that available to us to record the event, so that the onset of delamination and its subsequent propagation could be traced more accurately.

It should be noted that while conducting the energy analysis (see the results in Figure 5-11(b)), it was observed that the SOLID model could accurately predict the energy absorption capacity of the 3D-FMLs that were impacted at lower energies. For the 7 J case, the specimens were observed to have undergone extensive damage at an early stage during the event. Therefore, one would need to apply particular attention to the models in cases

when the FML is presumed to be undergoing extensive damage. Also, it can be seen that the TSHELL model underestimates the energy absorption capacity by at least 20% in all impact cases considered here.
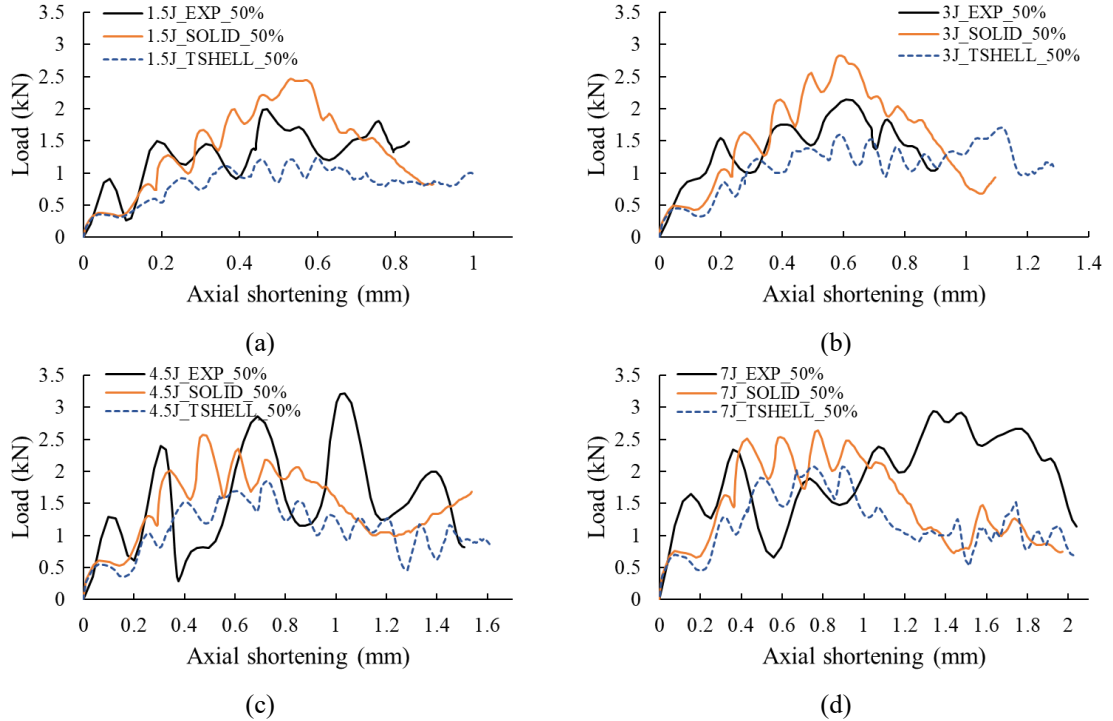
Figure 5-15. Comparison of experimental and numerical load-shortening curves of the of the specimens with 50% initial delamination under impact energies of: (a) 1.5 J, (b) 3 J, (c) 4.5 J and (d) 7 J.

As done for the baseline cases, a qualitative comparison of the overall deformation behaviour was also carried out for the specimens hosting a delamination, with the results presented in Figure 5-16. As can be seen, the SOLID model generated fairly accurate results at all recorded time instances; however, the local delaminated buckling of the magnesium skin observed at the 0.5 ms instance, could not be captured by the model. However, the observed phenomenon (i.e., the same microbunching mode) was indeed captured by the numerical model at a slightly later time instance (i.e., at 0.75 ms, not reported in the paper). At time 1 ms and later, the propagated length of delamination, the deformation shapes of the skin at delaminated region and other regions, and all other segments of the specimens, all agree with the deformation of the actual test specimens. In contrast, as visible in Figure 5-16(a), the TSHELL model could precisely capture the instance of onset of the local buckling delamination of the skin, but its location did not

correspond to the one observed experimentally. For later times, the TSHELL model also exhibits more discrepancies. Comparatively, the delaminated skin does not show the expected smooth shape, and partial delamination of the upper skin is also visible from the results captured at 1.5 ms. At 2 ms, modelling strategy of the boundary conditions seems to greatly affect the behaviour of the upper skin, while such phenomenon was not observed experimentally.
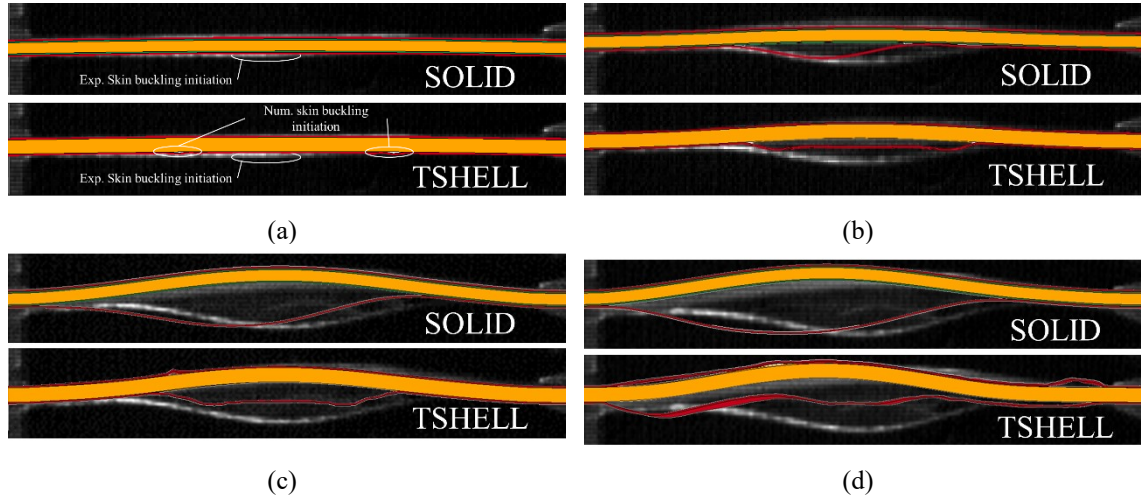
Figure 5-16. Qualitative comparison between the experimental and numerical deformed shapes at (a) 0.5 ms, (b) 1 ms, (c) 1.5 ms, and (d) 2 ms time instances during the event, for the specimens hosting 50% initial delamination.

5.5.5. Performance Comparison

The final point of interest in this study consists in the comparison of the computation CPU times for the developed models. Since the CPU times do not vary significantly when the analyses were conducted to examine the response under the impact energies considered here, only the results for the 7 J impact simulations are reported (see Figure 5-17). As expected, simulation with the SOLID model consumes the maximum time, consuming almost 600 s of CPU time. In comparison, the TSHELL model consumed only 50% of the CPU time, while when the SHELL model was used, the results could be obtained in just 14 seconds. The significant difference in the solution time obtained for the latter case can be attributed to two key points: (i) no contact stresses had to be calculated, which would have required the use of a numerical procedure that consumes a significant amount of CPU time, and (ii) efficient element formulations. The Belytschko-Tsay shell formulation is

computationally more efficient than the ones used to formulate the elements used to construct the TSHELL and SOLID models.

The solutions of the initially delaminated cases consumed similar CPU times; however, the TSHELL model appeared to produce results faster than in the case of intact specimens. Furthermore, as mentioned in a previous section, the computation time consumed by this model could be reduced by approximately 6 times with the use of the more effective element formulations and material models.

When considering the predictions of the buckling load, energy absorption, and axial-shortening history, the most accurate results for both the baseline and the initially delaminated cases were obtained with the SOLID model. However, for the non-delaminated case, the TSHELL model provided similar results, but required half the computation time. Finally, the SHELL model would be the model of choice in cases where the impact energy is relatively low, due to its extremely low run-time requirement, provided that only an estimation of the buckling load is desired. It also has the advantage of being easily implementable in available FE models that have been constructed using shell elements, without any requirement for mesh reconstruction. For example, an existing auto-body FE model, which is commonly constructed with shell elements, can be easily manipulated to accommodate the analysis of 3D-FMLs, virtually in matter of minutes.
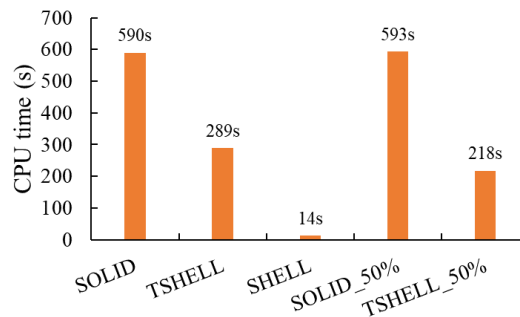
Figure 5-17. Consumed computation times for predicting the buckling load for different models (case of 3D-FML impacted by 7 J).

5.6. Conclusion

In this paper, the performance and reliability of different numerical modelling approaches for simulating the impact buckling response of 3D-FML were investigated using three modelling approaches. The following findings were realized through the study:

- Explicit modelling of the restraining fixture on the impacted side of the specimens led to slightly more accurate prediction of the deformed shape, when compared to the experimental results; however, its effect on the predicted buckling capacity and the post buckling behaviour was negligible.
- More accurate results could be obtained by modelling the pillars of the 3D fabric explicitly.
- The SOLID and TSHELL models produced very similar results for the pre- and immediate post-buckling behaviours. However, the computation time required by the TSHELL model was 50% lower than that consumed by the SOLID model.
- The simplest model (i.e., SHELL), ran 95% faster than the TSHELL model; however, its use is recommended for analysis of the cases in which the probability of damage developed during impact events is low, or when conducting static analysis.
- Large discrepancies in computed load-time curves were observed in modelling specimens that hosted an initial delamination, regardless of the element type. Notwithstanding, the SOLID model could predict the energy absorption capacity quite accurately.
- The SOLID model produced best predictions of the deformed shape and delamination growth.

In conclusion, both the SOLID and TSHELL models could be used to reliably predict the buckling capacity and energy absorption capacity of 3D fiber metal laminates. Choice of the specific modelling approach would depend upon the degree of accuracy and refinement of the solution that the user seeks. To further improve simulation of delamination response that could occur in such complexly configured hybrid composites,

special attention should be given to the formulation of the shell element that is used to simulate response of the thin metallic skins.

5.7. Acknowledgement

Chapter 6: Enhancement of Magnesium-Composite Bond-Interface by a Simple Combined Abrasion and Coating Method

Davide De Cicco and Farid Taheri

6.1. Abstract

Obtaining a strong bond when adhering magnesium alloys to other materials, especially to fiber-reinforced polymer composites, is challenging. Regardless of the strength of the adhesive used, it is the surface preparation that also significantly affects the overall bond strength and long-term performance of the mated surfaces. While optimal and established surface preparations are available for aluminum, steel alloys and polymer composites, the current method proposed for magnesium alloys is extremely onerous, time-consuming, and very expensive.

The aim of the research disclosed in this paper has been to develop a relatively simple, effective and economical procedure for enhancing the bond strength between magnesium alloy to fiber-reinforced polymer composites, which had been proven to be a challenging issue. The proposed method facilitates a superior interface-bond using a relatively low-cost epoxy resin. Enhanced Mode I fracture toughness and delamination resistance are obtained. Both static and impact tests are used to assess the effectiveness of the proposed procedure.

6.2. Introduction

[…]

Our experience with bonding magnesium alloys to FRP has shown that, even when the elaborate procedure outlined in (The Adhesives Design Toolkit, n.d.) was followed to bond a magnesium alloy to fiberglass-epoxy, a sufficient interface bond strength could not be

attained. Moreover, the cost and environmental impact of the chemicals used in the procedure (The Adhesives Design Toolkit, n.d.) also render the procedure as an undesirable one. Compounded to that, when one also considers the man-hour required for carrying out the procedure and the cost of the chemicals, the procedure becomes further unfeasible in most industrial settings.

The above-mentioned coating technique appears to be effective. However, the feasibility and practicality of the technique become questionable. This is due to the requirement that the treated (coated) surfaces must be immediately bonded, which puts constraints on the manufacturing process, thus impacting the overall cost of joining. In addition, while there exists a reasonable volume of research on the enhancement of bonding between FRP and steel or aluminum alloys, works that have investigated bonding of magnesium alloys to FRP are quite scarce. In fact, a vast majority of the available literature concerning magnesium alloys' coating is focused on applications in the medical field; more precisely, on the coating techniques for inhibiting corrosion of magnesium alloys and increasing their compatibility with living tissues (Cipriano et al., 2017; Gu et al., 2009; Radha & Sreekanth, 2017; Tang et al., 2013).

Therefore, an effort was expended to develop a simple and cost-effective abrasive-based technique, combined with a coating, that results in improved interfacial bonding strength of adhesively bonded joints mating magnesium-alloys and FRP. The advantage of the proposed technique is that, contrary to the mentioned coating procedures, it does not require the coating to be applied immediately before the actual bonding process. In other words, it can either be applied just before bonding the adherends, like the other mentioned effective technique, or be carried out well before the desired bonding and assembly stage. This attribute provides added manufacturing flexibility, which could decrease the overall cost associated with the bonding process in a mass-produced manufacturing setting. This aspect will be discussed further in the following sections.

Moreover, this study considered a total of four different bonding agents; two commercially available structural epoxies and two high-strength adhesives. The integrity of the bonded interfaces produced by the conventional and proposed procedures using the

different adhesives was examined by evaluating the fracture toughness of the adhesive, as well as examining the bond strength under static and impact loading conditions.

6.3. Materials and Procedures

6.3.1. Materials

The magnesium alloy used in this investigation was AZ31B-H24, obtained in the form of 0.5 mm thick sheets from MetalMart (Commerce, CA, USA). The unidirectional fiberglass fabric was obtained from Vectorply (Phenix City, AL, USA), and the 3D fiberglass fabric was acquired from China Beihai Fiberglass Co. Ltd. (Jiujiang City, Jiangxi, China). Also, the two-part, 8-lb high-density polyurethane foam was obtained from US Composites (West Palm Beach, FL, USA). As for the resins/adhesives, a hot-cured, two-part structural epoxy (Araldite LY1564 with hardener Aradur 2954) was purchased from Huntsman Co. (West Point, GA, USA), and the same company provided the adhesives Araldite 2011 (epoxy-based) and Araldite 2085 (methyl methacrylate-based). The room temperature-cured structural epoxy (i.e., 105 resin and 206 hardener) produced by West System (Bay City, MI, USA) was acquired locally. Finally, another methyl methacrylate adhesive, the Plexus MA300 was obtained from ITW Polymers Adhesives (Danvers, MA, USA). A summary of the used adhesive, as well as their acronyms, are provided in Table 6-1, and their mechanical properties are provided in Table 6-2.

6.3.2. Bonding Methods

The two surface preparation approaches used in this study are described in this section and schematized in Figure 6-1. The first one, simply referred to as "sandblasting" (SB) method, entailed wiping the magnesium bond surfaces with acetone to remove any oily residue, followed by sandblasting them with 20-30 grit coarse crushed-glass. After sandblasting, the surfaces were cleaned with a compressed air jet, wiped once again with acetone, and then let dry. Visual inspection was carried out after each treatment in order to ensure a consistent and uniform surface roughness. The aforementioned procedures

removed impurities from the surface and generated consistent irregularities that would enhance mechanical bonding to the adhesive.

Table 6-1. Summary of the resins and bonding techniques used in this study and their respective acronyms.

Company	Resin type	Cure Temperature	Resin designation	Surface preparation	Specimen designation
Huntsman	Epoxy - structural	Hot*	HCE	SB	SB-HCE
"	Epoxy – adhesive	Cold*	EA	SB	SB-EA
"	Methyl methacrylate - adhesive	Cold	MA	SB	SB-MA
West System	Epoxy - structural	Cold	CCE	SBC	SBC-CCE
Plexus	Methyl methacrylate – structural	Cold	PL	SB	-

SB: sandblasting.
SBC: sandblasting with resin coating.
MA: Methyl methacrylate adhesive.
PL: Plexus adhesive.
* "Cold" refers to room-cured adhesive/resin and "Hot" refers to hot-cured adhesive/resin.

Table 6-2. Material properties of the adhesives obtained through manufacturers' technical documents.

	HCE	CCE	EA	MA	QB	ME
Tensile strength (MPa)	75.2 – 80.0	50.3			30.06	27.6
Tensile elongation (%)	3.5 – 8.0	4.5				1
Tensile modulus (MPa)	2,800 – 3,300	3,171			2,268.45	
Lap-shear strength (MPa)		8.44*	14.7	17.7	10.02	

*Measured in-situ (Soltannia & Taheri, 2015b)
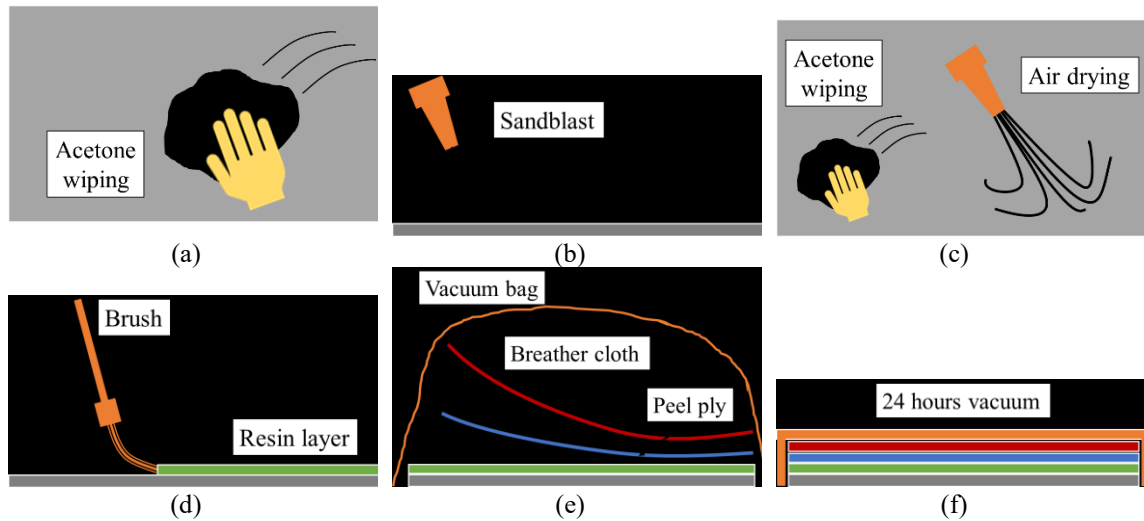
Figure 6-1. Steps of the surface preparation method. (a) to (c) SB, (a) to (f) SBC methods.

In the second method, referred to as "sandblasting with resin coating" (SBC) method, a thin layer of cold-cured West System structural epoxy was applied with a brush onto the surface of the magnesium plate following the aforementioned surface cleaning/roughening processes. Please note that the room temperature-cured (or cold-cured) resin is abbreviated as CCE, while the hot-cured epoxy is noted as HCE, hereafter. The applied resin was then covered with a layer of porous peel-ply and a layer of breather cloth, whose properties are reported in Table 6-3. The assembly was let cure under vacuum, at room temperature, for a minimum of 24 h. The combination of the bagging process and cloths ensures that a consistent amount of resin would cure on the bond surfaces and minimizes the existence of voids. Moreover, the peel ply leaves a rough finish resin imprint on the coated surface, which facilitates improved bonding.

Table 6-3. Properties of the peel ply and breather cloths used.

Peel ply		Breather cloth	
Thickness	0.004 in (0.1016 mm)	Thickness	3 mm (0.6 mm under vacuum)
Material	Nylon	Material	Polyester
Coating type	Silicone	Pressure use	< 40 psi (2.75 bar)
Max. temperature use	204°C	Max. temperature use	204°C

Note that, when using the SB procedure, the magnesium sheets had to be bonded to the substrate immediately after the surface preparation, so to prevent oxidation of the

108

surfaces, which would adversely affect the interfacial bond strength. However, using the proposed SBC procedure, one can either bond the magnesium right after the curing is completed, or storing the magnesium sheets for bonding at a later desired time, since the bond surfaces are protected by the applied layer of resin. This is an important and valuable attribute of the proposed technique from the manufacturing point of view, which will be discussed further in the following sections.

Finally, as mentioned previously, a chemical etching technique was also incorporated in this study, following the elaborate procedure described in (The Adhesives Design Toolkit, n.d.). However, the results obtained from testing the specimens produced by the etching method were found to be inconsistent, thus inconclusive; therefore, the results are not reported in this paper.

It is also worth noting that although it was mentioned that a total of four adhesives were considered in this study, we actually used a number of other adhesives as well. However, those adhesives produced insufficient bond strength. For instance, two paste-like epoxies (i.e., QuakeBond J201TC (QB) and MasterEmaco ADH 1420 (ME)), were used, whose results are not reported due to producing relatively very weak bond strength. In addition to the use of the mentioned peel ply material, a thin (paper-like) sheet of chopped-strand mat fiberglass (also called veiling cloth) and a thicker unidirectional fiberglass fabric were also considered as an interface ply adjacent to the adhesives; however, no discernible improvement in the interface strength was noted. Therefore, for the sake of brevity, the results associated to those tests are not reported in this paper. Table 6-1 reports the resins and bonding techniques used in this study and their respective acronyms used throughout this manuscript. It should be noted that our preliminary test results indicated that the performance of interface bonds produced by SBC-HCE was very similar to SBC-CCE; however, the hot-cured epoxy requires an extra curing process compared to the cold-cured epoxy, which reduces the feasibility of that combination at an industrial scale. Therefore, the results for that configuration are not reported in this paper.

At this juncture, it should be noted that, as noted in Table 6-1, the proposed surface preparation method was not used in conjunction with every adhesive listed in Table 6-1.

This is because, for instance, the material cost of PL adhesive is comparatively much greater than the other adhesives listed in the table. Therefore, even if the combination of the proposed method and that adhesive would render improved outcome, the utility of such expensive adhesives cannot be justified from the economic perspective in actual production settings when compared to the other adhesives considered here.

6.3.3. Mode I Fracture Specimen Preparation and Test Procedure

Mode I fracture test was performed in accordance with the procedure described in ASTM D5528-13 (ASTM Standard, 2014), with a modification applied to the configuration of the double-cantilever beam (DCB) specimen described in the Standard. The Standard stipulates the use of DCB specimens formed with unidirectional FRP adherends. However, in our case, since the objective was to assess the bond strength between a fiberglass-epoxy composite and a 0.5 mm thin sheet of magnesium alloy, the thin magnesium sheet could not be directly used as one of the adherends of the DCB, as the resulting bond strength would be significantly compromised due to the relatively very low bending stiffness of the thin sheet. Therefore, to maintain the admissibility of the spirit of the method presented in the standard, DCB specimens were fabricated from two custom-made adherends having different configurations but with the same flexural stiffness of 65 Pa m^3, as schematically shown in Figure 6-2(a). Accordingly, one of the adherends was a hybrid of magnesium and unidirectional fiberglass/epoxy with a stacking sequence of $Mg/(0)_6$, while the other consisted of nine unidirectional plies of fiberglass/epoxy with $(0/90/0/0/\overline{90})_s$ sequence.

The adherends forming the DCB specimens were cut to dimensions from larger plates using a water-cooled saw, equipped with a diamond-coated saw blade. First, the fiberglass plates were fabricated using unidirectional fiberglass fabric and HCE resin using the resin infusion technique. The plates were cured first at 60°C for two hours and subsequently at 120°C for eight hours. The magnesium sheet, treated using the SB procedure, was first bonded to the 6-ply FRP plates using a thin layer of PL adhesive and let cure for 24 h under vacuum. This hybrid plate was then bonded to the other FRP adherend plate using the adhesives and techniques reported in Table 6-1, thereby forming the aforementioned

DCB's configuration. The pre-crack region in DCB specimens was generated by inserting an appropriate size thin Teflon film between the interface of magnesium and FRP adherend plates. A uniform bond line thickness of 0.25 mm was obtained by placing a strip layer of copper shim-stock on the outer edges of the mating plates, and the bonded plates were let cure in between two clamped thick steel plates.

DCB specimens with dimensions of 150 mm x 25 mm were subsequently extracted out of the bonded plates using the water-cooled saw. Finally, the loading blocks were bonded to DCB specimens, and a thin layer of white paint was applied onto both outer lengthwise edges of the specimens as per the ASTM standard, to facilitate monitoring of crack propagation during the test.

The testing apparatus, presented in Figure 6-2(b), consisted of a servo-hydraulic Instron machine, equipped with a 5 kN load-cell and a jig specifically designed to apply a purely axial load to the blocks. Crack opening and load were obtained by the Instron instrumentation software, and the crack propagation length was obtained by recording specimen's deformation and crack propagation through a Canon Rebel T2i camera at a rate of 24 fps.

(a)   (b)
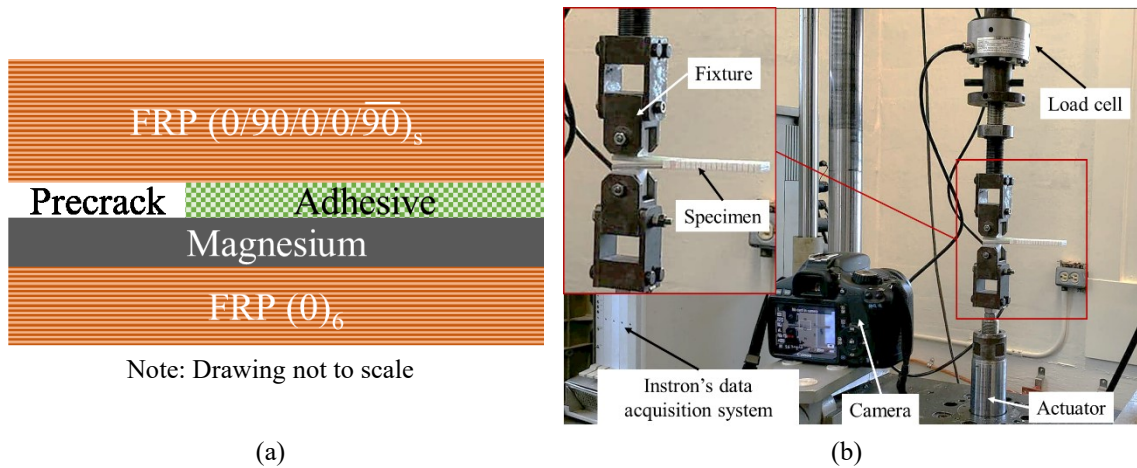
Figure 6-2. (a) DCB specimen's configuration and (b) testing apparatus.

6.3.4. Short-Column Compression Specimen Preparation and Testing Procedure

The short-column compression specimens were 90 mm x 20 mm 3D-FML beams, with a gage length of 50 mm, extracted from 100 mm x 100 mm plates. First, the core part of the composite was fabricated (here "core part" refers to the foam-filled 3D-fiberglass-fabric-epoxy constituents of the 3D-FML). HCE resin was applied to the 3D-FGF with a brush. Note that shortly after application of the resin, the nearly 2D-looking collapsed 3D fabric would start taking its 3D form. The resin coated fabric was then cured for two hours at 60°C and then for eight hours at 120°C. Once cured, polyurethane foam was aspired into the hollow core structure of the fabric using an in-house designed foam-aspiration jig and left to harden (cure) for at least 24 h. The magnesium skins, prepared using the methods SB and SBC, were then bonded to the cured core by the EA and CCE resins, respectively. In both cases, full vacuum was used to ensure consistent bonding between the metallic and FRP components. Specimens hosting an initial delamination corresponding to 50% of the gage length were also manufactured. For that purpose, a Teflon film was inserted between the magnesium skin and FRP core (on one of the interfaces) at the specimen's mid-span region, prior to bonding of the skins, as illustrated in Figure 6-3. Finally, after cutting the specimens to dimensions, the extremities were sanded to obtain smooth and flat surfaces. The baseline specimens (SB-HCE) data were retrieved from the authors' previous work (De Cicco & Taheri, 2016).
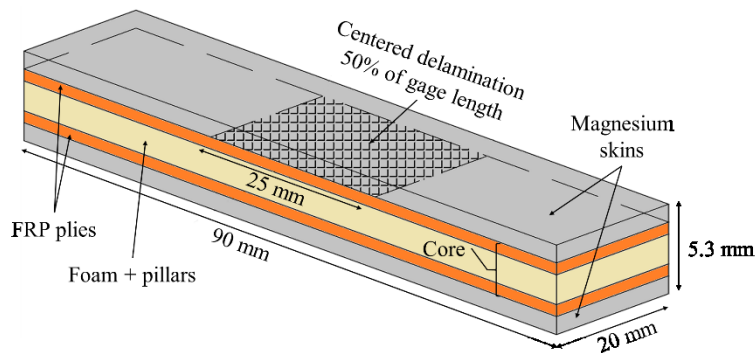
Figure 6-3. Schematic illustration of the 3D-FML specimen and overall dimensions. (Drawing not to scale).

The specimens were subjected to a concentric axial load, in the same manner as described in one of our previous studies (De Cicco & Taheri, 2016). The first 20 mm of each end of the specimen was clamped in a specially-designed fixture to prevent any potential rotation and translation of specimens' ends during the compressive loading. Aluminum tabs with a 45° round chamfer were used in order to reduce the stress concentration at the grip region, thereby preventing the potential of specimens failing prematurely at the grip region. An MTS universal testing machine equipped with a 250 kN load-cell was used to apply the compressive load at a quasi-static displacement-controlled rate of 0.5 mm/min. The load and displacement data was recorded by the MTS. A Dino-Lite digital microscope was used to record the compression event at a rate of one frame per second.

6.3.5. Out of Plane Impact Test Setup and Procedure

The 3D-FML specimens that were used in the out of plane impact (OPI) test had dimensions of 100 mm x 100 mm, fabricated using the same procedure as described in the previous section, using HCE and CCE resins as the bonding agents. A modified Charpy impact machine was used to apply the impact load to the specimens (please refer to reference (De Cicco & Taheri, 2018b) for more details). The specimens' edges were clamped by two 13 mm-thick steel plates, which had an 85 mm diameter opening. The steel impactor was hemispherical with a diameter of 16 mm. Specimens were subjected to an impact energy of 27 J, an energy level that would cause extensive delamination of the interface, but not perforating the specimens. Each specimen was impacted at its centre, in the direction normal to the surface. Impact force and displacement were recorded using a dynamic load-cell and a dynamic linearly variable differential transformer (DLVDT), respectively. The SignalExpress software was used for collecting the data at a sampling rate of 50 kHz. Furthermore, a Photron FASTCAM PCI high-speed camera was used for recording the movement of the impactor at a rate of 2000 fps, in order to verify the consistency of the impactor speed.

6.3.6. In-Plane Impact Test Setup and Procedure

The impact load was applied with the same equipment as used for conducting the out-of-plane impact tests, but a different jig was used to hold the specimens. In this case, a jig was designed and fabricated by which the ends of each 190 mm x 20 mm x 5.3 mm specimen could be clamped in a way that only the impacted end of the specimen would be allowed to displace axially. A detailed description of the apparatus and specimens can be found in reference (De Cicco & Taheri, 2018b). The first set of tests was extracted from one of our previous works (De Cicco & Taheri, 2018b), in which the specimens were fabricated using the SB method. The second set was fabricated using the SBC method. The specimens that were prepared using the SB technique were subjected to axial impact of 7 J, while the specimens bonded using the proposed technique were impacted with 10 J. The impact force and resulting displacement were recorded using the same apparatus as described in the previous section, with a difference that a Krontech Chronos high-speed camera was used to record the 10 J impact tests, at a rate of 4,489 fps.

6.4. Results and Discussion

The results of the tests conducted on different specimens are reported here to show the effectiveness of the proposed method on specimens that would undergo such severe loading conditions as described earlier.
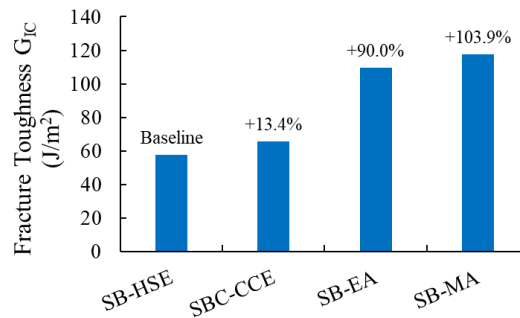
Figure 6-4. Mode I fracture toughness (G_{IC}) values for the tested adhesives and bonding methods.

6.4.1. Mode I Fracture Response

The results of the Mode I fracture (DCB) test in terms of fracture toughness (G_{IC}) values are reported in Figure 6-4; these values were obtained using the "modified beam theory method" as described in the ASTM standard (ASTM Standard, 2014). Note that this method was chosen for its simplicity and accuracy. It is worth noting that a study (Mohamed & Taheri, 2018) compared the outcomes of the three G_{IC} calculation methods suggested by the standard, applied to bonded joints having relatively stiff adherends. It was observed that the differences in values obtained by the three methods were insignificant.

As can be seen from Figure 6-4, the lowest G_{IC} value was produced by SB-HCE specimens, while the best performances were offered by SB-MA followed by SB-EA specimens, producing 103.9% and 90.0% increase in toughness, respectively, in comparison to SB-HCE specimens. In comparison, SBC-CCE specimens exhibited a modest 13.4% improvement in fracture toughness.
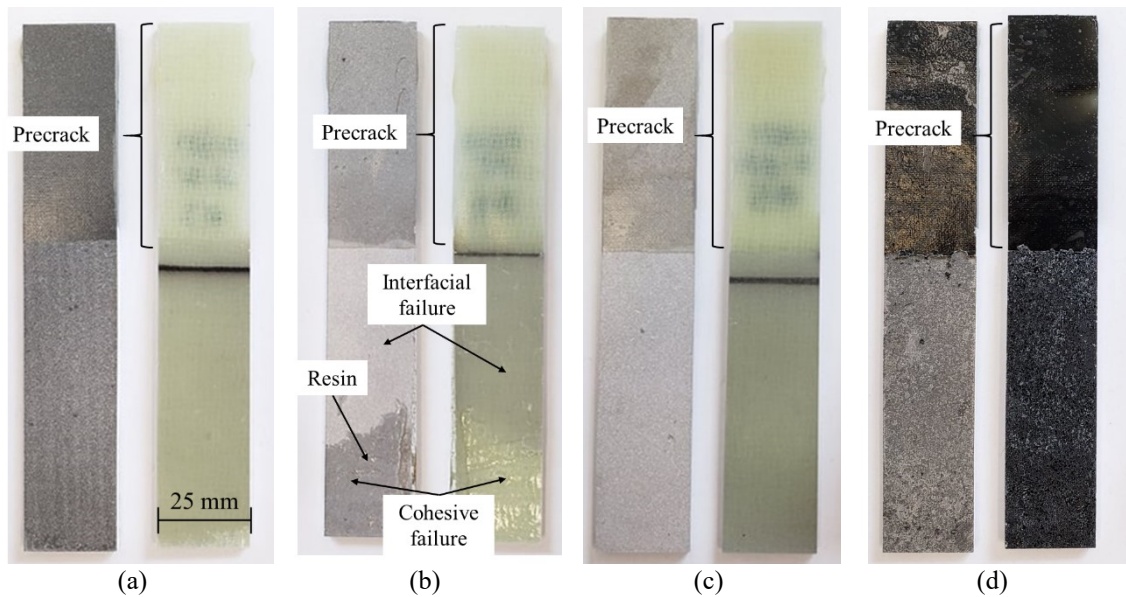
Figure 6-5. Fracture surfaces of specimens formed by various bonding techniques: (a) SB-HCE, (b) SBC-CCE, (c) SB-EA, and (d) SB-MA. In each picture, the magnesium adherend is on the left side. Note that, unless otherwise specified, the failure is of the interfacial type (in other words, no resin traces exist on the magnesium surface).

Typical fracture surfaces of all four specimen types are illustrated in Figure 6-5. Please note that the methyl methacrylate-based adhesive used was black in colour, while the other adhesives had a sort of creamy colour. In SB-HCE and SB-EA cases, the failure mode was

purely of interfacial type (i.e., the crack developed and propagated at the magnesium/adhesive interface). In SBC-CCE specimens, the crack started and propagated for a certain distance in interfacial mode, but it diverted into the cohesive mode (i.e., within the adhesive) as it travelled toward the end portion of the bond line. Finally, the failure mode observed in the case of SB-MA specimens cannot be classified as one of the standard failure modes. That is because some minute adhesive residues were present on the surface of magnesium adherends, however not to the extent that one could classify the failure as a cohesive fracture. This confirms the fact that bonding to magnesium alloys is a challenging task, which is primarily caused by the lack of strong chemical compatibility between magnesium and polymer resins. An interesting phenomenon was also observed when testing some of the specimens, which was the sudden failure of specimens occurring at the stage when the crack changed its course from interfacial mode to cohesive mode. This suggests that the crack propagated in an unstable fashion in the adhesive. Also visible in Figure 6-5(d), is the adhesive surface of a typical SB-MA specimen, which shows 20% apparent porosity (the value was obtained via image processing using the "bwconncomp" function of MATLAB); note that the porosity level was not observed in bonded surfaces prepared by the other adhesives. This is attributed to the much faster curing rate of this adhesive (which occurs in order of a few minutes), causing partial cure of the adhesive, thus, trapping the air before the bonded assembly could be secured between the clamping plates that were used to promote consolidation of the joint during their curing period. One can, therefore, postulate that a higher fracture toughness value could potentially be attained by reducing the amount of void in the adhesive achieved by an optimized bonding process.

For a more precise comparison, detailed views of the fracture surfaces were obtained by the digital microscope, as shown in Figure 6-6. When typical post-failure surfaces of the specimens bonded with the adhesives are compared, no differences are observed, apart from the surface of specimens bonded with MA adhesive. Note that the darker colour of the magnesium skin seen in the figure showing the HCE specimens is the consequence of the curing process that had to be carried out at a relatively high temperature; in other words, the dark regions do not correspond to adhesive residues. As for the case of specimens bonded with MA, the presence of adhesive residues left on the surfaces (see the left figure on Figure 6-6(d)) corroborates the observations that the failure does not conform to a

standard failure mode type. In addition, this would also indicate that a stronger bond between this adhesive and the magnesium had been created and that the failure was due (or at least partially due) to the coalescence of the pores created by the trapped air bubbles. This would corroborate the hypothesis that, with an optimized fabrication process, a much higher G_{IC} value could be obtained when using this adhesive. At this juncture, it should be stated that the G_{IC} quantity discussed in this paper does not represent the fracture energy of the adhesive in the classical sense; it actually represents an equivalent measure of the interface bonding energy between the adhesive and its magnesium substrate. This is because the failure mode is of the interfacial type instead of being the cohesive type. The measured G_{IC} values will be used as the main parameter in the cohesive zone model that will be incorporated in our future numerical investigations and should be regarded as a parameter representing the interface's macro-scale bonding behaviour.

(a)

(b) (c)

(d) (e)
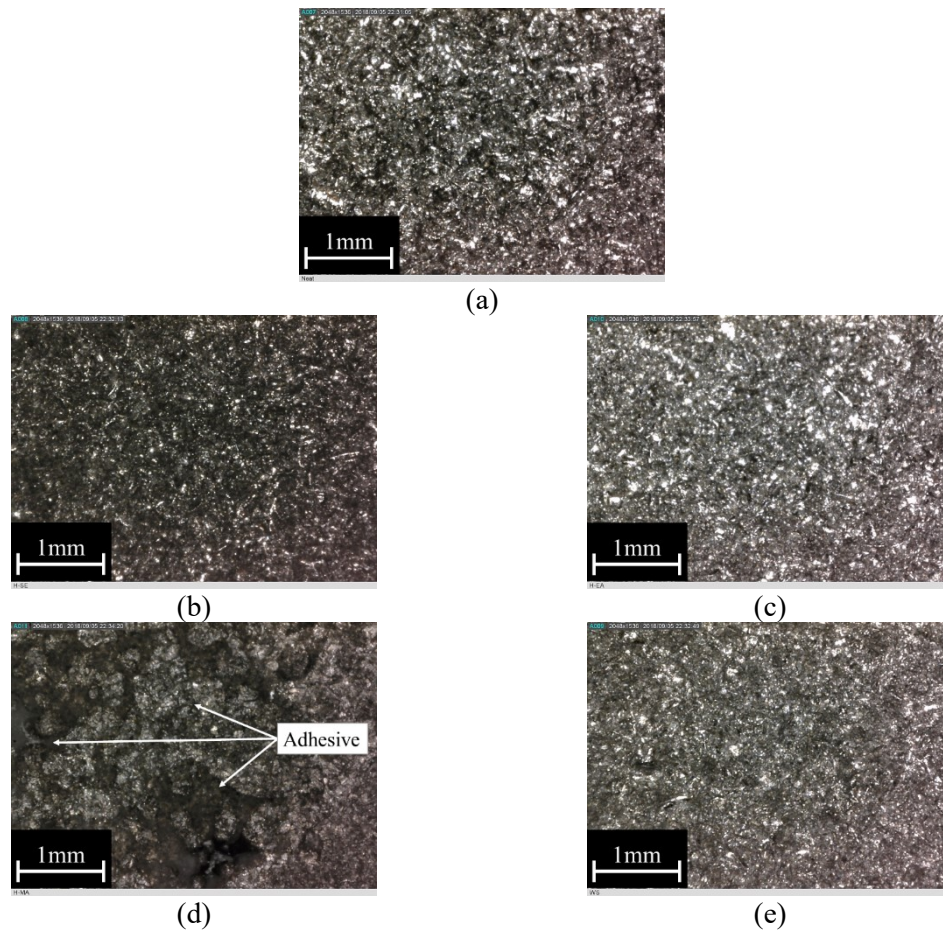
Figure 6-6. Close view of the magnesium adherends' fracture surfaces: (a) neat, (b) HCE, (c) EA, (d) MA, and (e) CCE.

117

6.4.2. Short-Column Compression Tests Results

In this section, the results of the short-column compression tests are reported. The test was used to characterize the behaviour of a short 3D-FML specimen under a quasi-static uniaxial compression loading with emphasis on the delamination-buckling of the magnesium skins from the core. The results for the SB-HCE specimens were extracted from our previous study (De Cicco & Taheri, 2016). Note that the specimen group produced by SB-MA procedure was not considered in this part of the investigation (even though they exhibited larger G_{IC} values than the considered specimens), because their fabrication was significantly more demanding, thus comparatively, not feasible from the perspective of the required man-hour (hence, cost) in industrial settings.

The load-shortening curves for the intact specimens (i.e., specimens without any pre-existing delamination), representative of the specimens' behaviour, are illustrated in Figure 6-7(a). In contrast, Figure 6-7(b) shows the response of specimens which had an initial delamination spanning across 50% of specimens' length. For the sake of clarity, only the response of one specimen per group of specimens is illustrated, with the proviso that the exhibited curves are close representatives of the response of all specimens tested within each respective group. Moreover, the actual failure responses of the specimens are also illustrated pictorially in Figure 6-8.
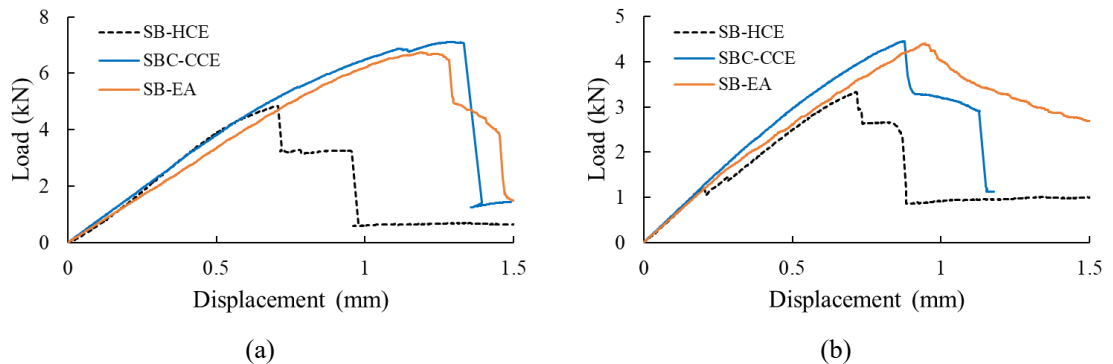
Figure 6-7. Short-column compression test load-shortening curves for (a) intact specimens and (b) specimens with 50% initial delamination.
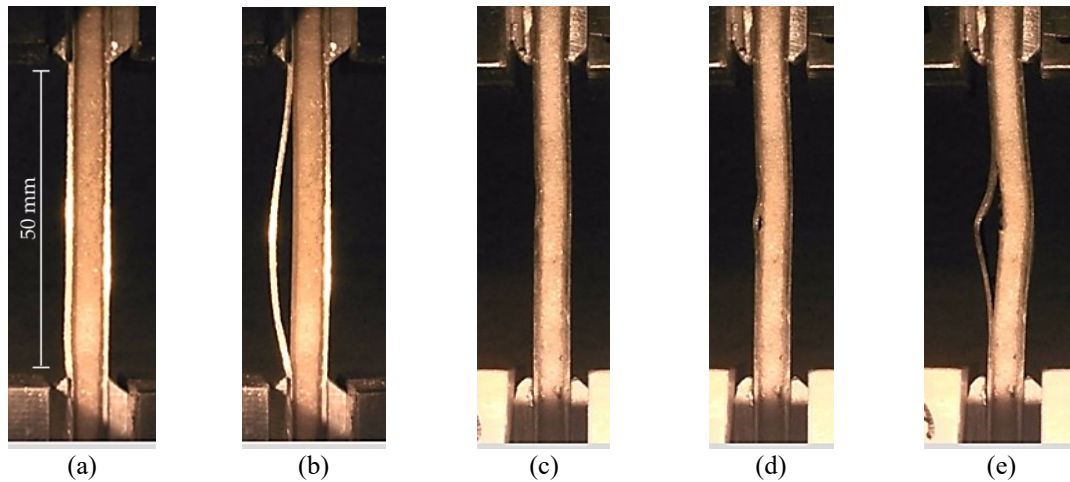
Figure 6-8. Comparison of the short-column compression test failure modes of the intact groups of specimens. (a) and (b): SB-HCE group, (c) to (e): SBC-CCE group.

In the case of intact specimens, the change in the behaviour of SB-HCE group compared to either SB-EA or SBC-CCE groups is evident. In the case of SB-HCE group, the magnesium skin delaminated and buckled at a compressive load of approximately 5 kN (the response is also seen pictorially in Figure 6-8(b)), leading to a sudden drop in the load-carrying capacity. However, the specimen could partially recover its load-carrying capacity until its full failure occurred, which was accompanied by a combined fracture of the fiberglass plies and delamination-buckling of its second magnesium skin. In the other two groups of specimens, the specimens first underwent bending, which resulted in the nonlinear response seen in the load-axial shortening curve, followed by localized delamination of the skins from the FRP core. In other words, the stress concentration caused by bending prompted the skin on the compressive side (see the left skin in Figure 6-8(c), (d) and (f)), to locally delaminate and subsequently buckle, leading to a sudden and complete failure of the specimen. This comparatively gradual failure mode facilitated 52.6% and 38.9% increase in load-carrying capacity in SBC-CCE and SB-EA groups, respectively, when compared to SB-HCE group (see also Figure 6-9).

In the case of the group of specimens that hosted an initial delamination, the maximum load capacity in SB-HCE group was accompanied by a combination of fiberglass ply cracking and delamination-buckling of the second skin, while the failure of the fiberglass plies caused the complete failure of the SBC-CCE and SB-EA specimens. In other words, the stronger bond attained by the new proposed surface preparation method and the epoxy

adhesive led to an overall higher load-carrying capacity. As seen from the results reported in Figure 6-9, compared to SB-HCE group, SBC-CCE and SB-EA groups exhibited improvements of 39.3% and 38.9% in their load-carrying capacity, respectively.
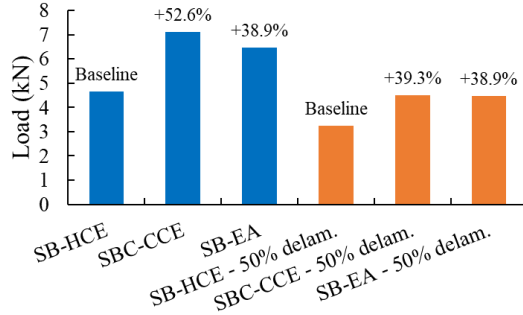
Figure 6-9. Comparison of the maximum load capacity of the intact and delaminated groups of specimens subjected to short-column compression.
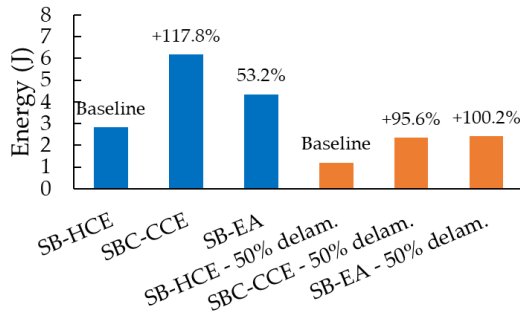
Figure 6-10. Comparison of the failure energy capacity of the intact and delaminated groups of specimens subjected to short-column compression.

Finally, the enhancements obtained by the new bonding technique are further evidenced by the amount of energy required to cause failure of the specimens. The average failure energies for all specimen groups are shown in Figure 6-10. Compared to the reference group, SBC-CCE and SB-EA groups without initial delamination consumed 117.8% and 53.2% more energy, respectively, while the results are reported to be 95.6% and 100.2% for the case with initial delamination. All in all, higher performances were exhibited by the SBC-CCE specimens, even though SB-EA group displayed higher fracture toughness. The observed results indicate that failure of the 3D-FMLs under axial compression loading is only partially governed by Mode I fracture mechanism.
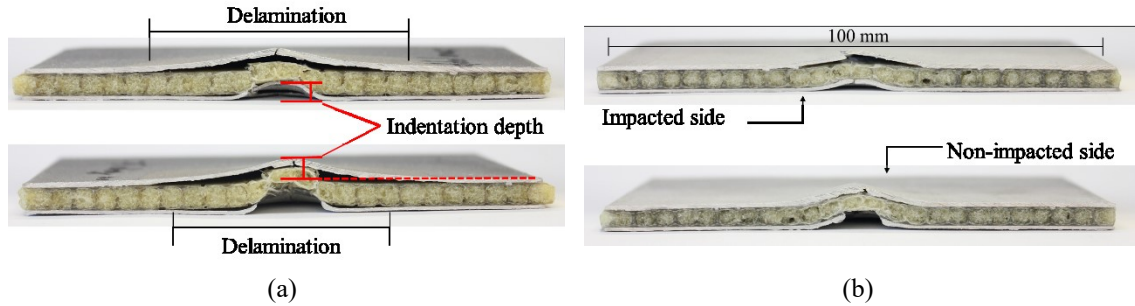
Figure 6-11. Cut-section view of the specimens: (a) SB-HCE and (b) SBC-CCE.
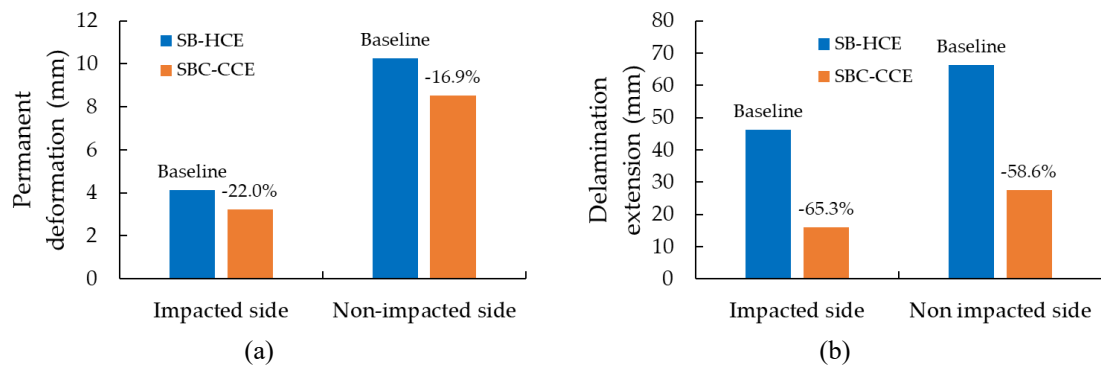
Figure 6-12. Average values of (a) the permanent deformation height and (b) the delamination extension diameters of the specimens subjected to out-of-plane impact loading.

6.4.3. Impact Test results

Based on the comparison of the results presented above, only the SB-HCE and SBC-CCE specimen groups were considered in this part of the study. After testing, the specimens were cut into half to measure the extent of delamination and provide a clear visual comparison of the damage caused by impact. The cross-section views of a representative specimen of each group are illustrated in Figure 6-11. While the overall damage modes are comparable for the specimens bonded using the conventional and proposed methods, however, the extent of the damage is significantly lower in the specimens prepared using the proposed surface preparation technique. The average indentation height of the deformed region (see Figure 6-11) of each group of specimens is shown in Figure 6-12(a). As can be seen, compared to the baseline group (SB-HCE), the permanent deformations measured on the impacted and non-impacted surfaces in SBC-CCE group are reduced by 22.0% and 16.9%, respectively. Moreover, the increase in

diameter of the delaminated region is reported in Figure 6-12(b). As can be seen, the proposed bonding process resulted in the reduction of the delaminated region by 65.3% (for the impacted side) and 58.6% (for the non-impacted side) and slightly higher load-carrying capacity; nonetheless, the magnitudes of the energy were essentially the same (cf. Figure 6-13(b)). This shows that a higher percentage of the impact energy was under the form of elastic deformation for specimens manufactured using the proposed technique.

| (a) | (b) |
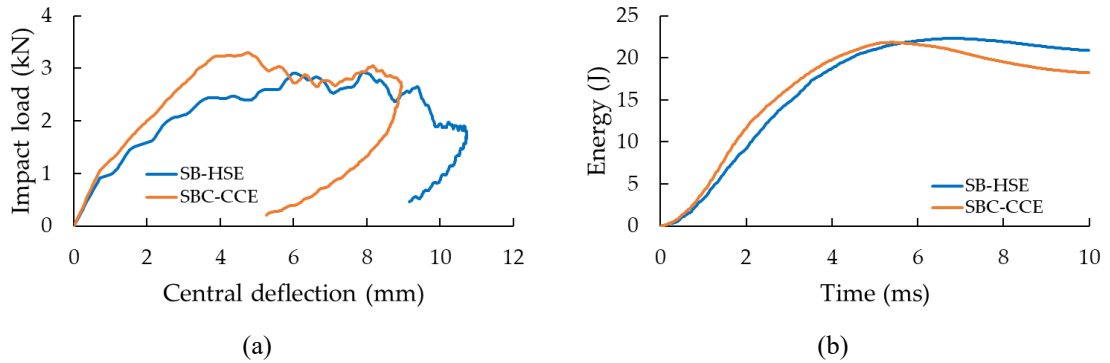
Figure 6-13. Response of the representative specimens that were subjected to out-of-plane impact loading: (a) load-axial shortening curves, and (b) energy versus time.

The qualitative results of the specimens that were subjected to the in-plane impact tests are reported in Figure 6-14. As seen, the impact caused extensive delamination of the skins of SB-HCE specimens, while no such outcome is observed in the SBC-CCE specimens, even though comparatively, they were subjected to 43% more impact energy. The positive attribute of the proposed method is also highlighted quantitatively in Figure 6-15. The axial load-shortening curves show that the proposed surface preparation technique did not affect the initial response of the specimens, since both groups responded with similar initial linear stiffness, followed by a similar behaviour up to approximately 1.5 mm of axial shortening. However, after that stage, the SBC-CCE specimens exhibit a greater load-carrying capacity compared to SB-HCE specimens. The graphs also indicate that, while the SB-HCE specimens essentially underwent a crushing stage after the onset of delamination and the subsequent buckling, the impactor bounced back in the case of the SBC-CCE specimens. This observation further highlights the gain in the capacity that could be attained by incorporating the proposed surface preparation technique.

(a)

(b)
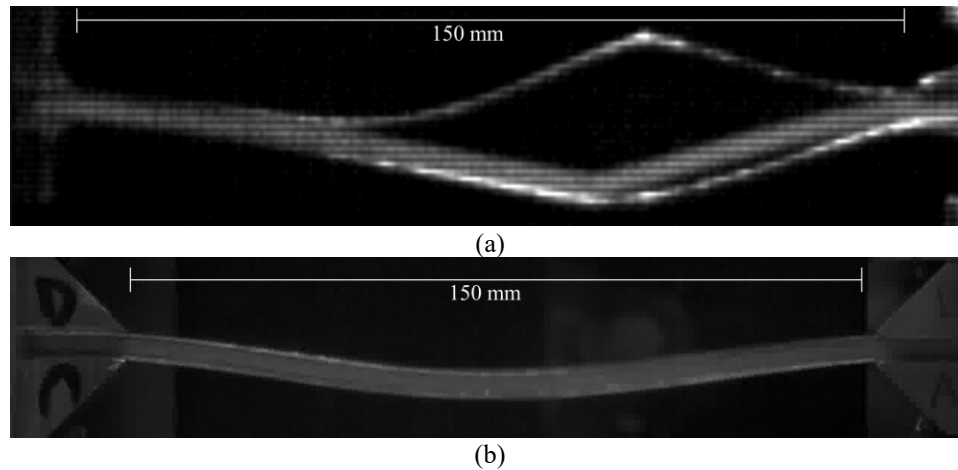
Figure 6-14. View of the specimens under in-plane impact (a) SB-HCE and (b) SBC-CCE.
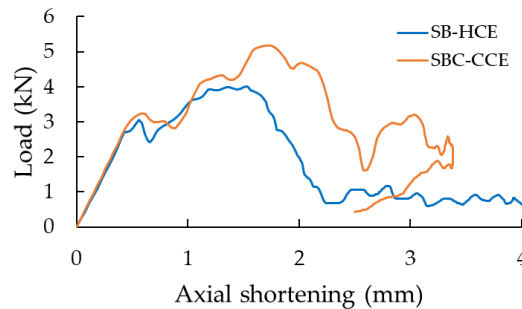
Figure 6-15. Load-axial shortening response curves for specimens subjected to in-plane impact loading.

6.4.4. Other Considerations

At this juncture, it is worth examining the level of effort required by the various methods considered in this study for bonding FRP to magnesium alloy, as well as considering the associated cost. Obviously, the proposed SBC method requires a few extra manufacturing steps compared to the conventional method (SB). However, because the prepared surface of the magnesium alloy is coated with resin, the oxidation process would be halted immediately after the sandblasting stage, and the material can be bonded at a later time, if desired so, as opposed to having had to be done immediately, as should be done when the conventional procedure is used. Following the proposed procedure, the magnesium skin can, therefore, be stored or shipped, as it would be ready for bonding to FRP at the desired time. Therefore, the skin preparation and the bonding of the metal to

various components can be done at different times and at different facilities. In turn, this could save both production effort/time and fabrication/assembly cost on an industrial scale. Moreover, as importantly, the quality assurance of the hybrid systems that are produced by magnesium alloys and FRP materials will also be significantly improved. Additionally, the enhanced interfacial capacity could further increase the safety factor and reliability of the components made of such hybrid materials. Finally, another positive attribute gained by the proposed method is that the surface preparation can easily be applied to either one or both metal surfaces at the same time, without significant change in labour, time, or cost.

In closing, we should also state other matters that once dealt, could further improve the feasibility of the suggested simple surface preparation technique. Firstly, the vacuum bagging, which is used to guarantee a homogeneous and consistent reparation of the resin onto the surface, should be replaced with a less laborious and resource-intensive procedure. Secondly, similarly to the technique briefly mentioned in Section 2.3. , nanoparticles could be dispersed in diluted resin as a mean to improve the mechanical interlocking of the resin onto the sandblasted surface. Finally, the resin type could be optimized so that the wettability of the metal surface is improved, in turn facilitating an even stronger and more resilient bond.

6.5. Summary and Conclusion

A new surface preparation technique was proposed, the use of which could facilitate enhanced bonding strength in adhesively bonded joints mating magnesium alloys to fiber-reinforced polymer composites. Various mechanical tests were conducted to assess the performance of the proposed technique (referred to as SBC) compared to the conventionally used method (SB), in conjunction with the use of various resins. In some of the tests, the interface bonds were subjected to critical stress states. In other words, besides the conventional ASTM DCB test, the interface bond strength in a complex 3D hybrid sandwich fiber-metal (magnesium) FRP laminate (referred to as 3D-FML) was evaluated under axial and lateral impact loadings. The results of the study can be summarized as follows:

- Huntsman's cold-cured high-strength epoxy and methyl-methacrylate adhesives provided the greatest fracture toughness (G_{IC}) values.

- The visual analysis of Mode I DCB specimens' fracture surfaces revealed that the crack propagated mostly in the interfacial mode in all the tested resins; however, cohesive failure mode was also observed in the specimens mated by the West System cold-cured epoxy (CCE).

- Short-column compression tests revealed that the specimens mated by the relatively inexpensive cold-cured West System epoxy that were prepared by the proposed surface preparation technique (SBC-CCE) performed as well as the specimens that were mated using the significantly more expensive Huntsman's cold-cured adhesive when the conventional surface preparation technique was incorporated. The tested specimens exhibited similar delamination-buckling resistance.

- The test results also revealed that more than 50% increase in load-bearing capacity could be achieved when specimens were prepared for bonding with the proposed surface preparation technique. The increase could be attained when the least-expensive resin was used in comparison to the bonded interfaces that were prepared by using the conventional surface preparation method and using along the more expensive hot-cured structural epoxy.

- In terms of out-of-plane impact performance, the proposed surface treatment technique decreased the damage extent by a significant margin. Specifically, it reduced the diameter of the delaminated region by up to 22% and reduced the permanent deformation of the specimens by up to 63%.

- Specimens manufactured using the proposed surface preparation method could resist in-plane impact of 10 J, remaining intact, while specimens manufactured using the conventional method were completely damaged when underwent a 7 J impact.

- The comparison of the results from the three performed tests let to the conclusion that surface preparation had a major influence on enhancing the performance of adhesively bonded magnesium/FRP interfaces, while fracture toughness of the adhesive/resin had a secondary contribution in enhancing the overall load-bearing capacity of such interfaces.

In closing, besides the abovementioned positive outcomes, one should also note the resulting cost-saving that one could attain when fabricating 3D-FML, or FML in general, by incorporating the proposed technique on an industrial scale. Our future study will concentrate on investigating the level of enhancement one could attain by combining a portion of the proposed technique with plasma activation or chemical etching methods. Another aspect that merits investigation is the influence of aging and moisture on the coating layer and bonding strength.

6.6. Acknowledgment

Chapter 7: Effect of Functionalized Graphene Nanoplatelets on the Delamination-Buckling and Delamination Propagation Resistance of 3D Fiber-Metal Laminates under Different Loading Rates

Davide De Cicco and Farid Taheri

7.1. Abstract

This paper presents an investigation into the effect of graphene nanoplatelets as a means of improving the impact buckling performance and delamination propagation resistance of a recently developed 3D fiber-metal laminate (3D-FML). One of the highlights of the investigation is the examination of the performance of the GNP-reinforced resin at a sub-freezing temperature (-50°C). 3D-FML beam specimens were subjected to axial impact of various intensities at room-temperature, while they were subjected to quasi-static axial compression load at the sub-freezing temperature. Moreover, the influence of two different surface preparation methods on the performance of the metallic/FRP interfaces of the hybrid system was also investigated in this study. Although the inclusion of the GNPs in the resin resulted in some gain in the buckling capacity of the 3D-FML, nevertheless, the results revealed that the lack of chemical bond between the GNP-reinforced resin and the magnesium skins of the hybrid material system significantly limited the potential influence of the GNPs. Therefore, a cost-effective and practical alternative is presented which will result in a significant improvement in the interfacial capacity.

7.2. Introduction

[…] as was presented in Section 2.3, and reported in (De Cicco et al., 2017), nanoparticles have been shown to positively contribute to the increase in lap-strap joint strength, and worked with many different substrate and adhesives.

In this paper, the in-plane compression and impact-buckling responses of 3D-FML whose metal/FRP interfaces are reinforced with NH_2-functionalized GNPs are investigated. In particular, the influence of an initial delamination is also considered. The responses of reinforced specimens are compared against the baseline specimens (i.e., with non-reinforced specimens). Moreover, the influence of sub-freezing temperature (-50°C) on the performance of the non-reinforced and GNP-reinforced interfaces subjected to quasi-static compression loading is also investigated.

7.3. Materials and Methods

7.3.1. Materials

The 3D fiberglass fabric and fiberglass veil were acquired from China Beihai Fiberglass Co. Ltd. (Jiujiang City, Jiangxi, China). A Huntsman produced two-part hot-cured epoxy resin (bisphenol-A-based Araldite LY1564 resin and its Aradur 2954 hardener) was acquired from the producer (West Point, GA, USA), while the cold-cured epoxy resin (105 resin with 206 hardener) used to mate the magnesium and FRP constituents (i.e., the interface region herein) was produced by West System (Bay City, MI, USA). An 8-lb, high-density polyurethane foam was obtained from US Composites (West Palm Beach, FL, USA). The NH_2 functionalized graphene nanoplatelets (hereafter referred to as GNPs for the sake of brevity), having an in-plane dimension of 1-2 μm and thickness of 4 nm, were purchased from CheapTubes Inc. (Cambridgeport, VT, USA). The lightweight AZ31B-H24 magnesium alloy sheets (or the skins) were acquired from MetalMart (Commerce, CA, USA). Finally, liquid nitrogen was obtained locally.

7.3.2. Specimen's Fabrication

All the beam-like specimens, schematized in Figure 7-1, with dimensions of 190 mm x 20 mm x 5.3 mm, were extracted from larger 3D-FML plates, using a water-cooled circular saw equipped with a diamond-coated blade. The sequence of procedures used to fabricate the plates is as follows. The two parts of the hot-cured epoxy resin were mixed at 100 rpm for 10 min. using a mixer, then degassed in a vacuum chamber for a minimum of 30 min. Then, the mix was applied homogeneously onto the 4-mm thick 3D fiberglass fabric (3D-FGF) using a brush. The resin-immersed fabric was cured at 60°C for two hours and subsequently at 120°C for eight hours, after which the fabric took its three-dimensional configuration with cavities in its core (see Figure 1-1). The cavities were then filled with the foam to provide support to the thin pillars connecting the two main biaxial E-glass constituents of the fabric, thereby increasing the overall specimen's stiffness and strength. The foam-filling process was done by drawing the foam into the cavities at its liquid stage under a negative pressure using an in-house designed jig, which guarantees a homogeneous repartition of the foam inside the cavities. The combination of the 3D fabric-epoxy and foam will be referred to as "core" hereafter.

The hybrid sandwich composite system was completed by bonding the magnesium plates (skins) to the core. Two bonding methods were used, thus leading to two different categories of specimens. In both methods, first, the magnesium skins' bonding surfaces were sandblasted with coarse 20-30 grit crushed glass abrasive in order to facilitate good mechanical bonding. The two bonding methods are as follows:

(i) in the first method (referred to SB, hereafter), the hot-cured resin was directly applied onto the substrates (skins and core), and then the resulting sandwich was vacuum bagged and cured for two hours at 60°C and eight hours at 120°C.

(ii) in the second method (referred to SBC, hereafter), the magnesium bonding surfaces were pre-coated with a thin layer of cold-cured resin, cured for 24 h under vacuum. Then, in a second step, another layer of cold-cured resin was applied to both adherends, sealed under vacuum and let cure at room temperature for 24 h. This second method was developed by the authors and the resulting gain in the interface bond strength under

different loading condition, including axial impact loading was reported in Chapter 6 (De Cicco & Taheri, 2019).

For the specimens hosting an initial delamination, a thin sheet of Teflon was inserted between the magnesium and the core during the bonding process. The resulting delamination had a length of 30%, 50% or 70% of the specimens' gauge length, and were placed at mid-length, on one of the interfaces only (see Figure 7-1).

In some specimens, GNPs were incorporated into the resin that was used to adhere the skins to core. This was done according to the detailed procedure described in (Soltannia & Taheri, 2013). In brief, the various weight percentages (wt%) of the functionalized-GNPs nanoparticles were accurately measured using a scale having a precision of 0.5 mg. The GNPs were mixed with the cold-cured resin (part 105) using a variable speed mixer for 15 min. with an initial speed of 400 rpm, gradually increasing to 2000 rpm. Then, the mixture was further homogenized by passing it seven times through a three-roll calendering machine to break the agglomerations and facilitate uniform dispersion of the particles. Finally, the hardener (part 206) was incorporated, and the whole mixture was mixed at 400 rpm for four minutes and subsequently degassed for five minutes. The short mixing and degassing times prevent the resin from partially curing before it is applied onto all the adherends' surfaces. After degassing, the resin was used as an adhesive in the same manner as described earlier.
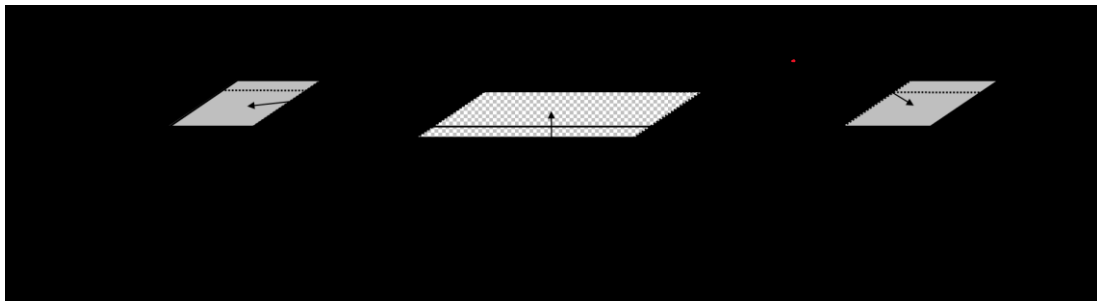
Figure 7-1. Schematic illustration of the 3D-FML specimen hosting a delamination and its overall dimensions (drawing not to scale).

7.3.3. Testing Apparatus, Procedures and Data Acquisition

7.3.3.1. Case Studies I and II

The experimental investigation of this study was organized within three distinct case studies (I, II, and III), as summarized in Figure 7-3.

Case Study I: In the first study, the integrity of the SB bonding method and the effect of GNP inclusion on the performance of the interface bond is studied. Specimens used in this category were fabricated with four different GNP contents (i.e., no GNPs (referred to as "neat" and identified by "N"), 0.5 wt%, 1 wt% and 2 wt% contents). Each specimen category was subjected to four impact energies (1.5 J, 3 J, 4.5 J, and 7 J). The impact energies were chosen according to an experimental investigation conducted earlier by the authors (De Cicco & Taheri, 2018b) and reported in Chapter 5. The selected energy levels were established such that they would subject the specimens to the following outcomes, respectively (i) elastic buckling; (ii) initiating a permanent deformation; (iii) causing propagation of the delamination and (iv) causing complete failure of the specimens.

Four initial delamination scenarios were considered for the neat specimen group; they were: intact (i.e., with no initial delamination), identified as ND; and those with three different initial delamination lengths equal to 30%, 50% and 70% of the specimens' gage length. For the specimens that contained GNPs, only the intact specimens and the specimens with initial delamination length of 50% were considered. Detailed justification of the selection criteria is provided in the next sections.

It should be noted that the effect of the inclusion of GNP on the interface bond strength (i.e., case study I) was performed previously. However, as will be explained in detail in the subsequent section, due to the lack of obtaining an adequate interface bond mechanism, the results from that study with respect to the benefits that could be gained by the inclusion of GNPs in resin were rendered inconclusive. Therefore, the new bonding procedure described in the previous section was used to form the case studies II and III.

Moreover, for the second case study, one delamination length (i.e., 50% of the gage length), one impact energy (2.85 J), and one GNP content (0.5 wt%) were considered. In this way, more statistical number of specimens could be considered per testing category. As also mentioned earlier, the selection of the parameters was done on a rational basis; for instance, the 2.85 J impact energy was selected on the basis that it would cause partial buckling of the specimens and propagating the initial delamination while preventing the complete failure of the specimens. Note that the complete delamination of the skin would defeat one of the objectives of the study (i.e., the examination of GNP's effect on the delamination growth). Furthermore, the inclusion of GNPs in the resins were done in two ways:

(i) in one case, only the resin used to coat the magnesium skins was reinforced with the GNPs (these specimens are identified as "C" specimens);

(ii) in the other case, the resins used to coat the skins and used for bonding the skins to FRP were both reinforced with the GNPs (specimens of this category are identified by "CA").

Aside from the GNPs, the effect of inserting a thin fiberglass veil between the magnesium and the core with the aim of improving the interface bond mechanism was also investigated (specimens in this category are identified as "V" specimens). Finally, the baseline specimens, which were fabricated with the neat resin (i.e., with no GNP or veil reinforcements) are identified as "N" specimens.

The impact testing apparatus used to test the specimens of case studies I and II is shown in Figure 7-3. The setup consisted of a modified Charpy impact testing machine equipped with an in-house designed fixture to support the specimen such that the specimen was subjected to a purely axial impact. Each specimen was clamped in the fixture over 20 mm length at each end in such a way that only the axial displacement at the impacted end was permitted, therefore, imposing a fixed-fixed boundary condition. The various impact energies were obtained through trial and error, by changing the pendulum angle and using an image-processing algorithm written in MATLAB, to extract the position and time information of the impactor. The impact load and axial-shortening history data were

captured by using a dynamic load cell and a dynamic linear variable displacement transducer (DLVDT), respectively, both operated at a sampling rate of 50 kHz. A Photron Fastcam PCI high-speed camera was used to record the impactor movement and specimens' deformation at a rate of 2000 fps. The impact energy was, therefore, obtained by knowing the impactor's speed and mass. Nine pendulum angles ranging from 10° to 50° were tested, leading to impact energies ranging from 0.4 J to 10.6 J. Subsequently, a quadratic curve was fitted to the data points to obtain the desired impact energy.

Prior to each test, the correct alignment of the specimen was verified using a digital level and a square ruler. The axial displacement and load data were acquired using a dynamic linear variable differential transformer (DLVDT) and a dynamic load cell, respectively. Both signals were transferred to a PC via a National Instruments data acquisition system device, synchronized using the Signal Express software. Lastly, the impact tests of the first case study were recorded using the Photron high-speed camera at a rate of 2000 fps, while the case study II tests were recorded using a Kronotek Chronos high-speed camera, at a rate of 4498 fps. Note that the latter camera was not available to the authors at the time the first case study was conducted (hence, the use of two different cameras).

7.3.3.2. Case Study III

The same parameters that were used in case study II were used in case study III, but the tests were conducted under quasi-static loading. This is because the sub-freezing temperature had to be conducted in an Instron thermal chamber that could not accommodate the impact test setup. The chamber was used in conjunction with an MTS servo-hydraulic testing machine, equipped with a 250 kN load cell. This test setup is illustrated in Figure 7-4. The compression actuation speed was set to 0.5 mm/min. The air inside the chamber was cooled using liquid nitrogen. A preliminary test was conducted to determine the time required for the specimen reaching the equilibrium temperature within the chamber (i.e., -50°C). This was done by inserting the thermocouple wire inside a specimen (through the filling foam) to monitor its cooling rate. It took three minutes for

the specimen to reach the equilibrium temperature. Therefore, the specimens were loaded after the initial three-minute conditioning time.

Finally, the load and displacement data were retrieved directly from the MTS machine using the MTS793 software that was used to control it, while the delamination-buckling event was captured on video at a rate of 30 fps using a Canon Rebel SL2 camera.

| (a) | (b) | (c) |
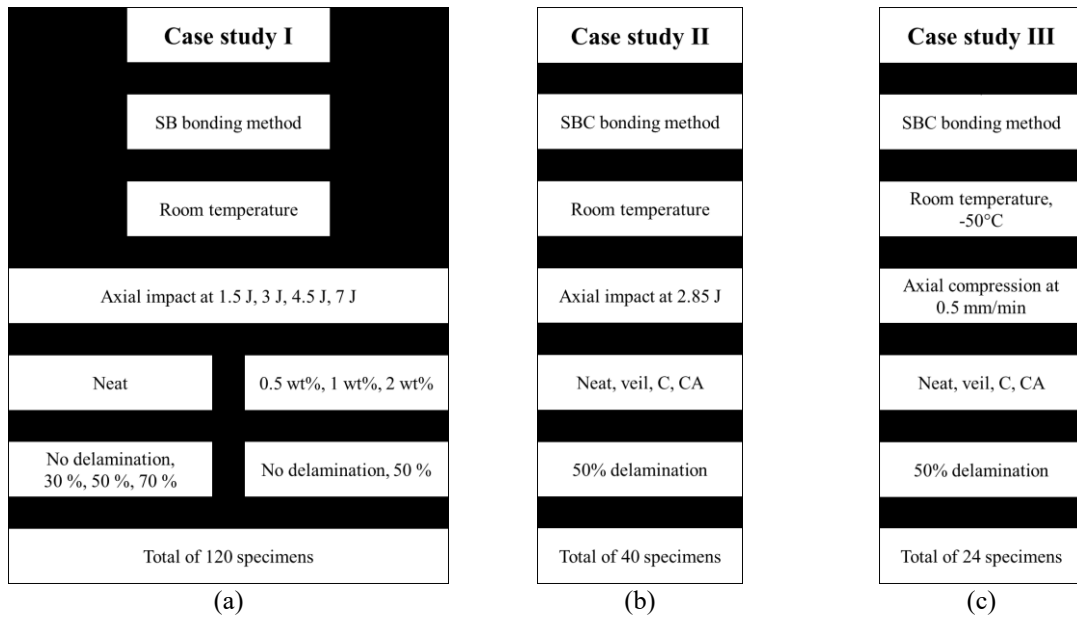
Figure 7-2. Summary of the case studies and their parameters: (a) I, (b) II, and (c) III.

| (a) | (b) |
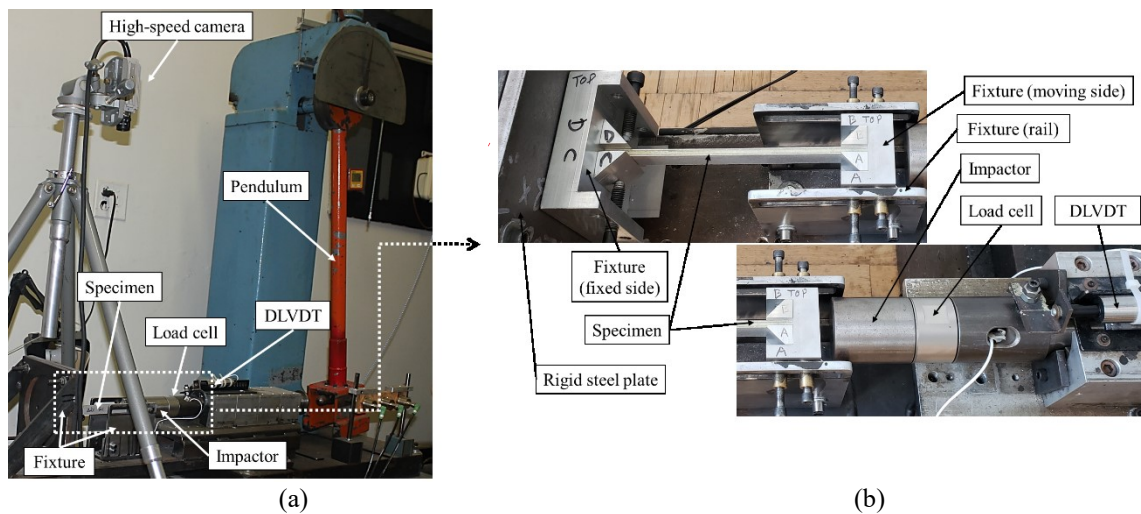
Figure 7-3. (a) Experimental setup for impact testing and (b) close-up view of the impactor and the specimen supported by the fixture.
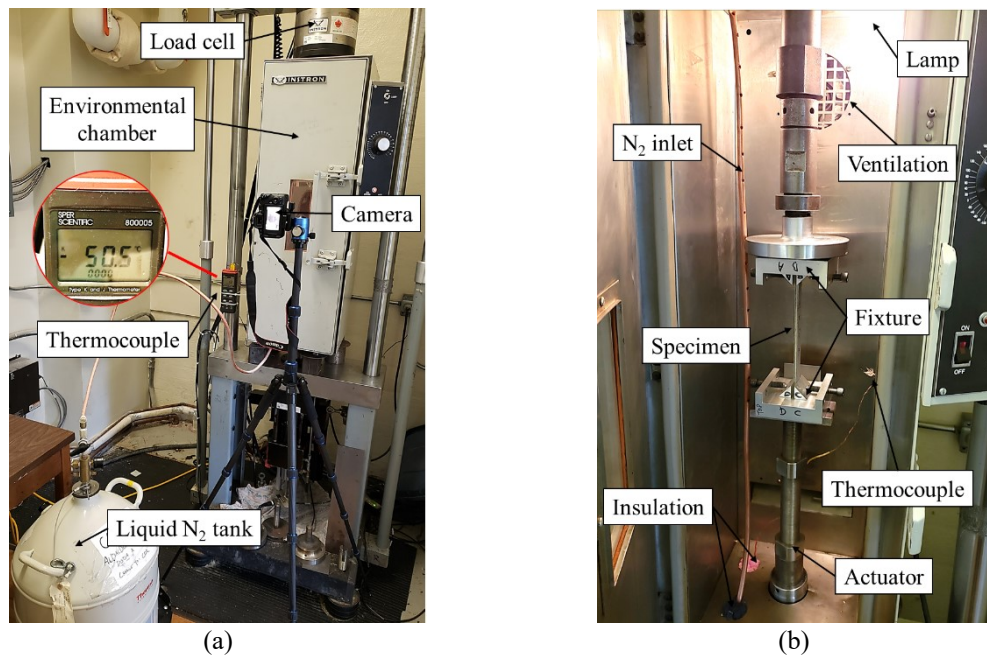
Figure 7-4. (a) Overall view of the static buckling test setup and (b) inside view of the thermal chamber.

7.3.3.3. Data Processing

A LabVIEW algorithm was written to facilitate the post-processing of the impact test data in a consistent and efficient manner. The only required operation of the user was the identification of the exact initial time of the impact event. Note that, because of the signal fluctuations (typical of impact tests), automation of the process to obtain this initial time would have been very challenging and time-consuming. The output of the LabVIEW code was a set of data points corresponding to three signals. First, the captured displacement-time signal was filtered to remove high-frequency noise, and the 60 Hz noise originated by the power supply, followed by filtering of the force-time signal. An example of such signals is illustrated in Figure 7-5(a). Moreover, since the inherent signal fluctuation makes it difficult to objectively compare the signals, therefore, the RMS of the signal was obtained, as illustrated in Figure 7-5(b). The RMS (acronym of the root-mean-square) data was established by evaluating the average of the load-history signal, computed using the RMS amplitude of the signal. This quantity is directly proportional to the signal's power and peak amplitude. Therefore, the information conveyed through the RMS signal is equivalent to the one from the filtered signal from which they are extracted. As clearly seen in Figure

135

7-6(b), this signal-processing procedure invokes a shift between the two signals. However, the signals' shift would be consistent for all signals, thus, no error is introduced when comparing the results. The application of this signal-processing procedure would not be necessary when analyzing the quasi-static test results, since there would be no such inherent fluctuation in the signals in such tests.

The video records obtained either with the high-speed cameras or the Canon camera were split into a succession of pictures so that they could be analyzed individually and be easily compared to one another. The overall behaviour of the specimens during impact and the resulting delamination growth were the information that could be obtained from the images (extracted from the recordings). To measure the delamination growth, the initial delamination was precisely measured using a digital microscope and its extremities were marked using a permanent marker. Then, tick marks, spaced at 5 mm intervals, were inscribed along the specimens' side, ensuring that they would be easily visible on the recorded videos/images. The delamination was then measured by comparing the images of a given specimen at its initial stage and when the skin had attained its maximum separation deformed state.
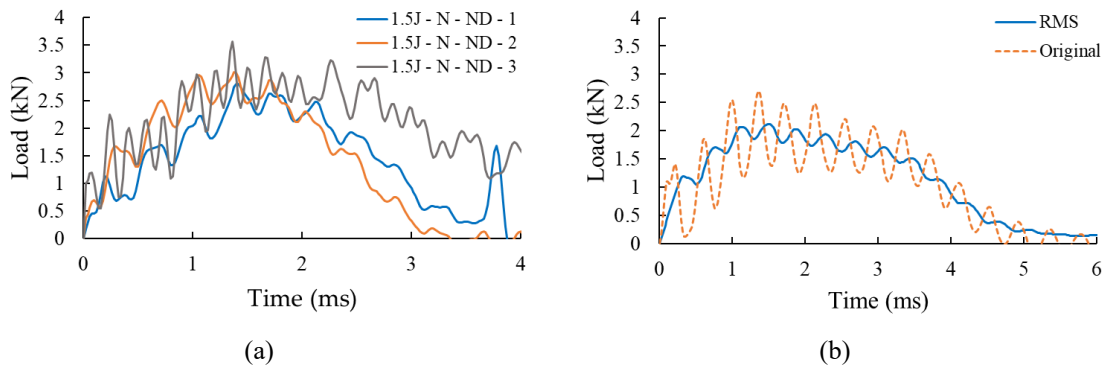
Figure 7-5. (a) The raw load history signals of neat specimens (i.e., without an initial delamination) impacted at 1.5 J, (b) A typical filtered signal and its RMS.

7.4. Results and Discussion

In this section, the results of the three case studies are reported and discussed. Note that as explained in the last section, the RMS of the signals is used to report the data for all the impact tests, while for the quasi-static tests, the reported signal is the one directly

obtained from the MTS testing machine. Also, for the sake of clarity and brevity, only the response of a typical specimen per group of specimens will be illustrated, with the proviso that the exhibited curves are close representatives of the response of all specimens tested within each respective group.

7.4.1. Case Study I

Typical qualitative responses of an intact (neat) and a specimen having an initial delamination are shown in Figure 7-6. In general, the specimens remained straight during the first instance upon the application of the impact load, regardless of the considered impact energies. Subsequently, the intact specimens experienced global buckling. The specimens that were subjected to 1.5 J impact energy endured the energy by elastic deformation and fully recovered their original status after the event. Those undergoing 3 J impact energy, also underwent global buckling, however, ending up with a permanent deformation since their magnesium skins endured some degree of plastic deformation. The behaviours of the specimens undergoing 4.5 J impact energy was similar to those subjected to 3 J impact energy, with the difference that one of the skins partially delaminates in this category. Finally, for 7 J impact energy case, the specimens' skin, on the side that underwent compression during the buckling event delaminated, and the FRP plies of the 3D-FGF on the compression side crushed, leading to the complete failure of the specimens.
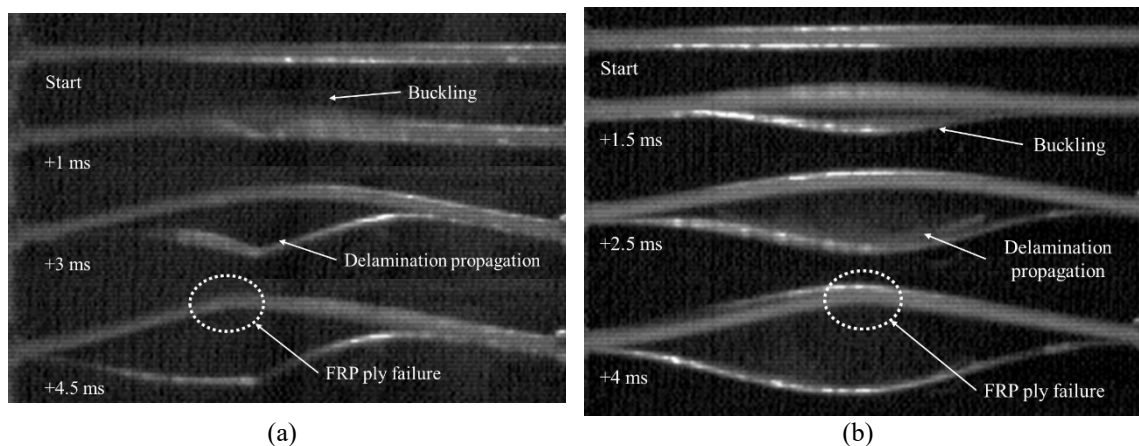
Figure 7-6. Illustration of the behaviour of the 3D-FML sandwich under axial impact, for the study case I neat specimens. (a) No initial delamination, 7 J and (b) 50% initial delamination, 4.5 J.

The specimens having an initial delamination, experienced a global buckling mode; whoever, during the buckling, the delaminated portion of the skin also experienced local buckling. The delamination then grew to a certain extent depending on the applied impact energy. The propagation of delamination was observed to be marginal in the specimens that were subjected to the lowest impact energy. However, the delamination propagated along the entire span of the specimens that were subjected to 3 J impact, but their core remained undamaged. Finally, the specimens that experienced 4.5 J energy case failed completely (i.e., in addition to complete separation of their skins, their FRP plies also failed in compression).

The influence of the presence of an initial delamination is presented in Figure 7-7 through the load-history graphs of the impact tests performed at 3 J and 7 J on the neat specimens (i.e. specimens without GNPs added to their interfaces). Note that the results of the tests conducted at other two energy levels were omitted for the sake of conciseness since they followed the same pattern. The graphs show a clear reduction of the load-carrying capacity for the specimens hosting an initial delamination compared to the intact specimens. More specifically, reductions in load-capacity of 26%, 36%, 38%, and 24%, respectively, are observed for specimens experiencing impact energies of 1.5 J, 3 J, 4.5 J and 7 J. Examination of the results indicates that the length of the delamination does not seem to affect the behaviour in a significant manner; in other words, the variation in the impact response is negligible for all three delamination lengths. Consequently, the 30% and 70% delamination cases were not considered for the remining portion of the study.

(a)   (b)
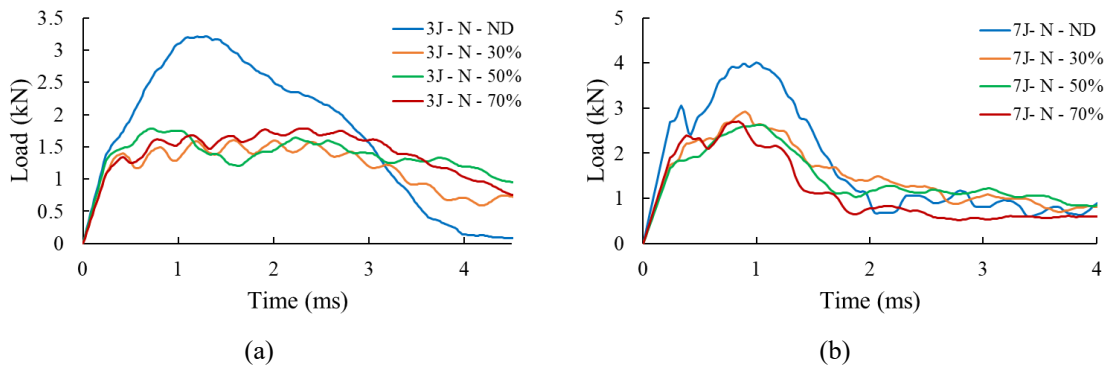
Figure 7-7. Effect of initial delamination for (a) 3 J and (b) 7 J cases.

Figure 7-8 illustrates the load-history graphs for specimens that were subjected to the four impact energies. As could be expected, a higher impact energy led to a higher measured maximum load-bearing capacity. Overall, the results are more consistent for the lowest and highest energies than for the two medium energies. As discussed in (De Cicco & Taheri, 2018b), this is attributed to the fact that 3 J and 4.5 J energies hover around the energy that corresponds to the damage threshold. Therefore, the sensitivity to the reaction of a given specimen at the onset of buckling, which is naturally volatile, is further amplified. It can also be seen that the specimens tested at the two higher impact energies appear to exhibit a residual load-bearing capacity. This response is not observed when considering the specimens of the other cases because, in those cases, the load drops to zero when the impactor detaches from the specimen (bounces back). In the event corresponding to 4.5 J impact, the impactor speed halts to zero but without further bouncing; in other words, the impact energy is absorbed fully by the specimens, while under 7 J energy, the specimens are completely crushed by the impact. This shows that once the skins are fully delaminated, the strength the core is fully compromised.
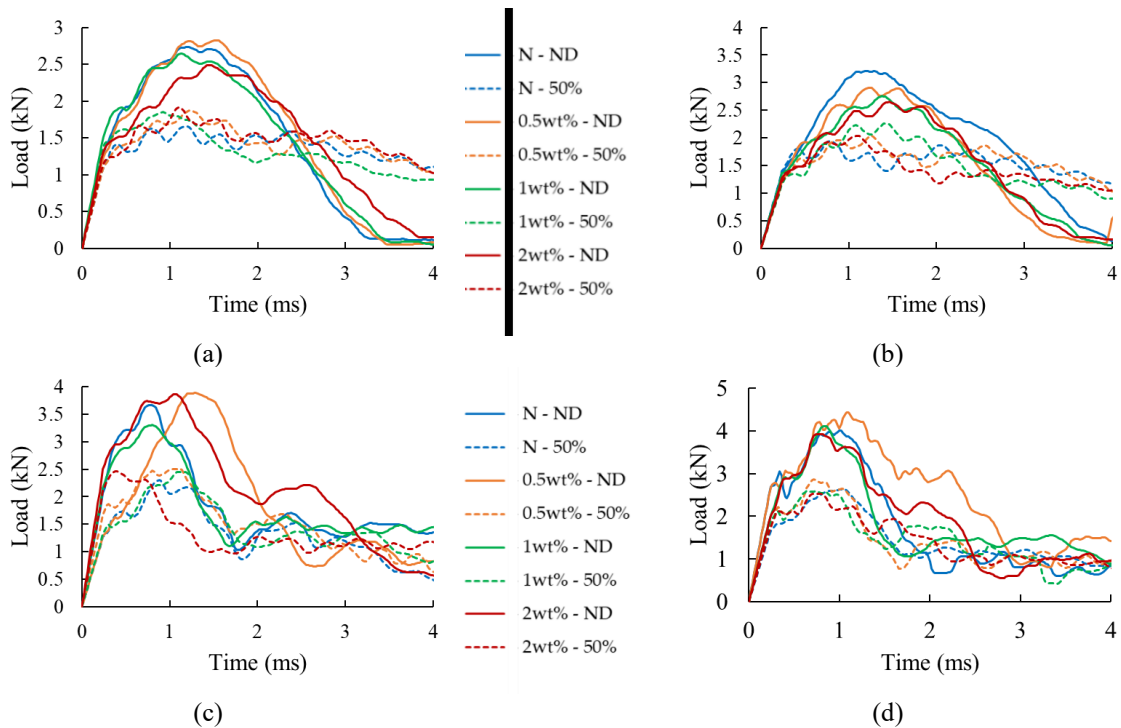
Figure 7-8. Effect of nanoparticles for specimens with and without delamination, and with and without 0.5 wt% GNP content subjected to the different impact energies: (a) 1.5 J, (b) 3 J, (c) 4.5 J, and (d) 7 J.

The effects of the GNPs inclusion can also be observed from the results reported in Figure 7-8, with a more concise comparison illustrated in Figure 7-9. Note that all the results shown in Figure 7-9 have been normalized with respect to the performance of the intact neat specimens, which are referred to as the "baseline" specimens hereafter. The standard deviations are also reported in the chart to better quantify the spread of the results.

Within the GNP weight contents considered, the specimens with 0.5 wt% of GNP content show the best overall improved performance under all tried energies, followed by those containing 1 wt% and 2 wt% GNP contents, respectively. The performance becomes more distinct and optimal in the specimens that were subjected to the highest impact energy, gaining a 28% increase in their load capacity. Such a significant gain in the capacity could not be exhibited when the specimens were subjected to the two lower energies. This is because in those cases, the specimens undergo buckling prior to experiencing other forms of damage (i.e., interface delamination). Moreover, in the specimens hosting an initial delamination, there is no distinct difference in the specimens' response as a function of the applied energies. The nanoparticles seem to have a distinctive enhancing effect on the behaviour/resistance of the specimens that are subjected to the highest energy, especially with a GNP content of 0.5 wt%. For the lower energies, such a positive effect is not as obvious. However, no noticeable reduction of the strength was reported (see the comparative bar chart identified by blue boxes).
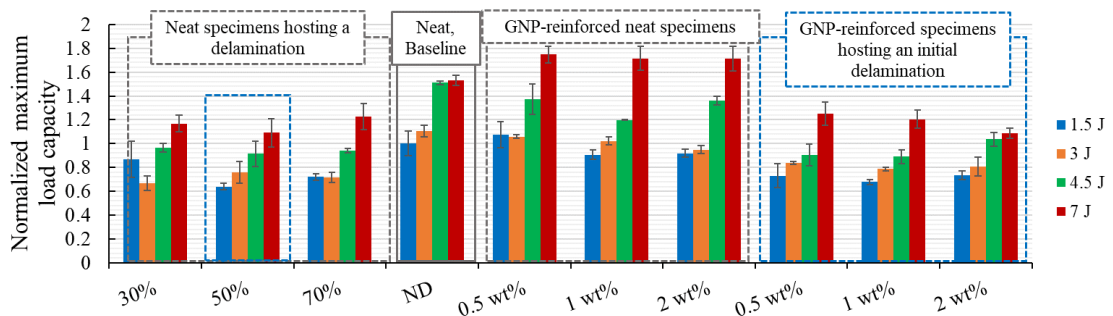
Figure 7-9. Average normalized maximum load-capacity for all specimen sets of case study I. Note that the blue boxes identify the comparable specimen categories.

Comparing the results with that of the baseline specimen, we can see that the highest gain (i.e., 12.5% increase in load-bearing capacity) is seen in the specimen that was reinforced with 0.5 wt% GNP, tested under 7 J impact energy. Next were the specimens

that were reinforced by 1 wt% and 2 wt% GNP contents, exhibiting 10.5% gain in load-bearing capacity. A similar conclusion can be drawn for the specimens that were subject to 1.5 J impact, but the gains are observed only for the specimen that had 0.5 wt% GNP inclusion. In fact, the nanoparticles seem to have included a negative effect in the specimens that were subjected the 3 J and 4.5 J cases, since the specimens' load-bearing capacity was reduced.

When the influence of initial delamination is considered, the best results are still shown by the specimens that were reinforced with 0.5 wt% of GNPs, followed by those with 1 wt% GNP content. The specimens containing 2 wt% GNP did not exhibit any gain in their strength. Note that for the case of 3 J, the specimens with 0.5 wt% GNP exhibited good performance, notwithstanding the fact that the outcome is marginally different when compared to the outcomes associated with specimens containing 1 wt% GNP. Similar to the results observed in the case of the intact specimens, GNP inclusion resulted in a detrimental effect when the specimens were subjected to 4.5 J impact energy; however, improvement in performance are also observed in the cases when the applied impact energies were 1.5 J and 3 J. Note that the specimens containing 2 wt% content GNP tested at the highest energy performed least favourably.

Based on the results, it can be concluded that the addition of nanoparticles can have beneficial effects on the impact load-bearing capacity of the 3D-FMLs so long as the system has no initial delamination. However, once a delamination is introduced, the lack of an adequate bonding mechanism between the magnesium skin and the resin does not allow the GNPs to play their supportive role in preventing crack initiation and arrest. In the presence of a delamination, the lack of chemical synergy between the magnesium alloy and epoxy resin leads to the catastrophic failure of the interface in the presence of a large magnitude of fracture energy developed by increased loading.

7.4.2. Case Study II

Further insight into the effect of inclusion of GNPs on the mitigation of delamination propagation is gained by reviewing the results of the second case study. The behaviour of

the specimens during a typical impact event in shown in Figure 7-10. Similar to the response of the specimens of the first case study, the specimens remained straight for the first compression phase of the loading, followed by the buckling of the delaminated portion of the skin, which initiated the subsequent delamination propagation stage of the event. Note that the delamination propagated in an unstable manner in specimens that are subjected to an in-plane impact loading. In other words, the delamination remained in its initial state as the specimen experienced the load which increased its curvature up to a certain stage of the event. At that stage, however, the critical stress was reached, causing the sudden incremental elongation of the delamination within the specimen after which the equilibrium was regained, leading to stabilization of the load-end shortening response. Finally, the maximum delamination length was attained at which stage the entire impact energy was consumed by the specimen, and the impactor bounced back.
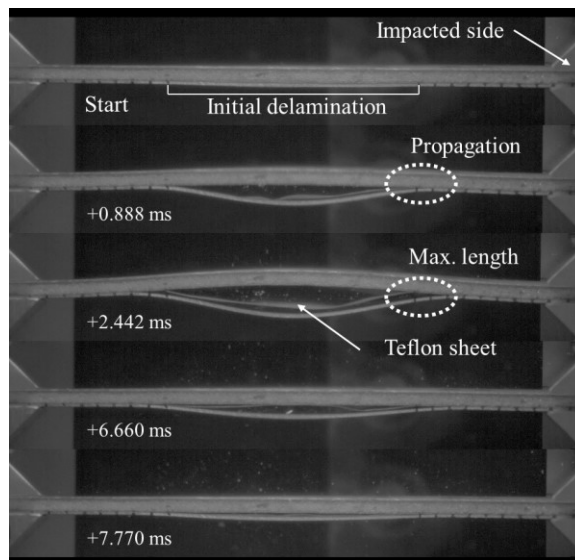
Figure 7-10. The progressive response of the 3D-FML sandwich under axial impact, for the neat specimens - case study II. (a) A specimen with no initial delamination subjected to 7 J impact, and (b) a specimen with 50% initial delamination subjected to 4.5 J impact.

A comparison of the delamination growth in the tested specimens is illustrated in Figure 7-11(a). The values have been normalized with respect to the average delamination propagation experienced by the neat specimens. The delamination is seen to increase with respect to the GNP content, with the worst case observed when the nanoparticles were added to both the magnesium coating and the resin used to bond the skins to FRP (CA specimens). In those specimens, the final delamination length extended twice that of the

142

length noted in the neat-resin specimens. The best results were achieved when the interface had the fiberglass veil incorporated within. The delamination propagation decreased in those specimens by an average of 46% when compared to the neat specimens. However, overall the results of the specimens exhibit large standard deviations. This is a consequence of the inherently unstable nature of delamination propagation in such brittle mediums. It is worth noting that the standard deviation associated with the specimens that had veiled interface, though relatively large, is the lowest amongst the specimen groups, revealing the slight stabilization of the delamination propagation in those specimens. The observed increase in delamination also corroborates with the observation reported by Siegfried et al. (2014); they noted the inclusion of their CNTs led to an increased level of matrix-cracking. This validates our hypothesis that the delamination extends more as the GNP content is increased.
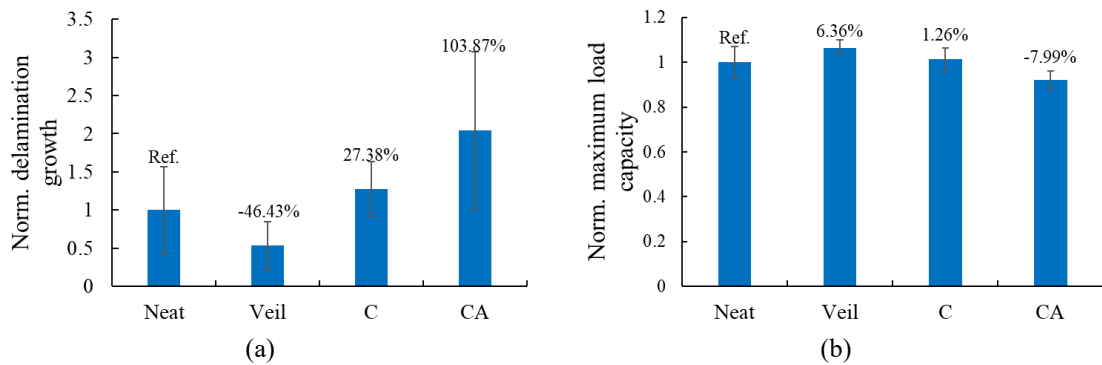
Figure 7-11. Normalized delamination-growth and load-bearing capacities for the specimens of case study II (normalized with respect to the "neat" group of specimens).

The load-bearing capacity of the specimens in this group is reported in Figure 7-11(b). The incorporation of the fiberglass veil into the interface seems to positively impact the load-bearing capacity by increasing it by 6% and also reducing the overall standard deviation of the data. In contrast when GNPs are included in the epoxy coating only (case C), a marginal improvement of 1% is gained. When the standard deviation values associated with the neat and C groups of specimens are considered, the 1% enhancement in the capacity cannot be considered as a conclusive measure of improvement. Nonetheless, the decrease in load-bearing capacity is more pronounced in the specimens of group CA.

143

Overall, one could see that the most improvement in terms of both mitigation of the delamination propagation and load-bearing capacity are obtained by incorporating a fiberglass veil between magnesium skins and FRP core during the interface bonding process. The amount of work required by this step is negligible compared to that consumed by the procedure of dispersing the nanoparticles into the resin, which requires mixing and calendaring efforts. Therefore, it can be appreciated that the suggested veil incorporation technique is the more cost-effective alternative.

7.4.3. Case Study III

The last case study aims to investigate the effect of sub-freezing temperature on the performances of the 3D-FML hosting an initial delamination and whether the interfacial delamination resistance could be enhanced by the inclusion of GNPs. It should be noted that initially the sub-freezing temperature tests were planned to be conducted under a loading rate of 40 mm/s in order to generate comparable results to those of the impact tests. The noted speed was the maximum theoretical speed noted in the documentations of the MTS testing machine. However, the testing machine did not respond well at the intended speed, resulting in erratic fluctuations in load-displacement data, thus rendering the preliminary analysis inconclusive. Consequently, specimens of this case study were tested at a quasi-static loading rate of 0.5 mm/min. The imposed displacement of 1.4 mm facilitated the desired state of delamination propagation without causing the complete failure of the specimens (similar to what was done in the second case study). As stated earlier, the sub-freezing environment of this case study was generated by using liquid nitrogen, hence, the specimens of this case study are referred to as the LN2 specimens, and the specimens tested at room temperature are referred to as RT specimens.

The qualitative response of the specimens was identical to the behaviour described for the specimens of case study II as was illustrated in Figure 7-10; therefore, for the sake of space, the images are not presented. However, the quantitative results of the static buckling tests conducted both at room and sub-freezing temperatures are reported in Figure 7-12 and Figure 7-13. The results illustrated in Figure 7-12 reveal that the LN2 specimens show a slightly higher stiffness compared with the RT specimens. Moreover, no clear distinction

between the responses of neat and GNP-reinforced specimens can be seen, except for the case of LN2-CA specimens, which show slightly higher stiffness compared to the other LN2 specimens. Moreover, similar to the performance of specimens of case study II, the specimens hosting the fiberglass veil exhibited the best performances amongst the tested specimens in terms of buckling capacity at both room and sub-freezing temperatures. As seen, a relatively better performance is shown by the specimens that were tested at the sub-freezing temperature.

To facilitate an easier comparison, the normalized buckling load capacities are reported in Figure 7-13(a). The values are normalized with respect to the average value corresponding to the neat specimens tested at room-temperature (RT-N). The buckling load was taken as the load at which the linear slope of the load-displacement curve changes to a nonlinear one (see point B on the graphs of Figure 7-12). The results also reveal that the inclusion of nanoparticles had a negligible effect on the buckling capacity of the specimens tested at both temperatures, while the inclusion of the veil within the interface increased the buckling capacity by 12% and 22%, respectively for specimens tested at RT and -50°C, respectively.
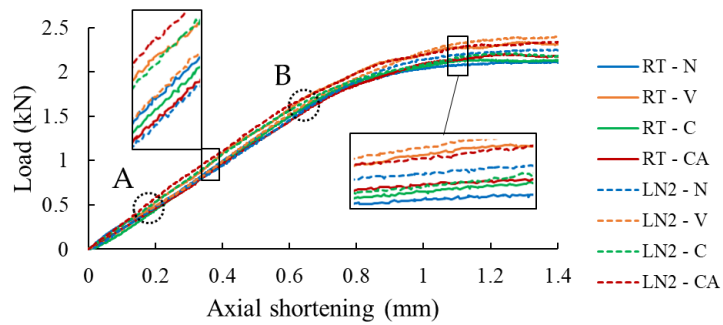
Figure 7-12. Axial load vs. axial shortening curves. Point A corresponds to the onset of buckling of the delaminated skin, while point B corresponds to the onset of global buckling of the specimen.

Lastly, the normalized delamination propagation response of the specimens are reported in Figure 7-13(b) (results normalized with respect to the RT-N case). The sub-freezing temperature caused the delamination to grow to a greater length compared to the response observed at RT. Specifically, the delamination length increased by 48%, 35%, 100%, and 78% for the specimens of categories neat, veil, C, and CA, respectively. Interestingly, while the presence of the interface veil reduced the growth of delamination

by 28% when specimens were tested at RT, the veil's effect diminished significantly in specimens that were tested at the sub-freezing temperature; nonetheless, the veil still helped to suppress the delamination growth when compared to the growth observed in specimens that did not have the veil at their interfaces. It can also be seen that, although the test results (i.e., load-axial shortening curves) are very consistent and have very low standard deviations, nevertheless, the standard deviations are relatively large when considering the delamination length results. This observation further validates our earlier statement that such large standard deviations are inherent to delamination growth being an unstable phenomenon in brittle materials. Also, similar to the results seen in the other case studies, the use of the veil resulted in the highest overall buckling capacity and in suppressing the growth of delamination, with the proviso that its effectiveness becomes adversely impacted by the sub-freezing temperature.
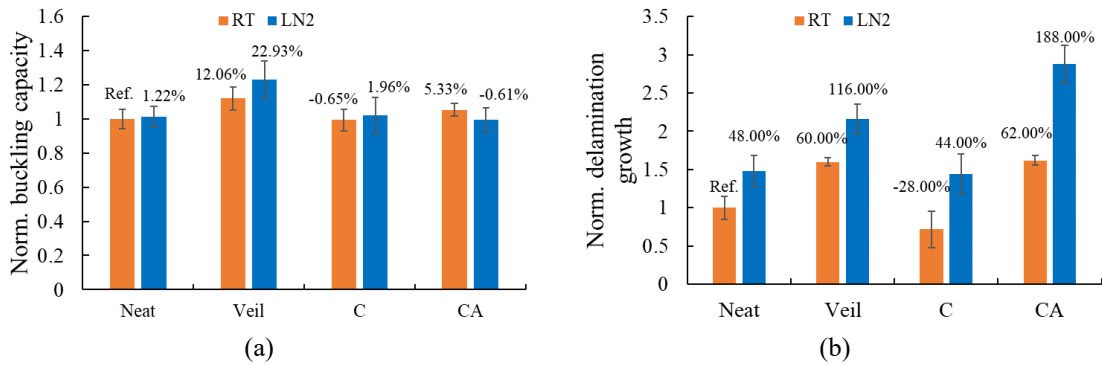
Figure 7-13. Normalized buckling capacity for specimens tested at room temperature and at -50°C.

7.4.4. Analysis of the Interface Surfaces

In an attempt to better understand the reason for unanticipated effectiveness of the nanoparticles in suppressing the interface delamination growth of the specimens, the interface bonding surfaces were examined by the use of a digital microscope. The morphology of the surfaces are shown in the images illustrated in Figure 7-14 for case study I (valid for all the impact energies resulting in delamination) and in Figure 7-15 for case study II. One can see that the dispersion of the nanoparticles is homogeneous on the surfaces of the specimens that were produced by both bonding methods (darker pixels represent GNPs' distribution), and the lighter colour regions seen at the lower portion of each picture correspond to the imprint left by the Teflon that was used to generate the initial

146

delamination. It should be noted that case study III's images are omitted because they were very similar to those shown in Figure 7-15. A greater number of voids is observed in the adhesive of the specimens that were prepared by the SB bonding method, while fewer voids are visible at the interface of the specimens that were prepared by the SBC bonding method. In fact, in the latter case, the voids seem to exist only in the specimens fabricated with the neat adhesive. These observations indicate that the use of nanoparticles and the veil resulted in a more homogeneous distribution of the resin during the curing process.

Moreover, the relatively small regions of resin residuals visible on the magnesium interface surfaces (see Figure 7-15(e)) suggest that the delamination initiated and propagated mainly at the interface between the magnesium skins and the resin layer. Please note the relatively darker colour regions of resin residuals that can be seen in two cases (i.e., Figure 7-15(g-h)). The two cases correspond to the specimens that were prepared by the SBC bonding method and containing GNPs (i.e., specimens C and CA). The darker colour is believed to represent regions with a higher concentration (agglomeration) of nanoparticles developed in specimens that contained GNP only in the coating and in both coating and adhesive, respectively.
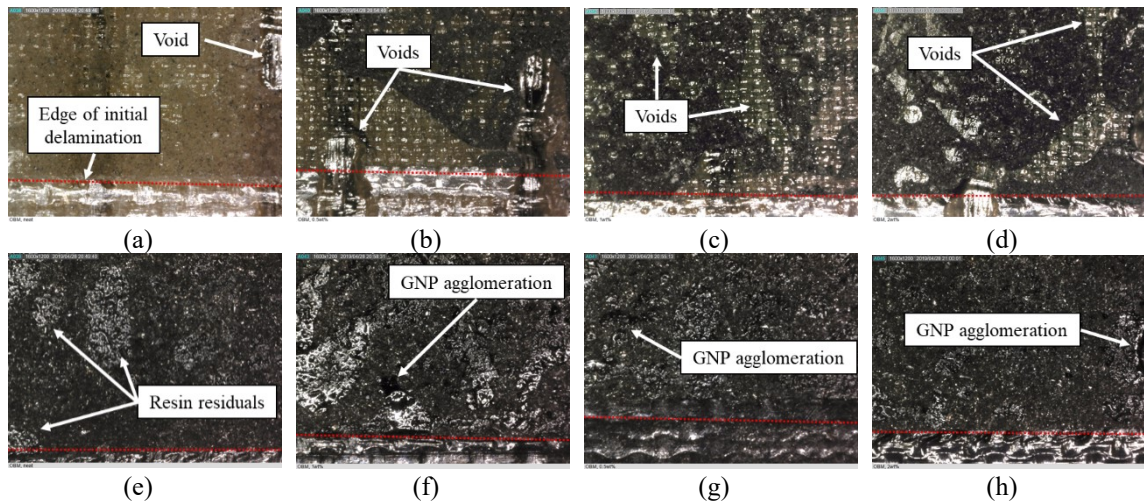
Figure 7-14. Magnified views of the adherends' fracture surfaces for specimens of case study I. Images (a) to (d) show the adhesive interfacial surfaces, while images (e) to (h) show the magnesium interfacial surfaces. From left to right: neat specimens and specimens with 0.5 wt%, 1 wt%, and 2 wt% GNP contents.

Overall, the failure falls under interfacial type classification, even when the new SBC bonding method was used to prepare the interfaces. This would suggest that, under the present circumstances, one could gain only a marginal enhancement as a result of the inclusion of nanoparticles in the interface unless one could generate a stronger bond between the epoxy adhesive, as a result of which the failure mode is changed from interfacial to cohesive failure. In comparison, more consistent and relatively substantive improvements could be gained by the inclusion of the more cost-effective fiberglass veil in the interface.

Furthermore, Figure 7-14(e-h) illustrate darker magnesium bonding surfaces, which are believed to have occurred as a result of the chemical reaction initiated by the elevated temperature caused during the curing process of the adhesive. The new suggested bonding method mitigates this issue since a cold-cured adhesive is used instead, which is believed to improve the interface compatibility, thus increasing the interface strength of the specimens of case study II.
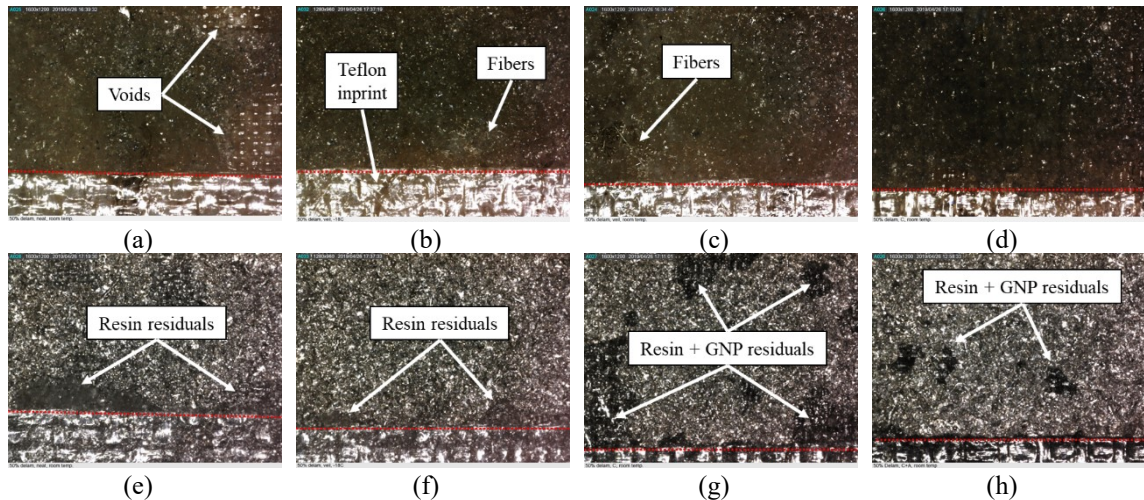
Figure 7-15. Magnified views of the adherends' fracture surfaces for specimens of case study II. Images (a) to (d) show the adhesive interfacial surfaces, while images (e) to (h) show the magnesium interfacial surfaces. From left to right: specimens "N", "V", "C" and "CA".

Finally, the delamination behaviour can be seen from Figure 7-16. The initial delamination (left side of the picture) clearly propagates along the magnesium skin, without deviating from it. Furthermore, the tip of the delamination kinks towards the magnesium at the initial stage of the propagation. This is in accordance with the numerical simulations

run by the authors in a previous study, using the extended finite element method (De Cicco & Taheri, 2018a) and reported in Chapter 9.
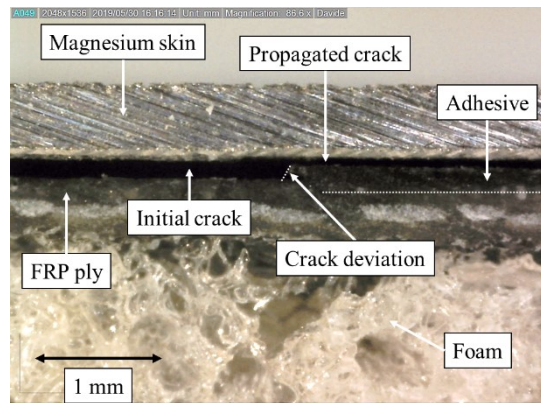
Figure 7-16. Close view of the delamination starting point.

7.5. Summary and Conclusion

A systematic investigation was conducted to examine the effect of graphene nanoplatelets (GNPs) used to reinforce a structural epoxy resin. The resin was used to mate the magnesium skins and composite core of a recently developed 3D fiber-metal laminate (3D-FML). The response of the resin and interface strength in the 3D-FML specimens were evaluated by subjecting the specimens to compressive loading at quasi-static and impact loading rates. Therefore, the impact buckling strength, delamination buckling strength, and delamination propagation were used as the evaluation criteria in this study. Two different techniques were used to join the skins to the FRP core. In the first method, the skins were directly bonded to the core using a hot-cured structural resin, with the mating skins surfaces prepared by the conventional abrasive (sandblasting) method. In the second method, a cold-cured less expensive structural resin was used, and a newly developed resin coating method was employed for preparing the skins' mating surface. The specimens prepared using the first technique (i.e., case study I specimens), were axially impacted at four energies (1.5 J. 3 J, 4.5 J and 7 J). Two different case studies were organized to examine the effect of initial delamination present in such 3D-FMLs by considering intact specimens and specimens with an initial delamination length of 30%, 50% and 70% (percentiles refer to the ratio of delamination length to specimen gage length). Moreover, GNP contents of 0.5 wt%, 1 wt%

and 2 wt% were used to reinforce the resin in this study. The results form the first case study can be summarized as follows:

- The presence of initial delamination greatly affected the load-bearing capacity of the specimens, but its length had a negligible effect;
- For the intact specimens (i.e., with no initial delamination), the incorporation of GNPs showed its maximum enhancing effect when the specimens were subjected to the highest impact energy (7 J). The observed enhancements were 12.5%, 10.9%, and 10.7% corresponding to GNP contents of 0.5 wt%, 1 wt%, and 2 wt%, respectively. Ironically, a degradation of the strength was noted in specimens that were subjected to 4.5 J impact energy.
- Among the specimens that hosted an initial delamination, the specimens that were reinforced with 0.5 wt% of GNP content exhibited the most gain in strength under three out of the four impact energies tried. The exception was the specimens that were subjected to 4.5 J impact energy, for which 2 wt% GNP content produced the best results.
- Microscopic examination revealed the existence of some voids at the bonding interface of the 3D-FMLs

To further explore the effect of GNP inclusion on the performance of the magnesium/FRP interface (and overall 3D-FML), additional case studies were considered. In the second case study, the specimens had the optimum GNP content of 0.5 wt%, with a fixed initial delamination of 50%, all tested under 2.85 J impact energy. The outcome of this case study is summarized as follows:

- The delamination propagated in an unstable manner.
- A higher GNP content led to a higher delamination length, with a 100% increase in delamination growth observed in the CA specimens.
  The use of a fiberglass veil interleaved between the magnesium and the FRP core mitigated the delamination extension by an average of 46% and increased the load-bearing capacity by 6%;

- The GNPs inclusion produced either no effect on the load capacity of most specimens or led to even negative effect in some (a reduction of 8% was observed in the CA specimens);

- The void content in the bonding region was drastically reduced when the SBC method was employed and voids were completely nullified when the veil or GNPs were incorporated within the interface; nonetheless, the delamination growth persisted owing to the lack of optimal chemical compatibility between magnesium and epoxy resin.

Further investigation was carried out in a case study (III) examining the effect of sub-freezing temperature (-50°C) on the delamination buckling and propagation of the 3D-FML and the effect of GNP inclusion. The specimens within this case study were tested under a quasi-static loading rate. The results are summarized as follows:

- The specimens' apparent stiffness increased when exposed to the sub-freezing temperature.

- The buckling load capacity was positively affected by the sub-freezing temperature, especially when the veil was used.

- The sub-freezing environment caused an increase in delamination growth, especially in the GNP-reinforced specimens.

Overall, it can be concluded that some improvement in performances could be gained by incorporating GNPs in the interface of the 3D-FMLs; however, one could also expect degradation of the performance under certain circumstances. In comparison, incorporation of the fiberglass veil as demonstrated in this study would be a more effective and less costly means for enhancing the performance of 3D-FMLs under in-plane compressive loading. Not only is the cost of the veil lower than that of GNPs, but the labor cost associated with its incorporation would be much less than that required for processing GNPs into resin. Moreover, a cheaper resin could be used when the veil is incorporated in the interface.

Finally, the lack of the expected gain in performance as a result of reinforcing the resin with GNP is believed to be due to the lack of chemical compatibility between the resin and magnesium. The incompatibility does not allow the GNPs to demonstrate their full

potential in enhancing the strength of the interface resin. This is mainly because the failure along the interface is in the interfacial mode (failure or resin/magnesium interface), as opposed to being of a cohesive type. Therefore, it is strongly believed that the future works should focus on improving the chemical compatibility between the resin and magnesium. Based on the results of this study and those reported in the literature, it is strongly believed that once the interface compatibility issue is resolved, the incorporation of nanoparticles will positively and significantly influence the interface strength and hence the overall performance of 3D-FMLs when subject to in-plane loadings.

7.6. Acknowledgments

Chapter 8: Performances of Magnesium- and Steel-based 3D Fiber-Metal Laminates Under Various Loading Conditions

Davide De Cicco and Farid Taheri

8.1. Abstract

The marriage of composites and metals is becoming an increasingly popular approach for obtaining resilient and lightweight materials. Our research group recently combined a 3D fiberglass/epoxy composite and thin magnesium sheets to render a significantly more effective and resilient light-weight material system. We are now interested in evaluating the feasibility of using steel as an alternative to magnesium due to the widespread use of steel in the automobile industry. Therefore, in this paper, the static buckling, impulse buckling, post-buckling, and lateral impact performances of the magnesium-based and steel-based 3D fiber-metal laminates (3D-FML) are systematically investigated and compared.

8.2. Introduction

[…]

However, as mentioned previously, the most commonly used material for the construction of such components has been, and still is, steel alloy. Therefore, the objective of this study is to evaluate the integrity of a 3D-FML whose magnesium skins are replaced by equivalent sheets of high-strength steel alloy and compare the two types FMLs' performances under various critical loading states. In other words, the static buckling, impulse buckling, post-buckling and axial impact responses of the 3D-FMLs will be systematically assessed.

8.3. Materials and Procedure

8.3.1. Materials

Two types of resins were used in this study. The first one was a room-cured structural epoxy system (105 resin and 206 hardener) by West System (Bay City, MI, US). This resin was used to mate the metallic sheets to FRP constituents of the FML. The other resin was hot-cured, two-part structural Araldite epoxy (LY1546 resin and Aradur 2954 hardener), which was acquired from Huntsman Co. (West Point, GA, US). This resin was used to impregnate the 3D fiberglass fabric, which was purchased from China Beihai Fiberglass Co. Ltd. (Jiujiang City, Jiangxi, China). In addition, a polyurethane foam was obtained from US Composites (Palm Beach, FL, US), which was used to fill the cavities of the 3D-fabric. The magnesium sheets were 0.5-mm thick AZ31B-H24 magnesium alloy, obtained from MetalMart (Commerce, CA, US), while the Precision Brand (Downers Grove, IL, US) 0.1-mm thick shim stock steel was acquired locally.

8.3.2. Specimens Manufacturing

All specimens, sketched in Figure 8-1, were extracted from 3D-FML plates fabricated following the same procedure regardless of skin material used. A water-cooled saw, equipped with a diamond-blade, was used to extract the specimens from the fabricated plates based on the required dimensions, i.e., 190 mm x 20 mm rectangular specimens used in the static and impact buckling tests, and 100 mm x 100 mm rectangular specimens used in the lateral impact tests. The specimens with magnesium sheets have a total thickness of 5.3 mm, while those with steel sheets have a total thickness of 4.4 mm. Three specimens were used in each individual test.

The manufacturing method is as follows. The metal skins were first wiped with acetone, then sandblasted using 20-30 grit size crushed glass. The dust residues were removed with compressed air followed by acetone wiping. The metal surfaces were, then, coated by a thin layer of cold cure epoxy resin and let curing at room temperature under full vacuum for 24 h. Note that this is a necessary step for promoting adhesion of

magnesium to FRP, which was developed in our previous research and discussed in detail in (De Cicco & Taheri, 2019). It should be noted that adhering magnesium to FRP presents serious challenges that cannot be overcome by the traditionally used surface preparation techniques, including those suggested by reference (The Adhesives Design Toolkit, n.d.). In parallel, the core component of the 3D-FML was processed by impregnating the 3D fiberglass fabric (3D-FGF) with the hot-cured epoxy resin, applied by brush. The impregnated fabric was cured in an oven at 60°C for 2 h, then at 120°C for 8 h. The resulting 4-mm thick composite will be referred to as 3D-glass fiber reinforced polymer, or 3D-GFRP. Its cavities were filled with the polyurethane foam, providing additional stiffness to the fabric, and were let fully cure for 24 h. Finally, the metal sheets were bonded to the composite core using the room-cured epoxy resin as the adhesive (hence FML). To ensure a strong bond between the components, the vacuum bagging process was used. The specimens were left four days under vacuum to reach the maximum strength (per West System resin's manufacturer instructions).
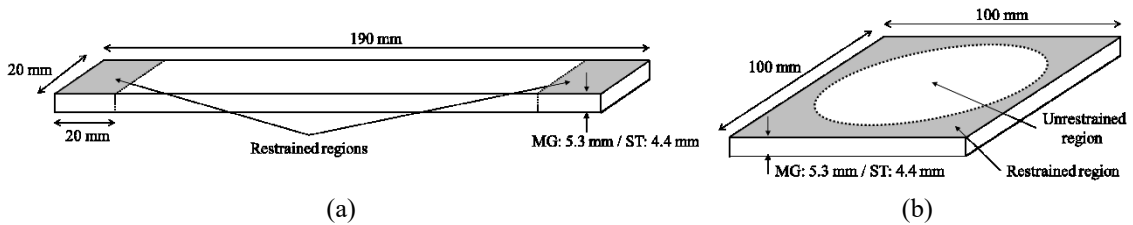
Figure 8-1. Configurations of (a) the static buckling and axial impact test specimens, and (b) lateral impact test specimens (drawings are not to scale).

8.3.3. Testing Apparatus

8.3.3.1. Static Buckling Test Apparatus

Static buckling tests were performed using an MTS servo-hydraulic testing machine, equipped with a 250 kN load cell. This testing scheme was selected because it subjects the weakest link of 3D-FMLs (i.e., the interface bond between metal sheets and 3D-GFRP core) to one of the harshest states of stress since it includes both Mode I and Mode II fracture loading states. The internal software, MTS793, was used to control the machine and obtain the load and displacement data. A Dino-Lite digital microscope was used to record the testing event at a rate of one frame per second. Fixed-fixed boundary conditions

155

were obtained by placing the specimens in a specially designed fixture that restrained rotation and translation of a given specimen's ends, allowing only axial translation at the other end of the specimen. Also, clamping tabs were made of aluminum and had a 45° chamfer to minimize the stress concentration generated by the clamping force. The compressive load was applied in displacement-controlled mode at a speed of 0.5 mm/min. The setup is shown in Figure 8-2, and the reader is invited to refer to reference (De Cicco & Taheri, 2016) for a more detailed description of the apparatus.
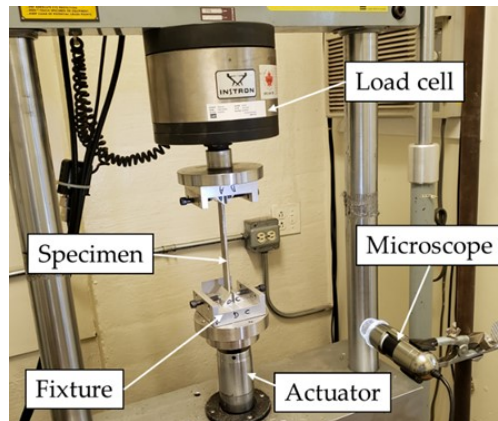
Figure 8-2. Static buckling experimental setup.

8.3.3.2. Impact Buckling and Lateral Impact Test Apparatus

Impact tests were performed using the modified Charpy impact test equipment shown in Figure 8-3(a). The system consisted of a pendulum bearing some weights, a 5.7 kg impactor tup mounted on a rail with minimal friction, and a fixture-jig to hold the specimens in place. In the case of lateral impact, this fixture consisted of two 13 mm-thick steel plates with a central hole of 85 mm, between which the specimens would be sandwiched, as shown in Figure 8-3(b). The impacting tup was made of steel and had a 16 mm-diameter hemispherical tip. In the case of axial impact tests, as shown in Figure 8-3(c), specimens were set into grips that mimicked fixed-fixed boundary conditions; note that, one of the grips was permitted to displace in the longitudinal (axial) direction of the impacted specimens. Moreover, the impactor tup was a 52 mm-diameter flat steel cylinder. In a given test, the tup impacted one of the grips holding the specimens, thus, not directly hitting an actual specimen's end. A more detailed description of the setups can be found in (De Cicco et al., 2016; De Cicco & Taheri, 2018b).

156
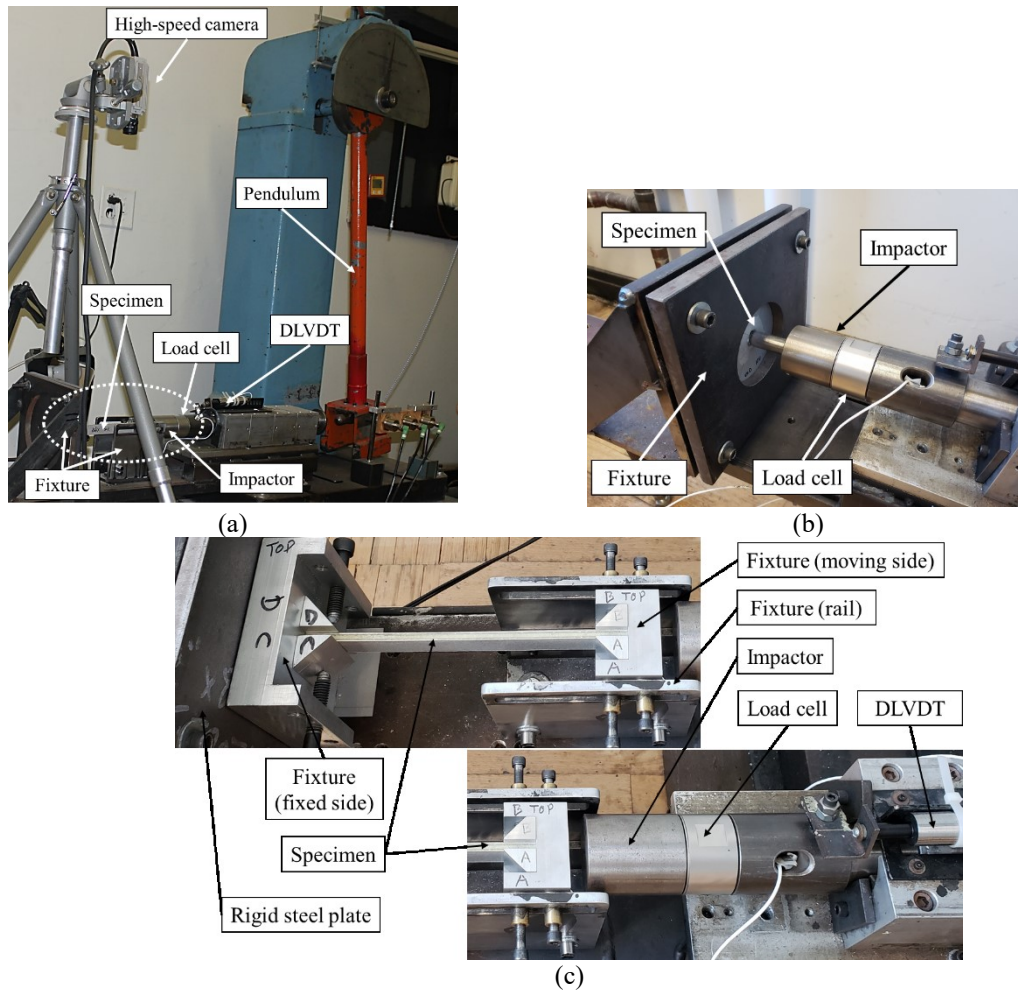
Figure 8-3. Impact test setup: (a) overall view of the testing machine, (b) close-up view of the lateral impact fixture, and (c) close-up view of the axial impact fixture.

The impact energy could be changed by swinging the pendulum from a pre-defined angle. The release angles were obtained based on a trial-and-error approach, developing impact energy of 20 J for the case of lateral impact, and 10 J for the axial impact tests. In each test, the displacement at impact location and the corresponding load data was obtained by incorporating a dynamic linearly variable differential transformer (DLVDT) and a dynamic load cell, respectively. The data was collected at a rate of 50 kHz for accurate detection of peak force. This data was, then, processed using a custom-made LabVIEW code, facilitating efficient data processing and ensuring the consistency of the results. Moreover, a Krontech Chronos high-speed camera was used to record the impact buckling tests, at a rate of 4,489 fps.

8.4. Results and Discussion

8.4.1. Static Buckling

The qualitative description of the static buckling behaviour of the specimens is reported in Figure 8-4. The magnesium-based specimens (hereafter referred to as MG) remained straight during the first stage of the compressive loading until the buckling capacity was reached. After this stage, the resulting curvature in the central section subjected the MG skins to compression on one side and tension on the other side. This was followed by the localized delamination and buckling of the skin on the compression side. In the case of steel-based specimens (hereafter referred to as ST), wrinkling of the skins was observed before the occurrence of the global buckling of the specimen. The subsequent global buckling led to a progressively more pronounced wrinkling of the metallic skins in the compression surface. Moreover, it should be noted that, as can be seen from the figures, the wrinkling propagated on the compression-side over the entire length of the specimens.

(a)   (b)
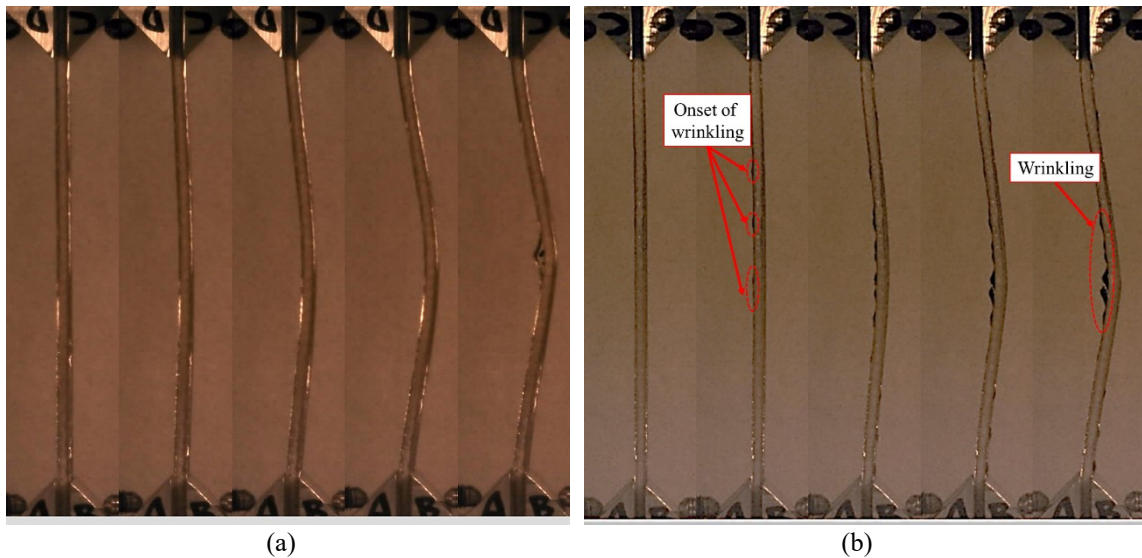
Figure 8-4. (a) MG- and (b) ST-based specimens' buckling response under static loading.

A more detailed view of the wrinkling developed on the skins of the ST specimens is reported in Figure 8-5. Note that wrinkles develop a maximum amplitude on the edge of the specimens and do not extend along the entire width of the specimens, stopping nearing the mid-width. Also, there is asymmetry of the wrinkle pattern on one surface, even though

all the wrinkles are similar in shape and size, while no such pronounced asymmetry is observed on the other surface. This suggests that the delamination wrinkling is also significantly influenced by the imbalance of in-plane and out-of-plane shear stresses developed near the free edges, leading to premature and localized delamination of the skins at the edges of the specimens. In fact, this is a more complex wrinkling behaviour than that described in (Zenkert, 1997) because of the three-dimensional effect, and should be explored further through a series of dedicated experiments in the future.
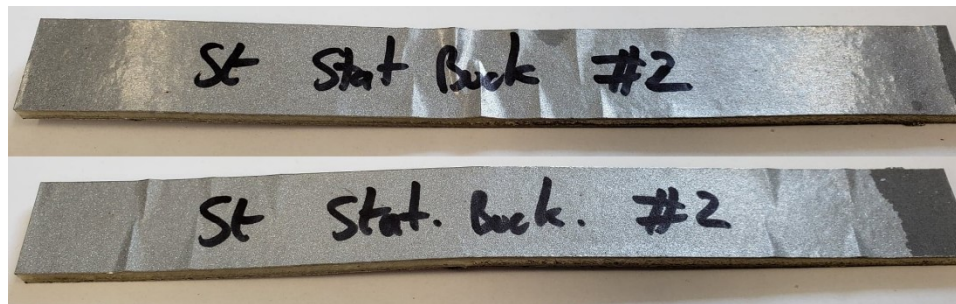
Figure 8-5. Wrinkling patterns developed on the steel skins after the onset of static buckling. Pictures show both sides of the same specimen.

The quantitative results are presented in Figure 8-6 in the form of load-axial shortening curves. For both MG and ST specimens, three tests were performed and were all reported to demonstrate the consistency of the results. As can be seen, there is a similarity in their overall behaviour; in other words, the specimen exhibits a linear trend for the first part, and then, after the onset of buckling, the load-bearing capacity is diminished gradually. Once the shortening values become greater, one sees a further drop in the load capacity, which is caused by the localized delamination of the skins. Note that the latter phenomenon is more pronounced for the MG specimens because of a more sudden delamination response compared to the ST specimens, which exhibited more progressive wrinkling. So, comparatively, there is a clear difference in the response between the MG and ST specimens; however, when the initial stiffness is considered, it is 50% lower in the case of ST specimens when compared to MG specimens. This behaviour was not expected since the specimens were designed to have the same bending stiffness. Further analysis revealed the presence of delamination at the location where the specimen ends were in contact with the grips.

159

In addition, numerical analysis, based on the methodology described in an earlier work of the authors (De Cicco & Taheri, 2017), was utilized to gain a better understanding of the phenomenon. In brief, the 3D-FML specimens were modelled with the finite element software LS-DYNA using a single layer of thin shell elements, subjected to quasi-static axial compression. The element is capable of accounting for the mechanical properties of all the constituents (i.e., the two magnesium skins, the fiberglass plies and the foam/pillars core). The *PART_COMPOSITE option of LS-DYNA facilitates the allocation of different materials based on the locations of the through-thickness integration points. The constituent materials of the 3D-FML were modelled as follows: the magnesium skins were modelled using a piecewise linear plasticity model, the fiberglass plies were modelled using a composite model with the Chang-Chang failure criterion, while the foam was modelled using a layered linear plasticity model, since the crushable foam model is not compatible with the *PART_COMPOSITE option. The pre-buckling and post-buckling responses were obtained using the arc-length algorithm and were compared to our experimental results to establish their integrity. The numerical results, reported in Figure 8-6, indicate that the two different type specimens should have exhibited the same initial stiffness, which also corroborates with the results obtained by the analytical solution. The numerical results also agree favourably to the experimental results of MG specimens. Therefore, lower than expected stiffness exhibited by the ST specimens may be due to two observed factors; i.e., (i) the progressive wrinkling of the skins and (ii) the potential unanticipated delamination caused by the grips. To fully understand this phenomenon, a more focus study is necessary.
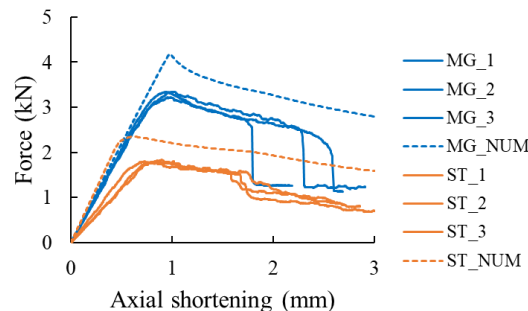
Figure 8-6. Load vs. axial shortening curves of the specimens tested under static compressive loading, including the numerically predicted results.

Another difference between the two sets of specimens is their load-bearing capacity. As predicted by the numerical simulations, the experimental curves in Figure 8-6 show that MG specimens have 82% higher buckling capacity than the ST ones. The load-axial shortening curves also show that buckling does not lead to the total failure of the specimens, and that load-bearing capacity diminishes gradually after the onset of buckling. Note that the tests were stopped after 3 mm of axial shortening had taken effect in the ST specimens since the maximum load capacity and skin delamination would both be reached under such loading condition. Also, worth mentioning is that the final failure of the specimens was concluded by the failure of the 3D-GFRP's bidirectional fabric on the side that underwent compressive stress. It should be noted that the ST specimens buckled at a lower load than the MG specimens, which was also corroborated with the numerical simulation outcomes. Hence, considering that the same imperfection amplitude was used to initiate the buckling, it may be concluded that a small imperfection has more influence on the slender steel specimens than the thicker magnesium specimens. Therefore, the use of magnesium would be beneficial in obtaining thicker specimens without an increased weight.

8.4.2. Impact Buckling

Similar to the static buckling analysis, the qualitative and quantitative comparisons of the performance of magnesium- and steel-based specimens were carried out. The deformed shapes under impact are reported in Figure 8-7. From a qualitative point of view, the MG specimens' behaviour is virtually identical to that observed under static loading (i.e., the specimens were slightly compressed axially while remaining straight and then buckled). However, the skins did not delaminate under the impact loading, though the specimens permanently deformed due to yielding of its magnesium skiIn the ST specimens, extensive wrinkling of the metallic skins occurred on both surfaces of the specimens before the onset of bending or global buckling. The global buckling took place after the faces underwent wrinkling, indicating that the buckling limit was mostly governed by the FRP skins and that the metallic skins had a limited influence on the global buckling capacity. Because less energy could be absorbed by ST specimens before buckling in comparison to MG specimens, ST specimens underwent additional compression, which ultimately led to the failure of the FRP ply in compression. Consequently, the damage in ST specimens was not

161

limited to a slight yielding of the faces but affected the core part of the 3D-FML. This phenomenon would have significant implications on actual structures formed by such an FML since components made of MG-based FML, that encounter such a loading condition, may survive and be considered as structurally sound or repairable, while the same would not hold for the ST-based FML structural components.

In the ST specimens, extensive wrinkling of the metallic skins occurred on both surfaces of the specimens before the onset of bending or global buckling. The global buckling took place after the faces underwent wrinkling, indicating that the buckling limit was mostly governed by the FRP skins and that the metallic skins had a limited influence on the global buckling capacity. Because less energy could be absorbed by ST specimens before buckling in comparison to MG specimens, ST specimens underwent additional compression, which ultimately led to the failure of the FRP ply in compression. Consequently, the damage in ST specimens was not limited to a slight yielding of the faces but affected the core part of the 3D-FML. This phenomenon would have significant implications on actual structures formed by such an FML since components made of MG-based FML, that encounter such a loading condition, may survive and be considered as structurally sound or repairable, while the same would not hold for the ST-based FML structural components.

Another interesting observation obtained from the high-speed images shown in Figure 8-7 is that the amplitude of the wrinkles seems to be slightly more pronounced on the half-span opposite to the impacted side. This behaviour also differs from the one observed in the static case, where the wrinkles were more centrally located along the specimens' length. This behaviour is commonly seen during the impact buckling of thin metallic members as reported in (Lindberg & Florence, 1987). Moreover, as observed in the static case, the wrinkles developed on the ST specimens is shown in more detail in Figure 8-8. The same pattern is visible; that is, wrinkling is asymmetric on one surface, with more delamination towards the edges of the specimens, while for the static case, the wrinkles were developed only in the zone where the skins were subjected to compression. Moreover, in such cases, the wrinkles were more widely extended along the specimen. In addition, the wavelength

of the wrinkles is generally shorter in the impact case, which is similar to the observations reported in (Lindberg & Florence, 1987).

(a)

(b)
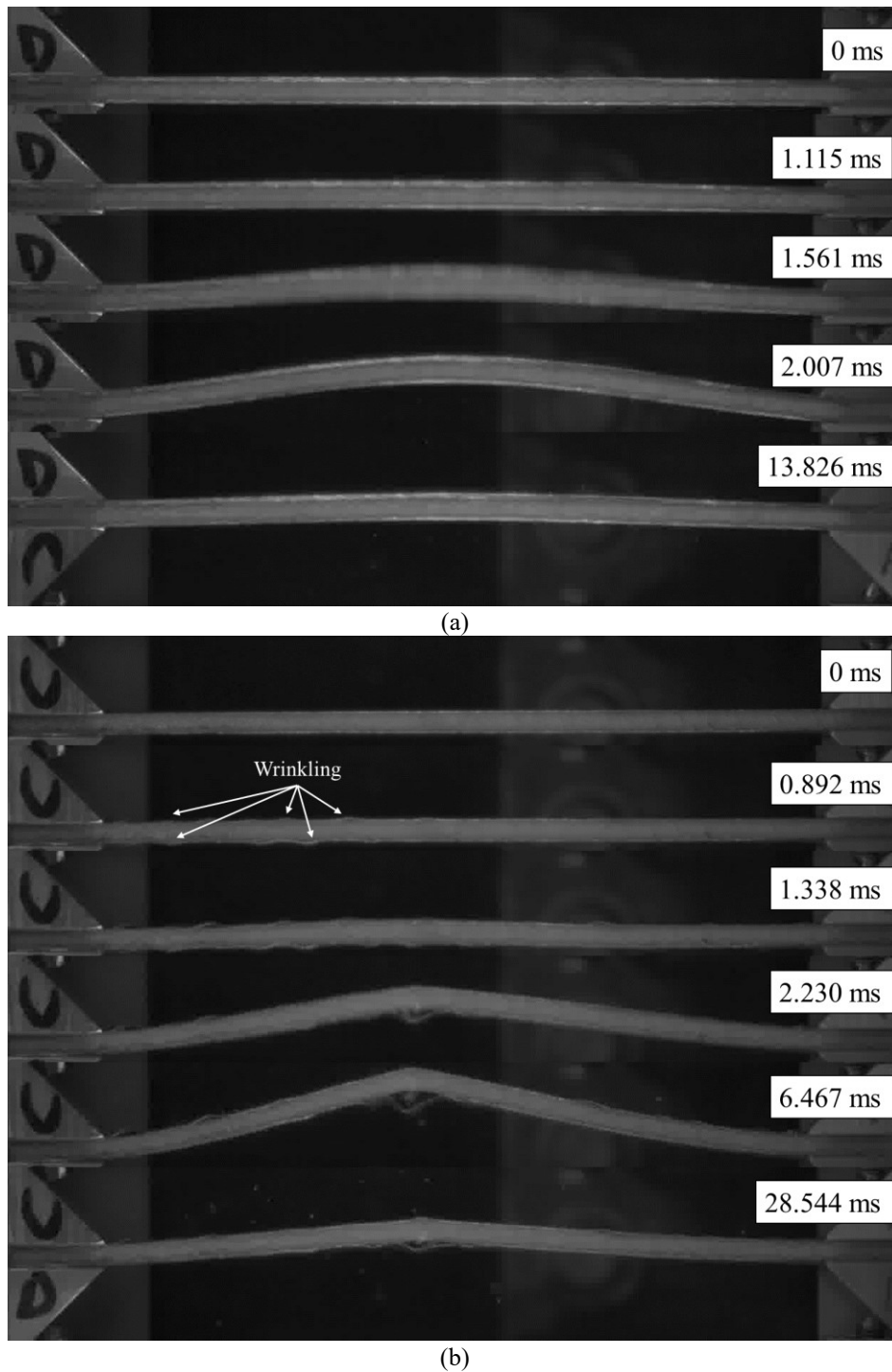
Figure 8-7. Deformed shapes of the (a) MG-based and (b) ST-based specimens, subjected to axial impact.
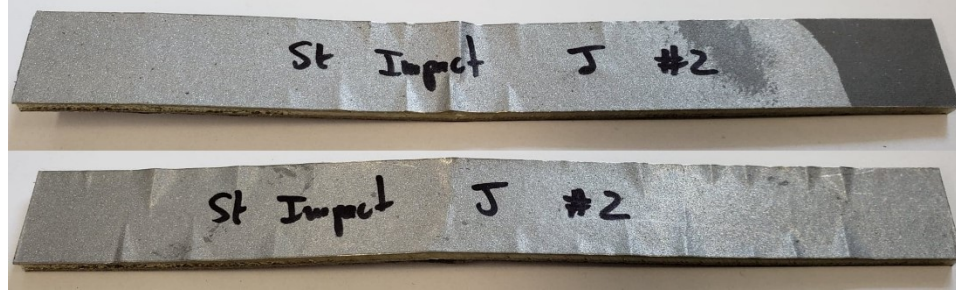
Figure 8-8. Typical wrinkling patterns developed on the steel skins after axial impact. Pictures show both sides of the same specimen.

The superiority of the MG-based specimens can also be seen qualitatively from the graphs shown in Figure 8-9. It should be noted that the load-axial shortening curves of Figure 8-9(b) were obtained using the root mean square (RMS) of the load-time signal. This approach was adopted in order to obtain a more explicit and clear view of the differences in behaviours of MG- and ST-based specimens. As clearly visible from Figure 8-9(a), the oscillations due to the vibratory motion of the specimen are attenuated, while the energy of the signal remains the same. From the load-axial shortening curves, it can be seen that the stiffness of the MG and ST specimens are very similar. Also, the load-bearing capacity of MG specimens is higher than ST specimens by 31%. Note that one would obtain the same value if one had used the original signals instead of the RMS. Moreover, although there are significant oscillations near the end portion of the MG-based curves, it would indicate that specimens behave in an elastic way and push the impactor back, therefore exhibiting potential additional energy absorption capacity. This is also shown by the slightly descending portion of the energy-time graph in Figure 8-9(c). Comparatively, the reduction in the load-carrying capacity is smaller in the case of MG specimens (i.e., an average of 2.5 kN load was carried by the specimens before the impactor bounced back). In contrast, in ST specimens' case, the load capacity was reduced to 1 kN after the impact event. The overall superior performance of the MG specimens can also be seen from the data reported in Figure 8-10, which tabulates the normalized maximum load capacity obtained for the two FML configuration under static and impact loadings, with the static capacity of the MG specimens taken as reference. It should be noted that the RMS values were used to generate the chart because they essentially represent the worst-case scenarios.
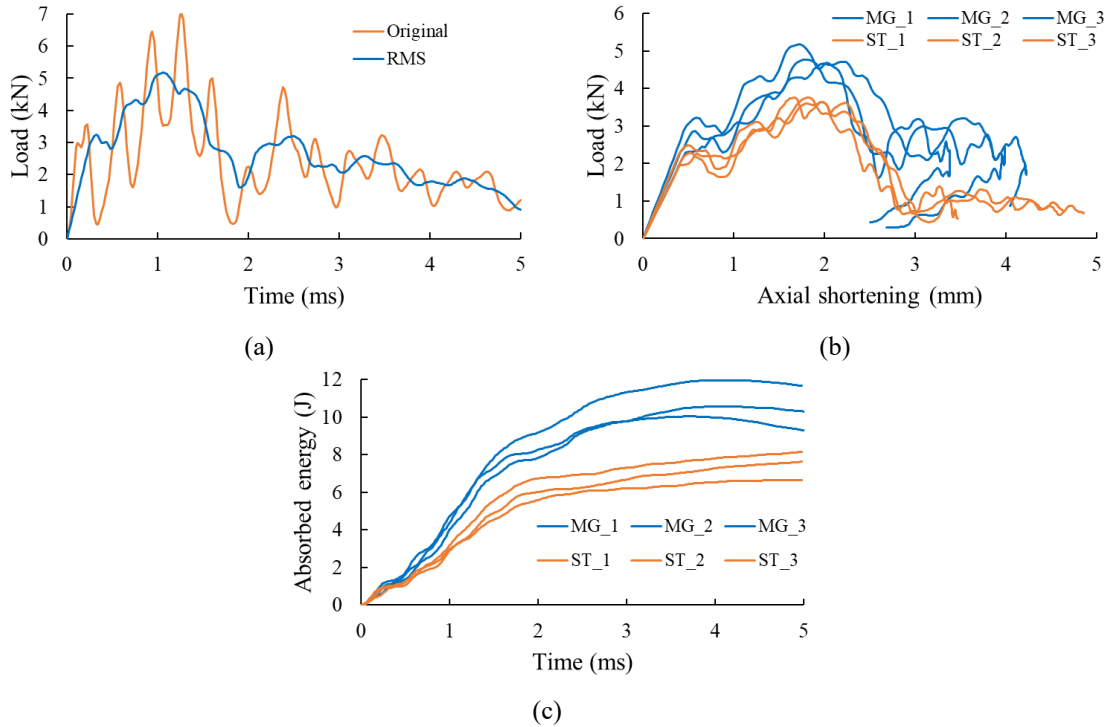
Figure 8-9. (a) The original and RMS curves of the load-time data, (b) load-axial shortening curves using the RMS signals, and (c) absorbed energy-time curves.
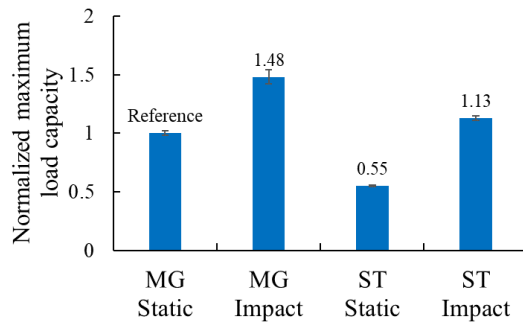
Figure 8-10. Comparison of the ultimate load capacities of MG- and ST-based FML specimens subject to static and impact loading.

8.4.3. Justification of the Wrinkling Phenomenon

To gain a better understanding of why the ST specimens exhibited face wrinkling while MG specimens did not, one could refer to Zenkert (1997), who stated that the critical stress, σ^{cr}, that leads to the wrinkling of the faces of a sandwich structure could be evaluated by:

$$\sigma^{cr} = 0.91\sqrt[3]{E_s E_c G_c} \tag{8-1}$$

where E_s and E_c are the moduli of elasticity of the sandwich skins and core, respectively, and G_c is the shear modulus of the core. In the context of the analytical solution and the 3D-FML under investigation, E_S would be the equivalent modulus of elasticity of the combined metal sheet (Mg or steel) and the bidirectional FRP plies that forms each surface of the 3D-GFRP, while E_C would be the equivalent (combined) modulus of elasticity of the constituents forming the core of the 3D-FML (i.e., the fiberglass pillars and the foam). Note that the formula considers sandwich materials with an isotropic core with a relatively low in-plane modulus, with the proviso that the core thickness should be such that any deformation in one skin would not be transmitted to the other skin. Furthermore, the core indentation (or the maximum displacement of the wrinkled wave) must be small compared to the half-thickness dimension of the core. In the case of our 3D-FML specimens, only the first condition is not fulfilled; however, for the purpose of this preliminary study, the anisotropy of the core is neglected. It should be noted that the accurate prediction of the phenomenon is not an objective of this research; we have, however, attempted to merely pinpoint a probable cause for the observed behaviour. We also realize that further analysis is warranted to fully and quantitatively characterize the wrinkling phenomenon.

From equation (8-1), the ratio between the critical stress developed in the steel skins, σ_{ST}^{cr}, and that developed in the magnesium skins, σ_{MG}^{cr} would be:

$$\frac{\sigma_{ST}^{cr}}{\sigma_{MG}^{cr}} = \frac{0.91\sqrt[3]{E_{ST} E_c G_c}}{0.91\sqrt[3]{E_{MG} E_c G_c}} = \sqrt[3]{\frac{E_{ST}}{E_{MG}}} = 1.8 \tag{8-2}$$

where the elastic properties of the constituents are reported in Table 8-1. Note that, as briefly described earlier, here the elastic moduli E_{ST} and E_{MG} represent the value of the equivalent modulus of respective constituents (i.e., steel/FRP and Mg/FRP), evaluated based on the rule-of-mixture. The obtained ratio of 1.8 signifies that the steel skins would require greater stress to undergo buckling compared to the magnesium skins. Furthermore, one can also estimate the stress ratio in the steel- and magnesium-based skins by using the

simple rule-of-mixture. If we consider the two configurations are subjected to the same magnitude of compressive load, then:

$$\sigma_{ST}A_{ST} + \sigma_c A_c = \sigma_{MG}A_{MG} + \sigma_c A_c \qquad (8\text{-}3)$$

with A_{ST}, A_{MG}, and A_c being the cross-sectional areas of the steel-based skins, the magnesium-based skins, and the core, respectively, while σ_{ST}, σ_{MG}, and σ_c are the compressive stresses within the three components. Using the material properties provided in Table 8-1, and knowing that the cross-sectional area of the FRP present in the skins is the same for both ST and MG cases, we have:

$$\sigma_{ST} = \frac{A_{MG}}{A_{ST}}\sigma_{MG} = 5\sigma_{MG} \qquad (8\text{-}4)$$

This shows that the stress in the steel-based skins would be five times higher than in the magnesium-based skins under a given load. Therefore, even though steel skins can withstand a 1.8 times greater stress, and having comparatively a lower slenderness ratio, they will micro-buckle (wrinkle) at an earlier stage.

Besides the above considerations, it is worth noting that the bending rigidity of the steel skins is 22.5 times lower than that of the magnesium skins due to their reduced thickness, which further promotes the manifestation of the wrinkling phenomenon.

Table 8-1. Material properties used in the numerical model.

	Magnesium	Steel	FRP	Core
E (GPa)	36	200	9	0.31
ν	0.35	0.3	0.254	0.07
Thickness (mm)	0.5	0.1	0.45	3.7
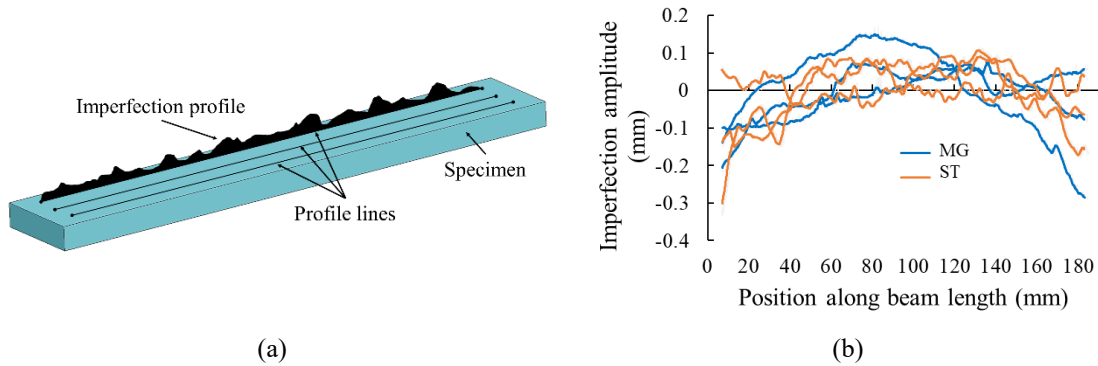
Figure 8-11. (a) Schematic showing the locations where the thickness imperfections were measured at; note that the drawn imperfection profile is not to scale. (b) Measured imperfection profiles of the MG- and ST-based 3D-FML specimens.

Furthermore, Zenkert (1997) has also mentioned that the theoretical critical wrinkling load is likely to be reduced by 80% if there are any initial imperfections in the skins. Therefore, here we investigated the out-of-plane imperfection amplitudes along the span of the specimens. The imperfections were measured using a Zeiss Duramax coordinate-measuring machine, along three profile paths along the longitudinal direction in each specimen. One of the three paths was taken at the centerline of the specimen, while the other two paths were along each side of the centerline, at a few millimeters away from the edges. The selected paths are shown in Figure 8-11(a), and the results are reported in Figure 8-11(b). The results show that the magnesium-based specimens had a smoother profile with a distinctive arc shape, indicating that the main imperfection was related to the global initial curvature inherent in each specimen, originated due to the fabrication procedure. For the steel-based specimens, a global curvature is also visible, but the variation is accompanied by significant fluctuations. This would indicate that the ST specimen's surfaces had more wavy imperfections when compared to the MG specimens. This issue, coupled with comparatively thinner skins, are believed to have contributed to the development of the wrinkling phenomenon discussed earlier. Moreover, it is also believed that the waviness of the thin steel skins was promoted due to the uneven nature of the 3D-fabric, which was invariably transferred to the thin steel skin during adhesion of the skins to fabric and the associated vacuum-bagging process. In contrast, the thicker magnesium skins could endure the negative pressure created by the vacuum-bagging process and were not affected by the inherent uneven surfaces of the 3D-fabric during the adhesion process.

8.4.4. Lateral Impact

The last parameter that was investigated in this study was the response of the two 3D-FML configurations subject to lateral impact. The typical responses are illustrated in Figure 8-12. Figure 8-12(a) and (b) show the impacted surface of the MG-based and ST-based specimens, respectively. The damage patterns are quite similar in the two configurations, consisting of a circular indentation with cracking of the metallic skin and crushing of the core; however, the diameter and depth of the indentation are greater in the case of ST-based specimens. As can be seen, in the case of MG specimens, the non-impacted side skin cracked, with the crack developed in the same direction as the rolling direction of the magnesium sheet, though being barely visible. In the case of the ST specimen, two perpendicular cracks were created on the non-impacted side skin, causing the complete fracture and opening of the fracture section, making a portion of the core visible. As reported in Figure 8-13(a), where each crack length is normalized with respect to the crack length appeared on the impacted side of the MG specimens. As seen, the average crack lengths for both the impacted and non-impacted sides of the ST specimens are slightly longer (11%) than those developed on the MG specimens. Note that the illustrated observations do not reflect the extent of the damage, but only the length of the longest cracks.
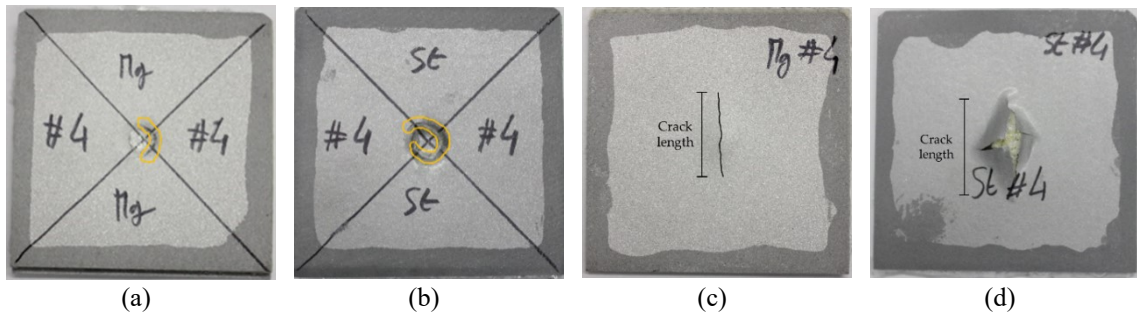
Figure 8-12. Typical failures patterns developed as a result of the lateral impact: (a) MG, impacted side; (b) ST, impacted side; (c) MG, non-impacted side; (d) ST, non-impacted side. The crack on the impacted side is highlighted in yellow.
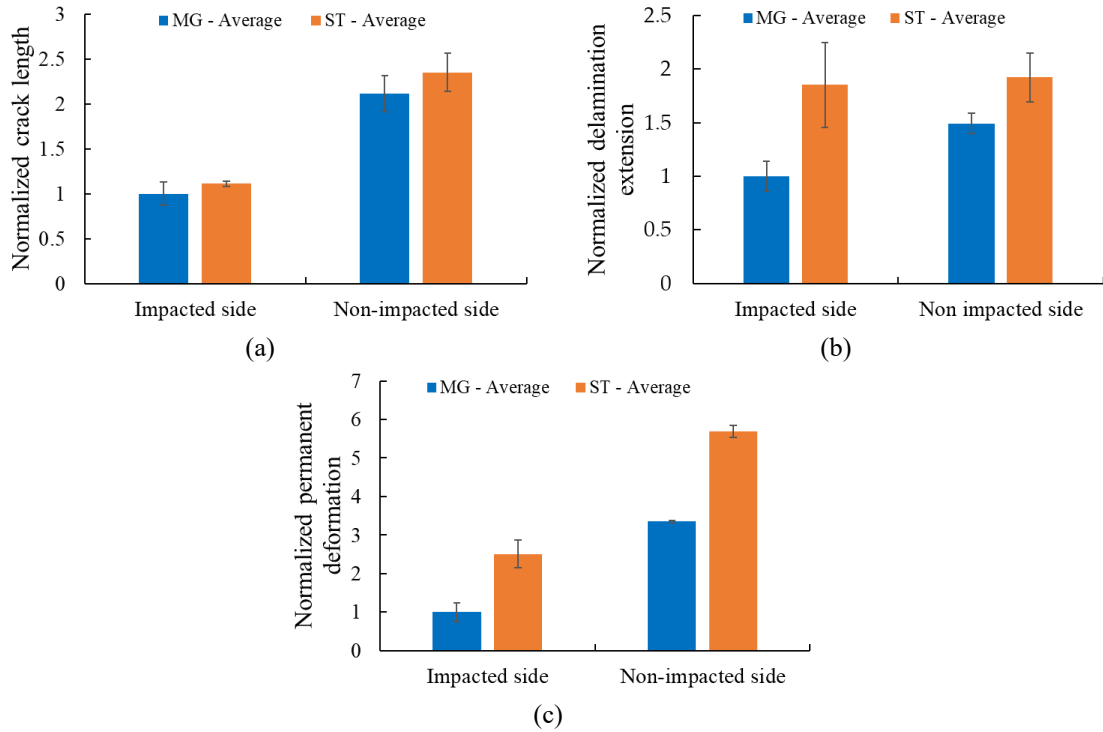
Figure 8-13. Normalized values of the (a) crack length, (b) delamination extension, and (c) permanent deformation for the MG-based and ST-based specimens.
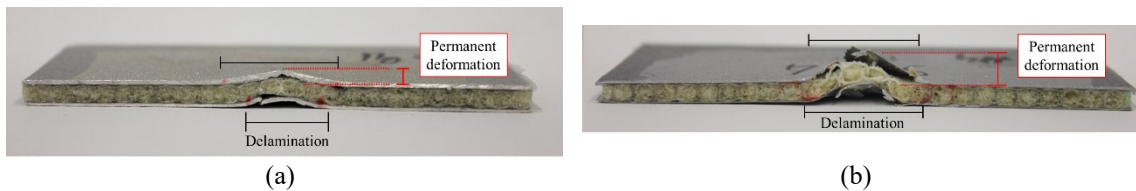
Figure 8-14. Sectioned views of the plates shown in Figure 8-12: (a) MG-based and (b) ST-based specimens.

To further explore the failure modes in the specimens, the specimens were sectioned at their mid-span. The sectioned views of the two configurations are illustrated in Figure 8-14(a) and (b), corresponding to MG and ST specimens, respectively. The section views clearly show the difference in damage extent, especially in the core, also revealing the extent of delaminations developed in the specimens. Indeed, the exploration of the extent of delamination in such hybrid composites is quite important, because in most practical cases, delamination in such composites could be undetectable visually. This, in turn, could significantly influence the longevity and cycle-life of structures formed by such materials. Here, the delamination was accurately measured on both impacted and non-impacted sides

170

for the two configurations; the specimens' cross-sections were analyzed using the Dino-Lite digital microscope to pinpoint the start and end of the delaminations. As one would expect, the extents of damage in the 3D-FML plates are not symmetrical; therefore, only the longest delaminations are reported in Figure 8-13(b). The values shown are normalized with respect to the delamination observed on the non-impacted side of magnesium-FML. Considering the impacted side, the ST specimens are found to be prone to delamination that extends in size 85% more than that observed in the MG specimens, while the difference becomes 29% when considering the non-impacted side. Therefore, the MG specimens have the advantage of containing the damage around the impacted zone, therefore reducing the risk of having undetected or invisible extended damage in the structure. Finally, the relative values of the measured permanent deformations of the specimens are reported in Figure 8-13(c). As it was done for the previous results, the values are normalized with respect to the average value of permanent deformation measured on the non-impacted side of the MG specimens. As can be seen, the deformations in the MG specimens are lower by 70% on the non-impacted side, and up to 150% on the impacted side compared to the ST specimens.
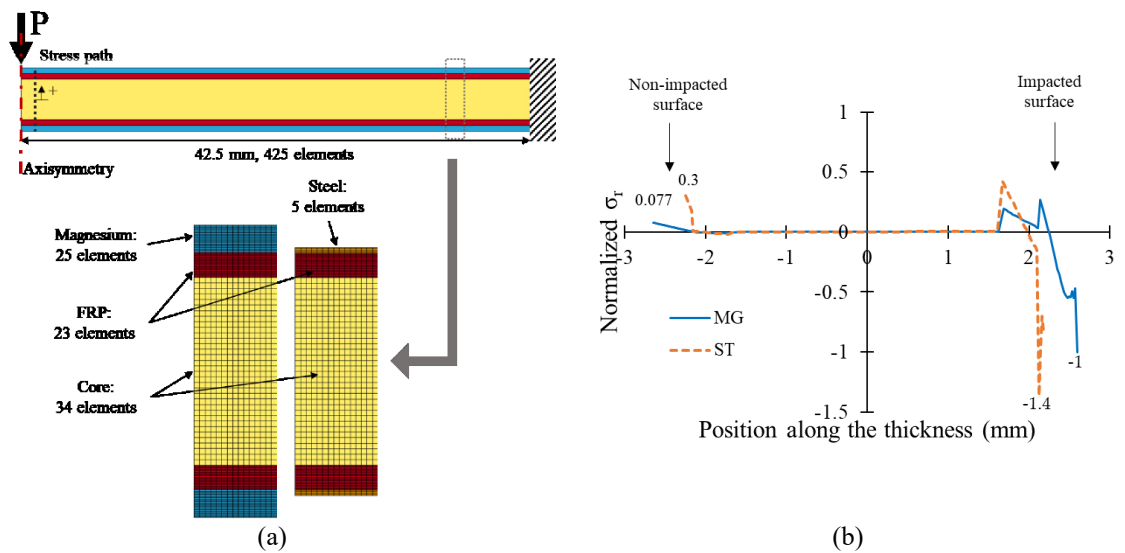
Figure 8-15. (a) Schematics of the model and its FE mesh. (b) Distribution of the normalized radial stresses along the specimen's thickness.

In an attempt to rationalize the difference in the damage extent observed for the two configurations, the simple linear elastic finite element model reported in Figure 8-15(a), and made available to the reader in Appendix B, was constructed using the LS-DYNA

software. The model includes three different components: the skins, the FRP plies, and the core part, which represents the 3D-GFRP's pillars and foam in a homogenized fashion. Each component (material) was modelled as an elastic, isotropic material, with the material properties, reported in Table 8-1, obtained from (De Cicco & Taheri, 2018b). The effect of the impactor was replaced by a concentrated force at the center of the specimen, and fully constrained boundary conditions were applied to the boundary nodes of the model to simulate the effect of the clamping restraint generated by the fixture. Furthermore, the geometry and boundary and loading conditions permitted us to model the system using axisymmetric elements. A very fine mesh was used so that the thin steel skins (i.e., the thinnest components) could be discretized using five layers of elements through-the-thickness. Note that the focus of the simulation is simply to highlight the difference in the generated stress magnitudes between the FMLs configured by MG and ST skins. To see a more complete, non-linear modelling approach used to model the response of the 3D-FML subjected to lateral impact, please consult Asaee et al. (Asaee et al., 2015; Asaee & Taheri, 2016).

The results of the analyzes in the form of distribution of the radial through-thickness stresses are reported in Figure 8-15(b) for both MG-FML and ST-FML specimens. The results are normalized with respect to the maximum stress developed in the MG-FML specimen (compressive in this case). As can be seen, the steel skins on the non-impacted surface experience up to four times more stress than the corresponding magnesium skin experience, while the strength of the steel sheets is just 2.8 times greater than that of the magnesium. On the impacted surface, the stress in the steel skins is 1.4 times greater than in the magnesium counterpart. It can also be seen that the stress in the FRP plies is greater in ST-FML specimens compared to the MG-FML specimens. These observations, therefore, provide an insight into why larger cracks were observed on the non-impacted surface of ST-FML specimens, accompanied by more extensive core damage in comparison to MG-FMLs.

8.5. Conclusion

Responses of two different configurations of 3D fiber-metal laminates (3D-FML) subject to static and axial compressive impact loadings, as well as lateral impact loading, are investigated and compared against one another. The two configurations of the 3D-FML differ by the type of metallic skins used in their formation; that is, magnesium-based (MG) and steel-based (ST). The findings of this investigation are summarized as follows:

- Even though the two 3D-FML configurations were designed to have the same bending stiffness, the static and impact buckling capacities of the MG-based specimens were found to be 82% and 31% greater than those of the ST-based specimens, respectively.

- The MG-based specimens that underwent static compressive loading developed localized delamination regions upon the onset of buckling, leading to a decrease in their load-bearing capacity. In contrast, the case of ST-based specimens, first wrinkling of the skins occurred, followed by global buckling of the specimens.

- Under an applied axial impact load, MG-based specimens were able to withstand a maximum of 7 J impact energy without any evidence of delamination of their metallic skins, while ST-based specimens completely delaminated and failed under the same magnitude of impact energy.

- The extents of delamination and damage produced by the lateral impact were greater in the ST-based specimens compared to MG-based specimens. This is attributed to the development of a higher magnitude of stresses developed in the skins. One can conclude that the relatively less stiff, but thicker magnesium skins would perform more effectively when such 3D-FMLs are subjected to impact loading.

Based on the findings of this study, the incorporation of thicker skins is recommended when fabricating such 3D-FMLs, as the thicker skins resist imperfection that could be induced by the inherent unevenness of the 3D glass fabric constituent of the FMLs. The equivalent ST-based specimens, having thinner skins compared to their MG-based

counterparts, were prone to more waviness caused by the glass fabric substrates, which in turn promoted wrinkling of the skins, thereby affecting their load-bearing capacity.

In summary, when designing a 3D-FML for a given stiffness, better performances could be attained by using relatively softer and thicker metallic skins as opposed to the use of stiffer and thinner skins. However, to establish the threshold of optimum performance, a detailed parametric study is warranted to examine the coupled effects of skin thickness and stiffness, with a special focus on minimization of skin wrinkling.

8.6. Acknowledgment

Chapter 9: Delamination Buckling and Crack Propagation Simulations in Fiber-Metal Laminates Using xFEM and Cohesive Elements

Davide De Cicco and Farid Taheri

9.1. Abstract

Simulation of fracture in fiber-reinforced plastics (FRPs) and hybrid composites is a challenging task. This paper investigates the potential of combining the extended finite element method (xFEM) and cohesive zone method (CZM), available through LS-DYNA commercial finite element software, for effectively modelling delamination buckling and crack propagation in fiber metal laminates (FMLs). The investigation includes modelling the response of the standard double cantilever beam test specimen, and delamination-buckling of a 3D-FML under axial impact loading. It is shown that the adopted approach could effectively simulate the complex state of crack propagation in such materials, which involves crack propagation within the adhesive layer along the interface, and its diversion from one interface to the other. The corroboration of the numerical predictions and actual experimental observations is also demonstrated. In addition, the limitations of these numerical methodologies are discussed.

9.2. Introduction

[…]

As stated, all the modelling facilities mentioned above are available in LS-DYNA. In this paper, we will focus on CZM and xFEM and, more precisely, on the possibility of combining them for conducting a more accurate modelling of crack propagation resulting from delamination buckling of a relatively complex 3D hybrid composite material (i.e., a new class of FML).

The authors are, therefore, interested in better understanding the response of 3D-FMLs under compressive impact loading, and the ensuing failure mechanism during their delamination buckling in order (i) to accurately predict their behaviour through numerical simulation and (ii) to enhance their load-carrying capacity of the 3D-FML by appropriate means.

9.3. Numerical Models

A systematic numerical investigation was conducted in this study, using a total of three different models in order to establish the integrity of the xFEM and CZM facilities of LS-DYNA. First, a model that was analyzed by another investigator (Tsuda et al., 2015) was tried to validate the integrity of our approach. Then, since the configuration of the materials forming our 3D-FML is relatively complex, it was decided to initially simulate the response of the standard double cantilever beam to further hone our skill in using the xFEM and calibrate the properties required for conducing such analysis. Finally, the response of a less-complex equivalent model of our 3D-FML material, subjected to an axial impact, was simulated.

As briefly mentioned, the first trial involved simulation of the response of a simply-supported rectangular cross-section cast iron beam specimen subjected to an impact load at its mid-span using xFEM. The parameters required for xFEM simulation of the specimen were extracted from reference (Tsuda et al., 2015). It should be noted that the efficient approach commonly used in simulating such simple 3D geometries is by modelling them as either 2D plane-stress or plane-strain geometry, depending on the aspect ratios of the specimen. Therefore, an attempt was made to simulate the beam's response by a plane-strain model. However, a convergent result could not be achieved when the xFEM was used in conjunction with the 2D plane strain element of LS-DYNA (even though LS-DYNA user-manual explicitly states admissibility of that element type in conjunction with xFEM). Consequently, LS-DYNA's shell elements (type 54 in conjunction with the fully integrated base element 16) were used to continue the modelling effort. It is reckoned that shell elements are not used conventionally to simulate such geometries (i.e., geometries with an appreciable thickness-to-depth ratio); nonetheless, an accurate fracture response

could be successfully predicted in comparison to the experimental results reported by Tsuda et al. (2015) (who incidentally used the same approach in modelling the specimen's response.) A detailed explanation of the modelling approach, as well as the discussion of the required parameters, are presented in the appendix section of this chapter. In addition, the value of the parameters used in our models are given in Table 9-1 of the appendix.

The simulated results confirmed the integrity of the selected algorithm and element type; thus, they were used in the subsequent phases of the analysis. However, before continuing with the remaining analyses, it warrants to discuss the material model and the required parameters that will be required when conducting xFEM modelling.

9.3.1. Material Model for Cohesive and xFEM Elements

In LS-DYNA, only one material model is currently available for use in conjunction with the xFEM formulation, which is: *MAT_COHESIVE_TH. This is a cohesive material law proposed by Tvergaard & Hutchinson (1992) with a tri-linear traction-separation behaviour (see Figure 9-1(a)), where the maximum traction stress and normal or tangential ultimate displacements are the governing and required parameters (LS-DYNA R9.0, 2016b). The model accepts only one value of the maximum stress; therefore, it could be either the maximum normal stress or maximum shear stress, accordingly. In this study, because mode I fracture is the dominant failure mode, the maximum tensile stress is chosen as the maximum stress governing the failure of the material. Note that the lack of differentiation between the maximum normal and shear stresses is an important limitation of this model.

This cohesive model is based on the non-dimensional parameters λ_1, λ_2, and λ_{fail}, defining the traction-separation law behaviour, as shown in Figure 9-1. These parameters correspond to various segments of the traction-separation curve (i.e., the peak traction, the beginning of softening segment, and the final failure, respectively). In other words, these parameters are used to represent a measure of the global dimensionless separation, λ, mathematically represented for the two-dimensional case as follows:

$$\lambda = \sqrt{\left(\frac{\langle \delta_N \rangle}{\delta_N^{fail}}\right)^2 + \left(\frac{\delta_T}{\delta_T^{fail}}\right)^2} \tag{9-1}$$

where δ_N and δ_T are the normal and tangent separation displacements, δ_N^{fail} and δ_T^{fail} are the respective separation values at failure, and the operator $\langle \cdot \rangle$ refers to the Mc-Cauley brackets, used to differentiate the behaviour under tension and compression.

The stress state is computed, using the trilinear traction-separation law parameters (see Figure 9-1), as follows:

$$\sigma(\lambda) = \begin{cases} \sigma_{max} \dfrac{\lambda}{\lambda_1/\lambda_{fail}}, & \lambda < \lambda_1/\lambda_{fail}; \\[3ex] \sigma_{max}, & \lambda_1/\lambda_{fail} < \lambda < \lambda_2/\lambda_{fail} \\[3ex] \sigma_{max} \dfrac{1-\lambda}{1-\lambda_2/\lambda_{fail}}, & \lambda_1/\lambda_{fail} < \lambda < 1; \end{cases} \tag{9-2}$$

where σ_{max} refers to the maximum tensile or shear stress, as mentioned previously.

Using a potential function, φ, defined as:

$$\varphi(\delta_N, \delta_T) = \delta_N^{fail} \int_0^\lambda \sigma(\hat{\lambda}) d\hat{\lambda}, \tag{9-3}$$

and the normal surface traction, σ_N, and the tangential surface traction, σ_T, are expressed by the following derivatives:

$$\sigma_N = \frac{\partial \varphi}{\partial \delta_N}, \qquad \sigma_T = \frac{\partial \varphi}{\partial \delta_T}, \tag{9-4}$$

Finally, the development of the derivatives leads to the traction vector, expressed as:

$$\begin{Bmatrix} \sigma_N \\ \sigma_T \end{Bmatrix} = \frac{\sigma(\lambda)}{\lambda} \begin{bmatrix} \dfrac{1}{\lambda_N^{fail}} & 0 \\ 0 & \dfrac{1}{\lambda_T^{fail}} \end{bmatrix} \begin{Bmatrix} \langle \delta_N \rangle \\ \delta_T \end{Bmatrix} \tag{9-5}$$

This model is totally reversible, in other words, the loading and unloading follow the same path. In addition, the difference in behaviour between tension and compression is accounted for, with the following equation describing the behaviour for $\delta_N < 0$:

$$\sigma_N = \kappa \frac{\sigma_{max}}{\delta_N^{fail} \lambda_1 \big/ \lambda_{fail}} \delta_N \tag{9-6}$$

where κ is the penetration stiffness multiplier, defined by the user.

As mentioned previously, the tri-linear behaviour is controlled by the three non-dimensional parameters, which affect term $\mathcal{A}$ in the following equation. These parameters are related to the material's fracture toughness, G_{IC} or G_{IIC} in the following manner:

$$G_{iC} = \mathcal{A}\delta_i \tag{9-7}$$

where the subscript "i" relates to the normal or tangential directions and $\mathcal{A}$ is the area under the normalized traction-separation curve (see Figure 9-1(a,b)).

The cohesive parameters used in this investigation, as reported in the Appendix, were obtained by calibrating the trial values in such a way that the numerical simulation-produced results would closely match the results obtained through the actual testing of the double cantilever beam (DCB) specimen, using the load-opening curve as the criterion, as shown in Figure 9-1(c). It should be noted that the experimental test data of DCB was obtained under a static loading, while the simulation of the 3D-FML specimen of our interest, as will be presented later, was carried out when the specimen was subjected to an impact loading state; therefore, there would be some discrepancies between the evaluated values and those exhibited by the actual specimen dynamically. The establishment of the CZM parameters as explained is based on matching the overall behaviour, which would not include while the fluctuations that could potentially develop locally. However, in this

paper, the authors' intent is to demonstrate the feasibility of the described method, not its accuracy. The selected calibration method is meant to simply establish the values of the cohesive zone's parameters used to facilitate the simulation. Moreover, the xFEM formulation is currently only available under the dynamic, explicit solution scheme of LS-DYNA. Therefore, to ensure a reasonable solution time, all the simulations were run in dynamic mode, with the simulated event being in the order of a millisecond.

| (a) | (b) | (c) |
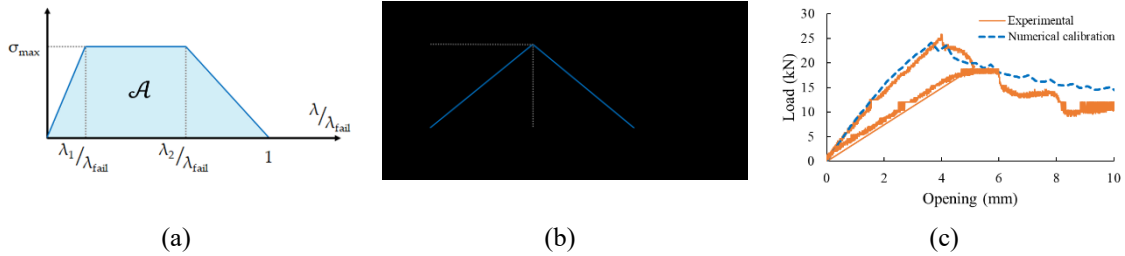
Figure 9-1. (a) Representation of the traction-separation law of the *COHESIVE_TH material model, and (b) the bi-linear traction-separation cohesive model used in this investigation. Note that $\mathcal{A}$ refers to the total area under the curve. (c) the load-opening curves of the double cantilever beam (DCB) experimental test used for establishing the cohesive zone method (CZM) parameters.

It is also worth mentioning that, during the calibration, no significant difference was found when reducing the tri-linear law to a bi-linear one (see Figure 9-1(b)), which facilitates a more CPU-efficient numerical solution. Consequently, λ_1 and λ_2 were both set to 0.5, thereby reducing the tri-linear model to a bi-linear model. Note that some researchers (Guo & Wu, 2010; Sam et al., 2005) have recommended the use of an initially-rigid cohesive law (i.e., $\lambda_1 = \lambda_2 \cong 0$) for obtaining a more reliable estimation of the state of stress prior to the onset of a crack. However, numerical instabilities were encountered when the approach was adopted in this study. Moreover, this is not to say that adaptation of the tri-linear law and/or the initially rigid cohesive response would lead to similar issues when simulating other cases. It should be noted that the main objective of the study presented here is to demonstrate the potential of the xFEM method in simulating the response of a complex material system under a relatively complex loading state, as opposed to targeting the degree of accuracy that could be attained when using the technique. Consequently, no further calibration effort was expended towards this issue.

Finally, as mentioned earlier, this cohesive model is the only one available for use within xFEM in LS-DYNA. Therefore, for the sake of consistency, this model was also

used with the cohesive elements, even though other cohesive models are available that could potentially produce more accurate predictions in the case of mixed mode fracture.

9.3.2. xFEM's Formulation

Here, a brief description of the xFEM formulation is presented. Consider a domain, noted Ω, that includes a crack represented by a surface discontinuity $\partial\Omega$, as shown in Figure 9-2. In xFEM, the following distance function (i.e., the function mapping the position of the closest points to the discontinuity), is used to represent the crack in Ω:

$$f(\underline{x}) = \min_{\underline{x} \in \partial\Omega} \|\underline{x} - \hat{\underline{x}}\| \, \text{sign}[\underline{n} \cdot (\underline{x} - \hat{\underline{x}})] \tag{9-8}$$

where $\underline{x}$ is the position vector, $\hat{\underline{x}}$ is the position of the closest point that is projected onto the discontinuity surface $\partial\Omega$, and $\underline{n}$ is the unity vector normal to $\partial\Omega$. Therefore, the discontinuity is represented by $f(\underline{x}) = 0$, and the sign of the function refers to each part of the domain, with positivity determined by $\underline{n}$.

In order to account for the presence of the discontinuity, the element formulation is enriched for the elements concerned by the crack. Let I be the set of all the nodes within the domain Ω and J be the set of all the nodes belonging to the enriched elements, excluding the one containing the crack tip, which is assigned to the set K. The nodal variable (e.g., displacement) can, therefore, be represented by (Tsuda et al., 2015):

$$\underline{u}(\underline{x}) = \sum_{i \in I \backslash (J \cup K)} N_i(\underline{x})\underline{u}_i + \sum_{i \in J} N_i^*(\underline{x})\underline{u}_i^* + \sum_{i \in K} N_i^{**}(\underline{x})\underline{u}_i^{**} \tag{9-9}$$

where $\underline{u}_i$, $\underline{u}_i^*$ and $\underline{u}_i^{**}$) are the regular and enriched nodal variables and N_i, N_i^* and N_i^{**}) are the regular and enriched shape functions. The enriched shape functions are as follow:

$$N_i^* = N_i \left[H\left(f(\underline{x})\right) + H\left(f(\underline{x}_i)\right) \right], \tag{9-10}$$

and

$$N_i^{**} = N_i \sum_{k=1}^{4} [\beta_k(\underline{x}) - \beta_k(\underline{x}_i)], \qquad (9\text{-}11)$$

where H is the Heaviside function and $\beta(r,\theta) = \left\{ \sqrt{r} \cos\frac{\theta}{2}, \sqrt{r} \sin\frac{\theta}{2}, \sqrt{r} \sin\theta \sin\frac{\theta}{2}, \sqrt{r} \sin\theta \cos\frac{\theta}{2} \right\}$, with r and θ given in Figure 9-2.

Note that the previously defined cohesive material behaviour is used to obtain the crack opening displacement, and either the maximum principal stress or the maximum shear stress can be used as a criterion to establish the onset of crack propagation and its direction (noting that the former criterion is used in our models). When the criterion is reached within the element containing the current crack tip, the element is considered as failed and the crack tip is advanced by one element.
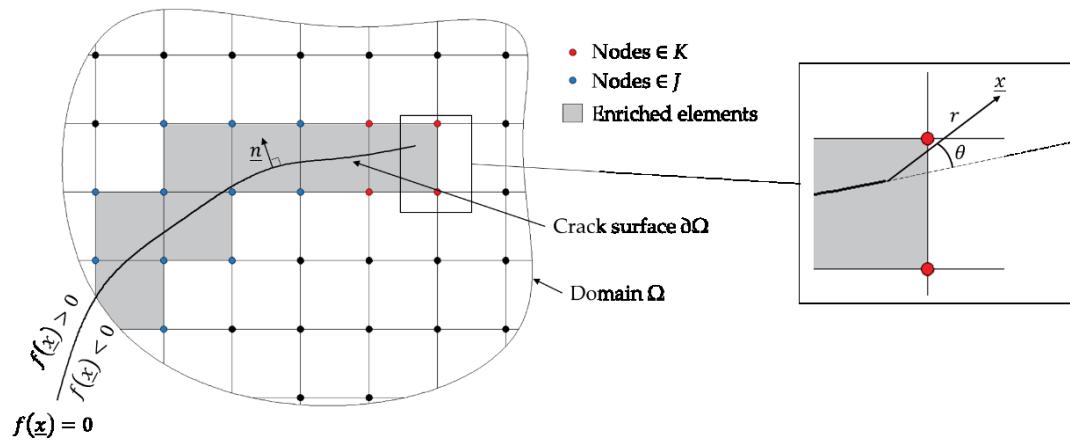
Figure 9-2. Illustration of the extended finite element method (xFEM) approach.

9.3.3. Double Cantilever Beam Model

The first of the two models, whose results are presented in this study, is the double cantilever beam (DCB), which is commonly used to assess the interlaminar fracture toughness of composite materials (ASTM Standard, 2014). The geometry and boundary conditions of this model, whose reduced input file enclosed in Appendix-B, are illustrated in Figure 9-3(a). This model was used to assess the feasibility of the contemporary use of xFEM and cohesive elements for modelling crack propagation within the adhesive layer bonding the two adherends of DCB. In addition, as briefly explained earlier, the case was

used to tune the materials properties that are required as input by both xFEM and cohesive elements.
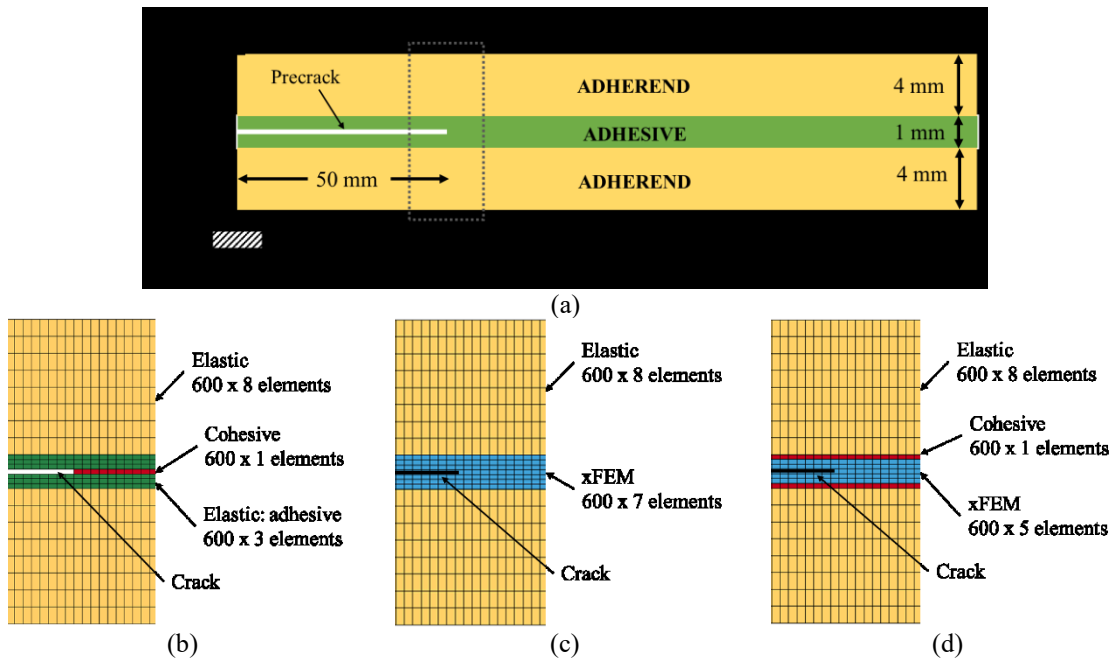
Figure 9-3. (a) DCB specimen's geometry, boundary conditions (not to scale), and zoom-up of the mesh around the crack-tip in the (b) COHESIVE model, (c) XFEM model, and (d) MIXED model.

The overall model's specimen dimensions are 150 mm x 25 mm x 9 mm, with the initial crack length of 50 mm embedded within the mid-plane of the adhesive, in one end of the specimen, (see Figure 9-3(a)). This model is a simplification of the hybrid composite used for the experimental tests, consisting of a hybrid magnesium sheet and FRP forming the upper adherend, and biaxial FRP forming the lower adherend. It should be noted that, to further simplify the analysis (without compromising the overall accuracy), each of the two 4-mm thick adherends was homogenized into an equivalent elastic material. In this way, the equivalent materials had the same flexural stiffness as the combined hybrid materials, but the analysis would consume significantly less CPU. The adopted scheme also facilitates more effective debugging. The 1-mm thick adhesive layer was modelled in three ways, by using (i) a combination of elastic and cohesive elements, as shown in Figure 9-3(b), (ii) xFEM elements only, as shown in Figure 9-3(c), and (iii) a combination of xFEM and cohesive elements, as shown in Figure 9-3(d). These models are referred to as COHESIVE, XFEM, and MIXED, respectively, hereafter. The same cohesive material model was used in conjunction with both cohesive and xFEM elements; moreover, the

xFEM elements were also assigned elastic model properties. In other words, the elements defined as xFEM would initially behave elastically until the stresses reach to a level at which xFEM's enrichment is activated, thereby using the assigned cohesive properties. It should be noted that one could also assign other material models (e.g., elasto-plastic) to the xFEM elements instead of the elastic model (Guo & Wu, 2010).

The generation of the precrack, for the XFEM and MIXED models, was done using the *BOUNDARY_PRECRACK keyword, which enriches the elements to account for the presence of an initial crack. Note that the conventional practice in fracture mechanics, that is, having a series of disconnected adjacent layers of elements to model the crack, cannot be used in conjunction with xFEM elements. This is because xFEM element formulation allows for the crack to propagate only within the element. For the COHESIVE case, however, the crack was generated as done conventionally, that is by simply deleting the appropriate number of elements corresponding to the location of the actual crack/delamination. Therefore, to maintain consistency of the results when comparing the results generated by the three models, only the elements forming a portion of the adhesive that would be cracking (i.e., at the midplane of adhesive) were modelled by the cohesive material model, while the remaining portions were modelled with the elastic model, hereafter referred to as "elastic element". This approach also saves CPU time.

Finally, the adhesive layer was discretized with seven layers of elements as shown in Figure 9-3 and its density was kept constant along the bond length. The mesh density was established upon conducting a convergence study by which a reasonable accuracy could be attained by consuming an optimal CPU time.

9.3.4. Delamination-Buckling Analysis

The delamination-buckling of an initially partially delaminated clamped-clamped fiber-metal laminate subjected to an axial impact was simulated, with the geometry and dimensions of the original sample reported in Figure 9-4(a). An equivalent simplified model, as shown in Figure 9-4(b), consisting of three components was constructed (the reduced input file is enclosed in Appendix B). The model consisted of a 0.5-mm thick

magnesium skin, a 0.5-mm thick adhesive layer, and a 2-mm thick fiberglass substrate. The symmetry in geometry and boundary conditions warranted modelling only one-half of the specimen, thus, reducing CPU computation. As shown in Figure 9-4(b), the transverse displacement (u_y) of the nodes located at the far-end of the specimen was restrained, and the same nodes were displaced at a rate of 1 m/s in the negative x-direction ($-u_x$), to simulate the applied impact. In addition, the rotation (in xy-plane) of the nodes were also restrained. This combination of restrains mimics the actual clamped boundary condition. As also shown in the figure, the symmetric boundary condition at the left end of the half-symmetry model was ensured by restraining the longitudinal displacement (u_x) and rotation about the y-axis at that location, while displacement in the transverse direction was permitted. Lastly, the out-of-plane displacement of all nodes (i.e., (u_z)) was restrained to guarantee a purely planar deformation.
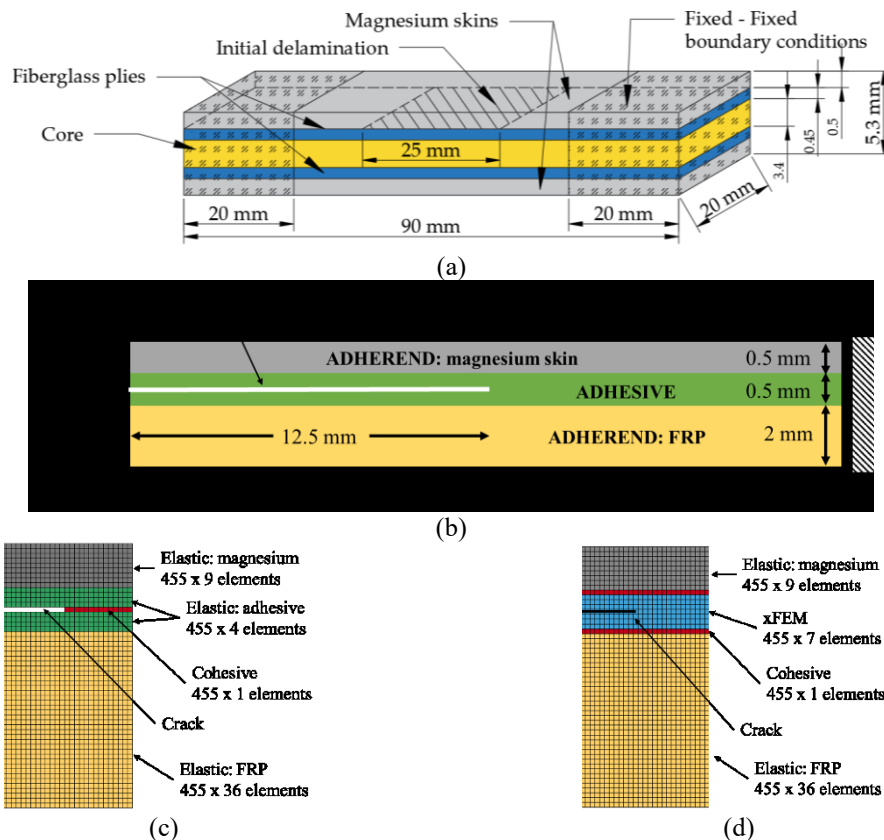
Figure 9-4. Geometry and boundary conditions of the partially delaminated fiber metal laminates (FML) specimen (not to scale): (a) sketch of the actual specimen (not to scale) (b) model used for numerical analysis, and the zoom-up views of the mesh around the delamination-tip in (c) the COHESIVE model and (d) the MIXED model.

185

Similar to the DCB specimen's model, the adherends of the FML were modelled using elastic elements, while the adhesive layer was modelled using (i) the cohesive element only and (ii) a combination of both xFEM and cohesive elements. Moreover, similar to the previous case-study, the models will be referred to as COHESIVE and MIXED. The XFEM model was not considered here because of the inconsistent results obtained when the xFEM element was used in modelling the DCB, as will be discussed in Section 9.3.1. Moreover, the adhesive thickness was assumed to be 0.5 mm, so to facilitate more discrete simulation of the influence of the through-thickness location of a crack within the adhesive layer. Therefore, the mesh, established based on a convergence study, has nine layers of elements through the thickness of the adhesive.

In addition, the upper and lower delaminated portions of the specimen were assumed to have a sinusoidal geometric imperfection with small amplitudes of 0.1 mm and −0.02 mm in the y-direction, respectively, to promote the instability and to ensure that the upper and lower adherends would deflect in two opposite directions.

9.4. Results and Discussion

9.4.1. Double Cantilever Beam Simulation Results

The simulations of the DCB were conducted to examine the feasibility and advantage of the proposed combined simulation methods (i.e., combined xFEM and cohesive elements). It is noted that the DCB tests were conducted under static loading scenario, which differs from the loading states our 3D-FML specimens were subjected to. However, as briefly stated earlier, the accuracy of the results is not a focus of this preliminary stage of our research, since the main objective was to examine the capabilities of the various approaches used here to model the crack propagation within a complex hybrid system subjected to a critical loading state (i.e., impact). The predicted crack propagation paths are reported in Figure 9-5. Note that LS-DYNA's post-processor exhibits the crack propagation path captured by XFEM models by a change in the elements' colour, while the deleted-element scheme exhibits the path in the case of COHESIVE models. In the COHESIVE model, as expected, the crack propagated in a straight path along the cohesive

elements. In the XFEM model, the crack did not propagate when the same magnitude of displacement as applied in the case of the COHESIVE model was used. However, upon the application of a greater magnitude of displacement (i.e., +45% for initiating the crack and +1132% at the end of calculations), the crack started propagating and deviated from its course towards the upper adherend/adhesive interface, travelling along that interface. At that stage, a second crack appeared at the initial kink location, propagating along the direction of the lower interface. It should be noted that the simulated crack propagation is not consistent with the experimental observations. Moreover, the resistance of crack to propagate led to an exaggerated opening of the delaminated portions of DCB when compared to the COHESIVE model.
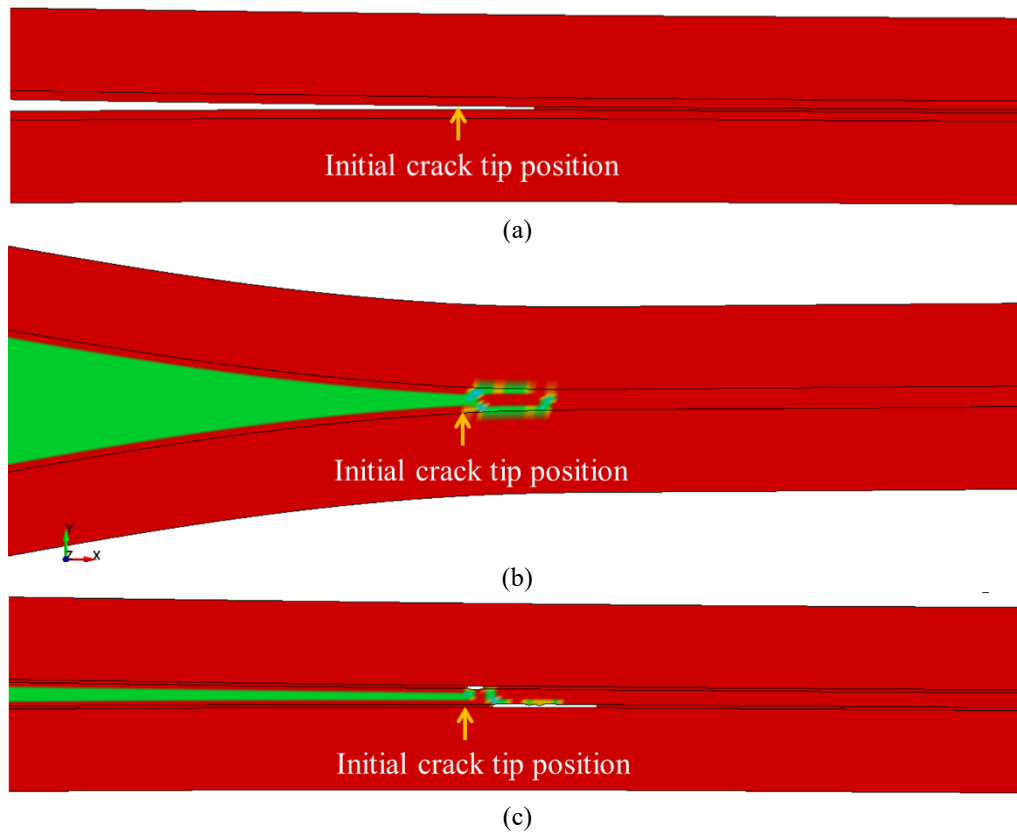
Figure 9-5. Qualitative comparison of the crack propagation under the DCB test predicted by the various models (a) COHESIVE, (b) XFEM, and (c) MIXED. For the sake of clarity, only the zone near the crack tip is shown.

It should be noted that, when a combination of the elements was used (i.e., the MIXED model), the resulting crack propagation path was found to be yet different, as shown in Figure 9-5(c). In that case, first the crack propagated through one element, and then it

diverted towards the upper interface and propagated along that interface. It subsequently changed its path towards the lower interface and traveled along that interface. The total length of propagation during the described event was limited to 6 mm, after which the simulation was halted due to computational issues caused by the development of a negative volume in one of the elements; nevertheless, the approach illustrates the potential of the method.

The initial stage of crack propagation obtained with the MIXED model is compared to that observed during the static testing of the DCB described in the previous section, as illustrated in Figure 9-6. Note that the tested adhesive layer of 1 mm is greater than the actual thickness of 0.2 mm used in the actual test. The change in the thickness had to be done to resolve the extremely fine mesh that would have been required, had we used the 0.2 mm thickness. In addition, it is necessary to mention that the hybrid DCB specimen was designed so that the difference in flexural stiffness between the two cantilever beam portions of DCB specimen was relatively equal (in fact, they differed by a mere 2%, and the variation of longitudinal strain induced by the applied load was limited to 8%). This unconventional DCB specimen was constructed for the sole purpose of being able to obtain satisfactory experimental data using the available 0.5-mm thin magnesium sheets. Therefore, one could appreciate that the qualitative results obtained through the presented model and the experimental results are comparable. The figure shows that the real crack deviated from its initial orientation towards the magnesium/adhesive interface, which is what the simulation captured. This kinking phenomenon can be captured by xFEM elements only, while in the case of the COHESIVE model, the crack had to follow the path occupied by the cohesive elements. The accuracy of the crack kinking captured by xFEM, however, will be discussed further in the following sections.

9.4.2. Delamination-Buckling Simulation Results

As mentioned previously, one of the main objectives of this study was to gain a better appreciation of the predictive capability of the described approaches in simulating a more complicated response. The interest was to determine whether the simulation techniques could capture the response of the 3D magnesium/FRP FML introduced earlier; specifically,

when the FML is subjected to an in-plane impact loading, which would potentially cause delamination buckling of its magnesium skins. In this phase of the study, the MIXED model's response is compared to that of the COHESIVE model, qualitatively (i.e., by comparison of the delamination propagation paths) and quantitatively (by comparison of the resulting axial-load shortening curves). The models consider the presence of a delamination (crack) located at the mid-plane, through-thickness of the adhesive. In addition, the effect of two parameters on the delamination behaviour is analyzed; the parameters are: (i) the through-thickness position of the delamination, and (ii) the ratio of the cohesive strength of the adhesive to the interfacial strength (i.e., the properties used in the xFEM and cohesive elements' material models).

(a)   (b)
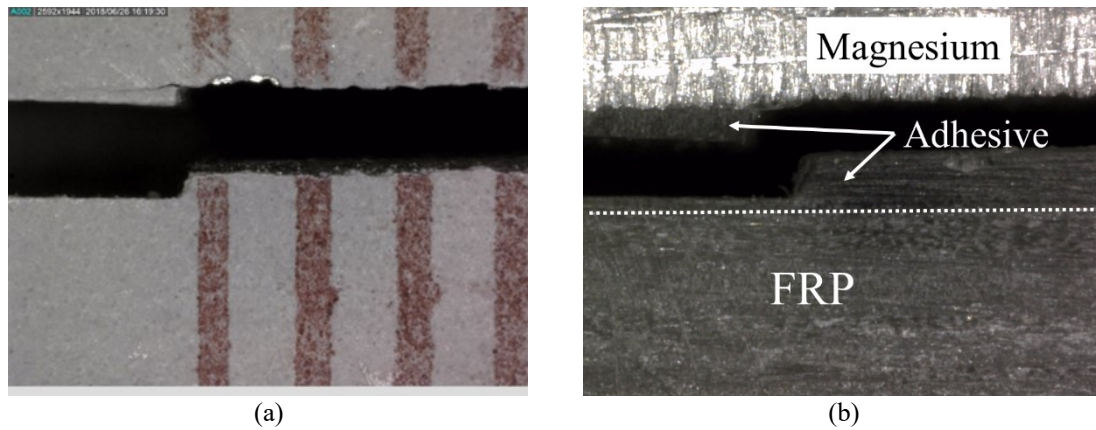
Figure 9-6. Close-up views of the crack propagation in the DCB, in which a magnesium skin is bonded to an epoxy/fiberglass composite, using a 0.2 mm thick layer of epoxy resin. Specimen (a) with the white coating used for monitoring crack propagation and (b) without the coating.

9.4.3. Influence of the Fracture Simulation Algorithms

The qualitative results are illustrated in Figure 9-7. The final delamination length captured by the COHESIVE model is 7.5% longer than that of the MIXED model, and the deflection of the delaminated skin is 10.5% greater, respectively. However, the deformed shapes are quite similar. The comparison of the axial-load shortening curves is presented in Figure 9-8. As seen, the two models predicted a similar response up to the stage when delamination starts propagating (i.e., when the elements are damaged but not yet failed); this stage corresponds to an axial shortening of approximately 0.12 mm. After that stage, the MIXED model depicted a stiffer response in comparison to the COHESIVE model.

189

The areas under the axial-load shortening curves, evaluated from the stage at which delamination starts propagating, which represent the impact resisting energies, are also compared. The comparison indicates that the specimen analyzed by the MIXED model could sustain 20% more energy than the one modelled by the COHESIVE model. Interestingly, this behaviour is opposite to what was reported by Curiel Sosa & Karapurath (2012), who showed that CZM has a tendency to overestimate fracture energy. The sustaining energies become closer to one another towards the end of the computation time. This is attributed to the presence of the residual stress captured by the xFEM elements. In other words, after xFEM elements fail, the stress inside the elements does not become null, which is in contrast to the behaviour exhibited by the cohesive elements. However, since the delamination continues propagating through the cohesive elements and the number of failed xFEM elements remains constant, the effect of the residual stress is reduced.
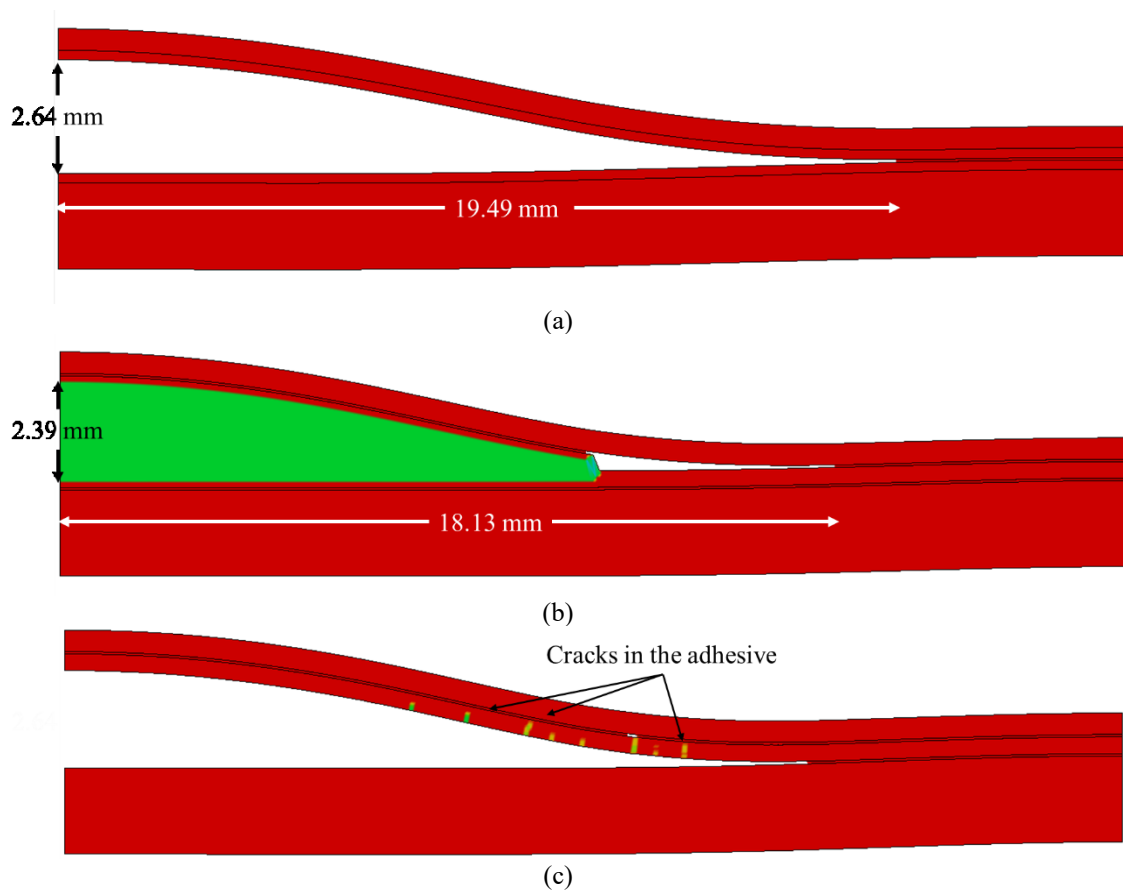
Figure 9-7. Delamination propagation and resulting deformed shapes captured by the (a) COHESIVE model, (b) MIXED model with initial delamination at the mid-height, and (c) MIXED model with initial delamination at the lower interface.
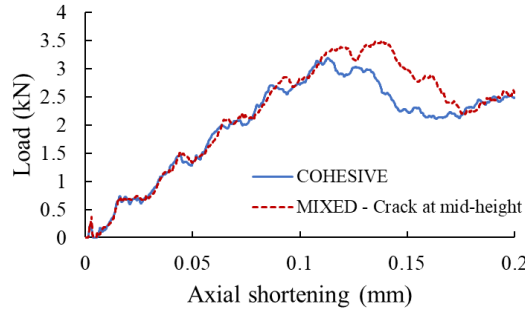
Figure 9-8. Axial-load shortening curve produced by COHESIVE and MIXED models.
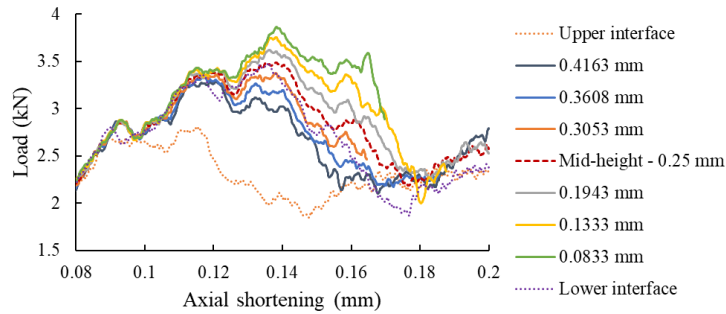
Figure 9-9. Axial-load shortening curves produced by the MIXED model for case studies having various through-thickness positions of the initial delamination. Note that the first portion of the graphs has been omitted for clarity, as it is the same for all the cases.

9.4.4. Influence of the Through-Thickness Position of Delamination

The analysis concerning the through-thickness position of the initial delamination, whose results are reported in Figure 9-9, indicates that a delamination located closer to the magnesium skin would lead to a lower load-sustaining capacity (apart from the cases where the delamination is located at any of the interfaces). This is attributed to a combination of factors. Firstly, the delamination path would become longer when it propagates towards the interface. Secondly, the skin will have higher apparent rigidity, because a thicker layer of resin is bonded to it. Lastly, a greater number of xFEM elements would have to be traversed by the delamination front, which would imply that there would be a higher number of elements with residual stress. The results, however, do not follow the mentioned pattern when the delamination is initiated within the cohesive elements. The lowest load

sustaining capacity is observed when the delamination is located at the upper interface; that is because no xFEM element is affected by the delamination. When the delamination is initiated at the lower interface, it does not propagate towards the upper interface, because the stress necessary for the delamination to kink is not attained. However, as can be seen from Figure 9-7(c), several cracks appear in the adhesive layer due to the bending (note that all the cracks are oriented normal to the delaminated surface); notwithstanding, experimental tests would be required to corroborate these findings.

Another important observation exposed by the result is that xFEM elements failed at a higher stress level in comparison to the cohesive elements, despite the fact that both element types were fed the same material properties (note that both cohesive and xFEM elements were described by the same bi-linear traction-separation law, cf. Section 9.3.1.). For practical applications, it is therefore recommended to consider a slightly larger traction when using the cohesive element in comparison to the xFEM element. The exact amount of the traction value would have to be established by tuning the numerical models with appropriate experimental data.

Another interesting phenomenon observed during this phase of the study is the change in the ensuing delamination kink angle. This angle is defined as the angle between a hypothetical non-kinked delamination path and the delamination orientation after it kinks, as shown in Figure 9-10(a). Note that for the reasons mentioned earlier, only the variation of the delamination in the xFEM elements could be considered.

| (a) | (b) |
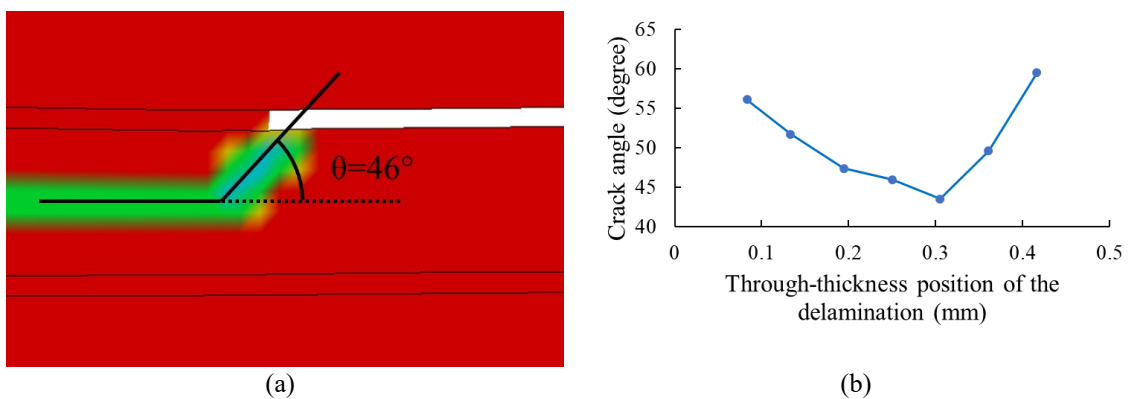
Figure 9-10. (a) Kinking of the delaminated front predicted by the MIXED model (initial delamination at the mid-height); (b) delamination kink angles for various through-thickness positions of the delamination, for the specimen under impact.

As seen from Figure 9-10(b), the closer the delamination is to the interfaces, the greater is the delamination kink angle (i.e., ~60°), while the minimum angle of 43° is observed when the delamination is located near the mid-thickness of the adhesive. This would indicate that, as the delamination becomes closer to an interface, its advancement will involve a greater presence of mode I compared to mode II. This is attributed to the stress state and the difference in the deformation responses of the relatively more flexible skins and the more rigid FRP core. Therefore, this could explain why an optimal surface preparation is of paramount importance for obtaining the maximum performance in such 3D-FMLs, in particular when the constituents bonded together have low chemical compatibility (such as in our case).

It should be noted that in another work that will be soon published, we proposed a new bonding technique for improving the interface adhesion strength between magnesium and fiber-reinforced epoxy composites. In that work, it is experimentally demonstrated that the overall observed improvement in the delamination-buckling response of 3D-FML was, in part, due to the transition of fracture from mode I to mixed mode. The numerical results presented here, therefore, has enabled us to gain a better understanding of the basis that facilitated the improved performances we observed experimentally.

9.4.5. Influence of the Strength Ratio and the Reference Strength

The choice of adhesive type is of primordial importance to guarantee a sound 3D-FML. However, an adhesive with excellent bonding capabilities may not have an adequate strength, and a very strong adhesive may succumb to interfacial failure because of the lack of adhesion compatibility with the mating adherends. Therefore, another aspect that was investigated was the influence of the ratio of the cohesive strength of the adhesive (modelled using xFEM) to the interfacial strength (modelled using CZM). Surprisingly, no significant difference was observed in the resulting axial-load shortening curves among all the considered cases; therefore, these results are not reported.

However, the influence of the reference (or the maximum traction) strength was investigated. For that, values of 0.016, 0.032, 0.08, and 0.8 GPa were considered. The

results are illustrated in Figure 9-11. The following conventions are used to distinguish the models' results. In the figures, "c" and "x" refer to the results produced by the cohesive and xFEM elements, respectively. The numbers appearing after "c" and "x" signify the value (multiplier) by which the base strength (traction) value reported in Table 9-2 of the appendix was increased. For instance, c-100 references to the COHESIVE model with the base strength of 0.8 GPa (i.e., 0.008 GPa × 100).

As seen, the higher is the adhesive strength, the more difficult would be for the delamination to propagate along the interface. This results in the evolution of successive cracks, all having the same inclination. However, an apparent limit is reached when the base strength approaches a relatively large value (i.e., c-100), in which case the delamination would no longer propagate longitudinally, leading to extensive local damage at the delamination tip. Note that the delamination initially kinks towards the upper interface but could not propagate within the cohesive elements due to the high traction strength. Moreover, due to the limitation of the xFEM formulation, the delamination was not capable of propagating along the interface of xFEM/cohesive elements either. This resulted in the development of successive delaminations parallel to the initial delamination. Of interest is also the behaviours of models x-2 to x-10. In these models, the delamination propagated towards the interface, and then traveled along that interface in both forward and reverse directions. This response became increasingly noticeable as the base strength was increased, which is facilitated by the comparatively lower interface strength. In the extreme case (x-100), where the interface strength is significantly weaker than the traction strength, the adhesive detaches almost completely from both neighboring materials. Note that the minute interpenetration seen in model x-100 (see Figure 9-11(h)) is the result of the failure of the cohesive elements, and the absence of a contact algorithm. It should be noted that incorporation of an appropriate contact algorithm would have increased CPU consumption significantly, resulting in no appreciable benefit in terms of further understanding of the behaviour.
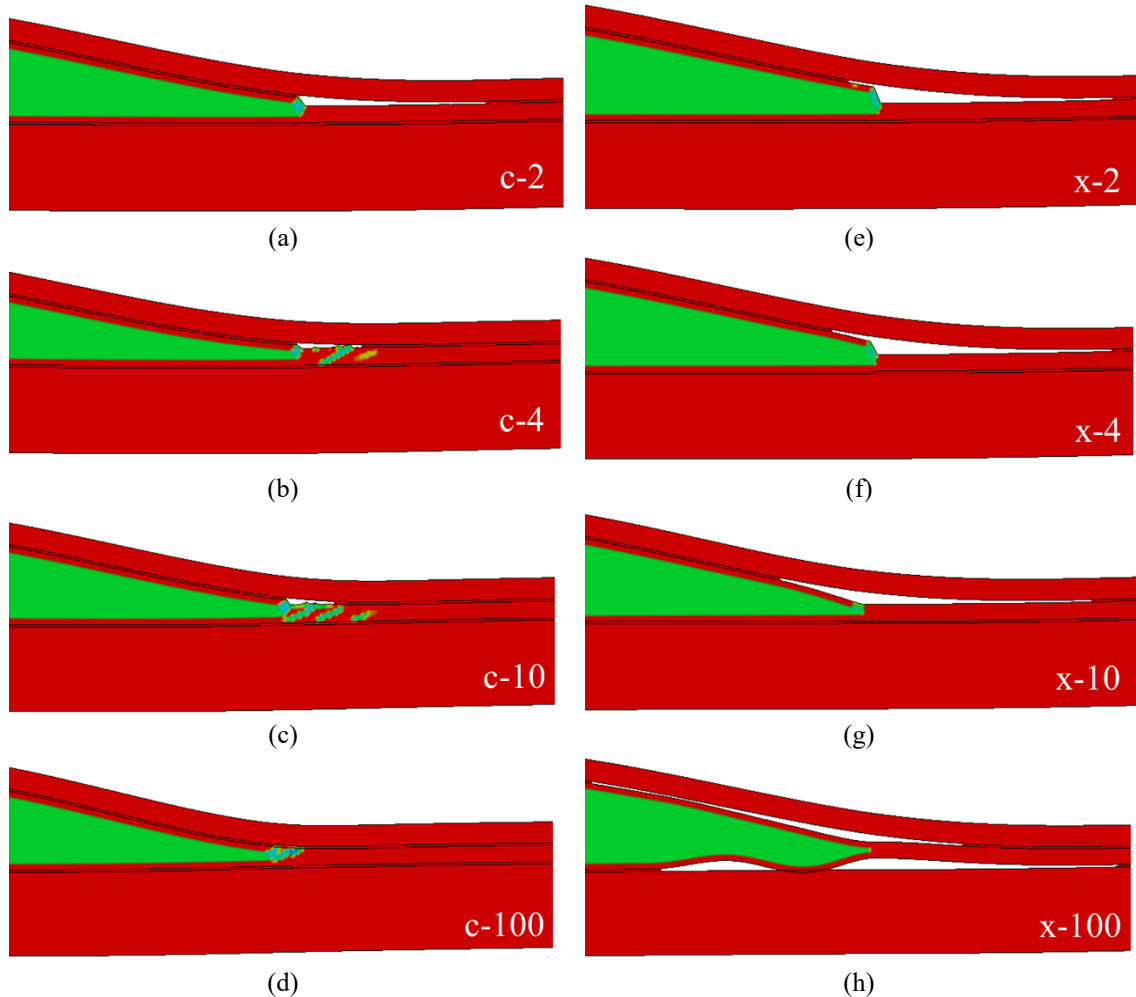
Figure 9-11. Influence of the base (traction) strength on delamination propagation captured by the MIXED model when the strength of the cohesive elements is 2-100 times greater than the strength of the xFEM elements (subfigures (a) to (d), respectively) and when the strength of the xFEM elements is 2-100 times greater than the strength of the cohesive elements (subfigures (e) to (h), respectively).

9.4.6. Computation Time

The final aspect of the analyses being investigated is the computation time, which is one of the most important constraints in a numerical analysis, especially in large-scale simulations. For the relatively small and geometrically simple models considered in this study, the COHESIVE model consumed 1445 s solution time on a workstation using eight cores of an E5520 Xeon processor. In contrast, the MIXED model analysis took 2320 s (i.e., 60% more time compared with the COHESIVE model). Therefore, the use of the MIXED approach has its merits for understanding the crack propagation mechanisms but may not be feasible for large-scale simulations. However, its use may be justifiable if the

crack path is either not known a priori or has a high influence on the outcome of the simulation. In cases where the crack path is predictable or confined, such as modelling the interfacial delamination in fiber-metal laminates, the use of cohesive elements could be considered as a more suitable choice.

9.5. Summary and Conclusions

In this study, the integrity and efficiency of the two modelling approaches used for assessing crack and delamination propagations in hybrid composites were examined. The approaches involved the use of cohesive and extended finite element (xFEM) elements available through the commercial finite element software LS-DYNA. More specifically, two separate case-studies were considered. First, crack propagation in a double cantilever beam (DCB) test specimen formed by two dissimilar adherends was considered. Then, delamination buckling response of a 3D fiber-metal laminate, subjected to a compressive impact loading, was simulated. The study also examined the integrity of a mixed approach; that is, the use of xFEM and cohesive elements within a single model. In the latter analysis, the cohesive elements were used to simulate the adhesive/adherend interface, while the xFEM elements were used to simulate the bulk portion of the adhesive. The summary of our findings is as follows:

- LS-DYNA's shell elements could be used to simulate plane strain conditions in circumstances when plane strain elements cannot be used to conduct the analysis.
- The analysis of the DCB specimens using the combined xFEM and cohesive approach proved that the crack kinking that was experimentally observed to occur within the adhesive could be simulated precisely. The model that used only the xFEM elements could not capture the phenomenon.
- The above-mentioned combined approaches could also successfully simulate the delamination buckling response of the FML model with good accuracy. The delamination was demonstrated to change its propagation path that was initially within the adhesive (i.e., through the xFEM elements) towards the adhesive/metal interface, and subsequently propagating along the interface (i.e., through the cohesive elements). The delamination path deviation response highlights the

importance of the role of surface preparation (i.e., interfacial integrity) in enhancing the performances of such FMLs under compressive loading states.

- Using the same material model and properties, the model constructed using only xFEM elements appeared to overestimate the energy required for the crack/delamination to propagate in comparison with the model constructed with the cohesive elements.

- The use of xFEM elements resulted in more accurate predictions of crack initiation and propagation. However, from a solution time perspective, especially when large complex geometries are to be modelled, the use of cohesive elements is deemed preferable, so long as the crack or delamination path is known a priori.

In closing, while the potentials of the different numerical approaches were demonstrated throughout this study, nonetheless, further effort is necessary to establish the accuracy of the solutions that are produced by these approaches. For instance, the future works should consider (i) precise calibration of the cohesive parameters required by the methods by experimental means, including investigation of strain effect on the properties, and (ii) verify the accuracy of the numerical results by comparing them with consistent experimental results. Another aspect that requires further investigation is understanding the origins of the numerical instabilities that at times halt and limit such solution processes. Finally, it would be worth exploring the capabilities of the element-free approaches, such as the element-free Galerkin (EFG) method and the discrete element method (DEM). These approaches have been proven to be efficient in simulating crack propagation (Guo & Wu, 2010; Tabiei & Zhang, 2016) and are available through LS-DYNA for both 2D and 3D simulations.

9.6. Acknowledgments

9.7. Appendix

The authors wish to provide further information regarding the models' implementation in LS-DYNA, to facilitate the use of the presented modelling approaches. The xFEM formulation is assigned to the elements via *SECTION_SHELL_XFEM keyword. For shell elements, the formulation ELFORM = 54 is used, while the parameter would be 52 when using the 2D plane strain element formulation. A base element (BASELM) must be designated as 16 for shell elements and 13 for the plane strain elements. Finally, the cohesive material model (CMID) is assigned. It should be noted that at the time the analyses were conducted, only *MAT_COHESIVE_TH was available for xFEM. The section properties are assigned to the mesh via the *PART keyword, which also requires a material model. As mentioned in Section 9.3.2. , this input material model will govern the behaviour until the stress state leads to the activation of the xFEM formulation, thereby switching the material behaviour to those assigned through the selected cohesive zone model. In our study, a linear elastic orthotropic material model was used (*MAT_ELASTIC); however, other models, such as a plasticity model, can also be used if large deformations or material nonlinearity are to be taken into account. Finally, the crack propagation path was captured by specifying an additional history variable for the output, by using the keyword *DATABASE_EXTENT_BINARY. This would enable the user to visualize the results in LS-DYNA's post-processor (LS-PrePost).

Table 9-1. Supplementary information related to the parameters required for implementation of the models in LS-DYNA.

*SECTION_SHELL	ELFORM = 2, NIP = 1
*SECTION_SHELL_XFEM	ELFORM = 54, NIP = 4, CMID = id of the cohesive material, BASELM = 16, DOMINT = 0, FAILCR = 1
*MAT_COHESIVE_TH	INTFALL = 1, STFSF = 100
*DATABASE_EXTENT_BINARY	NEIPS = 1

Table 9-2. Material properties and parameters of the material models.

Elastic (*MAT_ELASTIC)

FRP	$\rho = 1630$ kg/m^3	$E = 25$ GPa	$\nu = 0.254$
Magnesium	$\rho = 1740$ kg/m^3	$E = 36$ GPa	$\nu = 0.35$
Adhesive	$\rho = 1200$ kg/m^3	$E = 3$ GPa	$\nu = 0.3$

Cohesive (*MAT_COHESIVE_TH)

| $\rho = 1200$ kg/m^3 | $\sigma_{max} = 0.008$ GPa [*] | $\delta_{norm} = 0.015$ mm | $\delta_{tan} = 0.02$ mm |
| $\lambda_1 = 0.5$ | $\lambda_2 = 0.5$ | $\lambda_{fail} = 1$ | |

[*]The reference strength value. The values of 0.016, 0.032, 0.08, and 0.8 GPa are used in conducting the influence of material's strength study, outlined in Section 9.4.5.

Chapter 10: A Practical Analytical Procedure for Predicting the Behaviour of 3D Fiber-Metal Laminates under Low-Velocity Impact

Davide De Cicco and Farid Taheri

10.1. Introduction

Full-scale vehicle crash tests are necessary to assess a vehicle's performance, to assess structural integrity, and ensure passengers safety. In North America, they are performed following the US-NCAP protocol (*Laboratory Test Procedure For New Car Assessment Program*, 2012). The protocol consists of the following tests: (i) full-frontal impact into a rigid barrier, (ii) medium and moderate overlap impact, (iii) side moving deformable barrier impact, (iv) side oblique pole impact, and (v) rollover resistance test. The full-frontal impact, abbreviated FFI hereafter, involves crashing the vehicle at a speed of 56 km/h (35 mph) into a flat, rigid wall. The car's moving direction is normal to the wall surface, and there is no dissymmetry in the impact, as seen in Figure 10-1. This test is considered as a reference in this chapter.

Figure 10-1. Top view of a full-frontal crash test (VolvoCars, 2019).

Although necessary, only very few full-scale crash tests are performed, and ironically, it is usually conducted only when most of the design of a car is finalized. This is due to the exorbitant cost associated with such a test, since the test vehicle requires extensive and

expensive instrumentation, and it is sacrificed in the test. Therefore, nowadays most of the crash tests are conducted computationally, using the finite element (FE) method, either at the component scale (e.g. bumpers, longerons, doors) or at a full-scale (Kim et al., 2015; Mamalis et al., 2003). An example of such an analysis can be seen in (Marzi et al., 2008) in which the side impact of a body floor assembly was simulated using the commercial finite element software LS-DYNA, with a focus on the performance of the adhesively bonded joints. Good agreement with the experimental results was obtained. The effective use of cohesive elements for modelling bonded joints in large-scale models was also highlighted in that study. Li et al. (2003) also focused on the optimization of car bumpers. The authors were able to produce a lighter-weight bumper design by incorporating thinner high-strength steel sheets instead of thicker mild-steel sheets and maintaining the crashworthiness performance. As an example of a full-scale simulation, Kiani et al. (2014) conducted a series of full-scale car crash simulations with the aim of reducing the overall vehicle's weight without compromising the crash performance. The authors were able to replace 22 steel components with equivalent magnesium components while maintaining the car's crashworthiness. Crash simulations can also be used for improving pedestrian safety. Ahmed & Wei (2016) used FE to design a composite car hood able to reduce the head injury in the event of a pedestrian's head impacting the hood. The hood, originally made of steel, was modified to a combination of CFRP composite and CFRP/foam sandwich.

Although the numerical simulation is far more convenient than experimental testing, the complexity of the problem is such that significant time and high-level technical expertise are required for producing accurate and reliable simulations. Therefore, empirical and semi-empirical equations are often used as an alternative in the industry by practicing engineers to establish the preliminary design in a time-efficient manner. For instance Ryan et al. (2008) and Chen et al. (2017) used a series of FE simulations to provide semi-empirical equations for the prediction of high-velocity impact behaviour of composite sandwich panels for use in the aerospace industry. Barbero (2000) introduced an analytical constant for predicting the local and global buckling mode interaction in composite I-beams, and studied the sensitivity of the beams to initial imperfections. In reference to the 3D-FML, the focus of this study, a comprehensive semi-empirical model was developed

by Asaee & Taheri (2018) for predicting the out-of-plane low-velocity impact of this new hybrid composite material. The contribution of contact, bending and shear in the deformation process was highlighted, and the developed equations accounted for the magnitude of impact energy and specimen-to-impactor size ratio. However, a model for assessing the capacity of this new composite against an in-plane impact loading was not available.

In this chapter, a set of empirical equations are developed by which the buckling capacity and maximum load bearing capacity of one-way 3D-FML panels subjected to an in-plane low-velocity impact can be estimated. The prime intention was to develop a simple set of equations by which practicing engineers could conduct the preliminary designs of such panels, thus taking advantage of such an exemplary resilient hybrid composite, particularly for applications in the automotive industry.

10.2. Framework and Assumptions

As previously mentioned, this class of 3D-FMLs was developed with the aim of reducing fuel consumption in transport vehicles, especially targeting applications in auto-body components, which would have a high likelihood of impact. The FFI crash configuration will be considered in this chapter, and front doors of a car are taken as a reference for developing the model. Contrarily to the components that form the front section of a car (e.g., bumper, hood and fenders), which undergo significant bending deformations in a FFI test, and usually get completely destroyed by the crash, the doors undergo compressive in-plane loading with little or no damage (see Figure 10-1). In the other test configurations, either doors are completely crushed (e.g., in the small overlap test) or are damaged due to out-of-plane loading (e.g., in the lateral impact test).

In addition to the impact tests, a linear buckling analysis (eigenvalue analysis) is performed to provide the basis for developing the equations for predicting the impact-buckling behaviour. In fact, as it will be discussed in the forthcoming sections, the semi-empirical equations presented here are based on the static buckling equation of sandwich beams.

10.2.1. Impact Energy

According to the full-scale crash simulations performed by Chen et al. (2015) and the work of Griskevicius & Ziliukas (2003), in a frontal impact crash, most of the energy is absorbed by the car components that are designed to absorb most of the energy (i.e., the longerons, the rockers, and the subframe components). The energy absorbed by the door amounts to approximately only 0.12% of the total impact energy.

Considering that the average weight of a mid-size car is 1590 kg (note that the car modelled in (Chen et al., 2015) weighted 1580 kg) and using the well known equation of kinetic energy, it is possible to calculate the energy at which the car impacts the rigid wall:

$$E_{car} = \left[\frac{1}{2}m_v v_v^2\right] \tag{10-1}$$

where m_v is the mass of the vehicle, and v_v is its speed (15.5 m/s according to the NCAP test regulations, corresponding to a strain rate of 103 s^{-1}). Therefore, the total impact energy is 192,370 J, with 231 J reaching the door.

Finite element simulations of coupon-size specimens will be used to develop the semi-empirical model. Therefore, the energy needs to be scaled down to the considered coupon size (i.e., 20 mm in width). For this, we consider the average height of the front door of a mid-size car, excluding the window, which has a height of 681 mm. This leads to an estimated 0.34 J per unit millimetre of width. Therefore, the 20-mm wide specimens would be subjected to a 6.8 J impact. For practicality, an energy level of 7 J is taken into consideration. Furthermore, to account for variations in the applied energy during a crash, which can depend on the vehicle mass, type of impact, or impact angle, two other energy levels (i.e., 4 J and 10 J) will be considered in the study. These energies represent a ±40% change in the baseline energy.

10.2.2. Specimens' Dimensions, Imperfection, and Boundary Conditions

The 3D-FML specimens used for the numerical analyses have a width of 20 mm, a thickness of 5.3 mm, and varying gage lengths of 150 mm, 300 mm, and 600 mm.

Specimens with the 150 mm gage length correspond to all the specimens that were considered in both the numerical simulations and experimental tests presented in this thesis. The other lengths are a multiple of this reference specimen.

As also discussed in the previous chapters, specimens have an initial imperfection generated by the fabrication process. Precisely, the profilometry carried out for the experiments in Chapter 9 show that the specimens have an inherent slight curvature with an amplitude of 0.2 mm (other small variations are reported at the surface, but they are neglected compared to the main one). Note that these measurements were obtained for specimens having a gage length of 150 mm. Therefore, to maintain a consistent imperfection/curvature for the longer specimens, the ratio between the imperfection amplitude and the specimen's gage length is maintained constant. This leads to a 0.4-mm and 0.8-mm imperfection amplitudes for the 300-mm and 600-mm long specimens, respectively.

As for the boundary conditions, although in reality the doors are mounted on hinges, they are, however, designed on the basis that they are locked in place when closed. As a result, the specimens are considered clamped at both ends.

10.3. The Finite Element Models

The low-velocity impact finite element (FE) model used for the development of the proposed solution corresponds to the "SOLID" model reported in Chapter 5, and is briefly described hereafter. The modifications made for the linear buckling model will be presented successively. The validity of the FE model was demonstrated in Chapter 5; therefore, it will not be discussed further in this chapter.

The FE model was constructed using the 8-node, reduced integration isoparametric solid element of LS-DYNA (ELFORM = 1). The element was used to model all the constituents of the 3D-FML (i.e., the magnesium skins, the FRP plies, the pillars, and the reinforcing foam). A mesh convergence study was performed to guarantee an acceptable accuracy in a CPU-efficient manner. A portion of the resultant mesh is illustrated in Figure 10-2(a). Note that the LS-DYNA's hourglass control option was activated because the

reduced integration scheme was used. It was also verified that the hourglass energy constituted an insignificant percentile of the total energy of the simulated system. As seen in Figure 10-3, the hourglass energy at the onset of buckling accounts for only 1.3% of the total energy. This value is lower than the industry accepted standard value of 3%, according to (Chen et al., 2015). Therefore, no further attention was required.

(a)   (b)
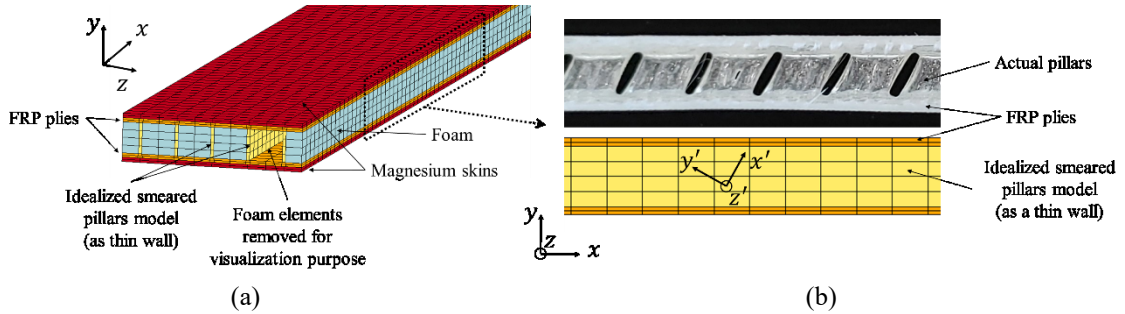
Figure 10-2. (a) FE model of a typical 3D-FML specimen, (b) close-up view of the actual configuration of the glass pillars and the actual material orientation and the corresponding equivalent FE modelling approach.
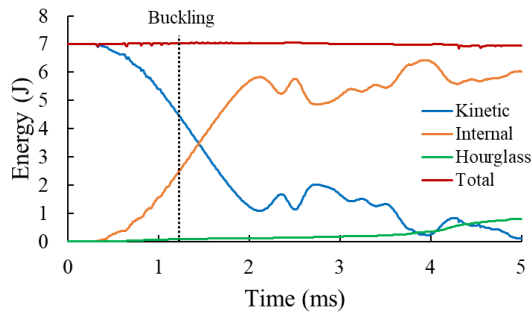
Figure 10-3. The repartitioned system energy for the 300 mm long specimen impacted with 7 J energy.

The magnesium skins were modelled using a piecewise linear plasticity material model (*MAT_024) that accounts for the actual stress-strain curve of the material. The FRP plies and pillars were both modelled using the orthotropic composite material model with Chang-Chang failure criterion (*MAT_054). It should be noted that the material properties of these two components are different. Moreover, the inclination of the pillars, visible in Figure 10-2(b), was accounted for by setting the principal direction of the fibers inclined by 30° with respect to the vertical direction in the elements representing the pillars. Finally, the foam was modelled using the linear elastic isotropic material model

205

(*MAT_001), coupled with a strain failure criterion keyword (*MAT_ADD_EROSION). In other words, the foam's behaviour is assumed to be elastic so long as its strain remains lower than a prescribed threshold value beyond which the elements are automatically nullified. This simplified approach was adopted because our trial studies revealed no substantial difference in the overall results when the more complex and CPU-intensive crushable foam material model was used in the modelling. The materials' properties are reported in Table 10-1.

Table 10-1. Material properties, tiebreak contact and other parameters used in the simulations and for developing the semi-empirical equations.

Magnesium	E (GPa)	ν	ρ kg/m^3	σ_y (GPa)		
	36	0.35	1740	0.231		
FRP plies	E_{11} (GPa)	E_{22} (GPa)	ν_{21}	G_{12} (GPa)	G_{13} (GPa)	G_{13} (GPa)
	9	9	0.05	1	1	1
	X_C (GPa)	X_T (GPa)	Y_C (GPa)	Y_T (GPa)	S_C (GPa)	ρ kg/m^3
	0.173	0.173	0.173	0.173	0.03	1750
Pillars	E_{11} (GPa)	E_{22} (GPa)	ν_{21}	G_{12} (GPa)	G_{13} (GPa)	G_{13} (GPa)
	3	1	0.05	1	1	1
	X_C (GPa)	X_T (GPa)	Y_C (GPa)	Y_T (GPa)	S_C (GPa)	ρ kg/m^3
	0.08	0.08	0.08	0.08	0.03	1750
Foam	E (GPa)	ν	ρ kg/m^3	ε_{ult}		
	0.05	0	128.1	0.15		
Tiebreak contact	NFLS (GPa)	SFLS (GPa)	OPTION			
	0.003	0.02	2			
Other parameters	D_{11} (kN-mm)	D_0 (kN-mm)	D_f (kN-mm)	G_c (GPa)	β	
	215.1	162.3	1.125	0.145	0.5	

The full length of the specimens was modelled, and the boundary conditions were applied such to simulate those in the actual fixture used in the experimental tests, as detailed and validated in Chapters 4 and 5. Therefore, the boundary conditions are applied to apply the restrains as shown in Figure 10-4. In other words, each of the 20-mm clamped sections

of the specimens was restrained in the transversal direction (u_y), and the non-impacted end was also restrained in the axial direction (u_x), while the impacted end was allowed to translate in that direction. As per good practice, the rigid-body motion was prevented by restraining the displacement in the z-direction (u_z). Moreover, partial lengths of the impactor tup and the fixture adjacent to the impacting tup were also explicitly modelled to increase the accuracy of the results (see the details in Chapter 5).
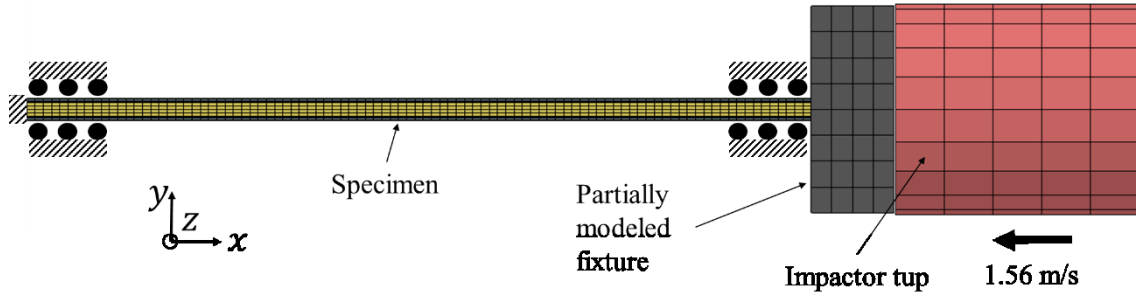
Figure 10-4. FE model of the impact test configuration and the boundary conditions.

To generate the actual inertia imposed by the tup and the fixture, the density of the materials used to model the partial segment was increased accordingly. The linear elastic isotropic material model was used for both the fixture and the impactor; aluminum and steel materials' properties were assigned to each of these components, respectively. The automatic surface-to surface algorithm (*CONTACT_AUTOMATIC_SURFACE_TO_ SURFACE) was used to model the contact in between the impactor and fixture so that the energy release as a result of the impactor rebound could be accounted for.

Contact algorithms were also used to account for the effect of initial delamination. A tiebreak contact algorithm (*CONTACT_AUTOMATIC_SURFACE_TO_SURFACE_ TIEBREAK) was used for mating the magnesium skins and the FRP plies. This contact was replaced by the simple contact algorithm for the delaminated portion to account for the lack of initial contact, while preventing interpenetration of the two constituents.

Last, the initial inherent curvature/imperfection of the specimens was modelled as a half-sine wave using the *PERTURBATION keyword. The amplitude and wavelength were matched to the specimens' length, as discussed in the previous section.

The static buckling model was obtained by simply changing the load. The fixture and impactor were deleted, and a compressive force was applied instead. As LS-DYNA's default solution scheme is explicit dynamics, therefore, the *CONTROL_IMPLICIT cards were implemented to solve the linear buckling problem in an implicit mode. The actual buckling capacity was obtained by multiplying the applied load by the eigenvalue outputted by the software. For both model types, a MATLAB code was written to automatically update the study parameters, rerun the analyses, and extract the desired information from the result files. This procedure reduced the user intervention by a significant margin, and facilitated consistency of the output processing, resulting in a significant saving in time.

It should be noted that two other FE models were constructed and used in this study to obtain the required material parameters used in developing the semi-empirical model. These parameters are the bending rigidity of the 3D-FML, D_{11}, and the shear modulus of the core, G_c, (comprised of the glass pillars and the reinforcing foam). Specifically, a set of linear static analysis were conducted to simulate the response of a 3D-FML specimen in the three-point bending test configuration, to evaluate the D_{11}, followed by a shear test configuration of the core to obtain the G_c. The models and their boundary conditions are illustrated in Figure 10-5. For the three-point bending test, the same FE mesh as used in the buckling analysis was used with the appropriate boundary conditions. The value of D_{11}=201.15 kN-mm was obtained as the FML's bending rigidity.
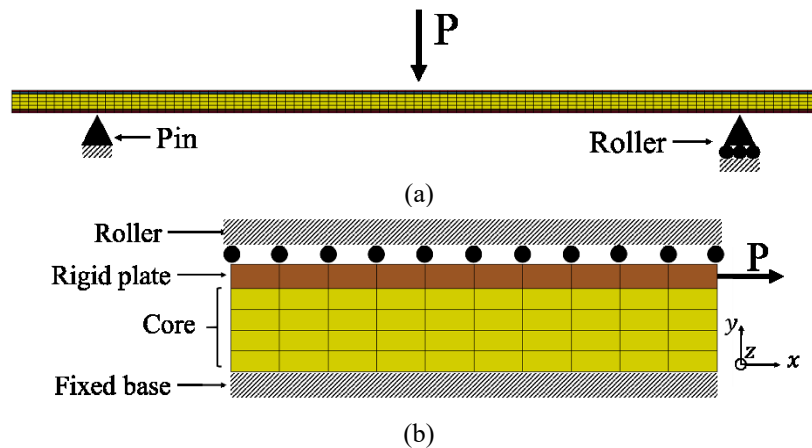
Figure 10-5. FE models of (a) 3-point bending test and (b) core shear test configurations.

To obtain core's shear modulus, only a 20-mm long section of the glass pillars and foam part of the FML was modelled (see Figure 10-5(b)). The bottom part of the model was fully restrained, while a rigid plate was attached to the top portion of the core specimen. The rigid plate was loaded such to create pure shear in the core, as illustrated in Figure 10-5(b). By evaluating the displacement of the plate and using the basic mechanics of materials, a value of G_c=0.145 GPa was established as the core's shear modulus. Note that knowing the shear properties of the core and the foam, a very similar shear modulus value was also obtained by using the rule of mixture.

10.4. Development of the Semi-Empirical Equations

10.4.1. Effect of the Impactor's Mass and Speed

As discussed in section 10.2.1, the FML specimens were subjected to impact energies of 4 J, 7 J, and 10 J, with the 7 J impact simulating the impact energy when an average-size car impacts a rigid wall at a speed of 56 km/h. Therefore, we can consider two approaches to define the impact energy in the FE simulations: (i) the impactor's initial velocity corresponds to the speed of the vehicle, and (ii) the rigid wall is modelled as a large mass moving at a slower speed. The issue with the first approach is that, in reality, the door (or the specimen herein) is not the first component that comes into contact with the wall. Therefore, the effective speed at which the door is impacted is lower than the vehicle's initial speed. In addition, the door is connected to the rest of the vehicle, which has a much greater mass than the door itself (the mass of the door has been estimated to be 4% of the total vehicle's mass using (Grujicic et al., 2009)). Therefore, it would be more realistic to model the event by considering the impactor as a large mass travelling at a lower speed.

Noting the aforementioned discussion, a preliminary test to analyze the effect of the impactor mass and speed was performed to validate the selected approach. The impact energy was fixed at 7 J, and three mass/speed ratios were tested. First, the impactor mass and speed were set to 62 g and 15.5 m/s (corresponding to 56 km/h), respectively. This case will be referred to as low-mass/high-speed and abbreviated as LM-HS. Note that the

use of the terminology "high speed" is relative to the other considered speeds and does not have the same connotation as the conventional high-speed impact tests. The second scenario, referred to as medium-mass/medium-speed (MM-MS) assumes the impactor travelling at 7.5 m/s (half the speed of the LM-HS case), with a mass of 249 g. The last case corresponds to the experimental tests performed to validate the models, i.e., a mass of 5.7 kg travelling at 1.56 m/s. This configuration will be referred to as high-mass/low-speed (HM-LS).

The results of the analysis in terms of load-axial shortening curves are reported in Figure 10-6. As can be seen from the graphs, all three configurations lead to a very similar initial response, yielding similar stiffness and maximum load values. However, while the HM-LS configuration causes the buckling of the specimen, the MM-MS and LM-HS configurations cause a vibratory response of the specimen. Many crash test videos available online illustrate that in such an impact event, a car's doors undergo buckling. Therefore, the HM-LS configuration will be adopted for this study.
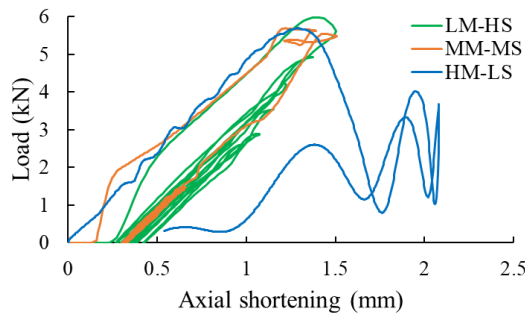
Figure 10-6. Load-axial shortening curve for three mass-speed combinations.

10.4.2. Effect of the Initial Imperfection

As mentioned earlier, the 3D-FML specimens have an inherent initial curvature (imperfection) originated as a result of the sand-blasting stage of the fabrication process. Therefore, the investigation of the effect of this initial imperfection on the buckling capacity is of interest. For this, the buckling capacity of three different lengths of 3D-FML, with and without imperfection, are evaluated by an eigenvalue FE analysis and reported in Figure 10-7. Note that, although a similar study was conducted in Chapter 4, here a more realistic model was used in conducting the analysis.
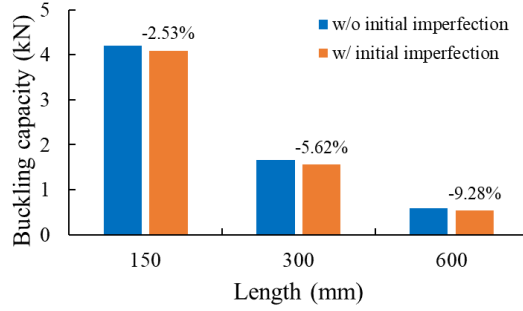
Figure 10-7. Comparison of the static buckling capacity for specimens with and without initial imperfection.

It can be seen from the graph that the maximum difference in the results of is less than 10%, associated with the predicted capacities of the longest specimens. Furthermore, as expected, the specimens having an initial imperfection exhibited a lower capacity. Therefore, the semi-empirical equations will be developed with the consideration of the inherent initial imperfection.

10.4.3. Linear Buckling Analysis

The first step in developing the semi-empirical equations entailed the comparison of the buckling capacities predicted by the eigenvalue analysis and these obtained using the equations available for evaluating the buckling capacity of sandwich beams (Zenkert, 1997).

The critical buckling capacity, P_{cr}, of a sandwich beam, having thin face sheets can be estimated using the following equations:

$$P_{cr}^{thin} = \frac{1}{\frac{1}{P_b} + \frac{1}{bS}}$$

(10-2)

with

$$P_b = \frac{\pi^2 b D_{11}}{(\beta L)^2} \qquad\qquad S = \frac{G_c d^2}{t_c^2}$$

(10-3)

211

where b, L, D_{11} are the width and length and bending rigidity of the specimen, and G_c and t_c are the core's shear modulus and thickness, respectively; d represents the distance between the mid-planes of the skins and β is the effective length parameter, as defined in Chapter 1. For the clamped-clamped boundary conditions considered here, $\beta = 0.5$. The values of all the parameters are reported in Table 10-1. The dimensions related to the geometry of the specimens were directly measured from an actual specimen, while the values of D_{11} and G_c were those obtained from the finite element analysis, as described earlier.

The buckling capacity in equation (10-2) is defined based on the assumption that the sandwich has thin faces. However, in our 3D-FML, the thickness of the skins (the combination of magnesium sheet and FRP plies) is 30% of the core thickness. Therefore, it is worth investigating the pertinence of using a different equation that accounts for the effect of thick skins. The critical buckling capacity for a sandwich beam with thick skins is given by Zenkert (1997):

$$P_{cr}^{thick} = \frac{\dfrac{2\pi^4 b^2 D_f D_0}{(\beta L)^4} + \dfrac{\pi^2 b^2 D_{11} S}{(\beta L)^2}}{\dfrac{\pi^2 b D_0}{(\beta L)^2} + bS} \tag{10-4}$$

where D_f is the flexural stiffness of the sandwich skins with respect to their neutral axis, D_0 the bending stiffness of the skins with respect to the mid-plane of the sandwich, both defined in the longitudinal direction.

Following the same procedure followed to determine D_{11}, the parameters D_f and D_0 were evaluated via three-point bending FE simulations, leading to values of $D_f = 1.125$ kN-mm and $D_0 = 162.3$ kN-mm.

The buckling capacity predicted by equations (10-2) and (10-4) are compared to the FE results, and shown in Figure 10-8. Although an overall good match between the analytical and numerical results is visible, however, the difference goes as high as 25% for the 600-mm length specimens. Interestingly, a better match is obtained using the thin faces equation compared to the thick faces one, especially for shorter specimens, which is

contrary to what one would have expected. Therefore, the thin faces equation was modified to account for the difference in behaviour as follows:

$$P_{cr}^{stat} = \alpha_{3D} P_{cr}^{thin} \qquad \text{with} \qquad \alpha_{3D} = 1.22 \times 10^{-3} L + 0.684 \qquad \text{(10-5)}$$

The coefficient α_{3D} represents the influence of the complex configuration of the 3D-FML and varies as a function of the specimen's length. The coefficient was evaluated based on the ratio of the power curve fitted to the FEM results and the analytical predictions. It can be seen from Figure 10-9(a) that the ratio has a highly nonlinear behaviour for any length shorter than 200 mm, but it has a linear trend otherwise. Therefore, equation (10-5) is admissible to panels longer than 200 mm, which from a practical perspective, it would be admissible to essentially all practical cases.
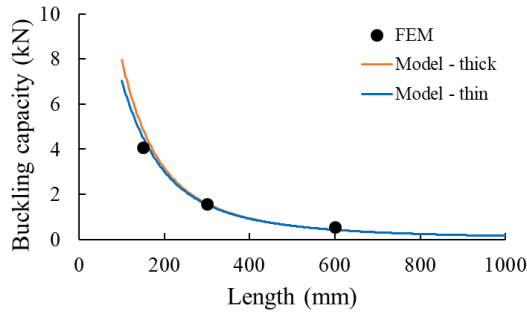
Figure 10-8. Comparison of the static buckling capacity and the analytical models without correction factor.

(a)

(b)
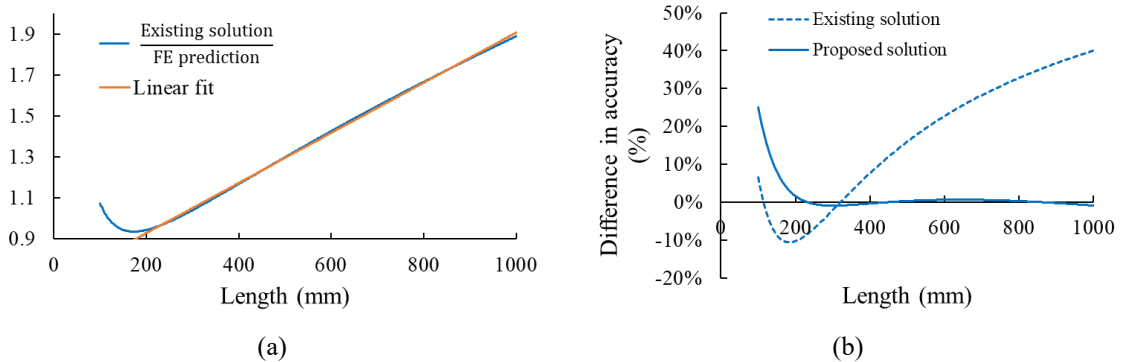
Figure 10-9. (a) Comparison of the existing solution with the FE prediction. (b) Accuracy of the existing and proposed models.

The performance of the proposed parameter is reported in Figure 10-9(b). As can be seen, the error between the analytical model and the FE model drops to less than 2% for specimens with a length greater than 200 mm. As stated, in reality, the use of this material system in very short panels is highly unlikely; therefore, the solution would be admissible to essentially all practical cases.

10.4.4. Low-Velocity Impact

The static buckling study was performed as a starting point for the development of a semi-empirical model for predicting the buckling behaviour of the 3D-FML under a low-velocity impact. In this section, FE simulations are used to modify equation (10-5) to account for the dynamic effects, as well as the presence of an initial delamination.

10.4.4.1. Intact Specimens

The same approach used in developing the static buckling solution was followed in developing the solution applicable to dynamic cases. The buckling capacities obtained by the FE simulations for various impact energies are plotted in Figure 10-10. A quadratic curve was found to provide the best fit to the data, for every given specimen length. Therefore, the equation of the buckling capacity can be written as follows:

$$f(E) = C_1 E^2 + C_2 E + C_3 \tag{10-6}$$

where E represents the impact energy, C_i are coefficients depending on the specimen's length. From the values shown on Figure 10-10, C_3 represent the static buckling capacity. The values of coefficients C_1 and C_2 vary between the 150 mm and 300 mm lengths but remain stationary for lengths greater than 300 mm. However, for simplicity, the coefficients are assumed to vary linearly between lengths of 150 mm and 300 mm, and remain stationary otherwise. Thus, the buckling capacity of a 3D-FML beam subjected to a low-velocity impact can be estimated by the following simple equation:

$$P_{cr}^{imp} = C_1 E^2 + C_2 E + P_{cr}^{stat} \tag{10-7}$$

with

$$\begin{cases} C_1 = -1.73 \cdot 10^{-4}L + 1.10 \cdot 10^{-2} \\ C_2 = 3.28 \cdot 10^{-3}L + 1.53 \cdot 10^{-1} \end{cases} \qquad \text{for } L \leq 300 \text{ mm} \qquad (10\text{-}8)$$

and

$$\begin{cases} C_1 = -0.0409 \\ C_2 = 1.137 \end{cases} \qquad \text{for } L > 300 \text{ mm} \qquad (10\text{-}9)$$

The predictions of the proposed solution are compared to the FE results in Figure 10-10. A good match can be observed for the 300 mm and 600 mm specimens, while a shift in value is observed for the 150-mm long specimen. In practical cases, the 3D-FML would be used in a very slender form. In addition, the quantitative comparison illustrated in Figure 10-11 shows that the maximum error in the predicted results is around 6%. Therefore, no further step is required to improve the model.
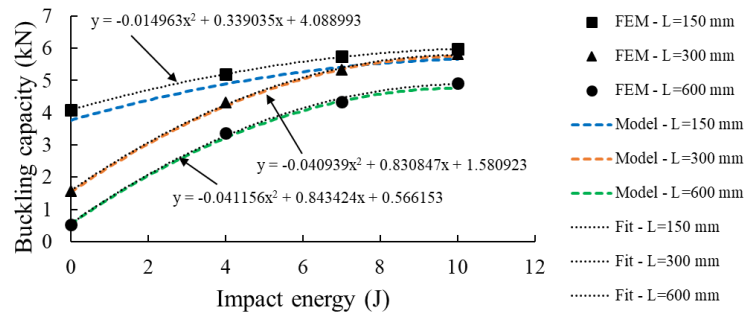
Figure 10-10. Comparison between the FE results and the proposed empirical equation. The fitting curves used for the creation of the empirical model are also shown.
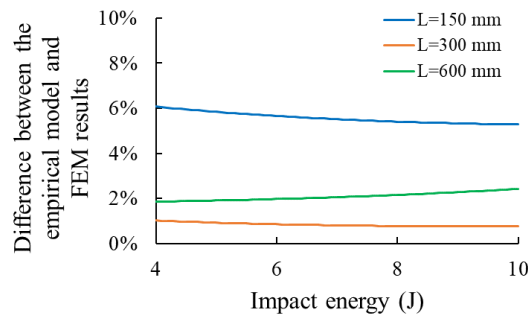
Figure 10-11. The percent difference between the FE results and the empirical model.

215

At this juncture, it should be stated that the buckling capacity is only one of the criteria commonly used for characterizing the impact response of a structural component. In other words, the energy required to destabilize the component is also indicative of the performance of the material under compressive loading states. Therefore, the buckling energy of the specimens is computed from the load-axial shortening data and reported in Figure 10-12(a). As can be seen, compared to the shorter specimens, interestingly, longer specimens require a relatively greater energy to buckle. This is due to two phenomena. First, under an impact load, the longer specimens do not buckle in the conventional first or globally flexural mode, but in the third mode configuration. Second, longer components undergo greater axial shortening, therefore, exhaust a greater amount of energy.

As mentioned, the internal energy of a member under axial compression can be calculated as follows:

$$E = F\delta \tag{10-10}$$

where F is the applied force and δ is the axial shortening. The axial shortening can also be calculated using the mechanics of materials equations:

$$\delta = \frac{LF}{EA} \tag{10-11}$$

where L is the length of the member, E is the modulus of elasticity, and A is the cross-sectional area.

The 3D-FML does not have a homogeneous cross-section. Therefore, the equivalent stiffness of the hybrid system would be $EI = bD_{11}$. This leads to the following formula for the buckling energy:

$$E = \frac{h^2 L}{12 b D_{11}} P_{cr}^2 \tag{10-12}$$

Where, as a reminder, b is the specimen's width, h its thickness, and P_{cr} is the buckling capacity, calculated using equation (10-7).

The difference between predictions of the FE and the proposed equation (10-12) is reported in Figure 10-12(b). A certain discrepancy can be seen; however, it tends to stabilize towards a value of 0.5 for longer specimens. Therefore, equation (10-7) can simply be modified by adding a coefficient κ to account for this change, leading to the practical equation for estimation of the buckling energy of 3D-FMLs:

$$E_{buck} = \kappa \frac{h^2 L}{12 b D_{11}} P_{cr}^2 \qquad \text{with} \qquad 0.5 < \kappa < 0.75 \qquad (10\text{-}13)$$

with 0.5 being the recommended value for very slender specimens.
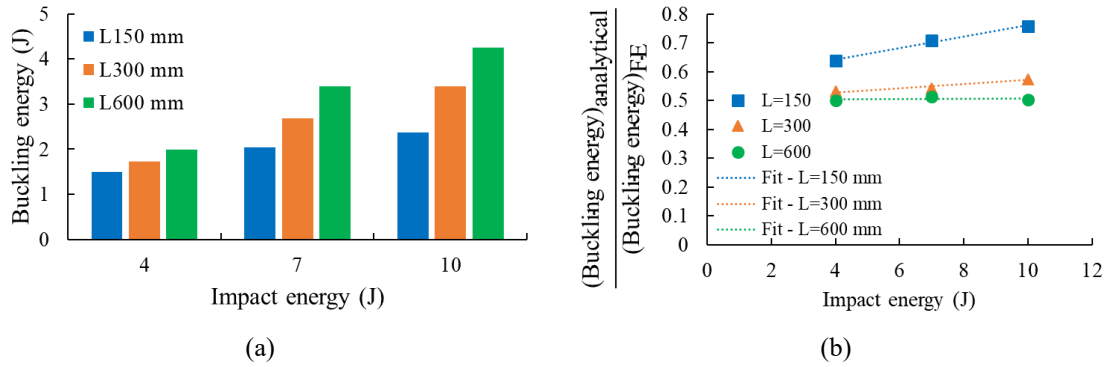
Figure 10-12. (a) Variation of the calculated buckling energy as a function of the impact energy. (b) the ratio of the theoretically (equation (10-12)) and numerically calculated buckling energies.

10.4.4.2. Specimens Hosting an Initial Delamination

As mentioned in previous chapters, similar to fiber-reinforced polymer composites (FRPs), FMLs are also susceptible to delamination, generating a similar detrimental effect. Therefore, it is necessary to account for the influences of delamination when calculating the buckling capacity of FRPs and FMLs. To account for the effect by a practical equation, as done in the preliminary study, the effect of the presence of an initial delamination with varying lengths subject to compressive static and dynamic loading conditions were analyzed numerically. Three delamination lengths were considered, that is 5%, 10% and 20% of the specimen's gage length. Note that in all the previous studies reported in the thesis, a minimum delamination length of 30% was considered. However, from a practical point of view, regular inspections carried out by various industries usually practically limits the length of potential delaminations in such material systems. This is why a shorter

delamination range is considered in this chapter. Moreover, a small delamination assumption will render a more conservative set of equations, which is often preferred by the industry.

The influence of the initial delamination on the buckling response of beams subjected to static and dynamic loading obtained through the FE analyses are shown in Figure 10-13. The capacities were normalized with respect to the buckling capacity of the beam in its intact (non-delaminated) configuration by the following procedure.

Examination of the results indicates that the length of the initial delamination seems to have a greater effect on the buckling capacity under a static loading compared to impact loading. Moreover, the effect of the delamination for the static case seems somewhat inconsistent; in other words, the buckling capacity fluctuates inconsistently, with no distinct trend with respect to the delamination length. Under an impact loading, the capacity of the shortest set of specimens (150 mm) is only marginally affected by the 5% delamination. For all other delamination lengths and impact energies, the normalized buckling capacity seems to stabilize around 0.5 with the increasing specimen length.
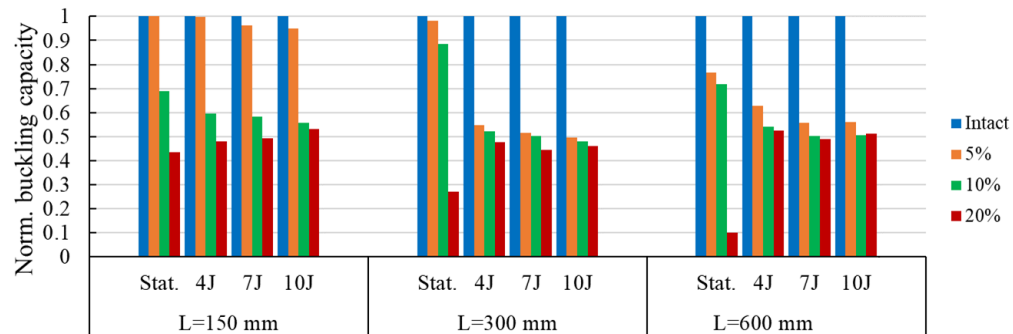
Figure 10-13. Normalized buckling capacity of 3D-FML specimens with various delamination lengths.

Therefore, in developing a simple practical equation for evaluating the buckling capacity of delaminated 3D-FMLs, one should also recognize the fact that in actual applications (e.g., vehicle doors or truck enclosures) the FML would have more slender configurations. Accordingly, therefore, the buckling capacity of slender 3D-FMLs hosting an initial delamination, denoted by P_{buck}^{delam}, can be simply taken as half of the buckling capacity of the intact or non delaminated counterparts, i.e.:

$$P_{buck}^{delam} = 0.5 \, P_{buck}^{imp} \tag{10-14}$$

The same approach can be used in estimating the buckling energy (see Figure 10-14). It should be noted that the fluctuations in the buckling capacity of the considered configurations are primarily amplified due to the quadratic nature of the relationship between the buckling energy and the buckling capacity. Therefore, larger variations in the reported buckling energy results are observed. Interestingly, relatively lower buckling energies are demonstrated by the specimens hosting a 5% initial delamination compared to the specimens having a longer delamination. Nonetheless, similar to the buckling capacity variations, there seems to be a particular range within which the normalized energies fluctuate; that is, within 0.2 and 0.3. Therefore, a simple conservative relationship can be established between the energy of an intact (non-delaminated) 3D-FML and that of a delaminated 3D-FML as:

$$E_{buck}^{delam} = 0.2 \, E_{buck}^{intact} \tag{10-15}$$
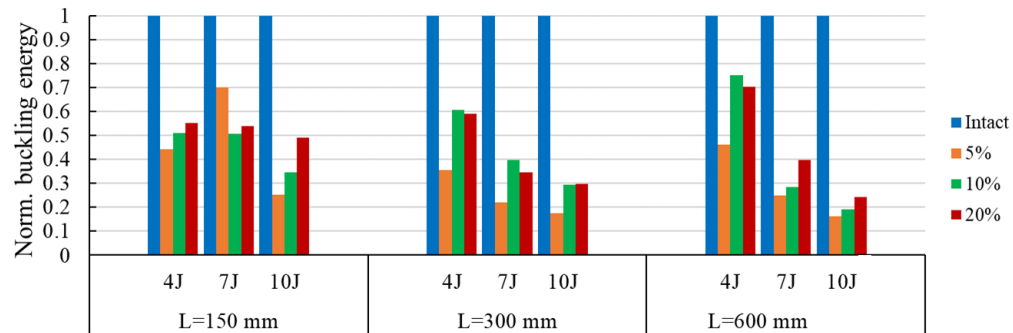
Figure 10-14. Normalized buckling energy of 3D-FML specimens with various delamination lengths.

10.5. Summary and Conclusion

In this chapter, a set of semi-empirical equations was provided as a tool for practicing engineers for a fast and reliable estimation of capacities of novel 3D fiber-metal laminates subject to in-plane static and impact loadings. The equations, which are developed for predicting both the buckling capacity and buckling energy, are based on the results obtained from a series of linear buckling and impact buckling finite element analyses. The

approach is relatively simple, in that a set of adjustment coefficients are provided by which the classical buckling equations of sandwich composites are modified to account for: (i) components length, (ii) the applied impact energy, and (iii) the presence of a potential initial delamination. In addition, while the influence of the inherent geometrical imperfection of 3D-FML specimens is accounted for, however, the potential variation of imperfection amplitude is not taken into account in the equations. A maximum discrepancy of ±8% is observed between the results produced by the equations and the FE results.

Another positive attribute of the proposed equations is the fact that they require only a few material parameters. The author believes that the imperfection issue would be resolved when 3D-FMLs are produced in a control and automated industrial setting. The presented equations are conservative, which is a positive attribute for reliable preliminary design purposes.

Chapter 11: Conclusion

11.1. Summary and Conclusion

The response of magnesium-based 3D fiber-metal laminates (3D-FMLs) subjected to in-plane compressive loading applied at different strain-rates, as well as different low-velocity impact energies, was systematically characterized in this thesis. The effects of specimen length and the presence of an initial delamination were also studied. The characterization was done qualitatively and quantitatively (i) by capturing the actual response of the specimens during the experiments using high-speed cameras; (ii) by examination of the load and displacement data obtained during the experiments, and (iii) by conducting a series of comprehensive finite element (FE) simulations. The evaluation and comparison of the buckling and maximum load-bearing capacities and absorbed energies were the main parameters used for conducting objective comparative analyses. This chapter presents a summary of the findings of the conducted studies.

- It was observed that the applied loads at the lower strain-rates had minimal influence on the load-bearing capacity of the 3D-FML specimens, while the specimens exhibited increased capacity under the low-velocity impact loadings.

- The presence of an initial delamination drastically reduced the load-bearing capacity of the specimens; the exception was the response of the relatively very short specimens.

- The energy required to initiate delamination in virgin specimens was much higher than the energy required to propagate a delamination present in a given specimen.

- The maximum load-bearing capacity of the short specimens corresponded to the onset of delamination-buckling in one of the skins since those specimens did not experience any global buckling. In the longer specimens, the performance observed under an applied quasi-static loading differed from that observed under an impact loading. In the former case, the maximum load was reached after the global buckling occurred, when the skin in the compression side locally delaminated. In the latter case, the maximum load was the load that caused global buckling. It was also observed that the delamination propagated in an unstable manner regardless of the strain rates and impact energies.

The interface bond strength has been found to be the Achilles' heel of all FMLs, including 3D-FMLs. Therefore, a part of this research focused on finding a remedy for this issue. Accordingly, a new surface preparation technique was proposed, consisting of coating the magnesium skins with a thin layer of cold-cured epoxy prior to bonding them to the 3D-FGF constituent. Various mechanical tests were conducted to assess the performance of the proposed technique compared to the conventional method. The outcome of that portion of the work is summarised below:

- The proposed bonding technique increased the load-bearing capacity of the short specimens by approximately 50%. Note that these specimens did not undergo the global buckling mode prior to delamination-buckling of one of their skins and showed significantly lower amount of damage compared to the longer specimens.

- Specimens manufactured using the proposed surface preparation method could resist in-plane impact of 10 J, and remained intact, while specimens manufactured using the conventional method were completely damaged when they underwent a 7 J impact.

- The visual analysis of the fracture surfaces revealed that the crack propagated mainly in the interfacial mode; however, some cohesive mode (the preferred failure mode), could also be observed in some specimens fabricated using the proposed bonding technique.

- The surface preparation had a major influence on enhancing the magnesium/FRP interface strength, while the fracture toughness of the resin had a secondary contribution in enhancing the overall load-bearing capacity of such interfaces.

- The proposed technique has the potential of significantly reducing the production cost of the 3D-FML at an industrial scale.

As a means to improve the bond strength (in conjunction with the proposed surface preparation procedure), the inclusion of graphene nanoplatelets (GNPs) in the resin used to adhere the magnesium skins to the FRP plies was also exported. Various tests were conducted, leading to the following findings:

- The optimal improvement was obtained with 0.5 wt% of GNPs, which enhanced the load-bearing capacity of the intact specimens (i.e., specimens with no initial delamination) by as much as 12.5%.

- It was also observed that the void content in the resin was drastically reduced by introducing the particles.

- The inclusion of GNPs increased the delamination propagation, and only marginally improved the facture response, which occurred predominantly as interfacial type.

- Ironically, the buckling capacity of the specimens tested at the sub-freezing temperature of -50°C was positively affected, especially when the proposed veil bonding technique was used. However, the sub-freezing environment caused an increase in delamination growth, especially in the GNP-reinforced specimens.

- Overall, it is postulated that the lack of chemical compatibility between the resin and magnesium, which led to the interfacial fracture mode, as opposed to the preferred cohesive mode, was the factor restricting the expected positive effect of the GNPs. As a result, it is concluded that the use of the proposed new bonding technique (i.e., the incorporation of fiberglass veil over the metallic bonding interface) would seem to be the more appropriate and cost-effective means for improving the delamination-buckling performance of such hybrid systems.

Since steel is the dominant material in use in the automobile industry, the feasibility of replacing the relatively thicker magnesium skins by thinner high-strength steel skins was also explored. For this, magnesium-based (MG) and steel-based (ST) 3D-FML specimens, having the same bending stiffness, were subjected to quasi-static and axial compressive and lateral impact loadings. The result of that investigation is summarized as follows:

- The ST-based specimens did not perform as well as the MG-based specimens under the imposed loading conditions. The static and impact buckling capacities of the MG-based specimens were 82% and 31% greater than those of the ST-based specimens.

- ST-based specimens exhibited greater delamination extent under lateral impact loading.

- The two types of FMLs also showed different reactions under the quasi-static loading. In the ST-based specimens, first wrinkling of the skin occurred, followed by their global buckling. In contrast, the MG-based specimens first underwent global buckling, which caused the local delamination-buckling of the skin on the compression side.

- The lower performances of the ST-based specimens were attributed to the development of higher magnitudes of stresses in the skins and to the fact that those specimens had

thinner metallic skins compared to their MG-based counterparts. The thinner skins are believed to have become affected by the wavy surface morphology of the glass fabric substrates, which in turn promoted wrinkling of the skins, thereby affecting their load-bearing capacity. Therefore, the use of thicker skins is recommended in the construction of such 3D-FMLs.

In addition to the experimental works, extensive finite element (FE) simulations were performed using LS-DYNA software with the major aims of (i) obtaining further insight into the response of the 3D-FML, (ii) developing a reliable and time-efficient approach for predicting the behaviour of components made of this new class of FML, and (iii) developing an adequate database for developing a set of semi-empirical equations by which practicing engineers could estimate the capacity of a given 3D-FML in a fast and reliable manner. The main conclusions obtained from the numerical investigation are as follows:

- The way in which the boundary conditions are accounted for when modelling the response of such 3D-FMLs under an axial impact has a significant effect on the predicted results. To obtain accurate results, one should explicitly model the actual experimental fixtures used to restrain the specimens.

- The variation in the initial imperfection of a given specimen influences the computed buckling capacity and post-buckling behaviour of the 3D-FMLs significantly, but it has a minor effect on the simulated behaviour within the pre-buckled regime.

- Since the ultimate load capacity of 3D-FMLs is governed by the debonding of the skin from FRP, therefore, the contact between the metallic skins and the FRP plies must be accounted for when simulating their response by FE. This mechanism cannot be detected when using the simplified SHELL model.

- The model constructed with the SOLID element produced the best predictions of the deformed shape and delamination growth, which is believed to be due to the explicit modelling of the pillars of the 3D fabric.

- The SOLID and TSHELL models produced very similar results for the pre- and immediate post-buckling behaviours. However, the computation time consumed by the TSHELL model was 50% lower than that of the SOLID model.

- The simplest model (i.e., SHELL), ran 95% faster than the TSHELL model; however, its use is recommended for analysis of the cases in which the probability of damage developed during impact events is low, or when conducting static analysis.

Finite element modelling was also used to obtain further insight into delamination initiation and propagation in hybrid composites. Specifically, the cohesive and extended finite element (xFEM) features of LS-DYNA were coupled and used within a single model. The model was used for simulating the delamination propagation in a double cantilever beam (DCB) test specimen, and the delamination buckling response of 3D-FML specimens subjected to in-plane compressive loading. Cohesive elements were used to simulate the adhesive/adherend interface, while xFEM elements were used to simulate the bulk portion of the adhesive and the ensuing delamination propagation. The summary of findings of that portion of the work is as follows:

- It was demonstrated that the crack kinking that was experimentally observed to occur within the adhesive could be simulated precisely by combining both the element types. The model that used only the xFEM elements could not capture the phenomenon.
- The above-mentioned combined approaches could also successfully simulate the delamination buckling response of the 3D-FML. The delamination was demonstrated to change its propagation path that had initially started within the adhesive (i.e., through the xFEM elements) towards the adhesive/metal interface, and subsequently propagating along the interface (i.e., through the cohesive elements). This highlights the importance of the role of surface preparation (i.e., interfacial integrity) in enhancing the performances of such FMLs under compressive loading states.
- The use of xFEM elements resulted in more accurate predictions of delamination initiation and propagation. However, from a solution time perspective, the use of cohesive elements is deemed preferable, especially when large complex geometries are to be modelled, so long as the crack or delamination path is known a priori.

Finally, a relatively simple set of semi-empirical equations was developed based on the Euler's buckling equations, adjusted for sandwich composites. The equations account for the effect of specimen's complex shape, initial imperfection and length, and the applied impact energy via a set of adjustment coefficients.

11.2. Recommendations and Future Works

The presented work examined several aspects involved in the in-plane buckling and delamination-buckling responses of 3D-FMLs. Nevertheless, additional works should be pursued to gain a more in-depth understanding of the overall behaviour of such 3D-FMLs subject to various loading and environmental conditions. It is believed that such studies would enable one to further improve the performance of this exemplary class of hybrid material system. Therefore, a series of recommendations are provided in this last section of the thesis.

- The main factor limiting the performances of the 3D-FML remains to be the bonding strength of the metallic skin/FRP interface. A comprehensive study should be performed to investigate the chemical compatibility of polymers and magnesium alloys and identify the compound(s) that could facilitate optimal bonding compatibility. The development of a specific chemical etching surface preparation process to enhance the bonding mechanism, as well as investigating the incorporation of the plasma activation technique for that purpose could also be pursued. The success of such studies would enable one to gain the expected performance usually offered by nanoparticles.

- The use of steel skin as an economical alternative to the magnesium skins was investigated in this project. However, the result of the somewhat limited study was not favourable. It was concluded that the use of the relatively softer and thicker metallic skins (i.e., Mg) as opposed to the stiffer and thinner skins (i.e., steel) would result in a more resilient 3D-FML. However, a detailed parametric study is warranted to examine the coupled effects of skin thickness and stiffness, with a special focus on minimization of the skin wrinkling that was observed in this work. Moreover, the use of aluminium, which has been used in forming the conventional 2D FMLs, should also be investigated.

- The performance and feasibility of coupling cohesive and xFEM elements for prediction of delaminations initiation propagation was demonstrated. However, the integrity of the technique for modelling delamination propagation of an entire 3D-FML specimen subjected to in-plane and out-of-plane impacts would need to be

investigated. To do such an analysis, one would need to precisely calibrate the cohesive parameters, which would have to be done by the use of appropriate experimental data, including the knowledge of the strain rate effect on the material properties.

- Shell elements are customarily used for simulating the performance of a complete vehicle during a crash event since they require much less computation time compared to that required by solid elements. Therefore, a user-defined material subroutine could be developed to account for the reduction in the load-bearing capacity of 3D-FML as a result of the metallic skins undergoing delamination. Being able to account for the sudden decrease in the capacity without performing a demanding delamination analysis could greatly simplify the simulation of the performance of this material system during a full-scale vehicle crash test, as well as lowering the CPU run-time significantly.

- It would also be worthwhile to explore the capabilities of the element-free approaches, such as the element-free Galerkin method and the discrete element method for modelling delamination initiation and propagation in 3D-FMLs. These approaches have been proven to be efficient in simulating crack propagation (Guo & Wu, 2010; Tabiei & Zhang, 2016) and are available through LS-DYNA for both 2D and 3D simulations.

- The research works investigating the performance of this 3D-FML have thus far considered both in-plane and out-of-plane static and dynamic loadings. Given the fact that the main target application of this material is in transport vehicles, the fatigue performance of this material system ought to be investigated and established. In addition, the long-term durability of the material would have to be investigated as well.

- Finally, one of the most important and critical issues encountered in the use of composites as structural materials is their joining and the associated costs of preparation/assembly and inspection. Therefore, appropriate and cost-effective techniques for joining of this material system would have to be developed. Without an effective and efficient joining technique, the application of this exemplary material system would be limited to a very few practical systems.

References

Abdullah, M. R., & Cantwell, W. J. (2006). The impact resistance of polypropylene-based fibre–metal laminates. *Composites Science and Technology*, *66*(11–12), 1682–1693. https://doi.org/10.1016/j.compscitech.2005.11.008

Abedrabbo, N., Mayer, R., Thompson, A., Salisbury, C., Worswick, M., & van Riemsdijk, I. (2009). Crash response of advanced high-strength steel tubes : Experiment and model. *International Journal of Impact Engineering*, *36*(8), 1044–1057. https://doi.org/10.1016/j.ijimpeng.2009.02.006

Abrate, S. (Ed.). (2011). *Impact Engineering of Composite Structures*. Springler Wien New York.

Ahmed, A., & Wei, L. (2016). Introducing CFRP as an alternative material for engine hood to achieve better pedestrian safety using finite element modeling. *Thin-Walled Structures*, *99*, 97–108. https://doi.org/10.1016/j.tws.2015.11.001

Alfano, G., de Barros, S., Champaney, L., & Valoroso, N. (2004). Comparison Between Two Cohesive-Zone Models for the Analysis of Interface Debonding. *European Congress on Computational Methods in Applied Sciences and Engineering ECCOMAS*, 1–18. Retrieved from http://imechanica.org/files/Alfano-Barros-Champaney-Valoroso-ECCM04.pdf

Ari-Gur, J., & Elishakoff, I. (1997). Dynamic instability of a transversely isotropic column subjected to a compression pulse. *Computers & Structures*, *62*(5), 811–815. https://doi.org/10.1016/S0045-7949(96)00295-7

Asaee, Z., Mohamed, M., De Cicco, D., & Taheri, F. (2017). Low-Velocity Impact Response and Damage Mechanism of 3D Fiber-Metal Laminates Reinforced with Amino-Functionalized Graphene Nanoplatelets. *International Journal of Composite Materials*, *7*(1), 20–36. https://doi.org/10.5923/j.cmaterials.20170701.03

Asaee, Z., Mohamed, M., Soumik, S., & Taheri, F. (2017). Experimental and numerical

characterization of delamination buckling behavior of a new class of GNP-reinforced 3D fiber-metal laminates. *Thin-Walled Structures*, *112*(December 2016), 208–216. https://doi.org/10.1016/j.tws.2016.12.015

Asaee, Z., Shadlou, S., & Taheri, F. (2015). Low-velocity impact response of fiberglass/magnesium FMLs with a new 3D fiberglass fabric. *Composite Structures*, *122*, 155–165. https://doi.org/10.1016/j.compstruct.2014.11.038

Asaee, Z., & Taheri, F. (2016). Experimental and numerical investigation into the influence of stacking sequence on the low-velocity impact response of new 3D FMLs. *Composite Structures*, *140*, 136–146. https://doi.org/10.1016/j.compstruct.2015.12.015

Asaee, Z., & Taheri, F. (2017). Enhancement of Performance of Three-Dimensional Fiber Metal Laminates under Low Velocity Impact– A coupled Numerical and Experimental Investigation. *Journal of Sandwich Structures and Materials*, *21*(6), 2127–2153. https://doi.org/10.1177/1099636217740389

Asaee, Z., & Taheri, F. (2018). A practical analytical model for predicting the low-velocity impact response of 3D-fiber metal laminates. *Mechanics of Advanced Materials and Structures*, *0*(0), 1–14. https://doi.org/10.1080/15376494.2018.1472328

ASTM Standard. (2010). ASTM C364-08 Standard Test Method for Edgewise Compressive Strength of Sandwich Constructions. *ASTM International*, *07*(Reapproved 2012), 24–31. https://doi.org/10.1520/C0364

ASTM Standard. (2014). ASTM D5528: Standard Test Method for Mode I Interlaminar Fracture Toughness of Unidirectional Fiber-Reinforced Polymer Matrix Composites. *American Standard of Testing Methods*, *03*(Reapproved 2007), 1–12. https://doi.org/10.1520/D5528-13.2

Asundi, A., & Choi, A. Y. N. (1997). Fiber metal laminates: An advanced material for future aircraft. *Journal of Materials Processing Technology*, *63*(1–3), 384–394. https://doi.org/10.1016/S0924-0136(96)02652-0

Baldan, A. (2004). Adhesively-bonded joints and repairs in metallic alloys, polymers and composite materials: Adhesives, adhesion theories and surface pretreatment. *Journal of Materials Science*, *39*(1), 1–49. https://doi.org/10.1023/B:JMSC.0000007726.58758.e4

Barbero, E. J. (2000). Prediction of buckling-mode interaction in composite columns. *Mechanics of Composite Materials and Structures*, *7*(3), 269–284. https://doi.org/10.1080/10759410050031130

Barenblatt, G. I. (1962). The mathematical theory of equilibrium cracks in brittle fracture. *Advances in Applied Mechanics*, *7*, 55–129. https://doi.org/10.1016/S0065-2156(08)70121-2

Bathe, K. J. (2013). The subspace iteration method - Revisited. *Computers and Structures*, *126*(1), 177–183. https://doi.org/10.1016/j.compstruc.2012.06.002

Beaumont, P., Riewald, P., & Zweben, C. (1975). Methods for improving the impact resistance of composite materials. *Foreign Object Impact Damage to Composites: A Symposium, Philadelphia, Pa., 20 Sept. 1973, Issue 568*, 244.

Belytschko, T., & Black, T. (1999). Elastic crack growth in finite elements with minimal remeshing. *International Journal for Numerical Methods in Engineering*, *45*(5), 601–620. https://doi.org/10.1002/(SICI)1097-0207(19990620)45:5<601::AID-NME598>3.0.CO;2-S

Bhattacharya, S., Singh, I. V., Mishra, B. K., & Bui, T. Q. (2013). Fatigue crack growth simulations of interfacial cracks in bi-layered FGMs using XFEM. *Computational Mechanics*, *52*(4), 799–814. https://doi.org/10.1007/s00466-013-0845-8

Chen, Hao, Yang, Y., & Wang, L. (2015). Vehicle Front Structure Energy Absorbing Optimization in Frontal Impact. *The Open Mechanical Engineering Journal*, *9*(1), 168–172. https://doi.org/10.2174/1874155x01509010168

Chen, Hong, Francesconi, A., Liu, S., & Lan, S. (2017). Effect of honeycomb core under hypervelocity impact: Numerical simulation and engineering model. *Procedia*

Engineering, *204*, 83–91. https://doi.org/10.1016/j.proeng.2017.09.759

Cipriano, A. F., Lin, J., Miller, C., Lin, A., Cortez Alcaraz, M. C., Soria, P., & Liu, H. (2017). Anodization of magnesium for biomedical applications – Processing, characterization, degradation and cytocompatibility. *Acta Biomaterialia*, *62*, 397–417. https://doi.org/10.1016/j.actbio.2017.08.017

Collaud, M., Groening, P., Nowak, S., & Schlapbach, L. (1994). Plasma treatment of polymers: the effect of the plasma parameters on the chemical, physical, and morphological states of the polymer surface and on the metal-polymer interface. *Journal of Adhesion Science and Technology*, *8*(10), 1115–1127. https://doi.org/10.1163/156856194X00979

Compston, P., Cantwell, W. J., Jones, C., & Jones, N. (2001). Impact perforation resistance and fracture mechanisms of a thermoplastic based fiber-metal laminate. *Journal of Materials Science Letters*, *20*(7), 597–599. https://doi.org/10.1023/A:1010904930497

Cortés, P., & Cantwell, W. J. (2005). The fracture properties of a fibre-metal laminate based on magnesium alloy. *Composites Part B: Engineering*, *37*(2–3), 163–170. https://doi.org/10.1016/j.compositesb.2005.06.002

Curiel Sosa, J. L., & Karapurath, N. (2012). Delamination modelling of GLARE using the extended finite element method. *Composites Science and Technology*, *72*(7), 788–791. https://doi.org/10.1016/j.compscitech.2012.02.005

Davalos, J. F., & Qiao, P. (1997). Analytical and experimental study of lateral and distortional buckling of FRP wide-flange beams. *Journal of Composites for Construction*, *1*(4), 150–159. https://doi.org/10.1061/(ASCE)1090-0268(1997)1:4(150)

De Cicco, D., Asaee, Z., & Taheri, F. (2016). Low-velocity impact damage response of fiberglass/magnesium fiber-metal laminates under different size and shape impactors. *Mechanics of Advanced Materials and Structures*, *24*(7), 1–11.

https://doi.org/10.1080/15376494.2016.1162343

De Cicco, D., Asaee, Z., & Taheri, F. (2017). Use of Nanoparticles for Enhancing the Interlaminar Properties of Fiber-Reinforced Composites and Adhesively Bonded Joints—A Review. *Nanomaterials*, *7*(11), 360. https://doi.org/10.3390/nano7110360

De Cicco, D., & Taheri, F. (2016). Delamination Buckling Response of 3D Fiber-Metal Laminates Subjected to Different Loading Rates. *Proceedings of the American Society for Composites: Thirty-First Technical Conference*, 12. Williamsburg, Virginia, USA: DEStech Publications, Inc.

De Cicco, D., & Taheri, F. (2017). Understanding the parameters that influence buckling of 3D fiber-metal laminates. *10th Canadian-International Conference on Composites (CANCOM2017)*. Ottawa, Ontario, Canada.

De Cicco, D., & Taheri, F. (2018a). Delamination Buckling and Crack Propagation Simulations in Fiber-Metal Laminates Using xFEM and Cohesive Elements. *Applied Sciences*, *8*(12), 2440. https://doi.org/10.3390/app8122440

De Cicco, D., & Taheri, F. (2018b). Robust numerical approaches for simulating the buckling response of 3D fiber-metal laminates under axial impact – Validation with experimental results. *Journal of Sandwich Structures and Materials*, *0*(0), 1–30. https://doi.org/10.1177/1099636218789614

De Cicco, D., & Taheri, F. (2018c). Use of a Simple Non-Destructive Technique for Evaluation of the Elastic and Vibration Properties of Fiber-Reinforced and 3D Fiber-Metal Laminate Composites. *Fibers*, *6*(1), 14. https://doi.org/10.3390/fib6010014

De Cicco, D., & Taheri, F. (2019). Enhancement of magnesium-composite bond-interface by a simple combined abrasion and coating method. *Journal of Magnesium and Alloys*, (Article in press). https://doi.org/10.1016/j.jma.2019.02.008

Difelice, R. A., Dillard, J. G., & Yang, D. (2005). An investigation of plasma processes in titanium(iv) isobutoxide: The formation of films on Ti and Si. *International Journal of Adhesion and Adhesives*, *25*(4), 277–287.

https://doi.org/10.1016/j.ijadhadh.2004.09.002

Dogan, F., Hadavinia, H., Donchev, T., & Bhonge, P. S. (2012). Delamination of impacted composite structures by cohesive zone interface elements and tiebreak contact. *Central European Journal of Engineering*, *2*(4), 612–626. https://doi.org/10.2478/s13531-012-0018-0

Esfahani, M. M. N., Ghasemnejad, H., & Barrington, P. E. (2010). Experimental and numerical buckling analysis of delaminated hybrid composite beam structures. *Applied Mechanics and Materials*, *24–25*, 393–400. https://doi.org/10.4028/www.scientific.net/AMM.24-25.393

Fernandes, J. C. S., Ferreira, M. G. S., Haddow, D. B., Goruppa, A., Short, R., & Dixon, D. G. (2002). Plasma-polymerised coatings used as pre-treatement for aluminium alloys. *Surf. Coat. Technol.*, *154*, 8–13. https://doi.org/10.1016/S0257-8972(01)01705-4

Frostig, Y. (1998). Buckling of sandwich panels with a flexible core—high-order theory. *International Journal of Solids and Structures*, *35*(97), 183–204. Retrieved from http://www.sciencedirect.com/science/article/pii/S0020768397000784

Fu, F., Lam, D., & Ye, J. (2007). Parametric study of semi-rigid composite connections with 3-D finite element approach. *Engineering Structures*, *29*(6), 888–898. https://doi.org/10.1016/j.engstruct.2006.07.003

Fuoss, E., Straznicky, P. V., & Poon, C. (1998). Effects of stacking sequence on the impact resistance in composite laminates. Part 2: prediction method. *Composite Structures*, *41*(2), 177–186. https://doi.org/10.1016/S0263-8223(98)00037-3

Gao, Y., & Hoo Fatt, M. S. (2012). Dynamic pulse buckling of single curvature composite shells under external blast. *Thin-Walled Structures*, *52*, 149–157. https://doi.org/10.1016/j.tws.2011.12.010

Gdoutos, E. ., Daniel, I. ., & Wang, K.-A. (2003). Compression facing wrinkling of composite sandwich structures. *Mechanics of Materials*, *35*(3–6), 511–522.

233

https://doi.org/10.1016/S0167-6636(02)00267-3

Giuliese, G., Pirondi, A., & Moroni, F. (2014). A Cohesive Zone Model for Three-dimensional Fatigue Debonding/Delamination. *Procedia Materials Science*, *3*, 1473–1478. https://doi.org/10.1016/j.mspro.2014.06.238

Gong, W., Chen, J., & Patterson, E. A. (2016). Buckling and delamination growth behaviour of delaminated composite panels subject to four-point bending. *Composite Structures*, *138*, 122–133. https://doi.org/10.1016/j.compstruct.2015.11.054

Gonzalez, E., Barankin, M. D., Guschl, P. C., & Hicks, R. F. (2010). Surface Activation of Poly(methyl methacrylate) via Remote Atmospheric Pressure Plasma. *Plasma Processes and Polymers*, *7*(6), 482–493. https://doi.org/Doi 10.1002/Ppap.200900113

Goyal, V. K., Johnson, E. R., & Dávila, C. G. (2004). Irreversible constitutive law for modeling the delamination process using interfacial surface discontinuities. *Composite Structures*, *65*(3–4), 289–305. https://doi.org/10.1016/j.compstruct.2003.11.005

Griskevicius, P., & Ziliukas, A. (2003). The crash energy absorption of the vehicles front structures. *Transport*, *18*(2), 97–101. https://doi.org/10.1080/16483840.2003.10414073

Grujicic, M., Arakere, G., Sellappan, V., Ziegert, J. C., & Schmueser, D. (2009). Multi-Disciplinary Design Optimization of a Composite Car Door for Structural Performance, NVH, Crashworthiness, Durability and Manufacturability. *Multidiscipline Modeling in Materials and Structures*, *5*(1), 1–28. https://doi.org/10.1108/15736105200900001

Grujicic, M., Sellappan, V., Omar, M. A., Seyr, N., Obieglo, A., Erdmann, M., & Holzleitner, J. (2008). An overview of the polymer-to-metal direct-adhesion hybrid technologies for load-bearing automotive components. *Journal of Materials Processing Technology*, *197*(1–3), 363–373.

https://doi.org/10.1016/j.jmatprotec.2007.06.058

Gu, B., & Xu, J. (2004). Finite element calculation of 4-step 3-dimensional braided composite under ballistic perforation. *Composites Part B: Engineering*, *35*(4), 291–297. https://doi.org/10.1016/j.compositesb.2004.01.001

Gu, H., & Chattopadhyay, A. (1999). An experimental investigation of delamination buckling and post buckling of composite laminates. *Composites Science and Technology*, *59*, 903–910. https://doi.org/10.1016/S0266-3538(98)00130-4

Gu, X., Zheng, Y., Cheng, Y., Zhong, S., & Xi, T. (2009). In vitro corrosion and biocompatibility of binary magnesium alloys. *Biomaterials*, *30*(4), 484–498. https://doi.org/10.1016/j.biomaterials.2008.10.021

Guo-dong, F., Jun, L., & Bao-lai, W. (2009). Progressive damage and nonlinear analysis of 3D four-directional braided composites under unidirectional tension. *Composite Structures*, *89*(1), 126–133. https://doi.org/10.1016/j.compstruct.2008.07.016

Guo, Y., & Wu, C. T. (2010). XFEM and EFG Cohesive Fracture Analysis for Brittle and Semi-Brittle Materials. *11th International LS-DYNA Users Conference*, (2), 21–32. Retrieved from http://www.dynalook.com/international-conf-2010/Simulation-2-3.pdf

Han, H. (2006). *Stability and crushing behavior of cylindrical tubes with a cutout*. Dalhousie University.

Han, H., & Taheri, F. (2006). Comparison of LS-DYNA and NISA in Solving Dynamic. *9th International LS-DYNA Users Conference*, (1), 33–44.

Han, H., Taheri, F., & Pegg, N. (2011). Crushing behaviors and energy absorption efficiency of hybrid pultruded and ±45° braided tubes. *Mechanics of Advanced Materials and Structures*, *18*(4), 287–300. https://doi.org/10.1080/15376494.2010.506103

Han, H., Taheri, F., Pegg, N., & Lu, Y. (2007). A numerical study on the axial crushing

response of hybrid pultruded and ±45° braided tubes. *Composite Structures*, *80*(2), 253–264. https://doi.org/10.1016/j.compstruct.2006.05.012

Harris, A. F., & Beevers, A. (1999). The ffects of grit-blasting on surface properties for adhesion. *International Journal of Adhesion and Adhesives*, *19*(6), 445–452. https://doi.org/10.1016/S0143-7496(98)00061-X

Hosseini, S. A., Sadighi, M., & Maleki Moghadam, R. (2015). Low-velocity impact behavior of hollow core woven sandwich composite: Experimental and numerical study. *Journal of Composite Materials*, *49*(26), 3285–3295. https://doi.org/10.1177/0021998314561811

Hwang, S.-F., & Liu, G.-H. (2002). Experimental Study for Buckling and Postbuckling Behaviors of Composite Laminates with Multiple Delaminations. *Journal of Reinforced Plastics and Composites*, *21*(4), 333–349. https://doi.org/10.1106/073168402026253

Ishida, H. (1984). A review of recent progress in the studies of molecular and microstructure of coupling agents and their functions in composites, coatings and adhesive joints. *Polymer Composites*, *5*(2), 101–123. https://doi.org/10.1002/pc.750050202

Johar, M., Kosnan, M. S. E., & Tamin, M. N. (2014). Cyclic Cohesive Zone Model for Simulation of Fatigue Failure Process in Adhesive Joints. *Applied Mechanics and Materials*, *606*, 217–221. https://doi.org/10.4028/www.scientific.net/AMM.606.217

Kenny, S., Pegg, N., & Taheri, F. (2002). Finite element investigations on the dynamic plastic buckling of a slender beam subject to axial impact. *International Journal of Impact Engineering*, *27*(2), 179–195. https://doi.org/10.1016/S0734-743X(01)00048-3

Kenny, S., Taheri, F., & Pegg, N. (2002). Experimental investigations on the dynamic plastic buckling of a slender beam subject to axial impact. *International Journal of Impact Engineering*, *27*(1), 1–17. https://doi.org/10.1016/S0734-743X(01)00026-4

Kenny, Shawn. (2001). *Dynamic Pulse Buckling of Slender Beams with Geometric Imperfections Subjected to an Axial Impact*. Dalhousie University.

Kharab, A., & Guenther, R. B. (2012). *Numerical Methods: A MATLAB Approach* (Third edit). Boca Raton, FL, USA: CRC Press.

Khorshidi, B., Soltannia, B., Thundat, T., & Sadrzadeh, M. (2017). Synthesis of thin film composite polyamide membranes: Effect of monohydric and polyhydric alcohol additives in aqueous solution. *Journal of Membrane Science*, *523*(2017), 336–345. https://doi.org/10.1016/j.memsci.2016.09.062

Kiani, M., Gandikota, I., Rais-Rohani, M., & Motoyama, K. (2014). Design of lightweight magnesium car body structure under crash and vibration constraints. *Journal of Magnesium and Alloys*, *2*(2), 99–108. https://doi.org/10.1016/j.jma.2014.05.005

Kim, D.-H., Kim, H.-G., & Kim, H.-S. (2015). Design optimization and manufacture of hybrid glass/carbon fiber reinforced composite bumper beam for automobile vehicle. *Composite Structures*, *131*, 742–752. https://doi.org/10.1016/j.compstruct.2015.06.028

Kim, H.-J., & Hong, C.-S. (1997). Buckling and Postbuckling Behavior of Composite Laminates With a Delamination. *Composites Science and Technology*, *57*(5), 557–564. https://doi.org/10.1016/S0266-3538(97)00011-0

Kim, J.-K., & Mai, Y.-W. (1998). *Engineered interfaces in fiber reinforced composites*. Elsevier.

Kim, M. C., Yang, S. H., Boo, J.-H., & Han, J. G. (2003). Surface treatment of metals using an atmospheric pressure plasma jet and their surface characteristics. *Surface and Coatings Technology*, *174–175*, 839–844. https://doi.org/10.1016/S0257-8972

Kim, Y. T., Lee, M. J., & Lee, B. C. (2011). Simulation of adhesive joints using the superimposed finite element method and a cohesive zone model. *International Journal of Adhesion and Adhesives*, *31*(5), 357–362. https://doi.org/10.1016/j.ijadhadh.2010.11.015

Ko, Y.-M., Choe, H.-C., Jung, S.-C., & Kim, B.-H. (2013). Plasma deposition of a silicone-like layer for the corrosion protection of magnesium. *Progress in Organic Coatings*, *76*(12), 1827–1832. https://doi.org/10.1016/j.porgcoat.2013.05.024

Kollár, L. (2003). Local buckling of fiber reinforced plastic composite structural members with open and closed cross sections. *Journal of Structural Engineering*, *129*(11), 1503–1513. https://doi.org/doi:10.1061/(ASCE)0733-9445(2003)129:11(1503)

Krueger, R. (2004). Virtual crack closure technique: History, approach, and applications. *Applied Mechanics Reviews*, *57*(2), 109–143. https://doi.org/10.1115/1.1595677

Kubit, A., Bucior, M., & Zielecki, W. (2016). The impact of the multiwall carbon nanotubes on the fatigue properties of adhesive joints of 2024-T3 aluminium alloy subjected to peel. *Procedia Structural Integrity*, *2*(21st European Conference on Fracture, ECF21, 20-24 June 2016, Catania, Italy), 334–341. https://doi.org/10.1016/j.prostr.2016.06.043

Laboratory Test Procedure For New Car Assessment Program. (2012). Retrieved from file:///C:/Users/NCAC/Downloads/Frontal_TP_NCAP.pdf

Lefebvre, D. R., Ahn, B. K., Dillard, D. A., & Dillard, J. G. (2002). The effect of surface treatments on interfacial fatigue crack initiation in aluminum / epoxy bonds. *International Journal of Fracture*, *114*, 191–202.

Lemmen, P., Meijer, G.-J., & Rasmussen, E. A. (1999). Dynamic behavior of composite ship structures (DYCOSS). Failure prediction tool. *70th Shock and Vibration Symposium*, 15–19. Albuquerque, NM, US.

Li, Y., Lin, Z., Jiang, A., & Chen, G. (2003). Use of high strength steel sheet for lightweight and crashworthy car body. *Materials and Design*, *24*(3), 177–182. https://doi.org/10.1016/S0261-3069(03)00021-9

Lifshitz, J. M. (1976). Impact Strength of Angle Ply Fiber Reinforced Materials. *Journal of Composite Materials*, *10*(1), 92–101. https://doi.org/10.1177/002199837601000108

Lindberg, H. E., & Florence, A. L. (1987). *Dynamic Pulse Buckling*. Boston, MA, USA: Martinus Nihoff Publishers.

Liu, Y. X., & Liaw, B. M. (2004). Drop-Weight Impact on Fiber-Metal Laminates Using Various Indenters. *SEM X International Congress & Exposition Exposition on Experimental and Applied Mechanics*, (386), 1–9. Retrieved from http://www.abdmatrix.com/phcdl/upload/fiber metal laminates/Drop Weight Impact on Fiber-Metal Laminates usig Various Indenters.pdf

Livadifiis, G. J. (1986). A chemical etching system for creating micromechanical retention in resin-bonded retainers. *The Journal of Prosthetic Dentistry*, *56*(2), 181–188.

LS-DYNA R9.0. (2016a). *KEYWORD USER'S MANUAL VOLUME I*. Livermore Software Technology Corporation (LSTC).

LS-DYNA R9.0. (2016b). *KEYWORD USER'S MANUAL VOLUME II*. Livermore Software Technology Corporation (LSTC).

Mactabi, R., Rosca, I. D., & Hoa, S. V. (2013). Monitoring the integrity of adhesive joints during fatigue loading using carbon nanotubes. *Composites Science and Technology*, *78*, 1–9. https://doi.org/10.1016/j.compscitech.2013.01.020

Mamalis, A. G., Manolakos, D. E., Ioannidis, M. B., & Kostazos, P. K. (2003). Crushing of hybrid square sandwich composite vehicle hollow bodyshells with reinforced core subjected to axial loading : numerical simulation. *Composite Structures*, *61*, 175–186. https://doi.org/10.1016/S0263-8223(03)00069-2

Marzi, S., Ramon-Villalonga, L., Poklitar, M., & Kleiner, F. (2008). Usage of cohesive elements in crash analysis of large, bonded vehicle structures. Experimental tests and simulation. *German LS-Dyna Forum*, 1–20. Bamberg, Germany: DYNAmore GmbH.

Menna, C., Asprone, D., Caprino, G., Lopresto, V., & Prota, A. (2011). Numerical simulation of impact tests on GFRP composite laminates. *International Journal of Impact Engineering*, *38*(8–9), 677–685. https://doi.org/10.1016/j.ijimpeng.2011.03.003

Miravete, A., Bielsa, J. M., Chiminelli, A., Cuartero, J., Serrano, S., Tolosana, N., & Guzman de Villoria, R. (2006). 3D mesomechanical analysis of three-axial braided composite materials. *Composites Science and Technology*, *66*(15), 2954–2964. https://doi.org/10.1016/j.compscitech.2006.02.015

Mitrevski, T., Marshall, I. H., Thomson, R., Jones, R., & Whittingham, B. (2005). The effect of impactor shape on the impact response of composite laminates. *Composite Structures*, *67*(2), 139–148. https://doi.org/10.1016/j.compstruct.2004.09.007

Moës, N., Dolbow, J., & Belytschko, T. (1999). A finite element method for crack growth without remeshing. *International Journal for Numerical Methods in Engineering*, *46*(1), 131–150. https://doi.org/10.1002/(SICI)1097-0207(19990910)46:1<131::AID-NME726>3.0.CO;2-J

Mohamed, M., & Taheri, F. (2018). Fracture response of double cantilever beam subject to thermal fatigue. *The Journal of Strain Analysis for Engineering Design*. https://doi.org/10.1177/0309324718791095

Mollenhauer, D., Zhou, E., Hoos, K., Iarve, E., Braginsky, M., Breitzman, T., & Rapking, D. (2016). Multi-Scale Simulation of Delamination Migration. *Proceedings of the American Society for Composites: Thirty-First Technical Conference*, 10. Williamsburg, Virginia: DEStech Publications, Inc.

Montemurro, M., Vincenti, A., & Vannucci, P. (2012). A Two-Level Procedure for the Global Optimum Design of Composite Modular Structures-Application to the Design of an Aircraft Wing. Part 2: Numerical Aspects and Examples. *Journal of Optimization Theory and Applications*, *155*(1), 24–53. https://doi.org/10.1007/s10957-012-0070-1

Monticelli, F., Osorio, R., Sadek, F. T., Radovic, I., Toledano, M., & Ferrari, M. (2008). Surface Treatments for Improving Bond Strength to Prefabricated Fiber Posts: A Literature Review. *Operative Dentistry*, *33*(3), 346–355. https://doi.org/10.2341/07-86

Motamedi, D., & Mohammadi, S. (2012). Fracture analysis of composites by time independent moving-crack orthotropic XFEM. *International Journal of Mechanical Sciences*, *54*(1), 20–37. https://doi.org/10.1016/j.ijmecsci.2011.09.004

Noeske, M., Degenhardt, J., Strudthoff, S., & Lommatzsch, U. (2004). Plasma jet treatment of five polymers at atmospheric pressure: Surface modifications and the relevance for adhesion. *International Journal of Adhesion and Adhesives*, *24*(2), 171–177. https://doi.org/10.1016/j.ijadhadh.2003.09.006

Palkowski, H., & Lange, G. (2008). Production of tailored high strength hybrid sandwich structures. *Steel Research International*, *79*(3), 178–185. https://doi.org/10.2374/SRI07SP119-79-2008-178-185

Pärnänen, T., Alderliesten, R., Rans, C., Brander, T., & Saarela, O. (2012). Applicability of AZ31B-H24 magnesium in Fibre Metal Laminates - An experimental impact research. *Composites Part A: Applied Science and Manufacturing*, *43*(9), 1578–1586. https://doi.org/10.1016/j.compositesa.2012.04.008

Pascoe, J. A., Alderliesten, R. C., & Benedictus, R. (2013). Methods for the prediction of fatigue delamination growth in composites and adhesive bonds - A critical review. *Engineering Fracture Mechanics*, *112–113*, 72–96. https://doi.org/10.1016/j.engfracmech.2013.10.003

Petras, A. (1999). *Design of sandwich structures*. University of Cambridge.

Prolongo, S. G., & Ureña, A. (2009). Effect of surface pre-treatment on the adhesive strength of epoxy-aluminium joints. *International Journal of Adhesion and Adhesives*, *29*(1), 23–31. https://doi.org/10.1016/j.ijadhadh.2008.01.001

Radha, R., & Sreekanth, D. (2017). Insight of magnesium alloys and composites for orthopedic implant applications – a review. *Journal of Magnesium and Alloys*, *5*(3), 286–312. https://doi.org/10.1016/j.jma.2017.08.003

Ranatunga, V. (2011). Finite Element Modeling of Delamination Crack Propagation in Laminated Composites. *Proceedings of the World Congress on Engineering*, *III*.

London, United Kingdom.

Remmers, J. J. C., & de Borst, R. (2001). Delamination buckling of fibre-metal laminates. *Composites Science and Technology*, *61*(15), 2207–2213. https://doi.org/10.1016/S0266-3538(01)00114-2

Ryan, S., Schaefer, F., Destefanis, R., & Lambert, M. (2008). A ballistic limit equation for hypervelocity impacts on composite honeycomb sandwich panel satellite structures. *Advances in Space Research*, *41*(7), 1152–1166. https://doi.org/10.1016/j.asr.2007.02.032

Sadighi, M., Pärnänen, T., Alderliesten, R. C., Sayeaftabi, M., & Benedictus, R. (2012). Experimental and Numerical Investigation of Metal Type and Thickness Effects on the Impact Resistance of Fiber Metal Laminates. *Applied Composite Materials*, *19*(3), 545–559. https://doi.org/10.1007/s10443-011-9235-6

Sam, C., Papoulia, K. D., & Vavasis, S. A. (2005). Obtaining initially rigid cohesive finite element models that are temporally convergent. *Engineering Fracture Mechanics*, *72*, 2247–2267. https://doi.org/10.1016/j.engfracmech.2004.12.008

Sang Park, Y., Choi, W. J., Choi, H. S., & Kwon, H. (2010). Effects of surface pre-treatment and void content on GLARE laminate process characteristics. *Journal of Materials Processing Technology*, *210*(8), 1008–1016. https://doi.org/10.1016/j.jmatprotec.2010.01.017

Sapora, A., & Paggi, M. (2014). A coupled cohesive zone model for transient analysis of thermoelastic interface debonding. *Computational Mechanics*, *53*(4), 845–857. https://doi.org/10.1007/s00466-013-0934-8

Schweizerhof, K., Weimar, K., Munz, T., & Rottner, T. (1998). Crashworthiness Analysis with Enhanced Composite Material Models in LS-DYNA - Merits and Limits. *LS-DYNA World Conference*, 17. Detroit, Michigan, USA.

Serna Moreno, M. C., Curiel-Sosa, J. L., Navarro-Zafra, J., Martínez Vicente, J. L., & López Cela, J. J. (2014). Crack propagation in a chopped glass-reinforced composite

under biaxial testing by means of XFEM. *Composite Structures*, *119*, 264–271. https://doi.org/10.1016/j.compstruct.2014.08.030

Shah, P. K. (2005). *Adhesion of injection molded PVC to silane primed steel*. MSc thesis, Departement of Chemical and Materials Engineering, University of Cincinnati.

Shahid, M., & Hashim, S. A. (2002). Effect of surface roughness on the strength of cleavage joints. *International Journal of Adhesion and Adhesives*, *22*(3), 235–244. https://doi.org/10.1016/S0143-7496(01)00059-8

Siegfried, M., Tola, C., Claes, M., Lomov, S. V., Verpoest, I., & Gorbatikh, L. (2014). Impact and residual after impact properties of carbon fiber/epoxy composites modified with carbon nanotubes. *Composite Structures*, *111*(1), 488–496. https://doi.org/10.1016/j.compstruct.2014.01.035

Sinmazçelik, T., Avcu, E., Bora, M. Ö., & Çoban, O. (2011). A review: Fibre metal laminates, background, bonding types and applied test methods. *Materials & Design*, *32*(7), 3671–3685. https://doi.org/10.1016/j.matdes.2011.03.011

Siow, Y. P., & Shim, V. P. W. (1998). An Experimental Study of Low Velocity Impact Damage in Woven Fiber Composites. *Journal of Composite Materials*, *32*(12), 1178–1202. https://doi.org/10.1177/002199839803201203

Sokolova, O. A., Kühn, M., & Palkowski, H. (2012). Deep drawing properties of lightweight steel/polymer/steel sandwich composites. *Archives of Civil and Mechanical Engineering*, *12*(2), 105–112. https://doi.org/10.1016/j.acme.2012.05.001

Soltannia, B., & Sameoto, D. (2014). Strong, reversible underwater adhesion via gecko-inspired hydrophobic fibers. *ACS Applied Materials and Interfaces*, *6*(24), 21995–22003. https://doi.org/10.1021/am5075375

Soltannia, B., & Taheri, F. (2013). Static, Quasi-Static and High Loading Rate Effects on Graphene Nano-Reinforced Adhesively Bonded Single-Lap Joints. *International Journal of Composite Materials*, *2013*(6), 181–190.

https://doi.org/10.5923/j.cmaterials.20130306.07

Soltannia, B., & Taheri, F. (2015a). Influence of nano-reinforcement on the mechanical behavior of adhesively bonded single-lap joints subjected to static, quasi-static, and impact loading. *Journal of Adhesion Science and Technology*, *29*(5), 424–442. https://doi.org/10.1080/01694243.2014.991060

Soltannia, B., & Taheri, F. (2015b). Influence of nano-reinforcement on the mechanical behavior of adhesively bonded single-lap joints subjected to static, quasi-static, and impact loading. *Journal of Adhesion Science and Technology*, *29*(5), 424–442. https://doi.org/10.1080/01694243.2014.991060

Song, S. H., Byun, Y. S., Ku, T. W., Song, W. J., Kim, J., & Kang, B. S. (2010). Experimental and Numerical Investigation on Impact Performance of Carbon Reinforced Aluminum Laminates. *Journal of Materials Science and Technology*, *26*(4), 327–332. https://doi.org/10.1016/S1005-0302(10)60053-9

Sotiropoulou, A. B., & Panayotounakos, D. E. (2004). Exact parametric analytic solutions of the elastica ODEs for bars including effects of the transverse deformation. *International Journal of Non-Linear Mechanics*, *39*(10), 1555–1570.

Stickler, P. B., & Ramulu, M. (2002). Parametric analyses of stitched composite T-joints by the finite element method. *Materials & Design*, *23*(8), 751–758. https://doi.org/10.1016/S0261-3069(02)00070-5

Sugiman, S., Crocombe, A. D., & Aschroft, I. A. (2013). Experimental and numerical investigation of the static response of environmentally aged adhesively bonded joints. *International Journal of Adhesion and Adhesives*, *40*, 224–237. https://doi.org/10.1016/j.ijadhadh.2012.08.007

Sun, X., & Sun, C. (2004). Mechanical properties of three-dimensional braided composites. *Composite Structures*, *65*(3–4), 485–492. https://doi.org/10.1016/j.compstruct.2003.12.009

Tabiei, A., & Zhang, W. (2016). Evaluation of Various Numerical Methods in LS-DYNA

for 3D Crack Propagation. *14th International LS-DYNA Users Conference*, 1–19. Detroit, MI, USA: Livermore Software Technology Corporation.

Taheri, F., & Moradi, S. (2000). A robust methodology for the simulation of postbuckling response of composite plates. *Computational Mechanics*, *26*, 295–301. https://doi.org/https://doi.org/10.1007/s004660000173

Taheri, Farid. (1997). Effect of Whisker Inclusion in Improving the Strength and Ductility of Composite/Metal Bonded Joints. *ASTM Journal of Composites Technology and Research*, *19*(2), 82–88.

Tang, J., Wang, J., Xie, X., Zhang, P., Lai, Y., Li, Y., & Qin, L. (2013). Surface coating reduces degradation rate of magnesium alloy developed for orthopaedic applications. *Journal of Orthopaedic Translation*, *1*(1), 41–48. https://doi.org/10.1016/j.jot.2013.06.003

The Adhesives Design Toolkit. (n.d.). Adhesive bonding - a guide to best practice. In Adhesive Toolkits. Retrieved May 23, 2018, from http://www.adhesivestoolkit.com/Docu-Data/SurfacePreTreatment.xtp#ref18

Tsuda, T., Ohnishi, Y., Ohtagaki, R., Cho, K., & Fujimoto, T. (2015). Three-Point Bending Crack Propagation Analysis of Beam Subjected to Eccentric Impact Loading by X-FEM. *10th European LS-DYNA Conference*, 10. Würwburg; Germany: Livermore Software Technology Corporation.

Tvergaard, V., & Hutchinson, J. W. (1992). The relation between crack growth resistance and fracture process parameters in elastic-plastic solids. *Journal of the Mechanics and Physics of Solids*, *40*(6), 1377–1397. https://doi.org/10.1016/0022-5096(92)90020-3

Varmint's Al. (n.d.). Varmint's Al's Engineering Page. Retrieved from http://www.varmintal.com/aengr.htm

Vlot, A., Vogelesang, L. B., & De Vries, T. J. (1999). Towards application of fibre metal laminates in large aircraft. *Aircraft Engineering and Aerospace Technology*, *71*(6), 558–570. https://doi.org/10.1108/00022669910303711

VolvoCars. (2019). Volvo S60 Crash Test Frontal Collision 35 mph Top. Retrieved June 10, 2019, from EuroCars News website: http://www.eurocarnews.com/20/0/0/1092/volvo-s60-crash-test-frontal-collision-35-mph-top/gallery-detail.html

Vonach, W. K., & Rammerstorfer, F. G. (2000). Wrinkling of thick orthotropic sandwich plates under general loading conditions. *Applied Mechanics*, *70*(January 1999), 338–348. https://doi.org/10.1007/s004199900065

Wang, B., Bai, Y., Hu, X., & Lu, P. (2016). Enhanced epoxy adhesion between steel plates by surface treatment and CNT/short-fibre reinforcement. *Composites Science and Technology*, *127*, 149–157. https://doi.org/10.1016/j.compscitech.2016.03.008

Wang, B., Hu, X., Hui, J., Lu, P., & Jiang, B. (2018). CNT-reinforced adhesive joint between grit-blasted steel substrates fabricated by simple resin pre-coating method. *The Journal of Adhesion*, *94*(7), 529–540. https://doi.org/10.1080/00218464.2017.1301255

Wang, B., Hu, X., & Lu, P. (2017). Improvement of adhesive bonding of grit-blasted steel substrates by using diluted resin as a primer. *International Journal of Adhesion and Adhesives*, *73*(December 2016), 92–99. https://doi.org/10.1016/j.ijadhadh.2016.11.012

Wang, C. M., & Wang, C. Y. (2004). *Exact solutions for buckling of structural members*. CRC press.

Wang, S., Harvey, C. M., Wang, B., & Watson, A. (2015). Post-local buckling-driven delamination in bilayer composite beams. *Composite Structures*, *133*, 1058–1066. https://doi.org/10.1016/j.compstruct.2015.08.012

Wang, Y., Cerigato, C., Waisman, H., & Benvenuti, E. (2017). XFEM with high-order material-dependent enrichment functions for stress intensity factors calculation of interface cracks using Irwin's crack closure integral. *Engineering Fracture Mechanics*, *178*, 148–168. https://doi.org/10.1016/j.engfracmech.2017.04.021

Wang, Y., & Waisman, H. (2015). Progressive delamination analysis of composite materials using XFEM and a discrete damage zone model. *Computational Mechanics*, *55*(1), 1–26. https://doi.org/10.1007/s00466-014-1079-0

Wang, Y., & Waisman, H. (2016). From diffuse damage to sharp cohesive cracks: A coupled XFEM framework for failure analysis of quasi-brittle materials. *Computer Methods in Applied Mechanics and Engineering*, *299*, 57–89. https://doi.org/10.1016/j.cma.2015.10.019

Wang, Y., & Waisman, H. (2017). Material-dependent crack-tip enrichment functions in XFEM for modeling interfacial cracks in bimaterials. *International Journal for Numerical Methods in Engineering*, *112*(11), 1495–1518. https://doi.org/10.1002/nme.5566

Williams, T. S., Yu, H., & Hicks, R. F. (2013). Atmospheric pressure plasma activation of polymers and composites for adhesive bonding. *Reviews of Adhesion and Adhesives*, *1*(1), 46–87. https://doi.org/10.7569/RAA.2013.097302

Xiao, X., Botkin, M. E., & Johnson, N. L. (2009). Axial crush simulation of braided carbon tubes using MAT58 in LS-DYNA. *Thin-Walled Structures*, *47*, 740–749. https://doi.org/10.1016/j.tws.2008.12.004

Xu, X.-P., & Needleman, A. (1994). Numerical simulations of fast crack growth in brittle solids. *Journal of the Mechanics and Physics of Solids*, *42*(9), 1397–1434. https://doi.org/10.1016/0022-5096(94)90003-5

Yap, C. W., Chai, G. B., Song, J., & Joshi, S. C. (2015). Upper and lower bound buckling load of perfect and delaminated fiber-reinforced composite columns. *Composite Structures*, *122*, 376–389. https://doi.org/10.1016/j.compstruct.2014.12.002

Yelve, N. P., & Khan, N. N. (2013). Analysis of Traction Separation in Double Cantilever Beam Using Cohesive Zone Modeling. *International Conference on Mechanical and Industrial Engineering (ICMIE)*, 47–50. Penang, Malaysia.

Yen, C. F. (2002). Ballistic Impact Modeling of Composite Materials. *7th International*

LS-DYNA Users Conference, *6*, 15–26. Retrieved from http://www.dynalook.com/international-conf-2002/Session_6-3.pdf

Zaldivar, R. J., Nokes, J., Steckel, G. L., Kim, H. I., & Morgan, B. a. (2009). The Effect of Atmospheric Plasma Treatment on the Chemistry, Morphology and Resultant Bonding Behavior of a Pan-Based Carbon Fiber-Reinforced Epoxy Composite. *Journal of Composite Materials*, *0*(00). https://doi.org/10.1177/0021998309345343

Zeng, T., Fang, D. N., & Lu, T. J. (2005). Dynamic crashing and impact energy absorption of 3D braided composite tubes. *Materials Letters*, *59*(12), 1491–1496. https://doi.org/10.1016/j.matlet.2005.01.007

Zenkert, D. (1997). *An introduction to sandwich construction*. Cradley Heath, England, UK: Engineering Materials Advisory Services.

Zhang, C., Curiel-Sosa, J. L., & Bui, T. Q. (2017a). A novel interface constitutive model for prediction of stiffness and strength in 3D braided composites. *Composite Structures*, *163*, 32–43. https://doi.org/10.1016/j.compstruct.2016.12.042

Zhang, C., Curiel-Sosa, J. L., & Bui, T. Q. (2017b). Comparison of periodic mesh and free mesh on the mechanical properties prediction of 3D braided composites. *Composite Structures*, *159*, 667–676. https://doi.org/10.1016/j.compstruct.2016.10.012

Zhang, Z., & Taheri, F. (2002a). Dynamic Pulsebuckling Analysis of FRP Composite Laminated Beams Using LS-DYNA. *7th International LS-DYNA Users Conference*, (1), 41–48.

Zhang, Z., & Taheri, F. (2002b). Numerical studies on dynamic pulse buckling of FRP composite laminated beams subject to an axial impact. *Composite Structures*, *56*(3), 269–277. https://doi.org/10.1016/S0263-8223(02)00012-0

Zhang, Z., & Taheri, F. (2004). Dynamic pulse-buckling behavior of "quasi-ductile" carbon/epoxy and E-glass/epoxy laminated composite beams. *Composite Structures*, *64*(3–4), 269–274. https://doi.org/10.1016/j.compstruct.2003.08.008

Zhao, S., Zhang, J., Weng, D., & Wu, X. (2003). A method to form well-adhered γ-Al2O3 layers on FeCrAl metallic supports. *Surface and Coatings Technology*, *167*(1), 97–105. https://doi.org/10.1016/S0257-8972(02)00859-9

Zhu, S., & Chai, G. B. (2012). Low-velocity impact response of fibre-metal laminates - Experimental and finite element analysis. *Composites Science and Technology*, *72*(15), 1793–1802. https://doi.org/10.1016/j.compscitech.2012.07.016

Zielecki, W., Kubit, A., Trzepieciński, T., Narkiewicz, U., & Czech, Z. (2017). Impact of multiwall carbon nanotubes on the fatigue strength of adhesive joints. *International Journal of Adhesion and Adhesives*, *73*, 16–21. https://doi.org/10.1016/j.ijadhadh.2016.11.005

Appendix A: Load Cell Specifications

2518/2525-100 Series Load Cells
Catalog number 2525-108/112
2518-100/101/102/103/107/111

INSTRON

Features

- Full-scale static rated capacities from
  ±5 kN to ±200 kN (500 kgf, 1,124 lbf to
  20,000 kgf, 44, 960 lbf)
  Full-scale dynamic rated capacities from
  ±2.5 kN to ±100 kN (250 kgf, 562 lbf
  to 10,000 kgf, 2,248 lbf)

- Fatigue rated, designed with an annular shear
  stressed element, which provides true axial
  loads transfer, high stiffness that has resistance
  to side loads and bending moments.

- Compact low profile design frees up
  valuable vertical testing space

- Operates in tension, compression and
  reverse stress modes

- Auto recognition and electrical calibration

- Load cells are designed to withstand
  150% of rated capacity

- Excellent linearity through tension
  and compression

- High axial and lateral stiffness

- All load cells comply with the highest
  applicable testing standards, including
  ISO DIS 7500/1, EN10002-2, BS1610 (1992)
  and JIS B7721, B7733

Description

Instron load cells are an integral part of the load
weighing system of a testing machine. The
proprietary design, manufacturing and quality
control are done with customer applicatons in
mind. They are certified in accordance with
international standards especially for use in materials
testing machines.

Interchangeability, along with transducer
recognition and single point calibration makes
them easy to use. System electronics provide overload
protection by stopping the test at 105% of full
scale output.

They maintain high alignment and are resistant to
offset loading throughout the test, even with large
size specimens. The cells can withstand up to 150% of
the rated capacity allowing the user to zero out the
weight of the fixture up to 50% of the rated load cell
capacity, and still maintain specified accuracy through
the full range.

Instron load cells are tested for accuracy and
repeatability on a calibration apparatus traceable to
international standards, with an uncertainty of
measurements not exceeding one third of the
permissible error of the load cell. Accuracy has been
found to be equal to or better than 0.025% of the load
cell rated output or 0.25% of the indicated load,
whichever is greater.

2525-100 Series load cell

Principle of Operation

Instron load cells are precision force transducers
containing a full bridge of strain gauges bonded to
internal load bearing structures. When mechanically
stressed the electrical resistance changes on the
gauges, thus changing the output signal. This signal
is then conditioned for display readouts in
accordance with international standards.

The load cell structure has high axial stiffness which
reduces stored energy that can transfer to the
specimen at break, giving false values. Increased
lateral stiffness reduces measurement errors from off
axis loading, commonly found when performing
compression and flexural tests or where specimens
fail by tearing.

These load cells are designed to perform tension,
compression, and reverse stress modes,
eliminating the need to change cells frequently.
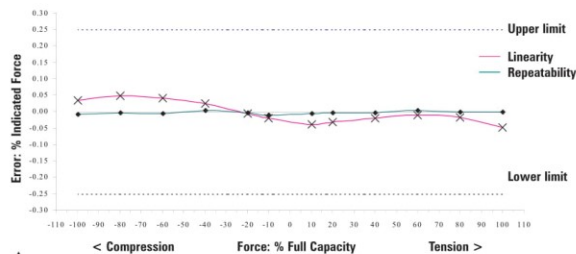
Typical load cell calibration test results

2518/2525-100 Series Load Cells

Catalog number 2525-108/112 2518-100/101/102/103/107/111

Specifications

| Catalog Number	Maximum Static Capacity	Maximum Dynamic Capacity	Mechanical Fitting (Frame)	Mechanical Fitting (Loadstring)	Mechanical Fitting (Central Thread)	Weight	Overal Diameter (A)	Effective Length (B)
2518-100	±100 kN (10,000 kgf, 22,480 lbf)	±50kN (5,000 kgf, 11,240 lbf)	M30 x 2 RH female end (type If)	6 x M10 on 100 PCD	M30 x 2 LH female end (type If)	8.5 kg (18.7 lb)	140 mm (5.5 in)	96 mm (3.8 in)
2518-101	±50 kN (5,000 kgf, 11,240 lbf)	±25kN (2,500 kgf, 562 lbf)	M30 x 2 RH female end (type If)	6 x M10 on 100 PCD	M30 x 2 LH female end (type If)	8.5 kg (18.7 lb)	140 mm (5.5 in)	96 mm (3.8 in)
2518-102	±20 kN (2,000 kgf 4,496 lbf)	±10kN (1,000 kgf, 2,248 lbf)	M30 x 2 RH female end (type If)	6 x M10 on 100 PCD	M30 x 2 LH female end (type If)	8.5 kg (18.7 lb)	140 mm (5.5 in)	96 mm (3.8 in)
2518-103	±10 kN (1,000 kgf, 2,248 lbf)	±5kN (500 kgf, 1,124 lbf)	M30 x 2 RH female end (type If)	6 x M10 on 100 PCD	M30 x 2 LH female end (type If)	8.5 kg (18.7 lb)	140 mm (5.5 in)	96 mm (3.8 in)
2518-107	±30 kN (3,000 kgf, 6,744 lbf)	±15kN (1,500 kgf, 3,372 lbf)	M30 x 2 RH female end (type If)	6 x M10 on 100 PCD	M30 x 2 LH female end (type If)	8.5 kg (18.7 lb)	140 mm (5.5 in)	96 mm (3.8 in)
2525-108	±5 kN (500 kgf, 1,124 lbf)	Static rated only	M30 x 2 RH female end (type If)	6 x M10 on 100 PCD	M30 x 2 LH female end (type If)	8.5 kg (18.7 lb)	140 mm (5.5 in)	96 mm (3.8 in)
2518-111	±200 kN (20,000 kgf 44,960 lbf)	±100kN (10,000 kgf, 22,480 lbf)	M48 x 2 RH female end (type IIf)	6 x M10 on 100 PCD 6 x M20 on 150 PCD	M48 x 2 LH female end (type If)	20 kg (44 lb)	210 mm (8.3 in)	170 mm (6.7 in)
2525-112	±150 kN (15,000 kgf, 33,720 lbf)	Static rated only	M48 x 2 RH female end (type IIf)	6 x M10 on 100 PCD 6 x M20 on 150 PCD	M48 x 2 LH female end (type If)	20 kg (44 lb)	210 mm (8.3 in)	170 mm (6.7 in)

Load Cells General Performance

Linearity	< ±0.25% of reading over a range of 100% to 0.4% of load cell static rating
Repeatability	< ±0.25% of reading over a range of 100% to 0.4% of load cell static rating
	Zero error. The residual indicated force after removing a series of forces is not greater than ±0.05% full rated output.
Hysteresis	0.1% of full rated output
Zero Recovery	0.1% of reading over 3 minutes
Bridge Resistance	350 Ohms ±5%
Sensitivity	2 mV/V at full static rating
Zero Balance	< ±1% full rated output
Overload	150% static rating without permanent zero shift
	300% static rating without mechanical failure
Deflection	0.15 mm at full static rating
Load Reversal Zero Shift	< ±0.50% full rated output (tension to compression)
Compensated Temperature Range	Temperature range 0 °C to 50 °C (32 °F to 122 °F)
Temperature Effect on Zero	< ±0.002% of full rated output per °C
Temperature Effect on Sensitivity	< ±0.002% of full rated output per °C

Load cell dimensions

Notes:
1. It is important to note that most other transducer manufactures specify linearity of their load cells as a percentage of the full rated output (% FRO). This can be misleading when using lower ranges (e.g. 1% of capacity). A load cell rated at 0.05% FRO could show a reading error of 5% at this low point.

Appendix B: LS-DYNA Reduced Input Files

Static, Non-Linear Buckling Model (Chapter 4)

```
*KEYWORD
*TITLE
$#                                                                         title
*CONTROL_CONTACT
$#   slsfac    rwpnal    islchk    shlthk    penopt    thkchg     orien    enmass
        0.1       0.0         1         0         1         0         2         0
$#   usrstr    usrfrc     nsbcs    interm     xpene     ssthk      ecdt   tiedprj
          0         0         0         0       4.0         0         0         0
$#    sfric     dfric       edc       vfc        th     th_sf    pen_sf
        0.0       0.0       0.0       0.0       0.0       0.0       0.0
$#   ignore    frceng   skiprwg    outseg   spotstp   spotdel   spothin
          0         0         0         0         0         0       0.0
$#     isym    nserod    rwgaps    rwgdth     rwksf      icov    swradf    ithoff
          0         0         1       0.0       1.0         0       0.0         0
$#   shledg    pstiff    ithcnt    tdcnof     ftall    unused    shltrw
          0         0         0         0         0                 0.0
*CONTROL_ENERGY
$#     hgen      rwen    slnten     rylen
          2         2         2         2
*CONTROL_HOURGLASS
$#      ihq        qh
          1       0.1
*CONTROL_IMPLICIT_BUCKLE
$#    nmode    bckmth
          8         1
*CONTROL_IMPLICIT_DYNAMICS
$#    imass     gamma      beta     tdybir     tdydth    tdybur     irate
          0       0.5      0.25       0.01.00000E281.00000E28         0
*CONTROL_IMPLICIT_GENERAL
$#   imflag       dt0    imform      nsbs       igs     cnstn      form    zero_v
          1       0.0         2         1         2         0         0         0
*CONTROL_IMPLICIT_SOLUTION
$#   nsolvr    ilimit    maxref     dctol     ectol     rctol     lstol    abstol
          1        11        15     0.001     0.011.00000E10       0.91.0000E-10
$#    dnorm     diverg     istif    nlprint    nlnorm   d3itctl     cpchk
          2         1         1         0         2         0         0
$#    arcctl    arcdir    arclen    arcmth    arcdmp    arcpsi    arcalf    arctim
          0         0       0.0         1         2         0         0         0
$#    lsmtd     lsdir      irad      srad      awgt      sred
          4         2       0.0       0.0       0.0       0.0
*CONTROL_TERMINATION
$#   endtim    endcyc     dtmin    endeng    endmas
        1.0         0       0.0      0.05.000000E8
*DATABASE_BNDOUT
$#       dt    binary      lcur     ioopt
       0.01         0         0         1
*DATABASE_ELOUT
$#       dt    binary      lcur     ioopt   option1   option2   option3   option4
       0.01         0         0         1         0         0         0         0
*DATABASE_GCEOUT
$#       dt    binary      lcur     ioopt
       0.01         0         0         1
*DATABASE_GLSTAT
$#       dt    binary      lcur     ioopt
       0.01         0         0         1
*DATABASE_NCFORC
$#       dt    binary      lcur     ioopt
       0.01         0         0         1
*DATABASE_NODFOR
$#       dt    binary      lcur     ioopt
       0.01         0         0         1
*DATABASE_NODOUT
$#       dt    binary      lcur     ioopt   option1   option2
```

```
      0.01         0         0         1       0.0         0
*DATABASE_RCFORC
$#       dt    binary      lcur     ioopt
      0.01         0         0         1
*DATABASE_SPCFORC
$#       dt    binary      lcur     ioopt
      0.01         0         0         1
*DATABASE_BINARY_D3PLOT
$#       dt      lcdt      beam     npltc    psetid
       0.1         0         0         0         0
$#    ioopt
         0
*DATABASE_NODAL_FORCE_GROUP
$#     nsid       cid
         1         0
*DATABASE_NODAL_FORCE_GROUP
$#     nsid       cid
         2         0
*DATABASE_HISTORY_NODE_SET
$#      id1       id2       id3       id4       id5       id6       id7       id8
         1         2         0         0         0         0         0         0
*BOUNDARY_SPC_SET_ID
$#      id                                                               heading
        0BC_x=0
$#     nsid       cid      dofx      dofy      dofz     dofrx     dofry     dofrz
         1         0         1         0         0         0         0         0
*SET_NODE_LIST_TITLE
x=0
$#      sid       da1       da2       da3       da4    solver
         1       0.0       0.0       0.0       0.0MECH
$#     nid1      nid2      nid3      nid4      nid5      nid6      nid7      nid8
         1        41        81       121       161       201       241       281
       321       361       401       441       481       521       561       601

$#      id                                                               heading
        0Fixed x=0
$#     nsid       cid      dofx      dofy      dofz     dofrx     dofry     dofrz
         3         0         0         1         0         0         0         0
*SET_NODE_LIST_TITLE
Fixture_x=0
$#      sid       da1       da2       da3       da4    solver
         3       0.0       0.0       0.0       0.0MECH
$#     nid1      nid2      nid3      nid4      nid5      nid6      nid7      nid8
      8092      8093      8094      8095      8096      8097      8098      8099
...
*BOUNDARY_SPC_SET_ID
$#      id                                                               heading
        0Fixed x=L
$#     nsid       cid      dofx      dofy      dofz     dofrx     dofry     dofrz
         4         0         0         1         1         0         0         0
*SET_NODE_LIST_TITLE
Fixture_x=L
$#      sid       da1       da2       da3       da4    solver
         4       0.0       0.0       0.0       0.0MECH
$#     nid1      nid2      nid3      nid4      nid5      nid6      nid7      nid8
      9569      9570      9571      9572      9573      9574      9575      9576
...
*BOUNDARY_SPC_SET_ID
$#      id                                                               heading
        0NO-Z-dir
$#     nsid       cid      dofx      dofy      dofz     dofrx     dofry     dofrz
         5         0         0         0         1         0         0         0
*SET_NODE_LIST_TITLE
Rig-Bod_x=0
$#      sid       da1       da2       da3       da4    solver
         5       0.0       0.0       0.0       0.0MECH
$#     nid1      nid2      nid3      nid4      nid5      nid6      nid7      nid8
         1       441       481       961      1001      1041      1081      1281
      1321      6772      6812      6852      8092      8132      8172      9467
      9523      9579     11315     11427     16243     16299     16355     16411
     17587     18203     19379     19435         0         0         0         0
```

```
*LOAD_NODE_SET
$#     nsid       dof      lcid        sf       cid        m1        m2        m3
          2         1         8     -0.01         0         0         0         0
*CONTACT_TIED_SURFACE_TO_SURFACE_ID
$#     cid                                                                  title
        0Top bond
$#     ssid      msid     sstyp     mstyp    sboxid    mboxid       spr       mpr
          1         2         0         0         0         0         1         1
$#       fs        fd        dc        vc       vdc    penchk        bt        dt
        0.0       0.0       0.0       0.0       0.0         0      0.01.00000E20
$#      sfs       sfm       sst       mst      sfst      sfmt       fsf       vsf
        1.0       1.0       0.0       0.0       1.0       1.0       1.0       1.0
$#     soft    sofscl    lcidab    maxpar     sbopt     depth     bsort    frcfrq
          2       0.1         0     1.025       2.0         2         0         1
$#   penmax    thkopt    shlthk     snlog      isym     i2d3d    sldthk    sldstf
        0.0         0         0         0         0         0       0.0       0.0
$#     igap ignodprfac/mpadtstif/mpar2    unused    unused    flangl   cid_rcf
          1         0       0.0       0.0                               0.0         0
*SET_SEGMENT_TITLE
SkinTop
$#      sid       da1       da2       da3       da4    solver
          1       0.0       0.0       0.0       0.0MECH
$#       n1        n2        n3        n4        a1        a2        a3        a4
      10957     11125     11124     10956       0.0       0.0       0.0       0.0
      10447     10615     10614     10446       0.0       0.0       0.0       0.0

*SET_SEGMENT_TITLE
Ply Top
$#      sid       da1       da2       da3       da4    solver
          2       0.0       0.0       0.0       0.0MECH
$#       n1        n2        n3        n4        a1        a2        a3        a4
      12235     12347     12348     12236       0.0       0.0       0.0       0.0
      13523     12235     12236     13524       0.0       0.0       0.0       0.0
...
*CONTACT_TIED_SURFACE_TO_SURFACE_ID
$#     cid                                                                  title
        3Bottom bond
$#     ssid      msid     sstyp     mstyp    sboxid    mboxid       spr       mpr
          4         3         0         0         0         0         0         0
$#       fs        fd        dc        vc       vdc    penchk        bt        dt
        0.0       0.0       0.0       0.0       0.0         0      0.01.00000E20
$#      sfs       sfm       sst       mst      sfst      sfmt       fsf       vsf
        1.0       1.0       0.0       0.0       1.0       1.0       1.0       1.0
$#     soft    sofscl    lcidab    maxpar     sbopt     depth     bsort    frcfrq
          2       0.1         0     1.025       2.0         2         0         1
$#   penmax    thkopt    shlthk     snlog      isym     i2d3d    sldthk    sldstf
        0.0         0         0         0         0         0       0.0       0.0
$#     igap ignodprfac/mpadtstif/mpar2    unused    unused    flangl   cid_rcf
          1         0       0.0       0.0                               0.0         0
*SET_SEGMENT_TITLE
Skin Bottom
$#      sid       da1       da2       da3       da4    solver
          4       0.0       0.0       0.0       0.0MECH
$#       n1        n2        n3        n4        a1        a2        a3        a4
      20787     20955     20956     20788       0.0       0.0       0.0       0.0
...
*SET_SEGMENT_TITLE
Ply Bottom
$#      sid       da1       da2       da3       da4    solver
          3       0.0       0.0       0.0       0.0MECH
$#       n1        n2        n3        n4        a1        a2        a3        a4
      18061     18117     18116     18060       0.0       0.0       0.0       0.0
      17854     17910     17909     17853       0.0       0.0       0.0       0.0
...
*PART
$#                                                                          title
Skin-Top
$#      pid     secid       mid     eosid      hgid      grav    adpopt      tmid
          1         1         2         0         0         0         0         0
*SECTION_SOLID_TITLE
Section-Solid
```

```
$#    secid    elform       aet
         1         1         0
*MAT_PIECEWISE_LINEAR_PLASTICITY_LOG_INTERPOLATION_TITLE
MAT_24-Mg
$#      mid        ro         e        pr      sigy      etan      fail      tdel
        21.74000E-6      36.0      0.35     0.231      0.01.00000E21       0.0
$#        c         p      lcss      lcsr        vp       lcf
        0.0       0.0         1         0       0.0         0
$#     eps1      eps2      eps3      eps4      eps5      eps6      eps7      eps8
        0.0       0.0       0.0       0.0       0.0       0.0       0.0       0.0
$#      es1       es2       es3       es4       es5       es6       es7       es8
        0.0       0.0       0.0       0.0       0.0       0.0       0.0       0.0
*PART
$#                                                                         title
Ply-Top
$#      pid     secid       mid     eosid      hgid      grav    adpopt      tmid
         2         1         1         0         0         0         0         0
*MAT_ENHANCED_COMPOSITE_DAMAGE_TITLE
MAT_54-fiberglass_Skins
$#      mid        ro        ea        eb      (ec)      prba     (prca)    (prcb)
        11.75000E-6       9.0       9.0      2.55      0.05      0.05     0.428
$#      gab       gbc       gca      (kf)      aopt      2way
        1.0       1.0       1.0       0.0       2.0       0.0
$#       xp        yp        zp        a1        a2        a3    mangle
        0.0       0.0       0.0       1.0       0.0       0.0       0.0
$#       v1        v2        v3        d1        d2        d3    dfailm    dfails
        0.0       0.0       0.0       0.0       0.0       1.0       0.0       0.0
$#    tfail      alph      soft      fbrt     ycfac    dfailt    dfailc       efs
        0.0       0.0       1.0       0.0       2.0       0.0       0.0       0.0
$#       xc        xt        yc        yt        sc      crit      beta
      0.173     0.173     0.173     0.173      0.03      54.0       0.0
$#      pel      epsf      epsr      tsmd     soft2
        0.0       0.0       0.0       0.0       1.0
$#   slimt1    slimc1    slimt2    slimc2     slims    ncyred     softg
        0.0       0.0       0.0       0.0       0.0       0.0       1.0
*PART
$#                                                                         title
Pillars
$#      pid     secid       mid     eosid      hgid      grav    adpopt      tmid
         3         1         7         0         0         0         0         0
*MAT_ENHANCED_COMPOSITE_DAMAGE_TITLE
MAT_54-fiberglass_Pillars
$#      mid        ro        ea        eb      (ec)      prba     (prca)    (prcb)
        71.75000E-6       3.0       1.0       2.0      0.05      0.05     0.428
$#      gab       gbc       gca      (kf)      aopt      2way
        1.0       1.0       1.0       0.0       2.0       0.0
$#       xp        yp        zp        a1        a2        a3    mangle
        0.0       0.0       0.0       0.5      0.86       0.0       0.0
$#       v1        v2        v3        d1        d2        d3    dfailm    dfails
        0.0       0.0       0.0       0.0       1.0       0.0       0.0       0.0
$#    tfail      alph      soft      fbrt     ycfac    dfailt    dfailc       efs
        0.0       0.0       1.0       0.0       2.0       0.0       0.0       0.0
$#       xc        xt        yc        yt        sc      crit      beta
       0.08      0.08      0.08      0.08      0.03      54.0       0.0
$#      pel      epsf      epsr      tsmd     soft2
        0.0       0.0       0.0       0.0       1.0
$#   slimt1    slimc1    slimt2    slimc2     slims    ncyred     softg
        0.0       0.0       0.0       0.0       0.0       0.0       1.0
*PART
$#                                                                         title
Foam
$#      pid     secid       mid     eosid      hgid      grav    adpopt      tmid
         4         1         4         0         0         0         0         0
*MAT_ELASTIC_TITLE
MAT_001-Elastic-foam
$#      mid        ro         e        pr        da        db  not used
        41.28100E-7      0.05       0.0       0.0       0.0         0
*PART
$#                                                                         title
Ply-Bottom
$#      pid     secid       mid     eosid      hgid      grav    adpopt      tmid
```

255

```
         5           1           1           0           0           0           0           0
*PART
$#                                                                                        title
Skin-Bottom
$#     pid     secid       mid     eosid      hgid      grav    adpopt      tmid
         6           1           2           0           0           0           0           0
*PART
$#                                                                                        title
Rigid End
$#     pid     secid       mid     eosid      hgid      grav    adpopt      tmid
         7           1           8           0           0           0           0           0
*MAT_RIGID_TITLE
Rigid aluminum
$#     mid        ro         e        pr         n    couple         m     alias
      82.70000E-6      70.0      0.33       0.0       0.0       0.0
$#     cmo      con1      con2
         0.0         0         0
$#lco or a1        a2        a3        v1        v2        v3
         0.0       0.0       0.0       0.0       0.0       0.0
*MAT_ADD_EROSION_TITLE
Foam-erosion
$#     mid      excl    mxpres     mneps    effeps    voleps    numfip       ncs
         4       0.0       0.0       0.0      0.15       0.0       1.0       1.0
$#   mnpres     sigp1     sigvm     mxeps     epssh     sigth   impulse    failtm
         0.0       0.0       0.0       0.0       0.0       0.0       0.0       0.0
$#     idam    dmgtyp     lcsdg     ecrit    dmgexp      dcrit    fadexp    lcregd
         0       0.0         0       0.0       1.0       0.0       1.0         0
$#    lcfld             epsthin    engcrt    radcrt
         0         0       0.0       0.0       0.0
*DEFINE_TABLE_TITLE
Table_Mg-Rate
$#     tbid       sfa      offa
         6
$#              value      lcid
               0.0         3
   9.9999997474e-005         4
               0.1         5
*DEFINE_CURVE_TITLE
Mg-Rate_0
$#     lcid      sidr       sfa       sfo      offa      offo    dattyp     lcint
         3         0       1.0       1.0       0.0       0.0         0         0
$#                  a1                  o1
               0.0              0.2317
             0.001            0.233996
             0.002            0.236232
             0.003             0.23841
             0.004             0.24053
             0.005            0.242595
             0.006            0.244605
             0.007            0.246561
             0.008            0.248465
             0.009            0.250317
              0.01            0.252119
             0.011            0.253872
             0.012            0.255576
             0.013            0.257234
             0.014            0.258845
             0.015            0.260411
             0.016            0.261933
             0.017            0.263412
             0.018            0.264849
             0.019            0.266245
              0.02            0.267601
             0.021            0.268918
             0.022            0.270196
             0.023            0.271437
             0.024            0.272641
             0.025             0.27381
             0.026            0.274944
             0.027            0.276044
             0.028            0.277112
```

0.029	0.278147
0.03	0.279151
0.031	0.280124
0.032	0.281068
0.033	0.281983
0.034	0.28287
0.035	0.283729
0.036	0.284562
0.037	0.285369
0.038	0.286151
0.039	0.286908
0.04	0.287641
0.041	0.288352
0.042	0.28904
0.043	0.289707
0.044	0.290352
0.045	0.290977
0.046	0.291583
0.047	0.292169
0.048	0.292737
0.049	0.293287
0.05	0.29382
0.051	0.294335
0.052	0.294835
0.053	0.295319
0.054	0.295788
0.055	0.296243
0.056	0.296683
0.057	0.29711
0.058	0.297525
0.059	0.297926
0.06	0.298316
0.061	0.298694
0.062	0.299061
0.063	0.299418
0.064	0.299764
0.065	0.300101
0.066	0.300428
0.067	0.300747
0.068	0.301057
0.069	0.301359
0.07	0.301654
0.071	0.301941
0.072	0.302221
0.073	0.302495
0.074	0.302762
0.075	0.303024
0.076	0.30328
0.077	0.303531
0.078	0.303777
0.079	0.304019
0.08	0.304256
0.081	0.304489
0.082	0.304719
0.083	0.304945
0.084	0.305168
0.085	0.305389
0.086	0.305606
0.087	0.305822
0.088	0.306035
0.089	0.306246
0.09	0.306456
0.091	0.306664
0.092	0.306871
0.093	0.307077
0.094	0.307282
0.095	0.307486
0.096	0.30769
0.097	0.307894
0.098	0.308097
0.099	0.308301

```
                        0.1                 0.308504
*DEFINE_CURVE_TITLE
Mg-Rate_0.0001
$#     lcid      sidr       sfa       sfo      offa      offo    dattyp     lcint
          4         0       1.0       1.0       0.0       0.0         0         0
$#                   a1                  o1
                    0.0              0.2478
                  0.001             0.25058
                  0.002            0.253233
                  0.003            0.255766
                  0.004            0.258181
                  0.005            0.260485
                  0.006            0.262681
                  0.007            0.264773
                  0.008            0.266766
                  0.009            0.268665
                   0.01            0.270472
                  0.011            0.272192
                  0.012            0.273829
                  0.013            0.275386
                  0.014            0.276868
                  0.015            0.278276
                  0.016            0.279616
                  0.017             0.28089
                  0.018            0.282102
                  0.019            0.283253
                   0.02            0.284349
                  0.021            0.285391
                  0.022            0.286383
                  0.023            0.287326
                  0.024            0.288225
                  0.025            0.289081
                  0.026            0.289896
                  0.027            0.290675
                  0.028            0.291417
                  0.029            0.292127
                   0.03            0.292806
                  0.031            0.293456
                  0.032            0.294079
                  0.033            0.294677
                  0.034            0.295252
                  0.035            0.295806
                  0.036             0.29634
                  0.037            0.296857
                  0.038            0.297357
                  0.039            0.297842
                   0.04            0.298314
                  0.041            0.298774
                  0.042            0.299223
                  0.043            0.299663
                  0.044            0.300094
                  0.045            0.300519
                  0.046            0.300937
                  0.047             0.30135
                  0.048            0.301758
                  0.049            0.302164
                   0.05            0.302567
                  0.051            0.302968
                  0.052            0.303368
                  0.053            0.303767
                  0.054            0.304167
                  0.055            0.304568
                  0.056            0.304969
                  0.057            0.305373
                  0.058            0.305779
                  0.059            0.306187
                   0.06            0.306598
                  0.061            0.307012
                  0.062             0.30743
                  0.063            0.307851
                  0.064            0.308276
```

```
                0.065                  0.308705
                0.066                  0.309138
                0.067                  0.309574
                0.068                  0.310015
                0.069                   0.31046
                 0.07                  0.310909
                0.071                  0.311361
                0.072                  0.311818
                0.073                  0.312278
                0.074                  0.312741
                0.075                  0.313208
                0.076                  0.313678
                0.077                  0.314151
                0.078                  0.314627
                0.079                  0.315105
                 0.08                  0.315585
                0.081                  0.316067
                0.082                   0.31655
                0.083                  0.317034
                0.084                  0.317519
                0.085                  0.318004
                0.086                   0.31849
                0.087                  0.318975
                0.088                  0.319459
                0.089                  0.319942
                 0.09                  0.320423
                0.091                  0.320902
                0.092                  0.321379
                0.093                  0.321853
                0.094                  0.322323
                0.095                   0.32279
                0.096                  0.323252
                0.097                   0.32371
                0.098                  0.324163
                0.099                   0.32461
                  0.1                  0.325051
*DEFINE_CURVE_TITLE
Mg-Rate_0.1
$#     lcid      sidr       sfa       sfo      offa      offo    dattyp     lcint
          5         0       1.0       1.0       0.0       0.0         0         0
$#                   a1                  o1
                  0.0                  0.2531
                0.001                  0.256577
                0.002                  0.259842
                0.003                  0.262909
                0.004                  0.265789
                0.005                  0.268493
                0.006                  0.271031
                0.007                  0.273414
                0.008                  0.275652
                0.009                  0.277754
                 0.01                  0.279729
                0.011                  0.281585
                0.012                  0.283332
                0.013                  0.284976
                0.014                  0.286525
                0.015                  0.287987
                0.016                  0.289367
                0.017                  0.290672
                0.018                  0.291909
                0.019                  0.293083
                 0.02                  0.294199
                0.021                  0.295262
                0.022                  0.296278
                0.023                   0.29725
                0.024                  0.298183
                0.025                   0.29908
                0.026                  0.299945
                0.027                  0.300782
                0.028                  0.301593
                0.029                  0.302382
```

0.03	0.303151
0.031	0.303901
0.032	0.304636
0.033	0.305358
0.034	0.306067
0.035	0.306766
0.036	0.307455
0.037	0.308136
0.038	0.30881
0.039	0.309478
0.04	0.31014
0.041	0.310797
0.042	0.311448
0.043	0.312095
0.044	0.312737
0.045	0.313375
0.046	0.314008
0.047	0.314635
0.048	0.315258
0.049	0.315874
0.05	0.316484
0.051	0.317088
0.052	0.317684
0.053	0.318272
0.054	0.318852
0.055	0.319422
0.056	0.319982
0.057	0.320532
0.058	0.321069
0.059	0.321595
0.06	0.322107
0.061	0.322606
0.062	0.32309
0.063	0.32356
0.064	0.324013
0.065	0.324451
0.066	0.324872
0.067	0.325276
0.068	0.325663
0.069	0.326032
0.07	0.326383
0.071	0.326717
0.072	0.327033
0.073	0.327332
0.074	0.327614
0.075	0.327879
0.076	0.328129
0.077	0.328363
0.078	0.328583
0.079	0.32879
0.08	0.328985
0.081	0.32917
0.082	0.329346
0.083	0.329516
0.084	0.329681
0.085	0.329844
0.086	0.330008
0.087	0.330174
0.088	0.330347
0.089	0.33053
0.09	0.330726
0.091	0.330938
0.092	0.331173
0.093	0.331432
0.094	0.331722
0.095	0.332048
0.096	0.332414
0.097	0.332827
0.098	0.333293
0.099	0.333817
0.1	0.334407

```
*DEFINE_CURVE_TITLE
Curve-Mg
$#    lcid      sidr       sfa       sfo      offa      offo    dattyp     lcint
         1         0       1.0       1.0       0.0       0.0         0         0
$#                 a1                  o1
                  0.0              0.2317
               0.0093              0.2558
               0.0219              0.2705
               0.0335              0.2826
               0.0597              0.2946
               0.1218              0.3161
                0.188              0.3295
               0.2501              0.3402
               0.3132              0.3429
*DEFINE_CURVE_TITLE
Curve-foam
$#    lcid      sidr       sfa       sfo      offa      offo    dattyp     lcint
         2         0       1.0       1.0       0.0       0.0         0         0
$#                 a1                  o1
                  0.0                 0.0
                 0.13             0.00749
                  0.2              0.0075
                  0.4              0.0076
                  0.5               0.011
                  0.6               0.017
                  0.7               0.029
                 0.75               0.035
*DEFINE_CURVE_TITLE
Damping mass
$#    lcid      sidr       sfa       sfo      offa      offo    dattyp     lcint
         7         0       1.0       1.0       0.0       0.0         0         0
$#                 a1                  o1
                  0.0                 1.0
                 16.0                 1.0
*DEFINE_CURVE_TITLE
For eigenvalue
$#    lcid      sidr       sfa       sfo      offa      offo    dattyp     lcint
         8         0       1.0       1.0       0.0       0.0         0         0
$#                 a1                  o1
                  0.0                 0.0
                  1.0                 1.0
*SET_NODE_LIST_TITLE
x=L
$#     sid       da1       da2       da3       da4    solver
         2       0.0       0.0       0.0       0.0MECH
$#    nid1      nid2      nid3      nid4      nid5      nid6      nid7      nid8
     21304     21305     21306     21307     21308     21309     21310     21311
     21312     21313     21314     21315     21316     21317     21318     21319
...
*SET_NODE_LIST_TITLE
3DFML
$#     sid       da1       da2       da3       da4    solver
         8       0.0       0.0       0.0       0.0MECH
$#    nid1      nid2      nid3      nid4      nid5      nid6      nid7      nid8
      6772      6773      6774      6775      6776      6777      6778      6779
      6780      6781      6782      6783      6784      6785      6786      6787
...
*SET_NODE_LIST_TITLE
Delamination
$#     sid       da1       da2       da3       da4    solver
         9       0.0       0.0       0.0       0.0MECH
$#    nid1      nid2      nid3      nid4      nid5      nid6      nid7      nid8
      9419      9420      9421      9475      9476      9477      9531      9532
      9533      9587      9588      9589      9643      9644      9645      9699
...
*SET_PART_LIST_TITLE
Part Mg
$#     sid       da1       da2       da3       da4    solver
         1       0.0       0.0       0.0       0.0MECH
$#    pid1      pid2      pid3      pid4      pid5      pid6      pid7      pid8
         1         2         3         4         5         6         0         0
```

```
*SET_SEGMENT_TITLE
End 3D-FML
$#      sid        da1        da2        da3        da4    solver
          5        0.0        0.0        0.0        0.0MECH
$#       n1         n2         n3         n4         a1         a2         a3         a4
      10139      10195      10363      10307        0.0        0.0        0.0        0.0
      18483      14451      16579      18539        0.0        0.0        0.0        0.0
...
*SET_SEGMENT_TITLE
Delamination Top
$#      sid        da1        da2        da3        da4    solver
          6        0.0        0.0        0.0        0.0MECH
$#       n1         n2         n3         n4         a1         a2         a3         a4
      10763      10931      10930      10762        0.0        0.0        0.0        0.0
      10764      10932      10931      10763        0.0        0.0        0.0        0.0
...
*SET_SEGMENT_TITLE
Delamination Bottom
$#      sid        da1        da2        da3        da4    solver
          7        0.0        0.0        0.0        0.0MECH
$#       n1         n2         n3         n4         a1         a2         a3         a4
      11994      12106      12107      11995        0.0        0.0        0.0        0.0
      13226      11994      11995      13227        0.0        0.0        0.0        0.0
...
*PERTURBATION_NODE
$#     type       nsid        scl        cmp     icoord        cid
          1          8        1.0          2          0          0
$#     ampl        xwl       xoff        ywl       yoff        zwl       zoff
         -0.2      380.0        0.0        0.0        0.0        0.0        0.0
*PERTURBATION_NODE
$#     type       nsid        scl        cmp     icoord        cid
          1          9        1.0          2          0          0
$#     ampl        xwl       xoff        ywl       yoff        zwl       zoff
          0.1       16.0      -90.0        0.0        0.0        0.0        0.0
*END
```

SHELL Model for Impact Buckling (Chapter 5)

```
*KEYWORD
*TITLE
$#                                                                       title
*CONTROL_CONTACT
$#   slsfac    rwpnal    islchk    shlthk    penopt    thkchg     orien    enmass
        0.1       0.0         1         0         1         0         2         0
$#   usrstr    usrfrc     nsbcs    interm     xpene     ssthk      ecdt   tiedprj
          0         0         0         0       4.0         0         0         0
$#    sfric     dfric       edc       vfc        th     th_sf    pen_sf
        0.0       0.0       0.0       0.0       0.0       0.0       0.0
$#   ignore    frceng   skiprwg    outseg   spotstp   spotdel   spothin
          0         0         0         0         0         0       0.0
$#     isym    nserod    rwgaps    rwgdth     rwksf      icov    swradf    ithoff
          0         0         1       0.0       1.0         0       0.0         0
$#   shledg    pstiff    ithcnt    tdcnof     ftall    unused    shltrw
          1         0         0         0         0                 0.0
*CONTROL_ENERGY
$#     hgen      rwen    slnten     rylen
          2         2         2         2
*CONTROL_HOURGLASS
$#      ihq        qh
          1       0.1
*CONTROL_TERMINATION
$#   endtim    endcyc     dtmin    endeng    endmas
        6.0         0       0.0      0.01.000000E8
*DATABASE_BNDOUT
$#       dt    binary      lcur     ioopt
       0.01         0         0         1
*DATABASE_ELOUT
$#       dt    binary      lcur     ioopt   option1   option2   option3   option4
       0.01         0         0         1         0         0         0         0
*DATABASE_GCEOUT
$#       dt    binary      lcur     ioopt
       0.01         0         0         1
*DATABASE_GLSTAT
$#       dt    binary      lcur     ioopt
       0.01         0         0         1
*DATABASE_NCFORC
$#       dt    binary      lcur     ioopt
       0.01         0         0         1
*DATABASE_NODFOR
$#       dt    binary      lcur     ioopt
       0.01         0         0         1
*DATABASE_NODOUT
$#       dt    binary      lcur     ioopt   option1   option2
       0.01         0         0         1       0.0         0
*DATABASE_RCFORC
$#       dt    binary      lcur     ioopt
       0.01         0         0         1
*DATABASE_BINARY_D3PLOT
$#       dt      lcdt      beam     npltc    psetid
       0.01         0         0         0         0
$#    ioopt
          0
*DATABASE_NODAL_FORCE_GROUP
$#     nsid       cid
          1         0
*DATABASE_NODAL_FORCE_GROUP
$#     nsid       cid
          2         0
*DATABASE_HISTORY_NODE_SET
$#      id1       id2       id3       id4       id5       id6       id7       id8
          1         2         0         0         0         0         0         0
*BOUNDARY_SPC_SET_ID
$#       id                                                               heading
          1BC_x=0
$#     nsid       cid      dofx      dofy      dofz     dofrx     dofry     dofrz
          1         0         1         0         0         0         0         0
```

263

```
*SET_NODE_LIST_TITLE
x=0
$#      sid       da1       da2       da3       da4    solver
          1       0.0       0.0       0.0       0.0MECH
$#     nid1      nid2      nid3      nid4      nid5      nid6      nid7      nid8
          1         2         3         4         5         6         7         0
*BOUNDARY_SPC_SET_ID
$#      id                                                              heading
          2BC_RigBod
$#     nsid       cid      dofx      dofy      dofz     dofrx     dofry     dofrz
          3         0         0         0         1         0         0         0
*SET_NODE_LIST_TITLE
RigBod_x=0
$#      sid       da1       da2       da3       da4    solver
          3       0.0       0.0       0.0       0.0MECH
$#     nid1      nid2      nid3      nid4      nid5      nid6      nid7      nid8
          1         0         0         0         0         0         0         0
*BOUNDARY_SPC_SET_ID
$#      id                                                              heading
          0BC_Fixture_x=0
$#     nsid       cid      dofx      dofy      dofz     dofrx     dofry     dofrz
          4         0         0         1         0         0         0         0
*SET_NODE_LIST_TITLE
Fixture_x=0
$#      sid       da1       da2       da3       da4    solver
          4       0.0       0.0       0.0       0.0MECH
$#     nid1      nid2      nid3      nid4      nid5      nid6      nid7      nid8
          1         2         3         4         5         6         7         8
...
*BOUNDARY_SPC_SET_ID
$#      id                                                              heading
          0BC_Fixture_x=L
$#     nsid       cid      dofx      dofy      dofz     dofrx     dofry     dofrz
          5         0         0         1         0         0         0         0
*SET_NODE_LIST_TITLE
Fixture_x=L
$#      sid       da1       da2       da3       da4    solver
          5       0.0       0.0       0.0       0.0MECH
$#     nid1      nid2      nid3      nid4      nid5      nid6      nid7      nid8
         94        95        96        97        98        99       100       101
...
*BOUNDARY_SPC_SET_ID
$#      id                                                              heading
          0BC_RigBod_x=L
$#     nsid       cid      dofx      dofy      dofz     dofrx     dofry     dofrz
          6         0         0         0         1         0         0         0
*SET_NODE_LIST_TITLE
RigBod_x=L
$#      sid       da1       da2       da3       da4    solver
          6       0.0       0.0       0.0       0.0MECH
$#     nid1      nid2      nid3      nid4      nid5      nid6      nid7      nid8
        105         0         0         0         0         0         0         0
*BOUNDARY_SPC_SET_ID
$#      id                                                              heading
          0RigBod-Impactor
$#     nsid       cid      dofx      dofy      dofz     dofrx     dofry     dofrz
          9         0         0         1         1         1         1         1
*SET_NODE_LIST_TITLE
RigBod-Impactor
$#      sid       da1       da2       da3       da4    solver
          9       0.0       0.0       0.0       0.0MECH
$#     nid1      nid2      nid3      nid4      nid5      nid6      nid7      nid8
       1381         0         0         0         0         0         0         0
*BOUNDARY_SPC_SET_ID
$#      id                                                              heading
          0RigBod-Fixture
$#     nsid       cid      dofx      dofy      dofz     dofrx     dofry     dofrz
         11         0         0         1         1         1         1         1
*SET_NODE_LIST_TITLE
RigBod fixture
$#      sid       da1       da2       da3       da4    solver
```

```
        11       0.0       0.0       0.0       0.0MECH
$#    nid1      nid2      nid3      nid4      nid5      nid6      nid7      nid8
      1675         0         0         0         0         0         0         0
*CONTACT_AUTOMATIC_SURFACE_TO_SURFACE_ID
$#     cid                                                               title
         0Contact_Impactor_Fixture
$#    ssid      msid     sstyp     mstyp    sboxid    mboxid       spr       mpr
         3         2         0         0         0         0         0         0
$#      fs        fd        dc        vc       vdc    penchk        bt        dt
       0.0       0.0       0.0       0.0       0.0         0      0.01.00000E20
$#     sfs       sfm       sst       mst      sfst      sfmt       fsf       vsf
       1.0       1.0       0.0       0.0       1.0       1.0       1.0       1.0
$#    soft    sofscl    lcidab    maxpar     sbopt     depth     bsort    frcfrq
         2       0.1         0     1.025       2.0         2         0         1
$#  penmax    thkopt    shlthk     snlog      isym     i2d3d    sldthk    sldstf
       0.0         0         0         0         0         0       0.0       0.0
$#    igap ignodprfac/mpadtstif/mpar2    unused    unused    flangl   cid_rcf
         1         0       0.0       0.0                               0.0         0
*SET_SEGMENT_TITLE
Fixture impactor
$#     sid       da1       da2       da3       da4    solver
         3       0.0       0.0       0.0       0.0MECH
$#      n1        n2        n3        n4        a1        a2        a3        a4
      1527      1532      1577      1572       0.0       0.0       0.0       0.0
...
*SET_SEGMENT_TITLE
Impactor
$#     sid       da1       da2       da3       da4    solver
         2       0.0       0.0       0.0       0.0MECH
$#      n1        n2        n3        n4        a1        a2        a3        a4
       766       765       771       772       0.0       0.0       0.0       0.0
...
*CONTACT_TIED_NODES_TO_SURFACE_ID
$#     cid                                                               title
         0Fixture specimen
$#    ssid      msid     sstyp     mstyp    sboxid    mboxid       spr       mpr
         2         1         4         0         0         0         0         0
$#      fs        fd        dc        vc       vdc    penchk        bt        dt
       0.0       0.0       0.0       0.0       0.0         0      0.01.00000E20
$#     sfs       sfm       sst       mst      sfst      sfmt       fsf       vsf
       1.0       1.0       0.0       0.0       1.0       1.0       1.0       1.0
$#    soft    sofscl    lcidab    maxpar     sbopt     depth     bsort    frcfrq
         2       0.1         0     1.025       2.0         2         0         1
$#  penmax    thkopt    shlthk     snlog      isym     i2d3d    sldthk    sldstf
       0.0         0         0         0         0         0       0.0       0.0
$#    igap ignodprfac/mpadtstif/mpar2    unused    unused    flangl   cid_rcf
         1         0       0.0       0.0                               0.0         0
*SET_NODE_LIST_TITLE
x=L
$#     sid       da1       da2       da3       da4    solver
         2       0.0       0.0       0.0       0.0MECH
$#    nid1      nid2      nid3      nid4      nid5      nid6      nid7      nid8
       104       105       667       671       672       679       680         0
*SET_SEGMENT_TITLE
Fixture-specimen
$#     sid       da1       da2       da3       da4    solver
         1       0.0       0.0       0.0       0.0MECH
$#      n1        n2        n3        n4        a1        a2        a3        a4
      1538      1533      1578      1583       0.0       0.0       0.0       0.0
...
*PART_COMPOSITE
$#                                                                       title
3D-FML
$#     pid    elform      shrf      nloc     marea      hgid    adpopt  ithelfrm
         1         2  0.833333       0.0       0.0         0         0         0
$#    mid1    thick1        b1     tmid1      mid2    thick2        b2     tmid2
         2       0.5       0.0         0         1      0.45       0.0         0
         6       1.7       0.0         0         6       1.7       0.0         0
         1      0.45       0.0         0         2       0.5       0.0         0
*PART
$#                                                                       title
```

```
Fixture
$#     pid    secid      mid    eosid     hgid      grav    adpopt     tmid
         2         1         5         0         0         0         0         0
*SECTION_SOLID_TITLE
Section-Solid
$#   secid    elform      aet
         1         1         0
*MAT_ELASTIC_TITLE
MAT_001-Fixture
$#     mid        ro         e        pr        da        db  not used
       52.70000E-6      70.0      0.33       0.0       0.0         0
*PART
$#                                                                      title
Impactor
$#     pid    secid      mid    eosid     hgid      grav    adpopt     tmid
         3         1         4         0         0         0         0         0
*MAT_ELASTIC_TITLE
MAT_001-Impactor
$#     mid        ro         e        pr        da        db  not used
       44.80000E-5     200.0       0.3       0.0       0.0         0
*MAT_ENHANCED_COMPOSITE_DAMAGE_TITLE
MAT_54-fiberglass
$#     mid        ro        ea        eb      (ec)      prba     (prca)    (prcb)
       11.75000E-6       6.0      4.25       1.2      0.05      0.05     0.428
$#     gab       gbc       gca      (kf)      aopt      2way
        4.7       4.7      3.28       0.0       2.0       0.0
$#      xp        yp        zp        a1        a2        a3    mangle
        0.0       0.0       0.0       1.0       0.0       0.0       0.0
$#      v1        v2        v3        d1        d2        d3    dfailm    dfails
        0.0       0.0       0.0       0.0       0.0       1.0       0.0       0.0
$#   tfail      alph      soft      fbrt     ycfac    dfailt    dfailc       efs
        0.0       0.0       1.0       0.0       2.0       0.0       0.0       0.0
$#      xc        xt        yc        yt        sc      crit      beta
       0.13      0.13     0.044     0.044      0.03      54.0       0.0
$#     pel      epsf      epsr      tsmd     soft2
        0.0       0.0       0.0       0.0       1.0
$#  slimt1    slimc1    slimt2    slimc2     slims    ncyred     softg
        0.0       0.0       0.0       0.0       0.0       0.0       1.0
*MAT_PIECEWISE_LINEAR_PLASTICITY_LOG_INTERPOLATION_TITLE
MAT_24-Mg
$#     mid        ro         e        pr      sigy      etan      fail      tdel
       21.74000E-6      36.0      0.35     0.231      0.01.00000E21       0.0
$#       c         p      lcss      lcsr        vp       lcf
        0.0       0.0         7         0       0.0         0
$#    eps1      eps2      eps3      eps4      eps5      eps6      eps7      eps8
        0.0       0.0       0.0       0.0       0.0       0.0       0.0       0.0
$#     es1       es2       es3       es4       es5       es6       es7       es8
        0.0       0.0       0.0       0.0       0.0       0.0       0.0       0.0
*MAT_LAYERED_LINEAR_PLASTICITY_TITLE
MAT_114-PlasticFoam
$#     mid        ro         e        pr      sigy      etan
       31.28100E-7      0.05       0.0       0.0       0.0
$#       c         p      lcss      lcsr
        0.0       0.0         2         0
$#    eps1      eps2      eps3      eps4      eps5      eps6      eps7      eps8
        0.0       0.0       0.0       0.0       0.0       0.0       0.0       0.0
$#     es1       es2       es3       es4       es5       es6       es7       es8
        0.0       0.0       0.0       0.0       0.0       0.0       0.0       0.0
*MAT_ELASTIC_TITLE
MAT_001-Foam
$#     mid        ro         e        pr        da        db  not used
       61.28100E-7      0.05       0.0       0.0       0.0         0
*INITIAL_VELOCITY
$#    nsid    nsidex     boxid    irigid      icid
         8         0         0         0         0
$#      vx        vy        vz       vxr       vyr       vzr
    -1.2512       0.0       0.0       0.0       0.0
*DEFINE_TABLE_TITLE
Table_Mg-Rate
$#    tbid       sfa      offa
         7
```

```
$#              value      lcid
                 0.0          4
    9.9999997474e-005          5
                 0.1          6
*DEFINE_CURVE_TITLE
Mg-Rate_0
$#   lcid      sidr      sfa       sfo      offa      offo    dattyp     lcint
        4         0       1.0       1.0       0.0       0.0         0         0
$#               a1                  o1
                0.0              0.2317
              0.001            0.233996
              0.002            0.236232
              0.003             0.23841
              0.004             0.24053
              0.005            0.242595
              0.006            0.244605
              0.007            0.246561
              0.008            0.248465
              0.009            0.250317
               0.01            0.252119
              0.011            0.253872
              0.012            0.255576
              0.013            0.257234
              0.014            0.258845
              0.015            0.260411
              0.016            0.261933
              0.017            0.263412
              0.018            0.264849
              0.019            0.266245
               0.02            0.267601
              0.021            0.268918
              0.022            0.270196
              0.023            0.271437
              0.024            0.272641
              0.025             0.27381
              0.026            0.274944
              0.027            0.276044
              0.028            0.277112
              0.029            0.278147
               0.03            0.279151
              0.031            0.280124
              0.032            0.281068
              0.033            0.281983
              0.034             0.28287
              0.035            0.283729
              0.036            0.284562
              0.037            0.285369
              0.038            0.286151
              0.039            0.286908
               0.04            0.287641
              0.041            0.288352
              0.042             0.28904
              0.043            0.289707
              0.044            0.290352
              0.045            0.290977
              0.046            0.291583
              0.047            0.292169
              0.048            0.292737
              0.049            0.293287
               0.05             0.29382
              0.051            0.294335
              0.052            0.294835
              0.053            0.295319
              0.054            0.295788
              0.055            0.296243
              0.056            0.296683
              0.057             0.29711
              0.058            0.297525
              0.059            0.297926
               0.06            0.298316
              0.061            0.298694
```

267

```
                  0.062                0.299061
                  0.063                0.299418
                  0.064                0.299764
                  0.065                0.300101
                  0.066                0.300428
                  0.067                0.300747
                  0.068                0.301057
                  0.069                0.301359
                   0.07                0.301654
                  0.071                0.301941
                  0.072                0.302221
                  0.073                0.302495
                  0.074                0.302762
                  0.075                0.303024
                  0.076                 0.30328
                  0.077                0.303531
                  0.078                0.303777
                  0.079                0.304019
                   0.08                0.304256
                  0.081                0.304489
                  0.082                0.304719
                  0.083                0.304945
                  0.084                0.305168
                  0.085                0.305389
                  0.086                0.305606
                  0.087                0.305822
                  0.088                0.306035
                  0.089                0.306246
                   0.09                0.306456
                  0.091                0.306664
                  0.092                0.306871
                  0.093                0.307077
                  0.094                0.307282
                  0.095                0.307486
                  0.096                 0.30769
                  0.097                0.307894
                  0.098                0.308097
                  0.099                0.308301
                    0.1                0.308504
*DEFINE_CURVE_TITLE
Mg-Rate_0.0001
$#     lcid      sidr       sfa       sfo      offa      offo    dattyp     lcint
          5         0       1.0       1.0       0.0       0.0         0         0
$#                   a1                  o1
                    0.0                 0.2478
                  0.001                0.25058
                  0.002               0.253233
                  0.003               0.255766
                  0.004               0.258181
                  0.005               0.260485
                  0.006               0.262681
                  0.007               0.264773
                  0.008               0.266766
                  0.009               0.268665
                   0.01               0.270472
                  0.011               0.272192
                  0.012               0.273829
                  0.013               0.275386
                  0.014               0.276868
                  0.015               0.278276
                  0.016               0.279616
                  0.017                0.28089
                  0.018               0.282102
                  0.019               0.283253
                   0.02               0.284349
                  0.021               0.285391
                  0.022               0.286383
                  0.023               0.287326
                  0.024               0.288225
                  0.025               0.289081
                  0.026               0.289896
```

0.027	0.290675
0.028	0.291417
0.029	0.292127
0.03	0.292806
0.031	0.293456
0.032	0.294079
0.033	0.294677
0.034	0.295252
0.035	0.295806
0.036	0.29634
0.037	0.296857
0.038	0.297357
0.039	0.297842
0.04	0.298314
0.041	0.298774
0.042	0.299223
0.043	0.299663
0.044	0.300094
0.045	0.300519
0.046	0.300937
0.047	0.30135
0.048	0.301758
0.049	0.302164
0.05	0.302567
0.051	0.302968
0.052	0.303368
0.053	0.303767
0.054	0.304167
0.055	0.304568
0.056	0.304969
0.057	0.305373
0.058	0.305779
0.059	0.306187
0.06	0.306598
0.061	0.307012
0.062	0.30743
0.063	0.307851
0.064	0.308276
0.065	0.308705
0.066	0.309138
0.067	0.309574
0.068	0.310015
0.069	0.31046
0.07	0.310909
0.071	0.311361
0.072	0.311818
0.073	0.312278
0.074	0.312741
0.075	0.313208
0.076	0.313678
0.077	0.314151
0.078	0.314627
0.079	0.315105
0.08	0.315585
0.081	0.316067
0.082	0.31655
0.083	0.317034
0.084	0.317519
0.085	0.318004
0.086	0.31849
0.087	0.318975
0.088	0.319459
0.089	0.319942
0.09	0.320423
0.091	0.320902
0.092	0.321379
0.093	0.321853
0.094	0.322323
0.095	0.32279
0.096	0.323252
0.097	0.32371

```
                 0.098            0.324163
                 0.099            0.32461
                 0.1             0.325051
*DEFINE_CURVE_TITLE
Mg-Rate_0.1
$#    lcid      sidr      sfa       sfo      offa      offo    dattyp     lcint
         6         0      1.0       1.0       0.0       0.0         0         0
$#               a1                 o1
                 0.0              0.2531
                 0.001            0.256577
                 0.002            0.259842
                 0.003            0.262909
                 0.004            0.265789
                 0.005            0.268493
                 0.006            0.271031
                 0.007            0.273414
                 0.008            0.275652
                 0.009            0.277754
                 0.01             0.279729
                 0.011            0.281585
                 0.012            0.283332
                 0.013            0.284976
                 0.014            0.286525
                 0.015            0.287987
                 0.016            0.289367
                 0.017            0.290672
                 0.018            0.291909
                 0.019            0.293083
                 0.02             0.294199
                 0.021            0.295262
                 0.022            0.296278
                 0.023            0.29725
                 0.024            0.298183
                 0.025            0.29908
                 0.026            0.299945
                 0.027            0.300782
                 0.028            0.301593
                 0.029            0.302382
                 0.03             0.303151
                 0.031            0.303901
                 0.032            0.304636
                 0.033            0.305358
                 0.034            0.306067
                 0.035            0.306766
                 0.036            0.307455
                 0.037            0.308136
                 0.038            0.30881
                 0.039            0.309478
                 0.04             0.31014
                 0.041            0.310797
                 0.042            0.311448
                 0.043            0.312095
                 0.044            0.312737
                 0.045            0.313375
                 0.046            0.314008
                 0.047            0.314635
                 0.048            0.315258
                 0.049            0.315874
                 0.05             0.316484
                 0.051            0.317088
                 0.052            0.317684
                 0.053            0.318272
                 0.054            0.318852
                 0.055            0.319422
                 0.056            0.319982
                 0.057            0.320532
                 0.058            0.321069
                 0.059            0.321595
                 0.06             0.322107
                 0.061            0.322606
                 0.062            0.32309
```

```
                    0.063               0.32356
                    0.064               0.324013
                    0.065               0.324451
                    0.066               0.324872
                    0.067               0.325276
                    0.068               0.325663
                    0.069               0.326032
                     0.07               0.326383
                    0.071               0.326717
                    0.072               0.327033
                    0.073               0.327332
                    0.074               0.327614
                    0.075               0.327879
                    0.076               0.328129
                    0.077               0.328363
                    0.078               0.328583
                    0.079                0.32879
                     0.08               0.328985
                    0.081                0.32917
                    0.082               0.329346
                    0.083               0.329516
                    0.084               0.329681
                    0.085               0.329844
                    0.086               0.330008
                    0.087               0.330174
                    0.088               0.330347
                    0.089                0.33053
                     0.09               0.330726
                    0.091               0.330938
                    0.092               0.331173
                    0.093               0.331432
                    0.094               0.331722
                    0.095               0.332048
                    0.096               0.332414
                    0.097               0.332827
                    0.098               0.333293
                    0.099               0.333817
                      0.1               0.334407
*DEFINE_CURVE_TITLE
Curve-Mg
$#    lcid      sidr       sfa       sfo      offa      offo    dattyp     lcint
         1         0       1.0       1.0       0.0       0.0         0         0
$#                  a1                  o1
                   0.0              0.2317
                0.0093              0.2558
                0.0219              0.2705
                0.0335              0.2826
                0.0597              0.2946
                0.1218              0.3161
                 0.188              0.3295
                0.2501              0.3402
                0.3132              0.3429
*DEFINE_CURVE_TITLE
Curve-foam
$#    lcid      sidr       sfa       sfo      offa      offo    dattyp     lcint
         2         0       1.0       1.0       0.0       0.0         0         0
$#                  a1                  o1
                   0.0                 0.0
                  0.13             0.00749
                   0.2              0.0075
                   0.4              0.0076
                   0.5               0.011
                   0.6               0.017
                   0.7               0.029
                  0.75               0.035
*DEFINE_CURVE_TITLE
Force ramp
$#    lcid      sidr       sfa       sfo      offa      offo    dattyp     lcint
         3         0       0.0       0.0       0.0       0.0         0         0
$#                  a1                  o1
                   0.0                 0.0
```

```
                         1.0                   1.0
*SET_NODE_LIST_TITLE
Impactor
$#      sid       da1       da2       da3       da4    solver
          8       0.0       0.0       0.0       0.0MECH
$#     nid1      nid2      nid3      nid4      nid5      nid6      nid7      nid8
        687       688       689       690       691       692       693       694
...
*SET_NODE_LIST_TITLE
3DFML for perturbation
$#      sid       da1       da2       da3       da4    solver
         10       0.0       0.0       0.0       0.0MECH
$#     nid1      nid2      nid3      nid4      nid5      nid6      nid7      nid8
          1         2         3         4         5         6         7         8
...
*DAMPING_FREQUENCY_RANGE_DEFORM
$#    cdamp      flow     fhigh      psid     blank    pidrel
         0.07      9.0      11.0         0         0         0
*ELEMENT_SHELL
$#   eid     pid     n1     n2     n3     n4     n5     n6     n7     n8
       1       1     224     227     229     223       0       0       0       0
...
*NODE
$#   nid               x                 y                 z        tc        rc
       1  -3.552714e-015              0.0               0.0         0         0
...
*PERTURBATION_NODE
$#     type      nsid       scl       cmp    icoord       cid
          1        10       1.0         2         0         0
$#     ampl       xwl      xoff       ywl      yoff       zwl      zoff
          1.0     388.0       0.0       0.0       0.0       0.0       0.0
*END
```

272

TSHELL Model for Impact Buckling (Chapter 5)

```
*KEYWORD
*TITLE
$#                                                                        title
*CONTROL_CONTACT
$#    slsfac    rwpnal    islchk    shlthk    penopt    thkchg     orien    enmass
         0.1       0.0         1         0         1         0         2         0
$#    usrstr    usrfrc     nsbcs    interm     xpene     ssthk      ecdt   tiedprj
           0         0         0         0       4.0         0         0         0
$#     sfric     dfric       edc       vfc        th     th_sf    pen_sf
         0.0       0.0       0.0       0.0       0.0       0.0       0.0
$#    ignore    frceng   skiprwg    outseg   spotstp   spotdel   spothin
           0         0         0         0         0         0       0.0
$#      isym     nserod    rwgaps    rwgdth     rwksf      icov    swradf    ithoff
           0         0         1       0.0       1.0         0       0.0         0
$#    shledg     pstiff    ithcnt    tdcnof     ftall    unused    shltrw
           1         0         0         0         0                 0.0
*CONTROL_ENERGY
$#      hgen      rwen    slnten     rylen
           2         2         2         2
*CONTROL_HOURGLASS
$#       ihq        qh
           1       0.1
*CONTROL_TERMINATION
$#    endtim    endcyc     dtmin    endeng    endmas
         6.0         0       0.0      0.01.000000E8
*DATABASE_BNDOUT
$#        dt    binary      lcur     ioopt
        0.01         0         0         1
*DATABASE_ELOUT
$#        dt    binary      lcur     ioopt   option1   option2   option3   option4
        0.01         0         0         1         0         0         0         0
*DATABASE_GCEOUT
$#        dt    binary      lcur     ioopt
        0.01         0         0         1
*DATABASE_GLSTAT
$#        dt    binary      lcur     ioopt
        0.01         0         0         1
*DATABASE_NCFORC
$#        dt    binary      lcur     ioopt
        0.01         0         0         1
*DATABASE_NODFOR
$#        dt    binary      lcur     ioopt
        0.01         0         0         1
*DATABASE_NODOUT
$#        dt    binary      lcur     ioopt   option1   option2
        0.01         0         0         1       0.0         0
*DATABASE_RCFORC
$#        dt    binary      lcur     ioopt
        0.01         0         0         1
*DATABASE_BINARY_D3PLOT
$#        dt      lcdt      beam     npltc    psetid
        0.01         0         0         0         0
$#     ioopt
           0
*DATABASE_NODAL_FORCE_GROUP
$#      nsid       cid
           1         0
*DATABASE_NODAL_FORCE_GROUP
$#      nsid       cid
           2         0
*DATABASE_HISTORY_NODE_SET
$#       id1       id2       id3       id4       id5       id6       id7       id8
           1         2         0         0         0         0         0         0
*BOUNDARY_SPC_SET_ID
$#        id                                                              heading
           1BC_x=0
$#      nsid       cid      dofx      dofy      dofz     dofrx     dofry     dofrz
           1         0         1         0         0         0         0         0
```

```
*SET_NODE_LIST_TITLE
x=0
$#      sid       da1       da2       da3       da4    solver
          1       0.0       0.0       0.0       0.0MECH
$#     nid1      nid2      nid3      nid4      nid5      nid6      nid7      nid8
          1         2         3         4         5         6         7         8
          9        10        11      1079      1080      1081      1082      1083
       1084      1085      1086      1087      1088      1089      2157      2255
       2353      2451      2549      2647      2745      2843      2941      3039
       3137      3235      3333      3431      3529      3627      3725      3823
       3921      4019      4117      4215         0         0         0         0
*BOUNDARY_SPC_SET_ID
$#       id                                                           heading
          2BC_RigBod_x=0
$#     nsid       cid      dofx      dofy      dofz     dofrx     dofry     dofrz
          3         0         0         0         1         0         0         0
*SET_NODE_LIST_TITLE
RigBod_x=0
$#      sid       da1       da2       da3       da4    solver
          3       0.0       0.0       0.0       0.0MECH
$#     nid1      nid2      nid3      nid4      nid5      nid6      nid7      nid8
          1      1079      2157      2255         0         0         0         0
*BOUNDARY_SPC_SET_ID
$#       id                                                           heading
          3BC_Fixture_x=0_TOP
$#     nsid       cid      dofx      dofy      dofz     dofrx     dofry     dofrz
          4         0         0         1         0         0         0         0
*SET_NODE_LIST_TITLE
Fixture_x=0_TOP
$#      sid       da1       da2       da3       da4    solver
          4       0.0       0.0       0.0       0.0MECH
$#     nid1      nid2      nid3      nid4      nid5      nid6      nid7      nid8
          1         2         3         4         5         6         7         8
...
*BOUNDARY_SPC_SET_ID
$#       id                                                           heading
          4BC_Fixture_x=0_BOTTOM
$#     nsid       cid      dofx      dofy      dofz     dofrx     dofry     dofrz
          5         0         0         1         0         0         0         0
*SET_NODE_LIST_TITLE
Fixture_x=0_BOTTOM
$#      sid       da1       da2       da3       da4    solver
          5       0.0       0.0       0.0       0.0MECH
$#     nid1      nid2      nid3      nid4      nid5      nid6      nid7      nid8
       1079      1080      1081      1082      1083      1084      1085      1086
...
*BOUNDARY_SPC_SET_ID
$#       id                                                           heading
          5BC_Fixture_x=L_TOP
$#     nsid       cid      dofx      dofy      dofz     dofrx     dofry     dofrz
          6         0         0         1         0         0         0         0
*SET_NODE_LIST_TITLE
Fixture_x=L_TOP
$#      sid       da1       da2       da3       da4    solver
          6       0.0       0.0       0.0       0.0MECH
$#     nid1      nid2      nid3      nid4      nid5      nid6      nid7      nid8
        947       948       949       950       951       952       953       954
...
*BOUNDARY_SPC_SET_ID
$#       id                                                           heading
          6BC_Fixture_x=L_BOTTOM
$#     nsid       cid      dofx      dofy      dofz     dofrx     dofry     dofrz
          7         0         0         1         0         0         0         0
*SET_NODE_LIST_TITLE
Fixture_x=L_BOTTOM
$#      sid       da1       da2       da3       da4    solver
          7       0.0       0.0       0.0       0.0MECH
$#     nid1      nid2      nid3      nid4      nid5      nid6      nid7      nid8
       2025      2026      2027      2028      2029      2030      2031      2032
...
*BOUNDARY_SPC_SET_ID
```

274

```
$#       id                                                                 heading
         7BC_RigBod_x=L
$#     nsid       cid      dofx      dofy      dofz     dofrx     dofry     dofrz
          8         0         0         0         1         0         0         0
*SET_NODE_LIST_TITLE
RigBod_x=L
$#      sid       da1       da2       da3       da4    solver
          8       0.0       0.0       0.0       0.0MECH
$#     nid1      nid2      nid3      nid4      nid5      nid6      nid7      nid8
       1068      2146      2254      2352         0         0         0         0
*BOUNDARY_SPC_SET_ID
$#       id                                                                 heading
         8BC_RigBod_Impactor
$#     nsid       cid      dofx      dofy      dofz     dofrx     dofry     dofrz
         10         0         0         1         1         1         1         1
*SET_NODE_LIST_TITLE
RigBod-Impactor
$#      sid       da1       da2       da3       da4    solver
         10       0.0       0.0       0.0       0.0MECH
$#     nid1      nid2      nid3      nid4      nid5      nid6      nid7      nid8
       4994         0         0         0         0         0         0         0
*BOUNDARY_SPC_SET_ID
$#       id                                                                 heading
         0BC_RigBod_Fixture
$#     nsid       cid      dofx      dofy      dofz     dofrx     dofry     dofrz
         12         0         0         1         1         1         1         1
*SET_NODE_LIST_TITLE
RigBod fixture
$#      sid       da1       da2       da3       da4    solver
         12       0.0       0.0       0.0       0.0MECH
$#     nid1      nid2      nid3      nid4      nid5      nid6      nid7      nid8
       5301         0         0         0         0         0         0         0
*CONTACT_AUTOMATIC_SURFACE_TO_SURFACE_TIEBREAK_ID
$#      cid                                                                   title
         0Skin-Top
$#     ssid      msid     sstyp     mstyp    sboxid    mboxid       spr       mpr
          2         1         0         0         0         0         0         0
$#       fs        fd        dc        vc       vdc    penchk        bt        dt
        0.0       0.0       0.0       0.0       0.0         0      0.01.00000E20
$#      sfs       sfm       sst       mst      sfst      sfmt       fsf       vsf
        1.0       1.0       0.0       0.0       1.0       1.0       1.0       1.0
$#   option      nfls      sfls     param    eraten    erates     ct2cn        cn
          2     0.003      0.02       0.0       0.0       0.0       0.0       0.0
$#     soft    sofscl    lcidab    maxpar     sbopt     depth     bsort    frcfrq
          2       0.1         0     1.025       2.0         2         0         1
$#   penmax    thkopt    shlthk     snlog      isym     i2d3d    sldthk    sldstf
        0.0         0         0         0         0         0       0.0       0.0
$#     igap ignodprfac/mpadtstif/mpar2    unused    unused    flangl   cid_rcf
          1         0       0.0       0.0                         0.0         0
*SET_SEGMENT_TITLE
Core_UP
$#      sid       da1       da2       da3       da4    solver
          2       0.0       0.0       0.0       0.0MECH
$#       n1        n2        n3        n4        a1        a2        a3        a4
       4080      4276      4277      4081       0.0       0.0       0.0       0.0
...
*SET_SEGMENT_TITLE
Skin-Top
$#      sid       da1       da2       da3       da4    solver
          1       0.0       0.0       0.0       0.0MECH
$#       n1        n2        n3        n4        a1        a2        a3        a4
       1031      1032      1021      1020       0.0       0.0       0.0       0.0
...
*CONTACT_AUTOMATIC_SURFACE_TO_SURFACE_TIEBREAK_ID
$#      cid                                                                   title
         2Skin-Bottom
$#     ssid      msid     sstyp     mstyp    sboxid    mboxid       spr       mpr
          3         4         0         0         0         0         0         0
$#       fs        fd        dc        vc       vdc    penchk        bt        dt
        0.0       0.0       0.0       0.0       0.0         0      0.01.00000E20
$#      sfs       sfm       sst       mst      sfst      sfmt       fsf       vsf
```

```
        1.0       1.0       0.0       0.0       1.0       1.0       1.0       1.0
$#   option      nfls      sfls     param    eraten    erates     ct2cn        cn
        2     0.003      0.02       0.0       0.0       0.0       0.0       0.0
$#     soft    sofscl    lcidab    maxpar     sbopt     depth     bsort    frcfrq
        2       0.1         0     1.025       2.0         2         0         1
$#   penmax    thkopt    shlthk     snlog      isym     i2d3d    sldthk    sldstf
      0.0         0         0         0         0         0       0.0       0.0
$#     igap ignodprfac/mpadtstif/mpar2    unused    unused    flangl   cid_rcf
        1         0       0.0       0.0                             0.0         0
*SET_SEGMENT_TITLE
Core_DOWN
$#      sid       da1       da2       da3       da4    solver
        3       0.0       0.0       0.0       0.0MECH
$#       n1        n2        n3        n4        a1        a2        a3        a4
     3571      3767      3766      3570       0.0       0.0       0.0       0.0
...
*SET_SEGMENT_TITLE
Skin-Bottom
$#      sid       da1       da2       da3       da4    solver
        4       0.0       0.0       0.0       0.0MECH
$#       n1        n2        n3        n4        a1        a2        a3        a4
     2051      2052      2041      2040       0.0       0.0       0.0       0.0
...
*CONTACT_AUTOMATIC_SURFACE_TO_SURFACE_ID
$#      cid                                                                 title
        0Impactor fixture
$#     ssid      msid     sstyp     mstyp    sboxid    mboxid       spr       mpr
       10         5         0         0         0         0         0         0
$#       fs        fd        dc        vc       vdc    penchk        bt        dt
      0.0       0.0       0.0       0.0       0.0         0      0.01.00000E20
$#      sfs       sfm       sst       mst      sfst      sfmt       fsf       vsf
      1.0       1.0       0.0       0.0       1.0       1.0       1.0       1.0
*SET_SEGMENT_TITLE
Fixture impactor
$#      sid       da1       da2       da3       da4    solver
       10       0.0       0.0       0.0       0.0MECH
$#       n1        n2        n3        n4        a1        a2        a3        a4
     5103      5108      5153      5148       0.0       0.0       0.0       0.0
...
*SET_SEGMENT_TITLE
Impactor
$#      sid       da1       da2       da3       da4    solver
        5       0.0       0.0       0.0       0.0MECH
$#       n1        n2        n3        n4        a1        a2        a3        a4
     4330      4356      4362      4336       0.0       0.0       0.0       0.0
...
*CONTACT_TIED_NODES_TO_SURFACE_ID
$#      cid                                                                 title
        0Fixture specimen
$#     ssid      msid     sstyp     mstyp    sboxid    mboxid       spr       mpr
        2         9         4         0         0         0         0         0
$#       fs        fd        dc        vc       vdc    penchk        bt        dt
      0.0       0.0       0.0       0.0       0.0         0      0.01.00000E20
$#      sfs       sfm       sst       mst      sfst      sfmt       fsf       vsf
      1.0       1.0       0.0       0.0       1.0       1.0       1.0       1.0
$#     soft    sofscl    lcidab    maxpar     sbopt     depth     bsort    frcfrq
        1       0.1         0     1.025       2.0         2         0         1
$#   penmax    thkopt    shlthk     snlog      isym     i2d3d    sldthk    sldstf
      0.0         0         0         0         0         0       0.0       0.0
$#     igap ignodprfac/mpadtstif/mpar2    unused    unused    flangl   cid_rcf
        1         0       0.0       0.0                             0.0         0
*SET_NODE_LIST_TITLE
x=L
$#      sid       da1       da2       da3       da4    solver
        2       0.0       0.0       0.0       0.0MECH
$#     nid1      nid2      nid3      nid4      nid5      nid6      nid7      nid8
     1068      1069      1070      1071      1072      1073      1074      1075
...
*SET_SEGMENT_TITLE
Fixture specimen
$#      sid       da1       da2       da3       da4    solver
```

```
         9        0.0        0.0        0.0        0.0MECH
$#        n1         n2         n3         n4         a1         a2         a3         a4
      5119       5114       5159       5164        0.0        0.0        0.0        0.0
...
*PART
$#                                                                         title
Skin-Top
$#       pid      secid        mid      eosid       hgid       grav     adpopt       tmid
         1          1          2          0          0          0          0          0
*SECTION_SHELL_TITLE
Section_SHELL
$#     secid     elform       shrf        nip      propt    qr/irid      icomp      setyp
         1          2        1.0          1        1.0          0          0          1
$#        t1         t2         t3         t4       nloc      marea       idof     edgset
       0.5        0.5        0.5        0.5        0.0        0.0        0.0          0
*MAT_PIECEWISE_LINEAR_PLASTICITY_LOG_INTERPOLATION_TITLE
MAT_024-Mg
$#       mid         ro          e         pr       sigy       etan       fail       tdel
     21.74000E-6       36.0       0.35      0.231            0.01.00000E21        0.0
$#         c          p       lcss       lcsr         vp        lcf
       0.0        0.0          7          0        0.0          0
$#      eps1       eps2       eps3       eps4       eps5       eps6       eps7       eps8
       0.0        0.0        0.0        0.0        0.0        0.0        0.0        0.0
$#       es1        es2        es3        es4        es5        es6        es7        es8
       0.0        0.0        0.0        0.0        0.0        0.0        0.0        0.0
*PART
$#                                                                         title
Skin-Bottom
$#       pid      secid        mid      eosid       hgid       grav     adpopt       tmid
         2          1          2          0          0          0          0          0
*PART_COMPOSITE_TSHELL
$#                                                                         title
Core
$#       pid     elform       shrf     unused     unused       hgid     unused     tshear
         3          5   0.833333                              0                      0
$#     mid1     thick1         b1      tmid1       mid2     thick2         b2      tmid2
         1       0.45        0.0          0          5        1.7        0.0          0
         5        1.7        0.0          0          1       0.45        0.0          0
*PART
$#                                                                         title
Fixture
$#       pid      secid        mid      eosid       hgid       grav     adpopt       tmid
         4          2          6          0          0          0          0          0
*SECTION_SOLID_TITLE
Section-Solid
$#     secid     elform        aet
         2          1          0
*MAT_ELASTIC_TITLE
Elastic fixture - aluminum
$#       mid         ro          e         pr         da         db   not used
     62.70000E-6       70.0       0.33        0.0        0.0          0
*PART
$#                                                                         title
Impactor
$#       pid      secid        mid      eosid       hgid       grav     adpopt       tmid
         5          2          4          0          0          0          0          0
*MAT_ELASTIC_TITLE
MAT_001-Impactor
$#       mid         ro          e         pr         da         db   not used
     44.80000E-5      200.0        0.3        0.0        0.0          0
*MAT_ENHANCED_COMPOSITE_DAMAGE_TITLE
MAT_54-fiberglass
$#       mid         ro         ea         eb       (ec)       prba      (prca)     (prcb)
     11.75000E-6       9.07        9.0       2.55       0.05       0.05      0.428
$#       gab        gbc        gca       (kf)       aopt       2way
       1.0        1.0        1.0        0.0        2.0        0.0
$#        xp         yp         zp         a1         a2         a3     mangle
       0.0        0.0        0.0        1.0        0.0        0.0        0.0
$#        v1         v2         v3         d1         d2         d3     dfailm     dfails
       0.0        0.0        0.0        0.0        0.0        1.0        0.0        0.0
$#     tfail       alph       soft       fbrt      ycfac     dfailt     dfailc        efs
```

277

```
       0.0         0.0         1.0         0.0         2.0         0.0         0.0         0.0
$#       xc          xt          yc          yt          sc        crit        beta
       0.173       0.173       0.173       0.173        0.03        54.0         0.0
$#      pel        epsf        epsr        tsmd       soft2
        0.0         0.0         0.0         0.0         1.0
$#   slimt1      slimc1      slimt2      slimc2       slims      ncyred       softg
        0.0         0.0         0.0         0.0         0.0         0.0         1.0
*MAT_CRUSHABLE_FOAM_TITLE
MAT_63-Foam
$#      mid          ro           e          pr        lcid         tsc        damp
        31.28100E-7        0.05         0.0           2         0.0         0.0
*MAT_ELASTIC_TITLE
Elastic foam
$#      mid          ro           e          pr          da          db  not used
        51.28100E-7        0.05         0.0         0.0         0.0           0
*INITIAL_VELOCITY
$#     nsid      nsidex       boxid      irigid        icid
          9           0           0           0           0
$#       vx          vy          vz         vxr         vyr         vzr
    -1.2512         0.0         0.0         0.0         0.0         0.0
*DEFINE_TABLE_TITLE
Table_Mg-Rate
$#     tbid         sfa        offa
          7
$#              value        lcid
                0.0           4
    9.9999997474e-005         5
                0.1           6
*DEFINE_CURVE_TITLE
Mg-Rate_0
$#     lcid        sidr         sfa         sfo        offa        offo      dattyp       lcint
          4           0         1.0         1.0         0.0         0.0           0           0
$#               a1                      o1
               0.0                  0.2317
             0.001                0.233996
             0.002                0.236232
             0.003                 0.23841
             0.004                 0.24053
             0.005                0.242595
             0.006                0.244605
             0.007                0.246561
             0.008                0.248465
             0.009                0.250317
              0.01                0.252119
             0.011                0.253872
             0.012                0.255576
             0.013                0.257234
             0.014                0.258845
             0.015                0.260411
             0.016                0.261933
             0.017                0.263412
             0.018                0.264849
             0.019                0.266245
              0.02                0.267601
             0.021                0.268918
             0.022                0.270196
             0.023                0.271437
             0.024                0.272641
             0.025                 0.27381
             0.026                0.274944
             0.027                0.276044
             0.028                0.277112
             0.029                0.278147
              0.03                0.279151
             0.031                0.280124
             0.032                0.281068
             0.033                0.281983
             0.034                 0.28287
             0.035                0.283729
             0.036                0.284562
             0.037                0.285369
```

```
          0.038                 0.286151
          0.039                 0.286908
           0.04                 0.287641
          0.041                 0.288352
          0.042                  0.28904
          0.043                 0.289707
          0.044                 0.290352
          0.045                 0.290977
          0.046                 0.291583
          0.047                 0.292169
          0.048                 0.292737
          0.049                 0.293287
           0.05                  0.29382
          0.051                 0.294335
          0.052                 0.294835
          0.053                 0.295319
          0.054                 0.295788
          0.055                 0.296243
          0.056                 0.296683
          0.057                  0.29711
          0.058                 0.297525
          0.059                 0.297926
           0.06                 0.298316
          0.061                 0.298694
          0.062                 0.299061
          0.063                 0.299418
          0.064                 0.299764
          0.065                 0.300101
          0.066                 0.300428
          0.067                 0.300747
          0.068                 0.301057
          0.069                 0.301359
           0.07                 0.301654
          0.071                 0.301941
          0.072                 0.302221
          0.073                 0.302495
          0.074                 0.302762
          0.075                 0.303024
          0.076                  0.30328
          0.077                 0.303531
          0.078                 0.303777
          0.079                 0.304019
           0.08                 0.304256
          0.081                 0.304489
          0.082                 0.304719
          0.083                 0.304945
          0.084                 0.305168
          0.085                 0.305389
          0.086                 0.305606
          0.087                 0.305822
          0.088                 0.306035
          0.089                 0.306246
           0.09                 0.306456
          0.091                 0.306664
          0.092                 0.306871
          0.093                 0.307077
          0.094                 0.307282
          0.095                 0.307486
          0.096                  0.30769
          0.097                 0.307894
          0.098                 0.308097
          0.099                 0.308301
            0.1                 0.308504
*DEFINE_CURVE_TITLE
Mg-Rate_0.0001
$#    lcid      sidr       sfa       sfo      offa      offo    dattyp     lcint
         5         0       1.0       1.0       0.0       0.0         0         0
$#                  a1                  o1
                  0.0              0.2478
                0.001             0.25058
                0.002            0.253233
```

279

0.003	0.255766
0.004	0.258181
0.005	0.260485
0.006	0.262681
0.007	0.264773
0.008	0.266766
0.009	0.268665
0.01	0.270472
0.011	0.272192
0.012	0.273829
0.013	0.275386
0.014	0.276868
0.015	0.278276
0.016	0.279616
0.017	0.28089
0.018	0.282102
0.019	0.283253
0.02	0.284349
0.021	0.285391
0.022	0.286383
0.023	0.287326
0.024	0.288225
0.025	0.289081
0.026	0.289896
0.027	0.290675
0.028	0.291417
0.029	0.292127
0.03	0.292806
0.031	0.293456
0.032	0.294079
0.033	0.294677
0.034	0.295252
0.035	0.295806
0.036	0.29634
0.037	0.296857
0.038	0.297357
0.039	0.297842
0.04	0.298314
0.041	0.298774
0.042	0.299223
0.043	0.299663
0.044	0.300094
0.045	0.300519
0.046	0.300937
0.047	0.30135
0.048	0.301758
0.049	0.302164
0.05	0.302567
0.051	0.302968
0.052	0.303368
0.053	0.303767
0.054	0.304167
0.055	0.304568
0.056	0.304969
0.057	0.305373
0.058	0.305779
0.059	0.306187
0.06	0.306598
0.061	0.307012
0.062	0.30743
0.063	0.307851
0.064	0.308276
0.065	0.308705
0.066	0.309138
0.067	0.309574
0.068	0.310015
0.069	0.31046
0.07	0.310909
0.071	0.311361
0.072	0.311818
0.073	0.312278

```
                      0.074                 0.312741
                      0.075                 0.313208
                      0.076                 0.313678
                      0.077                 0.314151
                      0.078                 0.314627
                      0.079                 0.315105
                       0.08                 0.315585
                      0.081                 0.316067
                      0.082                  0.31655
                      0.083                 0.317034
                      0.084                 0.317519
                      0.085                 0.318004
                      0.086                  0.31849
                      0.087                 0.318975
                      0.088                 0.319459
                      0.089                 0.319942
                       0.09                 0.320423
                      0.091                 0.320902
                      0.092                 0.321379
                      0.093                 0.321853
                      0.094                 0.322323
                      0.095                  0.32279
                      0.096                 0.323252
                      0.097                  0.32371
                      0.098                 0.324163
                      0.099                  0.32461
                        0.1                 0.325051
*DEFINE_CURVE_TITLE
Mg-Rate_0.1
$#     lcid      sidr       sfa       sfo      offa      offo    dattyp     lcint
          6         0       1.0       1.0       0.0       0.0         0         0
$#                   a1                  o1
                      0.0                 0.2531
                      0.001               0.256577
                      0.002               0.259842
                      0.003               0.262909
                      0.004               0.265789
                      0.005               0.268493
                      0.006               0.271031
                      0.007               0.273414
                      0.008               0.275652
                      0.009               0.277754
                       0.01               0.279729
                      0.011               0.281585
                      0.012               0.283332
                      0.013               0.284976
                      0.014               0.286525
                      0.015               0.287987
                      0.016               0.289367
                      0.017               0.290672
                      0.018               0.291909
                      0.019               0.293083
                       0.02               0.294199
                      0.021               0.295262
                      0.022               0.296278
                      0.023                0.29725
                      0.024               0.298183
                      0.025                0.29908
                      0.026               0.299945
                      0.027               0.300782
                      0.028               0.301593
                      0.029               0.302382
                       0.03               0.303151
                      0.031               0.303901
                      0.032               0.304636
                      0.033               0.305358
                      0.034               0.306067
                      0.035               0.306766
                      0.036               0.307455
                      0.037               0.308136
                      0.038                0.30881
```

281

```
                0.039              0.309478
                 0.04               0.31014
                0.041              0.310797
                0.042              0.311448
                0.043              0.312095
                0.044              0.312737
                0.045              0.313375
                0.046              0.314008
                0.047              0.314635
                0.048              0.315258
                0.049              0.315874
                 0.05              0.316484
                0.051              0.317088
                0.052              0.317684
                0.053              0.318272
                0.054              0.318852
                0.055              0.319422
                0.056              0.319982
                0.057              0.320532
                0.058              0.321069
                0.059              0.321595
                 0.06              0.322107
                0.061              0.322606
                0.062               0.32309
                0.063               0.32356
                0.064              0.324013
                0.065              0.324451
                0.066              0.324872
                0.067              0.325276
                0.068              0.325663
                0.069              0.326032
                 0.07              0.326383
                0.071              0.326717
                0.072              0.327033
                0.073              0.327332
                0.074              0.327614
                0.075              0.327879
                0.076              0.328129
                0.077              0.328363
                0.078              0.328583
                0.079               0.32879
                 0.08              0.328985
                0.081               0.32917
                0.082              0.329346
                0.083              0.329516
                0.084              0.329681
                0.085              0.329844
                0.086              0.330008
                0.087              0.330174
                0.088              0.330347
                0.089               0.33053
                 0.09              0.330726
                0.091              0.330938
                0.092              0.331173
                0.093              0.331432
                0.094              0.331722
                0.095              0.332048
                0.096              0.332414
                0.097              0.332827
                0.098              0.333293
                0.099              0.333817
                  0.1              0.334407
*DEFINE_CURVE_TITLE
Curve-Mg
$#    lcid      sidr      sfa      sfo      offa      offo     dattyp     lcint
         1         0      1.0      1.0       0.0       0.0          0          0
$#               a1                o1
               0.0             0.2317
            0.0093             0.2558
            0.0219             0.2705
            0.0335             0.2826
```

```
                 0.0597                  0.2946
                 0.1218                  0.3161
                  0.188                  0.3295
                 0.2501                  0.3402
                 0.3132                  0.3429
*DEFINE_CURVE_TITLE
Curve-foam
$#     lcid      sidr       sfa       sfo      offa      offo    dattyp     lcint
          2         0       1.0       1.0       0.0       0.0         0         0
$#                  a1                  o1
                   0.0                 0.0
                  0.13             0.00749
                   0.2              0.0075
                   0.4              0.0076
                   0.5               0.011
                   0.6               0.017
                   0.7               0.029
                  0.75               0.035
*DEFINE_CURVE_TITLE
Force ramp
$#     lcid      sidr       sfa       sfo      offa      offo    dattyp     lcint
          3         0       0.0       0.0       0.0       0.0         0         0
$#                  a1                  o1
                   0.0                 0.0
                   1.0                 1.0
*SET_NODE_LIST_TITLE
Impactor
$#      sid       da1       da2       da3       da4    solver
          9       0.0       0.0       0.0       0.0MECH
$#     nid1      nid2      nid3      nid4      nid5      nid6      nid7      nid8
       4313      4314      4315      4316      4317      4318      4319      4320
...
*SET_NODE_LIST_TITLE
3DFML
$#      sid       da1       da2       da3       da4    solver
         11       0.0       0.0       0.0       0.0MECH
$#     nid1      nid2      nid3      nid4      nid5      nid6      nid7      nid8
          1         2         3         4         5         6         7         8
...
*SET_SEGMENT_TITLE
Skin-Top_Fixture
$#      sid       da1       da2       da3       da4    solver
          6       0.0       0.0       0.0       0.0MECH
$#       n1        n2        n3        n4        a1        a2        a3        a4
       1068      1069      1058      1057       0.0       0.0       0.0       0.0
...
*SET_SEGMENT_TITLE
Core_Fixture
$#      sid       da1       da2       da3       da4    solver
          7       0.0       0.0       0.0       0.0MECH
$#       n1        n2        n3        n4        a1        a2        a3        a4
       3234      3332      3528      3430       0.0       0.0       0.0       0.0
...
*SET_SEGMENT_TITLE
Skin-Bottom_Fixture
$#      sid       da1       da2       da3       da4    solver
          8       0.0       0.0       0.0       0.0MECH
$#       n1        n2        n3        n4        a1        a2        a3        a4
       2146      2147      2136      2135       0.0       0.0       0.0       0.0
...
*DAMPING_FREQUENCY_RANGE_DEFORM
$#    cdamp      flow     fhigh      psid     blank    pidrel
       0.07       9.0      11.0         0         0         0
*PERTURBATION_NODE
$#     type      nsid       scl       cmp    icoord       cid
          1        11       1.0         2         0         0
$#     ampl       xwl      xoff       ywl      yoff       zwl      zoff
        1.0     388.0       0.0       0.0       0.0       0.0       0.0
...
*END
```

SOLID Model for Impact Buckling (Chapter 5)

```
*KEYWORD
*TITLE
$#                                                                       title
*CONTROL_CONTACT
$#   slsfac    rwpnal    islchk    shlthk    penopt    thkchg     orien    enmass
        0.1       0.0         1         0         1         0         2         0
$#   usrstr    usrfrc     nsbcs    interm     xpene     ssthk      ecdt   tiedprj
          0         0         0         0       4.0         0         0         0
$#    sfric     dfric       edc       vfc        th     th_sf    pen_sf
        0.0       0.0       0.0       0.0       0.0       0.0       0.0
$#   ignore    frceng   skiprwg    outseg   spotstp   spotdel   spothin
          0         0         0         0         0         0       0.0
$#     isym    nserod    rwgaps    rwgdth     rwksf      icov    swradf    ithoff
          0         0         1       0.0       1.0         0       0.0         0
$#   shledg    pstiff    ithcnt    tdcnof     ftall    unused    shltrw
          0         0         0         0         0                 0.0
*CONTROL_ENERGY
$#     hgen      rwen    slnten     rylen
          2         2         2         2
*CONTROL_HOURGLASS
$#      ihq        qh
          1       0.1
*CONTROL_TERMINATION
$#   endtim    endcyc     dtmin    endeng    endmas
        6.0         0       0.0      0.05.000000E8
*DATABASE_BNDOUT
$#       dt    binary      lcur     ioopt
       0.01         0         0         1
*DATABASE_ELOUT
$#       dt    binary      lcur     ioopt   option1   option2   option3   option4
       0.01         0         0         1         0         0         0         0
*DATABASE_GCEOUT
$#       dt    binary      lcur     ioopt
       0.01         0         0         1
*DATABASE_GLSTAT
$#       dt    binary      lcur     ioopt
       0.01         0         0         1
*DATABASE_NCFORC
$#       dt    binary      lcur     ioopt
       0.01         0         0         1
*DATABASE_NODFOR
$#       dt    binary      lcur     ioopt
       0.01         0         0         1
*DATABASE_NODOUT
$#       dt    binary      lcur     ioopt   option1   option2
       0.01         0         0         1       0.0         0
*DATABASE_RCFORC
$#       dt    binary      lcur     ioopt
       0.01         0         0         1
*DATABASE_SPCFORC
$#       dt    binary      lcur     ioopt
       0.01         0         0         1
*DATABASE_BINARY_D3PLOT
$#       dt      lcdt      beam     npltc    psetid
       0.01         0         0         0         0
$#    ioopt
          0
*DATABASE_NODAL_FORCE_GROUP
$#     nsid       cid
          1         0
*DATABASE_NODAL_FORCE_GROUP
$#     nsid       cid
          2         0
*DATABASE_HISTORY_NODE_SET
$#      id1       id2       id3       id4       id5       id6       id7       id8
          1         2         0         0         0         0         0         0
*BOUNDARY_SPC_SET_ID
$#       id                                                              heading
```

```
          0BC_x=0
$#      nsid       cid      dofx      dofy      dofz     dofrx     dofry     dofrz
           1         0         1         0         0         0         0         0
*SET_NODE_LIST_TITLE
x=0
$#       sid       da1       da2       da3       da4    solver
           1       0.0       0.0       0.0       0.0MECH
$#      nid1      nid2      nid3      nid4      nid5      nid6      nid7      nid8
           2       100       198       296       394       492       590       688
           0         0         0         0         0         0         0         0
*BOUNDARY_SPC_SET_ID
$#       id                                                               heading
          0BC_Fix_x=0_Top
$#      nsid       cid      dofx      dofy      dofz     dofrx     dofry     dofrz
           3         0         0         1         0         0         0         0
*SET_NODE_LIST_TITLE
Fixture_x=0_Top
$#       sid       da1       da2       da3       da4    solver
           3       0.0       0.0       0.0       0.0MECH
$#      nid1      nid2      nid3      nid4      nid5      nid6      nid7      nid8
       15321     15322     15323     15324     15325     15326     15327     15328
           0         0         0         0         0         0         0         0
*BOUNDARY_SPC_SET_ID
$#       id                                                               heading
          0BC_Fix_x=L_Top
$#      nsid       cid      dofx      dofy      dofz     dofrx     dofry     dofrz
           4         0         0         1         0         0         0         0
*SET_NODE_LIST_TITLE
Fixture_x=L_Top
$#       sid       da1       da2       da3       da4    solver
           4       0.0       0.0       0.0       0.0MECH
$#      nid1      nid2      nid3      nid4      nid5      nid6      nid7      nid8
       15408     15409     15410     15411     15412     15413     15414     15415
           0         0         0         0         0         0         0         0
*BOUNDARY_SPC_SET_ID
$#       id                                                               heading
          0BC_Fix_x=0_Bottom
$#      nsid       cid      dofx      dofy      dofz     dofrx     dofry     dofrz
           5         0         0         1         0         0         0         0
*SET_NODE_LIST_TITLE
Fixture_x=0_Bottom
$#       sid       da1       da2       da3       da4    solver
           5       0.0       0.0       0.0       0.0MECH
$#      nid1      nid2      nid3      nid4      nid5      nid6      nid7      nid8
       18359     18360     18361     18362     18363     18364     18365     18366
           0         0         0         0         0         0         0         0
*BOUNDARY_SPC_SET_ID
$#       id                                                               heading
          0BC_Fix_x=L_Bottom
$#      nsid       cid      dofx      dofy      dofz     dofrx     dofry     dofrz
           6         0         0         1         0         0         0         0
*SET_NODE_LIST_TITLE
Fixture_x=L_Bottom
$#       sid       da1       da2       da3       da4    solver
           6       0.0       0.0       0.0       0.0MECH
$#      nid1      nid2      nid3      nid4      nid5      nid6      nid7      nid8
       18446     18447     18448     18449     18450     18451     18452     18453
           0         0         0         0         0         0         0         0
*BOUNDARY_SPC_SET_ID
$#       id                                                               heading
          0NO-Z-dir
$#      nsid       cid      dofx      dofy      dofz     dofrx     dofry     dofrz
           7         0         0         0         1         0         0         0
*SET_NODE_LIST_TITLE
Rig-Bod_x=0
$#       sid       da1       da2       da3       da4    solver
           7       0.0       0.0       0.0       0.0MECH
$#      nid1      nid2      nid3      nid4      nid5      nid6      nid7      nid8
           2      1080      1178      2354      2452      2550      2648      3138
        3236     15125     15223     15321     18359     18457     18555         0
*BOUNDARY_SPC_SET_ID
```

```
$#       id                                                                 heading
        0RigBod foxture
$#     nsid       cid      dofx      dofy      dofz     dofrx     dofry     dofrz
         9         0         0         1         1         1         1         1
*SET_NODE_LIST_TITLE
RigBod fixture
$#      sid       da1       da2       da3       da4    solver
         9       0.0       0.0       0.0       0.0MECH
$#     nid1      nid2      nid3      nid4      nid5      nid6      nid7      nid8
      6282         0         0         0         0         0         0         0
*CONTACT_AUTOMATIC_SURFACE_TO_SURFACE_TIEBREAK_ID
$#      cid                                                                  title
        0Contact-Bottom
$#     ssid      msid     sstyp     mstyp    sboxid    mboxid       spr       mpr
         1         2         0         0         0         0         0         0
$#       fs        fd        dc        vc       vdc    penchk        bt        dt
       0.0       0.0       0.0       0.0       0.0         0      0.01.00000E20
$#      sfs       sfm       sst       mst      sfst      sfmt       fsf       vsf
       1.0       1.0       0.0       0.0       1.0       1.0       1.0       1.0
$#   option      nfls      sfls     param    eraten    erates     ct2cn        cn
         2     0.003      0.02       0.0       0.0       0.0       0.0       0.0
*SET_SEGMENT_TITLE
Skin-Bottom_UP
$#      sid       da1       da2       da3       da4    solver
         1       0.0       0.0       0.0       0.0MECH
$#       n1        n2        n3        n4        a1        a2        a3        a4
     20910     21204     21205     20911       0.0       0.0       0.0       0.0
         0         0         0         0       0.0       0.0       0.0       0.0
*SET_SEGMENT_TITLE
Bottom-Ply-DOWN
$#      sid       da1       da2       da3       da4    solver
         2       0.0       0.0       0.0       0.0MECH
$#       n1        n2        n3        n4        a1        a2        a3        a4
      9714       765       764      9713       0.0       0.0       0.0       0.0
         0         0         0         0       0.0       0.0       0.0       0.0
*CONTACT_AUTOMATIC_SURFACE_TO_SURFACE_TIEBREAK_ID
$#      cid                                                                  title
        2Contact-Top
$#     ssid      msid     sstyp     mstyp    sboxid    mboxid       spr       mpr
         4         3         0         0         0         0         0         0
$#       fs        fd        dc        vc       vdc    penchk        bt        dt
       0.0       0.0       0.0       0.0       0.0         0      0.01.00000E20
$#      sfs       sfm       sst       mst      sfst      sfmt       fsf       vsf
       1.0       1.0       0.0       0.0       1.0       1.0       1.0       1.0
$#   option      nfls      sfls     param    eraten    erates     ct2cn        cn
         2     0.003      0.02       0.0       0.0       0.0       0.0       0.0
*SET_SEGMENT_TITLE
Skin-Top_DOWN
$#      sid       da1       da2       da3       da4    solver
         4       0.0       0.0       0.0       0.0MECH
$#       n1        n2        n3        n4        a1        a2        a3        a4
     17851     18145     18144     17850       0.0       0.0       0.0       0.0
         0         0         0         0       0.0       0.0       0.0       0.0
*SET_SEGMENT_TITLE
Ply-Top_UP
$#      sid       da1       da2       da3       da4    solver
         3       0.0       0.0       0.0       0.0MECH
$#       n1        n2        n3        n4        a1        a2        a3        a4
      4845      8600      8601      4846       0.0       0.0       0.0       0.0
         0         0         0         0       0.0       0.0       0.0       0.0
*CONTACT_AUTOMATIC_SURFACE_TO_SURFACE_ID
$#      cid                                                                  title
        0Impactor-Fixture
$#     ssid      msid     sstyp     mstyp    sboxid    mboxid       spr       mpr
         7         8         0         0         0         0         0         0
$#       fs        fd        dc        vc       vdc    penchk        bt        dt
       0.0       0.0       0.0       0.0       0.0         0      0.01.00000E20
$#      sfs       sfm       sst       mst      sfst      sfmt       fsf       vsf
       1.0       1.0       0.0       0.0       1.0       1.0       1.0       1.0
*SET_SEGMENT_TITLE
Fixture-Move_ImpactorSide
```

286

```
$#      sid       da1       da2       da3       da4    solver
          7       0.0       0.0       0.0       0.0MECH
$#       n1        n2        n3        n4        a1        a2        a3        a4
       6119      6124      6169      6164       0.0       0.0       0.0       0.0
          0         0         0         0       0.0       0.0       0.0       0.0
*SET_SEGMENT_TITLE
Impactor
$#      sid       da1       da2       da3       da4    solver
          8       0.0       0.0       0.0       0.0MECH
$#       n1        n2        n3        n4        a1        a2        a3        a4
       5356      5355      5361      5362       0.0       0.0       0.0       0.0
          0         0         0         0       0.0       0.0       0.0       0.0
*CONTACT_TIED_SURFACE_TO_SURFACE_ID
$#      cid                                                               title
       03DFML-Fixture
$#     ssid      msid     sstyp     mstyp    sboxid    mboxid       spr       mpr
          5         6         0         0         0         0         1         1
$#       fs        fd        dc        vc       vdc    penchk        bt        dt
        0.0       0.0       0.0       0.0       0.0         0      0.01.00000E20
$#      sfs       sfm       sst       mst      sfst      sfmt       fsf       vsf
        1.0       1.0       0.0       0.0       1.0       1.0       1.0       1.0
*SET_SEGMENT_TITLE
x=L
$#      sid       da1       da2       da3       da4    solver
          5       0.0       0.0       0.0       0.0MECH
$#       n1        n2        n3        n4        a1        a2        a3        a4
      14634     14732     13262     13164       0.0       0.0       0.0       0.0
          0         0         0         0       0.0       0.0       0.0       0.0
*SET_SEGMENT_TITLE
Fixture-Move_x=L
$#      sid       da1       da2       da3       da4    solver
          6       0.0       0.0       0.0       0.0MECH
$#       n1        n2        n3        n4        a1        a2        a3        a4
       6145      6140      6185      6190       0.0       0.0       0.0       0.0
          0         0         0         0       0.0       0.0       0.0       0.0
*PART
$#                                                                         title
Ply-Bottom
$#      pid     secid       mid     eosid      hgid      grav    adpopt      tmid
          2         1         1         0         0         0         0         0
*SECTION_SOLID_TITLE
Section-Solid
$#    secid    elform       aet
          1         1         0
*MAT_ENHANCED_COMPOSITE_DAMAGE_TITLE
MAT_54-fiberglass_Skins
$#      mid        ro        ea        eb      (ec)      prba     (prca)    (prcb)
       11.75000E-6       9.0       9.0      2.55      0.05      0.05     0.428
$#      gab       gbc       gca      (kf)      aopt      2way
        1.0       1.0       1.0       0.0       2.0       0.0
$#       xp        yp        zp        a1        a2        a3    mangle
        0.0       0.0       0.0       1.0       0.0       0.0       0.0
$#       v1        v2        v3        d1        d2        d3    dfailm    dfails
        0.0       0.0       0.0       0.0       0.0       1.0       0.0       0.0
$#    tfail      alph      soft      fbrt     ycfac    dfailt    dfailc       efs
        0.0       0.0       1.0       0.0       2.0       0.0       0.0       0.0
$#       xc        xt        yc        yt        sc      crit      beta
      0.173     0.173     0.173     0.173      0.03      54.0       0.0
$#      pel      epsf      epsr      tsmd     soft2
        0.0       0.0       0.0       0.0       1.0
$#   slimt1    slimc1    slimt2    slimc2     slims    ncyred     softg
        0.0       0.0       0.0       0.0       0.0       0.0       1.0
*MAT_ADD_EROSION_TITLE
Foam-erosion
$#      mid      excl    mxpres     mneps    effeps    voleps    numfip       ncs
          4       0.0       0.0       0.0      0.15       0.0       1.0       1.0
$#   mnpres     sigp1     sigvm     mxeps     epssh     sigth   impulse    failtm
        0.0       0.0       0.0       0.0       0.0       0.0       0.0       0.0
$#     idam     dmgtyp     lcsdg     ecrit    dmgexp      dcrit    fadexp    lcregd
          0       0.0       0.0       0.0       1.0       0.0       1.0         0
$#    lcfld              epsthin     engcrt    radcrt
```

```
         0          0        0.0        0.0        0.0
*MAT_PIECEWISE_LINEAR_PLASTICITY_LOG_INTERPOLATION_TITLE
MAT_24-Mg
$#       mid         ro          e         pr       sigy       etan       fail       tdel
         21.74000E-6       36.0       0.35      0.231       0.01.00000E21        0.0
$#         c          p       lcss       lcsr         vp        lcf
         0.0        0.0          1          0        0.0          0
$#      eps1       eps2       eps3       eps4       eps5       eps6       eps7       eps8
         0.0        0.0        0.0        0.0        0.0        0.0        0.0        0.0
$#       es1        es2        es3        es4        es5        es6        es7        es8
         0.0        0.0        0.0        0.0        0.0        0.0        0.0        0.0
*MAT_CRUSHABLE_FOAM_TITLE
MAT_63-Foam
$#       mid         ro          e         pr       lcid        tsc       damp
         31.28100E-7       0.05        0.0          3        0.0        0.0
*MAT_ELASTIC_TITLE
MAT_001-Elastic-foam
$#       mid         ro          e         pr         da         db   not used
         41.28100E-7       0.05        0.0        0.0        0.0          0
*MAT_ELASTIC_TITLE
MAT_001-Aluminum
$#       mid         ro          e         pr         da         db   not used
         52.70000E-6       70.0       0.33        0.0        0.0          0
*MAT_ELASTIC_TITLE
MAT_001-Impactor
$#       mid         ro          e         pr         da         db   not used
         64.80000E-5      200.0        0.3        0.0        0.0          0
*MAT_ENHANCED_COMPOSITE_DAMAGE_TITLE
MAT_54-fiberglass_Pillars
$#       mid         ro         ea         eb       (ec)       prba      (prca)     (prcb)
         71.75000E-6        3.0        1.0        2.0       0.05       0.05      0.428
$#       gab        gbc        gca       (kf)       aopt       2way
         1.0        1.0        1.0        0.0        2.0        0.0
$#        xp         yp         zp         a1         a2         a3     mangle
         0.0        0.0        0.0        0.5       0.86        0.0        0.0
$#        v1         v2         v3         d1         d2         d3     dfailm     dfails
         0.0        0.0        0.0        0.0        1.0        0.0        0.0        0.0
$#      tfail       alph       soft       fbrt      ycfac     dfailt     dfailc        efs
         0.0        0.0        1.0        0.0        2.0        0.0        0.0        0.0
$#        xc         xt         yc         yt         sc       crit       beta
        0.08       0.08       0.08       0.08       0.03       54.0        0.0
$#       pel       epsf       epsr       tsmd      soft2
         0.0        0.0        0.0        0.0        1.0
$#     slimt1     slimc1     slimt2     slimc2      slims     ncyred      softg
         0.0        0.0        0.0        0.0        0.0        0.0        1.0
*INITIAL_VELOCITY
$#      nsid     nsidex      boxid     irigid       icid
           8          0          0          0          0
$#        vx         vy         vz        vxr        vyr        vzr
     -1.2512        0.0        0.0        0.0        0.0        0.0
*DEFINE_TABLE_TITLE
Table_Mg-Rate
$#      tbid        sfa       offa
           6
$#               value       lcid
                 0.0          3
   9.9999997474e-005          4
                 0.1          5
*DEFINE_CURVE_TITLE
Mg-Rate_0
$#      lcid       sidr        sfa        sfo       offa       offo     dattyp      lcint
           3          0        1.0        1.0        0.0        0.0          0          0
$#                  a1                    o1
                 0.0                0.2317
               0.001              0.233996
               0.002              0.236232
               0.003               0.23841
               0.004               0.24053
               0.005              0.242595
               0.006              0.244605
               0.007              0.246561
```

0.008	0.248465
0.009	0.250317
0.01	0.252119
0.011	0.253872
0.012	0.255576
0.013	0.257234
0.014	0.258845
0.015	0.260411
0.016	0.261933
0.017	0.263412
0.018	0.264849
0.019	0.266245
0.02	0.267601
0.021	0.268918
0.022	0.270196
0.023	0.271437
0.024	0.272641
0.025	0.27381
0.026	0.274944
0.027	0.276044
0.028	0.277112
0.029	0.278147
0.03	0.279151
0.031	0.280124
0.032	0.281068
0.033	0.281983
0.034	0.28287
0.035	0.283729
0.036	0.284562
0.037	0.285369
0.038	0.286151
0.039	0.286908
0.04	0.287641
0.041	0.288352
0.042	0.28904
0.043	0.289707
0.044	0.290352
0.045	0.290977
0.046	0.291583
0.047	0.292169
0.048	0.292737
0.049	0.293287
0.05	0.29382
0.051	0.294335
0.052	0.294835
0.053	0.295319
0.054	0.295788
0.055	0.296243
0.056	0.296683
0.057	0.29711
0.058	0.297525
0.059	0.297926
0.06	0.298316
0.061	0.298694
0.062	0.299061
0.063	0.299418
0.064	0.299764
0.065	0.300101
0.066	0.300428
0.067	0.300747
0.068	0.301057
0.069	0.301359
0.07	0.301654
0.071	0.301941
0.072	0.302221
0.073	0.302495
0.074	0.302762
0.075	0.303024
0.076	0.30328
0.077	0.303531
0.078	0.303777

```
          0.079               0.304019
           0.08               0.304256
          0.081               0.304489
          0.082               0.304719
          0.083               0.304945
          0.084               0.305168
          0.085               0.305389
          0.086               0.305606
          0.087               0.305822
          0.088               0.306035
          0.089               0.306246
           0.09               0.306456
          0.091               0.306664
          0.092               0.306871
          0.093               0.307077
          0.094               0.307282
          0.095               0.307486
          0.096                0.30769
          0.097               0.307894
          0.098               0.308097
          0.099               0.308301
            0.1               0.308504
*DEFINE_CURVE_TITLE
Mg-Rate_0.0001
$#     lcid      sidr       sfa       sfo      offa      offo    dattyp     lcint
          4         0       1.0       1.0       0.0       0.0         0         0
$#                   a1                  o1
            0.0               0.2478
          0.001               0.25058
          0.002              0.253233
          0.003              0.255766
          0.004              0.258181
          0.005              0.260485
          0.006              0.262681
          0.007              0.264773
          0.008              0.266766
          0.009              0.268665
           0.01              0.270472
          0.011              0.272192
          0.012              0.273829
          0.013              0.275386
          0.014              0.276868
          0.015              0.278276
          0.016              0.279616
          0.017               0.28089
          0.018              0.282102
          0.019              0.283253
           0.02              0.284349
          0.021              0.285391
          0.022              0.286383
          0.023              0.287326
          0.024              0.288225
          0.025              0.289081
          0.026              0.289896
          0.027              0.290675
          0.028              0.291417
          0.029              0.292127
           0.03              0.292806
          0.031              0.293456
          0.032              0.294079
          0.033              0.294677
          0.034              0.295252
          0.035              0.295806
          0.036               0.29634
          0.037              0.296857
          0.038              0.297357
          0.039              0.297842
           0.04              0.298314
          0.041              0.298774
          0.042              0.299223
          0.043              0.299663
```

```
                   0.044                0.300094
                   0.045                0.300519
                   0.046                0.300937
                   0.047                 0.30135
                   0.048                0.301758
                   0.049                0.302164
                    0.05                0.302567
                   0.051                0.302968
                   0.052                0.303368
                   0.053                0.303767
                   0.054                0.304167
                   0.055                0.304568
                   0.056                0.304969
                   0.057                0.305373
                   0.058                0.305779
                   0.059                0.306187
                    0.06                0.306598
                   0.061                0.307012
                   0.062                 0.30743
                   0.063                0.307851
                   0.064                0.308276
                   0.065                0.308705
                   0.066                0.309138
                   0.067                0.309574
                   0.068                0.310015
                   0.069                 0.31046
                    0.07                0.310909
                   0.071                0.311361
                   0.072                0.311818
                   0.073                0.312278
                   0.074                0.312741
                   0.075                0.313208
                   0.076                0.313678
                   0.077                0.314151
                   0.078                0.314627
                   0.079                0.315105
                    0.08                0.315585
                   0.081                0.316067
                   0.082                 0.31655
                   0.083                0.317034
                   0.084                0.317519
                   0.085                0.318004
                   0.086                 0.31849
                   0.087                0.318975
                   0.088                0.319459
                   0.089                0.319942
                    0.09                0.320423
                   0.091                0.320902
                   0.092                0.321379
                   0.093                0.321853
                   0.094                0.322323
                   0.095                 0.32279
                   0.096                0.323252
                   0.097                 0.32371
                   0.098                0.324163
                   0.099                 0.32461
                     0.1                0.325051
*DEFINE_CURVE_TITLE
Mg-Rate_0.1
$#     lcid      sidr       sfa       sfo      offa      offo    dattyp     lcint
          5         0       1.0       1.0       0.0       0.0         0         0
$#                   a1                  o1
                    0.0                0.2531
                  0.001              0.256577
                  0.002              0.259842
                  0.003              0.262909
                  0.004              0.265789
                  0.005              0.268493
                  0.006              0.271031
                  0.007              0.273414
                  0.008              0.275652
```

0.009	0.277754
0.01	0.279729
0.011	0.281585
0.012	0.283332
0.013	0.284976
0.014	0.286525
0.015	0.287987
0.016	0.289367
0.017	0.290672
0.018	0.291909
0.019	0.293083
0.02	0.294199
0.021	0.295262
0.022	0.296278
0.023	0.29725
0.024	0.298183
0.025	0.29908
0.026	0.299945
0.027	0.300782
0.028	0.301593
0.029	0.302382
0.03	0.303151
0.031	0.303901
0.032	0.304636
0.033	0.305358
0.034	0.306067
0.035	0.306766
0.036	0.307455
0.037	0.308136
0.038	0.30881
0.039	0.309478
0.04	0.31014
0.041	0.310797
0.042	0.311448
0.043	0.312095
0.044	0.312737
0.045	0.313375
0.046	0.314008
0.047	0.314635
0.048	0.315258
0.049	0.315874
0.05	0.316484
0.051	0.317088
0.052	0.317684
0.053	0.318272
0.054	0.318852
0.055	0.319422
0.056	0.319982
0.057	0.320532
0.058	0.321069
0.059	0.321595
0.06	0.322107
0.061	0.322606
0.062	0.32309
0.063	0.32356
0.064	0.324013
0.065	0.324451
0.066	0.324872
0.067	0.325276
0.068	0.325663
0.069	0.326032
0.07	0.326383
0.071	0.326717
0.072	0.327033
0.073	0.327332
0.074	0.327614
0.075	0.327879
0.076	0.328129
0.077	0.328363
0.078	0.328583
0.079	0.32879

```
                 0.08             0.328985
                 0.081            0.32917
                 0.082            0.329346
                 0.083            0.329516
                 0.084            0.329681
                 0.085            0.329844
                 0.086            0.330008
                 0.087            0.330174
                 0.088            0.330347
                 0.089            0.33053
                  0.09            0.330726
                 0.091            0.330938
                 0.092            0.331173
                 0.093            0.331432
                 0.094            0.331722
                 0.095            0.332048
                 0.096            0.332414
                 0.097            0.332827
                 0.098            0.333293
                 0.099            0.333817
                   0.1            0.334407
*DEFINE_CURVE_TITLE
Curve-Mg
$#     lcid      sidr      sfa      sfo     offa     offo    dattyp    lcint
          1         0      1.0      1.0      0.0      0.0         0         0
$#               a1                o1
                0.0            0.2317
             0.0093            0.2558
             0.0219            0.2705
             0.0335            0.2826
             0.0597            0.2946
             0.1218            0.3161
              0.188            0.3295
             0.2501            0.3402
             0.3132            0.3429
*DEFINE_CURVE_TITLE
Curve-foam
$#     lcid      sidr      sfa      sfo     offa     offo    dattyp    lcint
          2         0      1.0      1.0      0.0      0.0         0         0
$#               a1                o1
                0.0               0.0
               0.13           0.00749
                0.2            0.0075
                0.4            0.0076
                0.5             0.011
                0.6             0.017
                0.7             0.029
               0.75             0.035
*DEFINE_CURVE_TITLE
Damping mass
$#     lcid      sidr      sfa      sfo     offa     offo    dattyp    lcint
          7         0      1.0      1.0      0.0      0.0         0         0
$#               a1                o1
                0.0               1.0
               16.0               1.0
*SET_NODE_LIST_TITLE
x=L
$#      sid       da1      da2      da3      da4   solver
          2       0.0      0.0      0.0      0.0MECH
$#     nid1      nid2     nid3     nid4     nid5     nid6     nid7     nid8
         99       197      295      393      491      589      687      785
...
*SET_NODE_LIST_TITLE
Impactor
$#      sid       da1      da2      da3      da4   solver
          8       0.0      0.0      0.0      0.0MECH
$#     nid1      nid2     nid3     nid4     nid5     nid6     nid7     nid8
       5294      5295     5296     5297     5298     5299     5300     5301
...
*SET_NODE_LIST_TITLE
3DFML
```

```
$#       sid        da1        da2        da3        da4     solver
          11        0.0        0.0        0.0        0.0MECH
$#      nid1       nid2       nid3       nid4       nid5       nid6       nid7       nid8
       18359      18360      18361      18362      18363      18364      18365      18366
...
*SET_PART_LIST_TITLE
Part Mg
$#       sid        da1        da2        da3        da4     solver
           1        0.0        0.0        0.0        0.0MECH
$#      pid1       pid2       pid3       pid4       pid5       pid6       pid7       pid8
           1          2          3          4          5          8          0          0
*DAMPING_FREQUENCY_RANGE_DEFORM
$#     cdamp       flow      fhigh       psid      blank     pidrel
        0.07        9.0       11.0          1          0          0
*PERTURBATION_NODE
$#      type       nsid        scl        cmp     icoord        cid
           1         11        1.0          2          0          0
$#      ampl        xwl       xoff        ywl       yoff        zwl       zoff
         1.0      388.0        0.0        0.0        0.0        0.0        0.0
*END
```

Stress State Analysis Models (Chapter 8)

```
*KEYWORD
*TITLE
$#                                                                         title
3D-FML with Magnesium skin
*CONTROL_HOURGLASS
$#     ihq        qh
         1       0.1
*CONTROL_IMPLICIT_DYNAMICS
$#   imass     gamma      beta    tdybir    tdydth    tdybur     irate
         0       0.5      0.25      0.01.00000E281.00000E28         0
*CONTROL_IMPLICIT_GENERAL
$#  imflag       dt0    imform      nsbs       igs     cnstn      form    zero_v
         1       0.0         2         1         2         0         0         0
*CONTROL_IMPLICIT_SOLUTION
$#  nsolvr    ilimit    maxref     dctol     ectol     rctol     lstol    abstol
         1        11        15     0.001     0.011.00000E10       0.91.0000E-10
$#   dnorm     diverg     istif   nlprint    nlnorm   d3itctl     cpchk
         2         1         1         0         2         0         0
$#  arcctl    arcdir    arclen    arcmth    arcdmp    arcpsi    arcalf    arctim
         0         0       0.0         1         2         0         0         0
$#   lsmtd     lsdir      irad      srad      awgt      sred
         4         2       0.0       0.0       0.0       0.0
*CONTROL_TERMINATION
$#  endtim    endcyc     dtmin    endeng    endmas
       1.0         0       0.0      0.01.000000E8
*BOUNDARY_SPC_SET_ID
$#      id                                                                heading
         0Fixed
$#    nsid       cid      dofx      dofy      dofz     dofrx     dofry     dofrz
         1         0         1         1         0         0         0         0
*SET_NODE_LIST_TITLE
Fixed
$#     sid       da1       da2       da3       da4    solver
         1       0.0       0.0       0.0       0.0MECH
$#    nid1      nid2      nid3      nid4      nid5      nid6      nid7      nid8
     14876     14877     14878     14879     14880     14881     14882     14883
...
*BOUNDARY_SPC_SET_ID
$#      id                                                                heading
         0Symm
$#    nsid       cid      dofx      dofy      dofz     dofrx     dofry     dofrz
         2         0         1         0         0         0         0         0
*SET_NODE_LIST_TITLE
Symm
$#     sid       da1       da2       da3       da4    solver
         2       0.0       0.0       0.0       0.0MECH
$#    nid1      nid2      nid3      nid4      nid5      nid6      nid7      nid8
         1         2         3         4         5         6         7         8
...
*LOAD_NODE_POINT
$#     nid       dof      lcid        sf       cid        m1        m2        m3
     24709         2         1     -0.01         0         0         0         0
*PART
$#                                                                         title
Magnesium top
$#     pid     secid       mid     eosid      hgid      grav    adpopt      tmid
         1         1         1         0         0         0         0         0
*SECTION_SHELL_TITLE
Shell 15 axisymm
$#   secid     elform      shrf       nip     propt   qr/irid     icomp     setyp
         1        15       1.0         2       1.0         0         0         1
$#      t1        t2        t3        t4      nloc     marea      idof    edgset
       0.0       0.0       0.0       0.0       0.0       0.0       0.0         0
*MAT_ELASTIC_TITLE
Magnesium
$#     mid        ro         e        pr        da        db  not used
        11.74000E-6      36.0      0.35       0.0       0.0         0
*PART
```

```
$#                                                                        title
FRP top
$#     pid    secid     mid    eosid     hgid     grav   adpopt     tmid
         2        1        2        0        0        0        0        0
*MAT_ELASTIC_TITLE
FRP
$#     mid       ro        e       pr       da       db not used
       21.75000E-6      9.0    0.254      0.0      0.0        0
*PART
$#                                                                        title
Core
$#     pid    secid     mid    eosid     hgid     grav   adpopt     tmid
         3        1        3        0        0        0        0        0
*MAT_ELASTIC_TITLE
Core
$#     mid       ro        e       pr       da       db not used
       32.70000E-7     0.31     0.07      0.0      0.0        0
*PART
$#                                                                        title
FRP bottom
$#     pid    secid     mid    eosid     hgid     grav   adpopt     tmid
         4        1        2        0        0        0        0        0
*PART
$#                                                                        title
Magnesium bottom
$#     pid    secid     mid    eosid     hgid     grav   adpopt     tmid
         5        1        1        0        0        0        0        0
*DEFINE_CURVE
$#    lcid     sidr      sfa      sfo     offa     offo   dattyp    lcint
         1        0      1.0      1.0      0.0      0.0        0        0
$#              a1                o1
               0.0               0.0
               1.0               1.0
*END




$# LS-DYNA Keyword file created by LS-PrePost(R) V4.3.20 - 09Jan2018
$# Created on Aug-21-2019 (10:48:06)
*KEYWORD
*TITLE
$#                                                                        title
3D-FML with Steel skin
*CONTROL_HOURGLASS
$#     ihq       qh
         1      0.1
*CONTROL_IMPLICIT_DYNAMICS
$#   imass    gamma     beta    tdybir    tdydth    tdybur    irate
         0      0.5     0.25      0.01.00000E281.00000E28        0
*CONTROL_IMPLICIT_GENERAL
$#  imflag      dt0    imform     nsbs      igs    cnstn     form   zero_v
         1      0.0        2        1        2        0        0        0
*CONTROL_IMPLICIT_SOLUTION
$#  nsolvr   ilimit   maxref    dctol    ectol    rctol    lstol   abstol
         1       11       15    0.001    0.011.00000E10       0.91.0000E-10
$#   dnorm    diverg    istif   nlprint   nlnorm  d3itctl    cpchk
         2        1        1        0        2        0        0
$#  arcctl   arcdir   arclen   arcmth   arcdmp   arcpsi   arcalf   arctim
         0        0      0.0        1        2        0        0        0
$#   lsmtd    lsdir     irad     srad     awgt     sred
         4        2      0.0      0.0      0.0      0.0
*CONTROL_TERMINATION
$#  endtim   endcyc    dtmin   endeng   endmas
       1.0        0      0.0      0.01.000000E8
*BOUNDARY_SPC_SET_ID
$#      id                                                              heading
         0Fixed
$#    nsid      cid     dofx     dofy     dofz    dofrx    dofry    dofrz
         1        0        1        1        0        0        0        0
*SET_NODE_LIST_TITLE
```

```
Fixed
$#       sid       da1       da2       da3       da4    solver
           1       0.0       0.0       0.0       0.0MECH
$#      nid1      nid2      nid3      nid4      nid5      nid6      nid7      nid8
       14876     14877     14878     14879     14880     14881     14882     14883
...
*BOUNDARY_SPC_SET_ID
$#        id                                                           heading
           0Symm
$#       nsid       cid      dofx      dofy      dofz     dofrx     dofry     dofrz
           2         0         1         0         0         0         0         0
*SET_NODE_LIST_TITLE
Symm
$#       sid       da1       da2       da3       da4    solver
           2       0.0       0.0       0.0       0.0MECH
$#      nid1      nid2      nid3      nid4      nid5      nid6      nid7      nid8
           1         2         3         4         5         6         7         8
...
*LOAD_NODE_POINT
$#       nid       dof      lcid        sf       cid        m1        m2        m3
       24729         2         1     -0.01         0         0         0         0
*PART
$#                                                                            title
Magnesium top
$#       pid     secid       mid     eosid      hgid      grav    adpopt      tmid
           1         1         1         0         0         0         0         0
*SECTION_SHELL_TITLE
Shell 15 axisymm
$#     secid     elform      shrf       nip     propt   qr/irid     icomp     setyp
           1        15       1.0         2       1.0         0         0         1
$#        t1        t2        t3        t4      nloc     marea      idof    edgset
         0.0       0.0       0.0       0.0       0.0       0.0       0.0         0
*MAT_ELASTIC_TITLE
Steel
$#       mid        ro         e        pr        da        db  not used
       17.80000E-6     200.0       0.3       0.0       0.0         0
*PART
$#                                                                            title
FRP top
$#       pid     secid       mid     eosid      hgid      grav    adpopt      tmid
           2         1         2         0         0         0         0         0
*MAT_ELASTIC_TITLE
FRP
$#       mid        ro         e        pr        da        db  not used
       21.75000E-6       9.0     0.254       0.0       0.0         0
*PART
$#                                                                            title
Core
$#       pid     secid       mid     eosid      hgid      grav    adpopt      tmid
           3         1         3         0         0         0         0         0
*MAT_ELASTIC_TITLE
Core
$#       mid        ro         e        pr        da        db  not used
       32.70000E-7      0.31      0.07       0.0       0.0         0
*PART
$#                                                                            title
FRP bottom
$#       pid     secid       mid     eosid      hgid      grav    adpopt      tmid
           4         1         2         0         0         0         0         0
*PART
$#                                                                            title
Magnesium bottom
$#       pid     secid       mid     eosid      hgid      grav    adpopt      tmid
           5         1         1         0         0         0         0         0
*DEFINE_CURVE
$#      lcid      sidr       sfa       sfo      offa      offo    dattyp     lcint
           1         0       1.0       1.0       0.0       0.0         0         0
$#                 a1                  o1
                  0.0                 0.0
                  1.0                 1.0
*END
```

297

Double Cantilever Beam Model (Chapter 9)

```
*KEYWORD
*TITLE
$#                                                                         title
Mode 1 shell XFEM
*CONTROL_ENERGY
$#     hgen      rwen    slnten     rylen
          2         2         2         2
*CONTROL_HOURGLASS
$#      ihq        qh
          1       0.1
*CONTROL_TERMINATION
$#   endtim     endcyc     dtmin     endeng    endmas
       10.0         0       0.0       0.01.000000E8
*CONTROL_TIMESTEP
$#   dtinit    tssfac      isdo    tslimt     dt2ms      lctm     erode     ms1st
        0.0       0.9         2       0.0       0.0         0         0         0
$#   dt2msf    dt2mslc     imscl    unused    unused     rmscl
        0.0         0         0                           0.0
*DATABASE_NODFOR
$#       dt    binary      lcur     ioopt
       0.01         0         0         1
*DATABASE_BINARY_D3PLOT
$#       dt      lcdt      beam     npltc    psetid
       0.01         0         0         0         0
$#    ioopt
          0
*DATABASE_EXTENT_BINARY
$#    neiph     neips    maxint    strflg    sigflg    epsflg    rltflg    engflg
          0         1         3         0         1         1         1         1
$#   cmpflg    ieverp    beamip     dcomp      shge     stssz    n3thdt   ialemat
          0         0         0         1         1         1         2         1
$# nintsld    pkp_sen      sclp     hydro     msscl     therm    intout    nodout
          0         0       1.0         0         0         0
$#     dtdt    resplt     neipb
          0         0         0
*DATABASE_NODAL_FORCE_GROUP
$#     nsid       cid
          1         0
*DATABASE_NODAL_FORCE_GROUP
$#     nsid       cid
          2         0
*BOUNDARY_PRESCRIBED_MOTION_SET_ID
$#       id                                                                heading
          0Load
$#     nsid       dof       vad      lcid        sf       vid     death     birth
          2         2         2         1      15.0        01.00000E28       0.0
*BOUNDARY_SPC_SET_ID
$#       id                                                                heading
          0Fixed
$#     nsid       cid      dofx      dofy      dofz     dofrx     dofry     dofrz
          1         0         1         1         0         0         0         0
*SET_NODE_LIST_TITLE
Fixed
$#      sid       da1       da2       da3       da4    solver
          1       0.0       0.0       0.0       0.0MECH
$#     nid1      nid2      nid3      nid4      nid5      nid6      nid7      nid8
      23305     23314     23323     23332     23341     23350         0         0
*BOUNDARY_SPC_SET_ID
$#       id                                                                heading
          0No Z
$#     nsid       cid      dofx      dofy      dofz     dofrx     dofry     dofrz
          3         0         0         0         1         0         0         0
*SET_NODE_LIST_TITLE
Whole model
$#      sid       da1       da2       da3       da4    solver
          3       0.0       0.0       0.0       0.0MECH
$#     nid1      nid2      nid3      nid4      nid5      nid6      nid7      nid8
      23305     23306     23307     23308     23309     23310     23311     23312
```

```
...
*BOUNDARY_PRECRACK
$#      pid     ctype       np
          2         1        0
$#        x         y        z
        0.0       4.5      0.0
         50         4        0
*PART
$#                                                                  title
Beam top
$#      pid     secid      mid     eosid      hgid      grav    adpopt      tmid
          1         1        1         0         0         0         0         0
*SECTION_SHELL_TITLE
Shell
$#    secid    elform      shrf       nip     propt    qr/irid     icomp     setyp
          1         2       1.0         1       1.0         0         0         1
$#       t1        t2        t3        t4      nloc     marea      idof    edgset
       25.0      25.0      25.0      25.0       0.0       0.0       0.0         0
*MAT_ELASTIC_TITLE
Fiberglass
$#      mid        ro         e        pr        da        db  not used
       11.60000E-6      25.0       0.3       0.0       0.0         0
*PART
$#                                                                  title
Adhesive
$#      pid     secid      mid     eosid      hgid      grav    adpopt      tmid
          2         2        5         0         0         0         0         0
*SECTION_SHELL_XFEM_TITLE
Shell XFEM
$#    secid    elform      shrf       nip     propt    qr/irid     icomp     setyp
          2         2       1.0         4       1.0         0         0         1
$#       t1        t2        t3        t4      nloc     marea
       25.0      25.0      25.0      25.0       0.0       0.0
$#     cmid     baselm    domint    failcr    propcr    lprint
          2        16         0         1         0         1
*MAT_ELASTIC_TITLE
Adhesive elastic
$#      mid        ro         e        pr        da        db  not used
       51.18000E-6       3.0       0.3       0.0       0.0         0
*PART
$#                                                                  title
Beam Bottom
$#      pid     secid      mid     eosid      hgid      grav    adpopt      tmid
          3         1        1         0         0         0         0         0
*PART
$#                                                                  title
Cohesive top
$#      pid     secid      mid     eosid      hgid      grav    adpopt      tmid
          4         3        3         0         0         0         0         0
*SECTION_SHELL_TITLE
Shell Cohesive
$#    secid    elform      shrf       nip     propt    qr/irid     icomp     setyp
          3        29       1.0         1       1.0         0         0         1
$#       t1        t2        t3        t4      nloc     marea      idof    edgset
       25.0      25.0      25.0      25.0       0.0       0.0       0.0         0
*MAT_COHESIVE_TH_TITLE
COHESIVE_TH cohesive
$#      mid        ro      roflg   intfall    sigmax       nls       tls
       31.20000E-6         0       1.0     0.008     0.015      0.02
$#   lamda1    lamda2    lamdaf     stfsf
        0.5       0.5       1.0      10.0
*PART
$#                                                                  title
Cohesive bottom
$#      pid     secid      mid     eosid      hgid      grav    adpopt      tmid
          5         3        3         0         0         0         0         0
*MAT_COHESIVE_TH_TITLE
COHESIVE_TH xfem
$#      mid        ro      roflg   intfall    sigmax       nls       tls
       21.20000E-6         0       1.0     0.008     0.015      0.02
$#   lamda1    lamda2    lamdaf     stfsf
```

```
        0.5          0.5          1.0         10.0
*DEFINE_CURVE_TITLE
Curve
$#     lcid      sidr       sfa       sfo      offa      offo    dattyp     lcint
          1         0       1.0       1.0       0.0       0.0         0         0
$#                   a1                  o1
                    0.0                 0.0
                   10.0                 1.0
*SET_NODE_LIST_TITLE
Load
$#      sid       da1       da2       da3       da4    solver
          2       0.0       0.0       0.0       0.0MECH
$#     nid1      nid2      nid3      nid4      nid5      nid6      nid7      nid8
      33530     33539     33548     33557     33566     33575         0         0
*END
```

Impact Model using Cohesive and xFEM Elements (Chapter 9)

```
*KEYWORD
*TITLE
$#                                                                        title
Skin delamination xFEM + Cohesive
*CONTROL_ENERGY
$#     hgen      rwen    slnten     rylen
          2         2         2         2
*CONTROL_HOURGLASS
$#      ihq        qh
          1       0.1
*CONTROL_TERMINATION
$# endtim    endcyc     dtmin    endeng    endmas
       0.2         0       0.0      0.01.000000E8
*CONTROL_TIMESTEP
$# dtinit    tssfac      isdo    tslimt     dt2ms      lctm     erode     ms1st
       0.0       0.5         0       0.0       0.0         0         0         0
$# dt2msf   dt2mslc     imscl    unused    unused     rmscl
       0.0         0         0                           0.0
*DATABASE_ELOUT
$#       dt    binary      lcur     ioopt   option1   option2   option3   option4
1.00000E-4         0         0         1         0         0         0         0
*DATABASE_GLSTAT
$#       dt    binary      lcur     ioopt
1.00000E-4         0         0         1
*DATABASE_NODFOR
$#       dt    binary      lcur     ioopt
1.00000E-4         0         0         1
*DATABASE_NODOUT
$#       dt    binary      lcur     ioopt   option1   option2
1.00000E-4         0         0         1       0.0         0
*DATABASE_BINARY_D3PLOT
$#       dt      lcdt      beam     npltc     psetid
1.00000E-4         0         0         0         0
$#    ioopt
          0
*DATABASE_EXTENT_BINARY
$#    neiph     neips    maxint    strflg    sigflg    epsflg    rltflg    engflg
          0         1         0         0         1         1         1         1
$#   cmpflg    ieverp    beamip     dcomp      shge     stssz    n3thdt   ialemat
          0         0         0         1         1         1         2         1
$# nintsld   pkp_sen      sclp     hydro     msscl     therm    intout    nodout
          0         0       1.0         0         0         0
$#     dtdt    resplt     neipb
          0         0         0
*DATABASE_NODAL_FORCE_GROUP
$#     nsid       cid
          1         0
*DATABASE_NODAL_FORCE_GROUP
$#     nsid       cid
          2         0
*BOUNDARY_PRESCRIBED_MOTION_SET_ID
$#       id                                                               heading
          0Compression
$#     nsid       dof       vad      lcid        sf       vid     death     birth
          2         1         2         1     -10.0        01.00000E28       0.0
*BOUNDARY_SPC_SET_ID
$#       id                                                               heading
          0No Y
$#     nsid       cid      dofx      dofy      dofz     dofrx     dofry     dofrz
          2         0         0         1         0         0         0         0
*SET_NODE_LIST_TITLE
Load
$#      sid       da1       da2       da3       da4    solver
          2       0.0       0.0       0.0       0.0MECH
$#     nid1      nid2      nid3      nid4      nid5      nid6      nid7      nid8
          1         2         5         6         7         8         9        10
...
*BOUNDARY_SPC_SET_ID
```

```
$#       id                                                          heading
        0Symm
$#      nsid        cid       dofx       dofy       dofz      dofrx      dofry      dofrz
           1          0          1          0          0          0          0          0
*SET_NODE_LIST_TITLE
Symm
$#       sid        da1        da2        da3        da4     solver
           1        0.0        0.0        0.0        0.0MECH
$#      nid1       nid2       nid3       nid4       nid5       nid6       nid7       nid8
       15071      15253      15435      15436      15437      15438      15439      15440
...
*BOUNDARY_SPC_SET_ID
$#       id                                                          heading
        0No Z
$#      nsid        cid       dofx       dofy       dofz      dofrx      dofry      dofrz
           4          0          0          0          1          0          0          0
*SET_NODE_LIST_TITLE
Whole
$#       sid        da1        da2        da3        da4     solver
           4        0.0        0.0        0.0        0.0MECH
$#      nid1       nid2       nid3       nid4       nid5       nid6       nid7       nid8
           1          2          3          4          5          6          7          8
...
*BOUNDARY_PRECRACK
$#      pid      ctype         np
           3          1          2
$#         x          y          z
         0.0     2.3053        0.0
          12          2          0
*PART
$#                                                                     title
Skin
$#      pid      secid        mid      eosid       hgid       grav     adpopt       tmid
           1          1          1          0          0          0          0          0
*SECTION_SHELL_TITLE
Shell
$#    secid     elform       shrf        nip      propt    qr/irid      icomp      setyp
           1          2        1.0          1        1.0          0          0          1
$#       t1         t2         t3         t4       nloc      marea       idof     edgset
        25.0       25.0       25.0       25.0        0.0        0.0        0.0          0
*MAT_ELASTIC_TITLE
Elastic - Magnesium
$#      mid         ro          e         pr         da         db   not used
        11.65000E-6       36.0       0.35        0.0        0.0          0
*PART
$#                                                                     title
Cohesive Top
$#      pid      secid        mid      eosid       hgid       grav     adpopt       tmid
           2          3          5          0          0          0          0          0
*SECTION_SHELL_TITLE
Shell Cohesive
$#    secid     elform       shrf        nip      propt    qr/irid      icomp      setyp
           3         29        1.0          1        1.0          0          0          1
$#       t1         t2         t3         t4       nloc      marea       idof     edgset
        25.0       25.0       25.0       25.0        0.0        0.0        0.0          0
*MAT_COHESIVE_TH_TITLE
Cohesive 185 COHESIVE
$#      mid         ro      roflg    intfall     sigmax        nls        tls
        51.50000E-6          0        1.0      0.008      0.015       0.02
$#   lamda1     lamda2     lamdaf      stfsf
         0.5        0.5        1.0      100.0
*PART
$#                                                                     title
Adhesive XFEM
$#      pid      secid        mid      eosid       hgid       grav     adpopt       tmid
           3          2          2          0          0          0          0          0
*SECTION_SHELL_XFEM_TITLE
Shell XFEM
$#    secid     elform       shrf        nip      propt    qr/irid      icomp      setyp
           2          2        1.0          4        1.0          0          0          1
$#       t1         t2         t3         t4       nloc      marea
```

302

```
        25.0      25.0      25.0      25.0       0.0       0.0
$#    cmid    baselm    domint    failcr    propcr    lprint
         4        16         0         1         0         0
*MAT_ELASTIC_TITLE
Elastic - Epoxy
$#     mid        ro         e        pr        da        db  not used
        21.50000E-6       3.0      0.25       0.0       0.0         0
*PART
$#                                                                         title
Cohesive Bottom
$#     pid     secid       mid     eosid      hgid      grav    adpopt      tmid
         4         3         5         0         0         0         0         0
*PART
$#                                                                         title
Beam
$#     pid     secid       mid     eosid      hgid      grav    adpopt      tmid
         5         1         3         0         0         0         0         0
*MAT_ELASTIC_TITLE
Elastic - Fiberglass
$#     mid        ro         e        pr        da        db  not used
        31.60000E-6       5.0     0.254       0.0       0.0         0
*MAT_COHESIVE_TH_TITLE
Cohesive 185 xFEM
$#     mid        ro     roflg   intfall    sigmax       nls       tls
        41.50000E-6         0       1.0     0.008     0.015      0.02
$#  lamda1    lamda2    lamdaf     stfsf
       0.5       0.5       1.0     100.0
*MAT_ELASTIC_TITLE
Elastic - Foam
$#     mid        ro         e        pr        da        db  not used
        61.00000E-7      0.05       0.0       0.0       0.0         0
*DEFINE_CURVE_TITLE
Compression curve
$#    lcid      sidr       sfa       sfo      offa      offo    dattyp     lcint
         1         0       1.0       1.0       0.0       0.0         0         0
$#              a1                  o1
               0.0                 0.0
              10.0                 1.0
*SET_NODE_LIST_TITLE
Perturbation Skin
$#     sid       da1       da2       da3       da4    solver
         3       0.0       0.0       0.0       0.0MECH
$#    nid1      nid2      nid3      nid4      nid5      nid6      nid7      nid8
       240      1969      2241      2513     12842     12939     13211     13483
...
*SET_NODE_LIST_TITLE
Perturbation Beam
$#     sid       da1       da2       da3       da4    solver
         5       0.0       0.0       0.0       0.0MECH
$#    nid1      nid2      nid3      nid4      nid5      nid6      nid7      nid8
         4       292       293       294       295       296       297       298
...
*PERTURBATION_NODE
$#    type      nsid       scl       cmp    icoord       cid
         1         3       1.0         2         0         0
$#    ampl       xwl      xoff       ywl      yoff       zwl      zoff
       0.1   49.7012      12.5       0.0       0.0       0.0       0.0
*PERTURBATION_NODE
$#    type      nsid       scl       cmp    icoord       cid
         1         5       1.0         2         0         0
$#    ampl       xwl      xoff       ywl      yoff       zwl      zoff
     -0.02   49.7012      12.5       0.0       0.0       0.0       0.0
*END
```

Appendix C: Copyright Permissions

Copyright Permission for Chapter 3

Copyright Permission for Chapter 4

June 14, 2019

Dr. François Robitaille, Co-Chair of the CANCOM2017 conference,

I am preparing my Ph.D. thesis for submission to the Faculty of Graduate Studies at Dalhousie University, Halifax, Nova Scotia, Canada. I am seeking your permission to include a manuscript version of the following conference paper as a chapter in the thesis:

Davide De Cicco and Farid Taheri. *Understanding the Parameters that Influence Buckling of 3D Fiber-Metal Laminates*. In 10th Canadian-International Conference on Composites (CANCOM2017), Ottawa, Ontario, Canada, July 17–20, 2017.

Canadian graduate theses are reproduced by the Library and Archives of Canada (formerly National Library of Canada) through a non-exclusive, world-wide license to reproduce, loan, distribute, or sell theses. I am also seeking your permission for the material described above to be reproduced and distributed by the LAC(NLC). Further details about the LAC(NLC) thesis program are available on the LAC(NLC) website (www.nlc-bnc.ca).

Full publication details and a copy of this permission letter will be included in the thesis.

Yours sincerely,

Davide De Cicco

Permission is granted for:

a) the inclusion of the material described above in your thesis.

b) for the material described above to be included in the copy of your thesis that is sent to the Library and Archives of Canada (formerly National Library of Canada) for reproduction and distribution.

Name: Francois Robitaille

Title: Professor, Mechanical Engineering, Director, Engineering Management Graduate Programs, University of Ottawa

Co-Chair, CANCOM2017
The Canadian - International Conference on Composites, 2017

Signature: _____   Date: June 17, 2019

Copyright Permission for Chapter 5

Copyright Clearance Center

RightsLink®

Home | Create Account | Help | LIVE CHAT

SAGE Publishing

Title: Robust numerical approaches for simulating the buckling response of 3D fiber-metal laminates under axial impact – Validation with experimental results

Author: Davide De Cicco, Farid Taheri

Publication: Journal of Sandwich Structures and Materials

Publisher: SAGE Publications

Date: 07/22/2018

Copyright © 2018, © SAGE Publications

LOGIN

If you're a copyright.com user, you can login to RightsLink using your copyright.com credentials.

Already a RightsLink user or want to learn more?

If you are a SAGE journal author requesting permission to reuse material from your journal article, please note you may be able to reuse your content without requiring permission from SAGE. Please review SAGE's author re-use and archiving policies at https://us.sagepub.com/en-us/nam/journal-author-archiving-policies-and-re-use for more information.

If your request does not fall within SAGE's reuse guidelines, please proceed with submitting your request by selecting one of the other reuse categories that describes your use. Please note, a fee may be charged for reuse of content requiring permission. Please contact permissions@sagepub.co.uk if you have questions.

BACK | CLOSE WINDOW

Copyright Permission for Chapter 6

June 9, 2109

Journal of Magnesium and Alloys

I am preparing my Ph.D. thesis for submission to the Faculty of Graduate Studies at Dalhousie University, Halifax, Nova Scotia, Canada. I am seeking your permission to include a manuscript version of the following paper(s) as a chapter in the thesis:

Davide De Cicco and Farid Taheri. *Enhancement of Magnesium-Composite Bond-Interface by a Simple Combined Abrasion and Coating Method*. Journal of Magnesium and Alloys, in press, 2019.

Canadian graduate theses are reproduced by the Library and Archives of Canada (formerly National Library of Canada) through a non-exclusive, world-wide license to reproduce, loan, distribute, or sell theses. I am also seeking your permission for the material described above to be reproduced and distributed by the LAC(NLC). Further details about the LAC(NLC) thesis program are available on the LAC(NLC) website (www.nlc-bnc.ca).

Full publication details and a copy of this permission letter will be included in the thesis.

Yours sincerely,

Davide De Cicco

Davide De Cicco
PhD candidate – composite materials
Dept. of Mechanical Engineering
Dalhousie University
Office D304 – D building
1360 Barrington Street, PO Box 15000
Halifax, NS, B3H 4R2, Canada
Cell: + 902.292.0381

ELSEVIER

Dear Davide De Cicco

We hereby grant you permission to reprint the material below at no charge **in your thesis** subject to the following conditions:

RE: Davide De Cicco and Farid Taheri. Enhancement of Magnesium-Composite Bond-Interface by a Simple Combined Abrasion and Coating Method. Journal of Magnesium and Alloys, in press, 2019.

1.   If any part of the material to be used (for example, figures) has appeared in our publication with credit or acknowledgement to another source, permission must also be sought from that source. If such permission is not obtained then that material may not be included in your publication/copies.

2.   Suitable acknowledgment to the source must be made, either as a footnote or in a reference list at the end of your publication, as follows:
"This article was published in Publication title, Vol number, Author(s), Title of article, Page Nos, Copyright Elsevier (or appropriate Society name) (Year)."

3.   Your thesis may be submitted to your institution in either print or electronic form.

4.   Reproduction of this material is confined to the purpose for which permission is hereby given

5.   This permission is granted for non-exclusive world **English** rights only. For other languages please reapply separately for each one required. Permission excludes use in an electronic form other than submission. Should you have a specific electronic project in mind please reapply for permission.

6.   This includes permission for UMI to supply single copies, on demand, of the complete thesis. Should your thesis be published commercially, please reapply for permission

7.   Posting of the full article online is not permitted. You may post an abstract with a link to the Elsevier website www.elsevier.com, or to the article on ScienceDirect if it is available on that platform.

Thanks & Regards,
Roopa Lingayath
Sr Copyrights Coordinator – Global Rights
Elsevier | Health Content Operations
(A division of Reed Elsevier India Pvt. Ltd.)

International Tech Park | Crest – 5th Floor | CSIR Road | Taramani | Chennai 600 113 | India
Tel: +91 44 3378 4167 | Fax: +91 44 4299 4568
E-mail: r.lingayath@elsevier.com | url: www.elsevier.com

Copyright Permission for Chapter 9